南臺科技大學
Southern Taiwan University of Science and Technology

ISBN 978-626-92572-6-3（平裝）

2026 功能性材料研討會暨國科會專題研究計畫成果發表會 論文集

南臺科技大學
Southern Taiwan University of Science and Technology

2026
功能性材料研討會暨國科會專題研究計畫成果發表會
論文集

研討會日期 /
2026 年 *5* 月 *29* 日(星期五)

研討會地點 /
南臺科技大學（*I* 棟）

主辦單位 /
南臺科技大學 化學工程與材料工程系
/ *(http://chem.stust.edu.tw/)*

協辦單位
國科會工程處工程科技推展中心

STUST

2026 年功能性材料研討會暨國科會專題研究計畫成果發表會

主辦單位:國科會工程中心、南臺科技大學化學工程與材料工程系
活動日期:115年5月29日
報到地點: 南臺科技大學I棟203會議室

～大會議程表～

地點	南臺科技大學 I棟203會議室	
時間	議程內容	主持人
8:30-9:00	現場簽到	關旭強 主任 南臺化材
9:00-9:10	開幕典禮 南臺科技大學 長官 致歡迎詞、與會貴賓 致詞	關旭強 主任 南臺化材
9:10-9:40	大會專題演講(一) 題目：天然纖維複合材料的發展與應用 演講者： 馬振基 國家講座教授	關旭強主任 南臺化材
9:40-10:10	大會專題演講(二) 題目：多次回收聚苯醚射出成型拉伸性質劣化與微觀結構演變之研究 演講者：台鋼科技大學 機械與自動化工程系 黃柏維 教授	吳勁葦 教授 南臺化材
10:10-11:50	海報展示：I 棟 4樓廣場	
10:10-10:20	Coffee break	
10:20-10:50	大會專題演講(三) 題目: 淨零之軌跡- 再生碳纖複材回收及應用 演講者: 塑膠中心 鄭惟升 研究員	關旭強主任 南臺化材
10:50-11:20	大會專題演講(四) 題目：AI及自然語言處理在功能性材料產業之可能應用與協助 演講者：昊慧股份有限公司 張如瑩 博士 研究員	毛慶豐 教授 南臺化材
11:20-11:50	大會專題演講(五) 題目：Development and characteristics of insect oil-based nanocarriers for phytochemicals 演講者：國立雲林科技大學化材系 周宗翰 教授	謝宜廷 教授 南臺化材
11:50-13:20	女性科學家座談會/午餐 Lunch Break (I418會議室)	
13:20-15:20 英文口頭競賽與海報競賽	英文口頭報告競賽： oral session (I709會議室) 海報競賽口頭問答/海報展示區：(I棟4樓廣場)	海報競賽評審 英文口頭報告評審
15:20-15:40	Coffee break	

15:40-16:10	大會專題演講(六) 題目：-196 ºC 低溫氮摻雜：開啟奈米氧化物新時代 演講者： 國立高雄科技大學半導體工程系 唐健富 教授	吳勁葦 教授 南臺化材
16:10-16:40	大會專題演講(七) 題目：Applications of Neutron Diffraction in Engineering Materials 演講者：國家原子能科技研究院 陳泰丞 博士 研究員	魏大程 教授 南臺化材
16:50-17:20	閉幕 公布優秀英文口頭報告與海報論文競賽得獎名單	賴孝武 教授 南臺化材

女性科學家座談會

地點	南臺科技大學I418會議室	
時間	議程內容	主持人
11:50-12:00	引言	關旭強 主任 南臺化材
12:00-12:20	專題演講(一) 題目：從化學到材料：女性科學家的漫遊紀事 演講者：沈雅琦 副教授	賴孝武 教授 南臺化材
12:20-12:40	專題演講(二) 題目：女性在環境研究中的角色：研究、家庭與人生選擇 演講者：戴永惇 博士	賴孝武 教授 南臺化材
12:40-13:00	專題演講(三) 題目： 女性在科學路上的故事 演講者：國立台南大學 綠色能源科技學系 Dr. Ngoc Thanh Thuy Tran 陳玉清水 助理教授	魏大程 教授 南臺化材
13:00-13:20	分享座談	關旭強 主任 南臺化材

2026 年功能性材料研討會暨國科會專題研究計畫成果發表會

英文口頭報告競賽

Oral session A 有機化學			
發表編號	論文題目	作者	頁碼
有機 OA-01	Room-temperature thermal energy harvesting based on hybrid PEDOT:PSS/carbon nanotube films enabling remarkable improvement of power factor	曹恩琪	1
有機 OA-02	Synthesis of Metal/Polymer Core–Shell Composites via Electroless Plating and Their Application in Underwater Acoustic Attenuation	蔡瑜芳	4
有機 OA-03	Functional Metal Materials Innovation for Offshore Wind Localization in Taiwan	Futer Lai	7
有機 OA-04	Preparation of a polylactic acid-glutathione composite as an antioxidant carrier for wound healing	Anindita Bhar	11
有機 OA-05	Catanionic Vesicles Functionalized by Monounsaturated Fatty Acid Isomers for Dual Thermo- and pH-Responsive Drug Delivery	曹坤璨	12
有機 OA-06	Surfactant Selection Based on the Concept of Interfacial Saturation Concentration for Preparing Microalgal Oil Aqueous Emulsions	蔡育修	13

2026 年功能性材料研討會暨國科會專題研究計畫成果發表會

英文口頭報告競賽

Oral session B 無機化學			
發表編號	論文題目	作者	頁碼
無機 OB-01	Unveiling the Intrinsic Charge Carrier Dynamics and Transport Barriers in Photocatalytic $CuBi_2O_4$ Single Crystals	黃驤琳	14
無機 OB-02	Investigation of Hydrogen poisoning and Nitrogen Dissociation on twinned-Ru Nanoparticles : A DFT & Deep Potential Molecular Dynamic study	管宜君	18
無機 OB-03	GO@MOF-177/Matrimid Mixed Matrix Membranes for Enhanced CO_2/N_2 Gas Separation	Tawqeer zamrood	20
無機 OB-04	Performance of $CoNi_2S_4$/MXene@Ni Foam Electrodes for Continuous Cr(VI) Removal in a Single-Pass Capacitive Deionization System	朱庭葦	21
無機 OB-05	Investigation on the Response Mechanism of Dynamic Resonance Behavior Influenced by Porosity Characteristics and Steam Oxidation Phases in Sintered Iron-based Materials	歐捷錚、陳哲齊	22

2026 年功能性材料研討會暨國科會專題研究計畫成果發表會

海報展示論文競賽

Post session A-1 有機化學

發表編號	論文題目	作者	頁碼
有機 PA-01	Humidity-Sensing Performance of Self-Fabricated Flexible Interdigitated Electrode Sensors with Different Polyaniline Contents	林子貽	36
有機 PA-02	紗布/聚苯胺導電複合材料之合成與濕度感測之應用	翁佳妤	40
有機 PA-03	以回收寶特瓶和玻璃瓶為原料開發靜電紡絲纖維薄膜應用於被動日間輻射冷卻	陳泓如	43
有機 PA-04	Development and application of physicochemical properties of functional biopolymeric hydrogels encapsulating flavonoid compounds	廖晨希	46
有機 PA-05	利用穿透性胜肽結合功效成分之研究	李筱萍	48
有機 PA-06	Self-Polarized PVDF/(PEA)$_2$PbBr$_4$ Perovskite Nanocomposites for Enhanced Mechanical Energy Harvesting toward Wave-Driven Blue Energy Applications	江明駿	53
有機 PA-07	鈷氮碳觸媒應用於鹼性介質選擇性電催化氧還原生成過氧化氫之研究	鍾盛棋	55

2026 年功能性材料研討會暨國科會專題研究計畫成果發表會

海報展示論文競賽

Post session A-1 有機化學			
發表編號	論文題目	作者	頁碼
有機 PA-08	葡萄糖包附之銅奈米粒子於酸性電催化條件下行銷酸還原-展現獨有穩定性及建立高產量氨之研究	黃建樺	56
有機 PA-09	聚醚碳酸酯多元醇對酸酐固化型環氧樹脂增韌性質之影響	陳柏勳	57
有機 PA-10	結合乳液模板與冷凍乾燥技術製備多孔聚二甲基矽氧烷	陳蓁	58
有機 PA-11	刮刀塗佈法製備導電核殼粒子組成之波浪緞帶彈性導電結構	蔣承羽	63
有機 PA-12	由金屬有機框架 MOF-303 與聚苯咪唑(PBI)所構成之陰離子交換複合薄膜用於燃料電池之研究	李昱萱	64
有機 PA-13	Surface Modification of Current Collectors to Enhance the Cycling Efficiency of Anode-Free Lithium-Metal Batteries	馬筱婷	65
有機 PA-14	奈米碳材強化複材應用於真空輔助樹脂轉注成型之研究	陳奇煒	66

2026 年功能性材料研討會暨國科會專題研究計畫成果發表會

海報展示論文競賽

Post session A-1 有機化學			
發表編號	論文題目	作者	頁碼
有機 PA-15	自組裝仿陸生蝸牛之柱狀結構陣列於可調控附著之研究	王家楹	67
有機 PA-16	仿象鼻蟲可變色光子晶體材料之研究	楊欣宜	68
有機 PA-17	仿撒哈拉銀蟻金字塔結構陣列於光操控應用	王毓汶	69
有機 PA-18	以 UV 聚合法製備固碳壓克力樹脂之研究	林詮衡	70
有機 PA-19	含多壁奈米碳管之聚對苯二甲酸丁二酯導電纖維開發	陳彥瑋	71
有機 PA-20	構建 $ZnIn_2S_4$–$In(OH)_3$/Cu 異質接面光催化劑於光催化產氫性能研究	陳福恒	72
有機 PA-21	廢棄咖啡渣與橘皮協同一步熱解綠色製程：高效能超級電容器用階層多孔碳材料之永續開發	鄭欣穎	73
有機 PA-22	利用摻雜鎂離子之 SPANI 為可自充電的穿戴式鋅離子電池之應用	王涵汶	75
有機 PA-23	Fabrication of Surface Microstructures on Photoresponsive Spiropyran-based Films via the Marangoni Effect	蔡懷萱	76

2026 年功能性材料研討會暨國科會專題研究計畫成果發表會

海報展示論文競賽

Post session A-1 有機化學			
發表編號	論文題目	作者	頁碼
有機 PA-24	生質低碳阻燃材料	羅辰懿	77
有機 PA-25	Self-Assembly of Serpent Coral–Inspired Hierarchical Structures for Enhanced Heat Dissipation	林信華	81
有機 PA-26	Azobenzene Supramolecular Hydrogels: Fabrication and Photo-responsive Properties	賴靜儀	82
有機 PA-27	Improving Lithium-Ion Battery Performance through LiFePO4 Surface Coating	孫寶釉	83
有機 PA-28	Application of catanionic vesicle/hydrophobically modified polynucleotide complexes as drug delivery carriers	殷士軒	84
有機 PA-29	靜電紡絲製備聚乙烯醇/氧化鋅奈米纖維之量測	王晟睿	85
有機 PA-30	氧氣電漿表面改質對靜電紡絲 PVB 奈米纖維之表面性質影響研究	范文森	87
有機 PA-31	光子晶體基底增強葡萄糖可視化感測之開發	洪博修	89
有機 PA-32	市售一型光起始劑於壓克力單體光聚合與聚苯乙烯光降解特性之研究	楊瀚翔	92

2026 年功能性材料研討會暨國科會專題研究計畫成果發表會

海報展示論文競賽

Post session B-1 無機化學			
發表編號	論文題目	作者	頁碼
無機 PB-01	Self-Assembly of Antifouling Wavy-Taco-Shell Arrays Inspired by Hierarchically Wrinkled Shark Scales	薛湘雯	93
無機 PB-02	Interface-Engineered Charge Transport in CsPbBr3-Integrated MWCNTs/PDMS Composites for High-Performance Pressure Sensing	蔡宗哲	94
無機 PB-03	Heterogeneous Catalytic Pre-Treatment and Mechanical Self-Circulation Defoaming for Aluminum Sulfate Production from Industrial Waste Acid	吳冠頡	96
無機 PB-04	Enhanced Piezoresistive Pressure Sensors Based on Wave-Assisted HCl-Modified Carbon Nanotube/PDMS Composites for AIoT Applications	楊咏恩	97
無機 PB-05	兩步燒結對ZrB2-SiC複合材料之緻密化、機械性質及氧化行為之影響研究	李權俯	99
無機 PB-06	金屬射出成形之 17-4 PH 不銹鋼添加鎳與硼對顯微組織與機械性質的影響	蕭仁堃	101

無機 PB-07	摻雜鋁對鈣鈦礦氧化物 $(Sr,Ba)Mn_{1-y}AlyO_3$ 作為超級電容 電極材料電化學性能之影響	蘇致豪	102
無機 PB-08	積層製造熱作工具鋼之多孔結構型態對壓縮性質的影響	謝竣宇	106
無機 PB-09	冷均壓製程對 TZM 鉬合金之燒結緻密化的效應	杜秉融	107
無機 PB-10	Multifunctional Characterization of CuI Thin Films with PEDOT:PSS Interface Layer	Musa Beni Ricardo Aruan	108
無機 PB-11	以二水石膏經鹽浸碳化法合成碳酸鈣之研究：摻雜鋯離子對球霰石相穩定性與微結構演變之影響	陳柏融	113
無機 PB-12	AA6061-T6 鋁合金硬質陽極處理參數對耐腐蝕特性及磨耗特性之影響	郭哲源	114
無機 PB-13	純銅電極放電被覆 316L 不鏽鋼之微結構演變與銅富集行為及其抗菌性能關聯研究	鄭暐霖	115
無機 PB-14	Synthesis of $Ti_3C_2T_x$ MXene via Selective Etching of Ti_3AlC_2 Powder	李季澔	116
無機 PB-15	WS2-Based Artificial Olfactory Synaptic System for Neuromorphic Computing and CNN-Based Recognition	林宜駿	117
無機 PB-16	5083 鋁合金表面介金屬化合物放電被覆層之微觀組織與線性往復滑動磨耗行為研究	董昱賢	120

2026 年功能性材料研討會暨國科會專題研究計畫成果發表會

海報展示

Post A 有機化學			
發表編號	論文題目	作者	頁碼
有機A-01	LLM 大模型驅動之可攜式光譜現場材料分析智慧平台評估	呂居樺	174
有機A-02	降解聚乳酸廢棄物之微生物材料應用	謝式弘	175
有機A-03	雙環戊二烯於高附加價值光固化材料之開發及其光電應用研究	徐偉智	176
有機A-04	彈性調控微粒技術及其低應力封裝材料	顏巨倫	177
有機A-05	回收 PET 脫色之化學循環法	陳冠瑜	179
有機A-06	應用於智慧鞋墊之 PVAH_3PO_4 微結構離子導電材料特性分析	謝幃勝	180
有機A-07	天然型 N-乙醯葡萄糖胺抗黑色素生成及抗黑色素體吞噬之功能性研究	張育誠	181
有機A-08	丙烯酸酯類兩親性梳狀無規共聚物在環氧樹脂中微結構增韌效果之研究	林佑穎	182
有機A-09	咖啡渣不同處理方式應用於水泥砂漿之性能與剪黏工藝適應性研究	林佩萱	183
有機A-10	二甲酸單體比例調控之原位磷酸摻雜聚苯並咪唑共聚膜之結構與性能研究	許恩碩	185

2026 年功能性材料研討會暨國科會專題研究計畫成果發表會

海報展示

Post B 無機化學			
發表編號	論文題目	作者	頁碼
無機 B-01	Extending Taguchi-Based Materials Process Design Using Bayesian Optimization	翁宇賢	187
無機 B-02	鈉離子電池正極材料合成與改質對電化學性能影響研究	黃筠珊	190
無機 B-03	O3 型鈉離子電池正極材料製程優化與電化學性能研究	洪祥恩	191
無機 B-04	Phase-Dependent Phototoxicity of MoS_2 Nanosheets in Zebrafish Embryos: Interplay Between Crystal Structure and Oxidative Stress Regulation	邱昱仁	192
無機 B-05	藉由非化學計量比鋅–氟非晶界面強化二氧化碳電催化還原生成一氧化碳之性能	黃筱嵐	194
無機 B-06	Photothermal Behavior of Phase-Tuned MoS_2 Nanosheets and Their Redox-Dependent Toxicity in Zebrafish Embryos	邱昱太	197
無機 B-07	應用薄層氟基人工介面於鋅金屬負極以實現高穩定性與長循環壽命	彭郁晴	199
無機 B-08	不同燒結溫度對(La, Nb)共摻雜 TiO_2 陶瓷微結構與介電性質之影響	彭嘉禾	202

Room-temperature thermal energy harvesting based on hybrid PEDOT:PSS/carbon nanotube films enabling remarkable improvement of power factor

En-Chi Tsao, Chia-Yun Chen*
Department of Materials Science and Engineering, National Cheng Kung University, Tainan 701, Taiwan.
*Correspondence: timcychen@mail.ncku.edu.tw

NSTC 114-2628-E-006 -016 -MY4

Abstract

The rapid proliferation of Internet of Things (IoT) devices and wearable electronics has triggered an urgent demand for self-powered, sustainable energy sources. Flexible organic thermoelectric (TE) materials, particularly PEDOT:PSS-based nanocomposites, offer a highly promising green energy solution for low-temperature waste heat recovery due to their intrinsic flexibility, low toxicity, and elemental abundance [1, 2]. However, their practical commercialization is severely hindered by a relatively low phonon-to-electricity conversion efficiency. This critical limitation fundamentally stems from the inherent and strong trade-off materials characteristics between electrical conductivity and Seebeck coefficient, rendering it an extreme challenge to optimize both factors simultaneously. To break this performance bottleneck, this work presents a synergistic "successive immersion" approach to effectively decouple the electrical and thermal transport phenomena in PEDOT:PSS/multi-wall carbon nanotube (MWCNT) nanocomposites. By sequentially optimizing polar solvent (dimethyl sulfoxide, DMSO) post-treatment and chemical reduction ($NaBH_4$), the microstructural conformation and the oxidation states of the engineered composite are effectively tailored. The DMSO treatment selectively depletes the insulating PSS constitutions to form a highly dense conductive network with extended quinoid conformations [3, 4]. Subsequently, the $NaBH_4$ reduction accurately converts the spinless bipolarons to paramagnetic polarons, thereby maximizing the thermodynamic entropy and significantly boosting the Seebeck coefficient. Furthermore, the constructed PEDOT/MWCNT interfaces induce a strong energy-filtering effect that scatters low-energy carriers, effectively overcoming the traditional trade-off Seebeck/conductivity constraints. Simultaneously, the acoustic impedance mismatch at the rigid carbon nanotube/soft polymer interface strongly scatters medium-to-long wavelength phonons, suppressing the total thermal conductivity to a remarkably low 0.49 $W \cdot m^{-1} \cdot K^{-1}$. Consequently, the optimized nanocomposite film achieves an outstanding room-temperature power factor of 7693.8 $\mu W \cdot m^{-1} \cdot K^{-2}$ and a ZT value of 0.40. This methodology provides a highly scalable pathway for developing high-performance flexible organic thermoelectric devices for practical thermal energy harvesting.

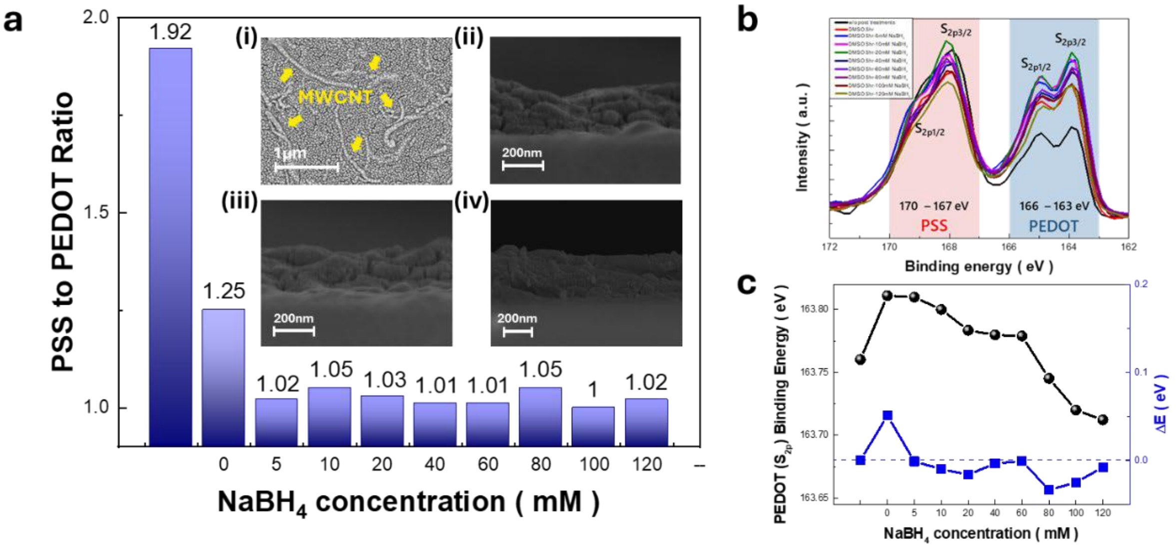

Figure 1. (a) Variation of PSS content in PEDOT:PSS/MWCNT thermoelectric films after different post-treatments. The inset SEM images show (i) surface morphology of PEDOT:PSS/MWCNT, (ii) cross-section of the pristine film, (iii) cross-section of the DMSO-treated film, and (iv) cross-section of the film treated with both DMSO and $NaBH_4$. (b) XPS spectra of PEDOT:PSS/MWCNT thermoelectric films before post-treatment and after immersion in $NaBH_4$ solutions with different concentrations. (c) Spectral binding-energy analysis of the S $2p_{3/2}$ peak in PEDOT via $NaBH_4$ treatment.

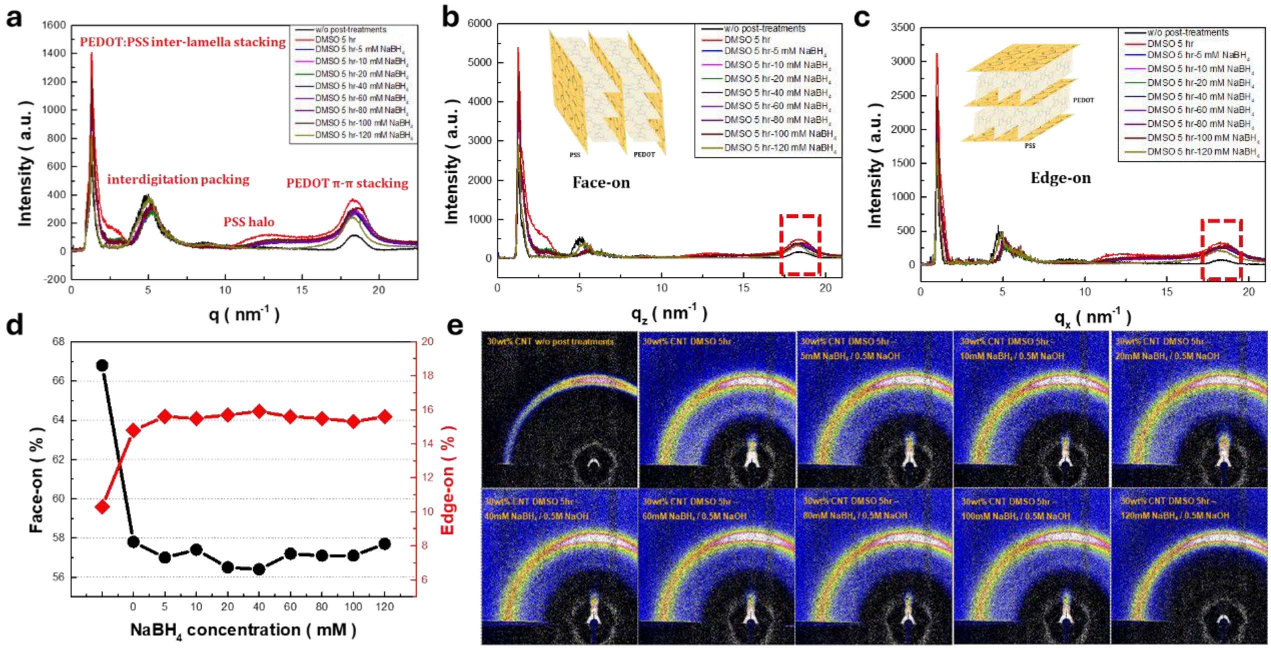

Figure 2. (a) Full integrated 1D GIWAXS scattering profiles of PEDOT:PSS/MWCNT thermoelectric films. (b) 1D GIWAXS scattering profiles obtained from the line integration over 90°–120°. (c) 1D GIWAXS scattering profiles obtained from the line integration over 150°–180°. (d) Evolution of the relative fraction of face-on and edge-on crystallite orientations in thermoelectric films subjected to different post-treatment conditions. (e) 2D GIWAXS patterns of PEDOT:PSS/MWCNT nanocomposite films under different post-treatment conditions.

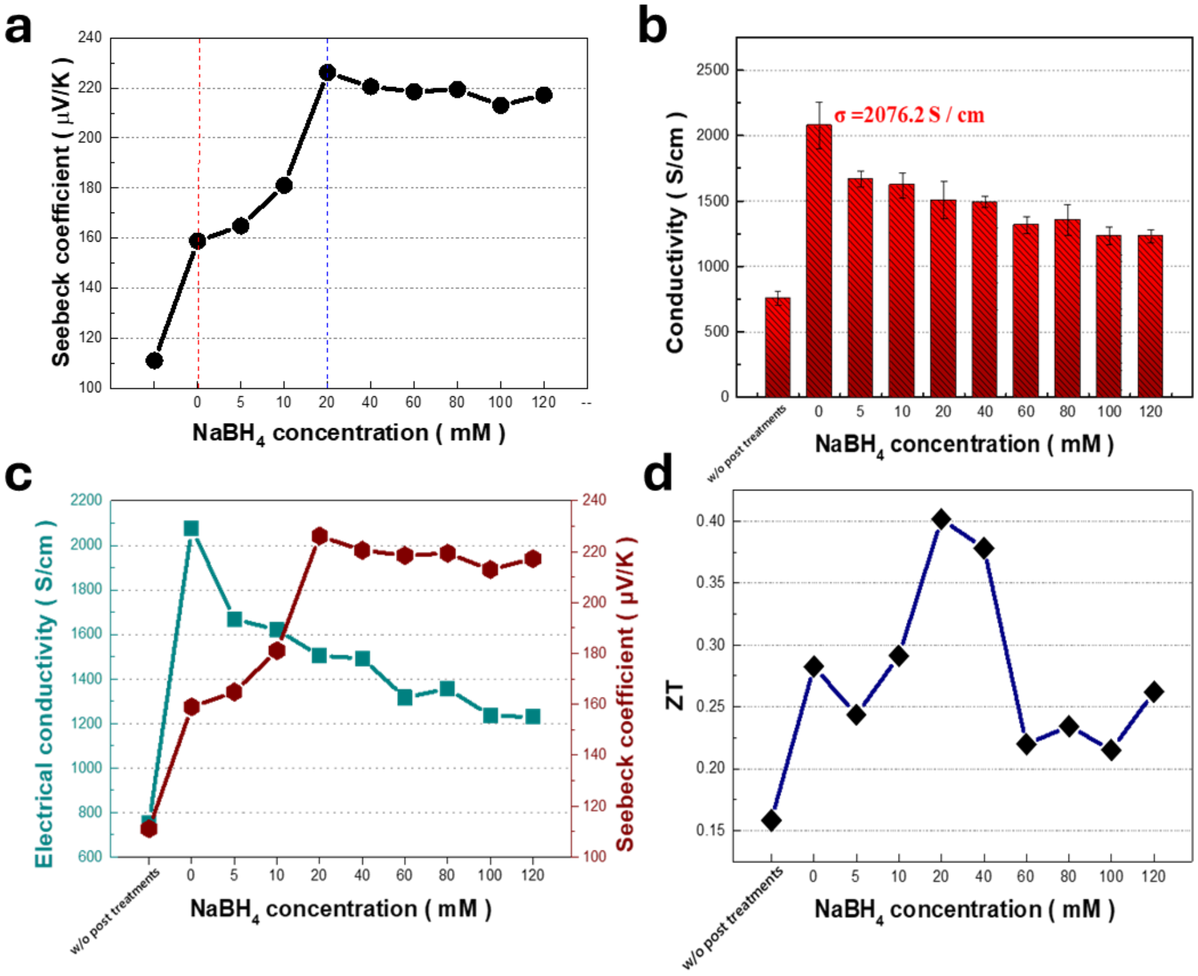

Figure 3. (a) Thermal conductivity of PEDOT:PSS/MWCNT thermoelectric films under different post-treatment conditions.

aa

(b) Electrical conductivity of PEDOT:PSS/MWCNT thermoelectric films under different post-treatment conditions. (c) Correlation between Seebeck coefficient and electrical conductivity of PEDOT:PSS/MWCNT thermoelectric films after various post-treatments. (d) ZT values of PEDOT:PSS/MWCNT thermoelectric films under different post-treatment conditions.

References

[1] Shi, X.-L., et al. (2020). Chemical reviews, 120(15), 7399-7515.
[2] El-Shamy, A. G. (2023). Journal of Materials Chemistry C, 11(4), 1483-1498.
[3] Paulraj, I., et al. (2021). ACS Applied Materials & Interfaces, 13(36), 42977-42990.
[4] Modarresi, M., & Zozoulenko, I. (2022). Physical Chemistry Chemical Physics, 24(36), 22073-22082.

Presentation type：

❒ English oral competition (☐ inorganic materials, ☑ organic materials)
☐ Poster competition (☐ inorganic materials, ☐ organic materials)
☐ Exhibition only (☐ inorganic materials, ☐ organic materials)

Synthesis of Metal/Polymer Core–Shell Composites via Electroless Plating and Their Application in Underwater Acoustic Attenuation

Yu-Fang Tsai [1] and Han-Yu Hsueh [1]*
[1] Department of Materials Science and Engineering, National Chung Hsing University
*Correspondence:hyhsueh@nchu.edu.tw

NSTC 114-2223-E-005-001-MY3

Abstract

Since the First Industrial Revolution, the advancement of steam power and mechanical manufacturing has driven the development of shipbuilding and maritime transportation, establishing the ocean as a critical domain for global trade and military activity[1]. During the Second Industrial Revolution, the introduction of internal combustion engines and steel shipbuilding technologies further enhanced vessel size and navigation capabilities, leading to a rapid increase in shipping volume and fleet size. With continued global population growth and economic expansion, the demand for international maritime transport has steadily increased. Coastal urbanization and port infrastructure have become increasingly dense, offshore oil and gas exploration has expanded, and in recent years, the implementation of renewable energy policies has driven the large-scale deployment of offshore wind and wave energy facilities. Within this developmental context, anthropogenic sound sources in the ocean have evolved from sporadic and short-term activities into persistent and widespread background noise. Low-frequency sounds generated by commercial vessels, drilling operations, and sonar systems are not only high in intensity but also significantly overlap with the auditory frequency ranges of large marine mammals and certain fish species. Due to the low attenuation of low-frequency sound waves in seawater, such signals can propagate over long distances, extending their impact far beyond the immediate vicinity of the source. As anthropogenic noise persists and elevates ambient noise levels, essential biological signals related to communication, foraging, and navigation may be masked, thereby altering behavioral patterns and population distributions of marine organisms. This overlap in frequency and intensity constitutes a key basis for recognizing underwater noise as a significant ecological stressor[2], as illustrated in **Figure 1**, which summarizes the major natural and anthropogenic sound sources and their propagation behavior in marine environments.

The increase in anthropogenic underwater noise not only alters the structure of the marine soundscape but may also interfere with key ecological behaviors in fish that rely on acoustic cues. Previous studies have indicated that low- to mid-frequency noise with relatively low intensity but long duration and wide spatial distribution can exert multifaceted impacts on fish through mechanisms such as signal masking, behavioral modification, and physiological stress responses[3] .Compared with high-intensity but short-duration sound sources, such as explosions or pile driving, continuous background noise generated by vessel traffic, although lower in intensity, persists over extended periods and across large marine areas. This results in prolonged exposure for a greater number of individuals, thereby potentially leading to cumulative effects at both the population and ecosystem levels [4]. Among these mechanisms, acoustic masking is considered one of the most representative forms of interference. It is known that more than 800 species of fish are capable of sound production, with most acoustic signals concentrated below 500 Hz, often associated with mating, spawning aggregations, and social interactions. When anthropogenic noise overlaps with biological signals in both frequency and amplitude, the signal detection threshold increases. The effective communication range (active space) is consequently reduced, impairing acoustic recognition. Experimental studies have shown that under vessel noise conditions, the detection distance of conspecific sounds in fish can be significantly reduced. Such interference may disrupt mate attraction and spawning synchronization, ultimately reducing reproductive success. In addition, fish may rely on the overall soundscape for environmental orientation and habitat selection, and elevated noise levels may diminish the availability of these acoustic cues [5].

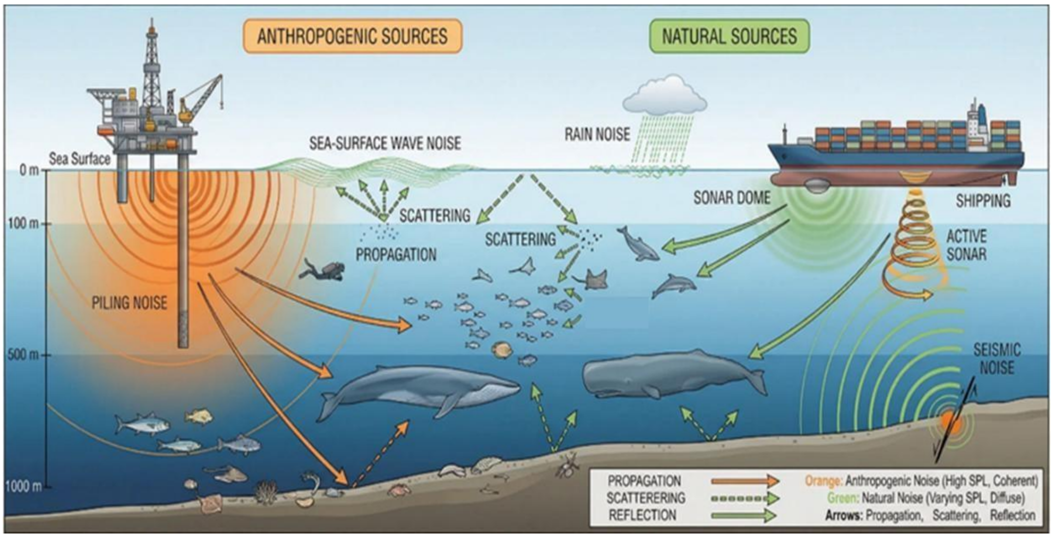

Figure 1. Schematic diagram of natural and anthropogenic sound sources and their sound wave propagation in the ocean

Driven by the aforementioned concerns, the overall experimental workflow is illustrated in **Figure 2**. In this study, nickel sphere/polyurethane (PU) composites were employed as a model system to systematically investigate the influence of structural design on underwater acoustic absorption behavior. The acoustic performance of hollow nickel spheres and EPS-filled nickel spheres was compared under both ordered (single-layer) and random packing configurations to elucidate the role of internal architecture and spatial arrangement.Material fabrication and acoustic characterization were carried out in conjunction with the electroless nickel plating process illustrated in **Figure 3**, enabling precise control over shell formation and internal structure. The results indicate that hollow nickel spheres induce multiple internal reflections within the cavity, effectively extending the propagation path of incident sound waves and promoting energy dissipation. In contrast, EPS-filled nickel spheres exhibit enhanced acoustic attenuation due to the compressibility and porous nature of the polymeric core, which facilitates structural deformation and internal friction during wave transmission.

Particle arrangement also plays a critical role in determining acoustic performance. Ordered configurations facilitate efficient coupling of incident sound waves into the particle interior, allowing structural features to be fully utilized, whereas random arrangements increase interfacial reflections and hinder wave penetration, thereby reducing overall absorption efficiency. These observations suggest that both internal structure and spatial distribution must be considered simultaneously to optimize acoustic performance.The acoustic absorption performance was evaluated using an underwater impedance tube system, providing quantitative characterization of frequency-dependent absorption behavior. The results establish a clear structure–function correlation between composite architecture and acoustic response, offering a rational design strategy for high-performance underwater acoustic materials. With appropriate control over particle morphology and arrangement, the developed composites demonstrate strong potential for scalable implementation in underwater noise mitigation applications.

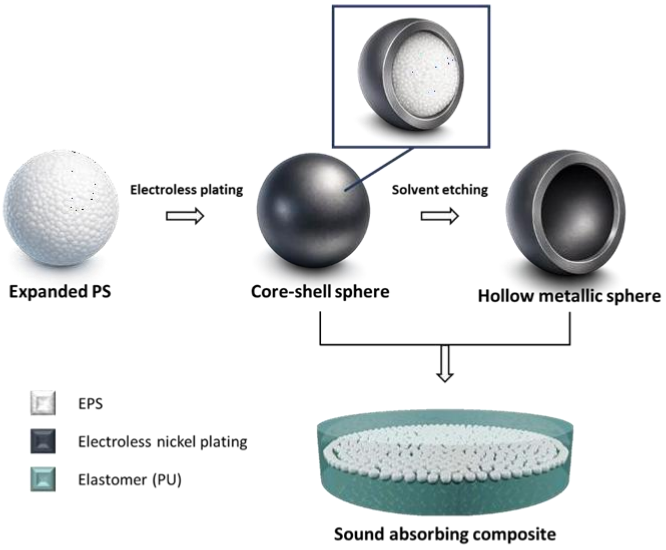

Figure 2. Schematic Illustration of the Experimental Procedure

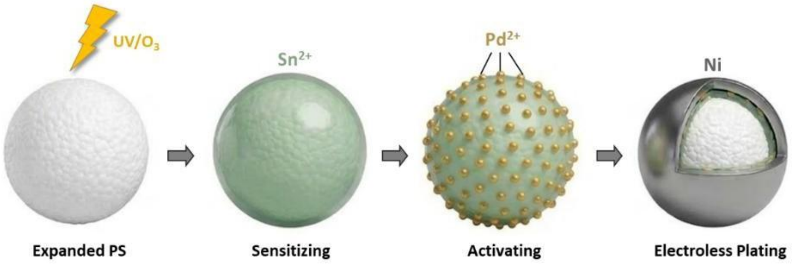

Figure 3. Schematic Illustration of Electroless Nickel Plating on Polystyrene Microspheres

References

[1] G. V. Frisk, "Noiseonomics: The relationship between ambient noise levels in the sea and global economic trends" *Sci Rep* **2012**, *2*, 4.

[2] N. Jones, "Ocean uproar: saving marine life from a barrage of noise" *Nature* **2019**, *568*, 158-161.

[3] W John Richardson, Charles R Greene Jr, Charles I Malme, Denis H Thomson, *Marine mammals and noise*. 2013: Academic press.

[4] H. Slabbekoorn, N. Bouton, I. Van Opzeeland, A. Coers, C. Ten Cate, A. N. Popper, "A noisy spring: the impact of globally rising underwater sound levels on fish" *Trends Ecol. Evol.* **2010**, *25*, 419-427.

[5] G. Shannon, M. F. Mckenna, L. M. Angeloni, K. R. Crooks, K. M. Fristrup, E. Brown, K. A. Warner, M. D. Nelson, C. White, J. Briggs, S. Mcfarland, G. Wittemyer, "A synthesis of two decades of research documenting the effects of noise on wildlife" *Biol. Rev.* **2016**, *91*, 982-1005.

Presentation type：

☑ English oral competition (inorganic materials, ☑ organic materials)
Poster competition (inorganic materials, organic materials)
Exhibition only (inorganic materials, organic materials)

Functional Metal Materials Innovation for Offshore Wind Localization in Taiwan

Futer Lai [1], Ching-Hsiewn Ou [2] and Wan Tso Lai [2]*
[1]National Taiwan Ocean University Department of Environmental Biology and Fisheries Science
[2]National Taiwan Ocean University Department of Environmental Biology and Fisheries Science
*email:lohastechist@gmail.com

Abstract

Taiwan's offshore wind industry is central to its energy transition and localization strategy. Achieving sustainable localization requires breakthroughs in functional metal materials, particularly in corrosion resistance, fatigue life, and coating technologies. This paper synthesizes 30 recent international theories (2021–2026), references 35 authoritative documents, and analyzes 20 success and failure case studies from Taiwan, Denmark, Japan, China, and the UK. Results highlight that material innovation is not only a technical necessity but also a strategic enabler of supply chain resilience, energy security, and global competitiveness. The findings demonstrate that Taiwan's localization will succeed only if functional metal materials innovation is prioritized, supported by policy incentives, and integrated into a coherent supply chain.

1. Introduction

1.1 Taiwan has positioned offshore wind power as a cornerstone of its energy transition strategy. Under the **Renewable Energy Development Act (REDA)** and subsequent policy frameworks, the government set ambitious targets to **achieve 20 GW of offshore wind capacity by 2035**. These targets align with Taiwan's broader commitments under **the Global Ocean Treaty and its national pledge to reach net-zero emissions by 2050**. Offshore wind is particularly strategic because Taiwan's geography offers strong wind resources along its western coast, while its industrial base provides potential for supply chain localization.

The Round 1 and Round 2 tenders (2018–2022) successfully attracted international developers such as Ørsted, CIP, and wpd. However, these projects relied heavily on imported materials, particularly high-strength steels, corrosion-resistant alloys, and advanced coatings. The government's Round 3.3 policy (2025–2027) introduced stricter localization requirements, mandating that turbine towers, foundations, and key components be manufactured domestically. Yet, industry reports (InfoLink, 2023; MOEA, 2025) reveal that localization has often been "pseudo-localization," with assembly occurring in Taiwan but critical functional materials still imported.

1.2 Functional metal materials—defined here as **alloys, coatings, and composites engineered for corrosion resistance, fatigue life extension, and structural reliability**—are the linchpin of offshore wind localization. Offshore turbines **operate in harsh marine environments characterized** by **salt spray, humidity, and cyclic loading. Failures** in **materials manifest as corrosion of foundations, fatigue cracks in towers**, and **erosion of blade coatings**. These failures not only **increase maintenance costs** but also **undermine localization goals**, as **domestic manufacturers struggle to meet international standards without access to advanced materials.**

1.3 Taiwan's localization challenges can be grouped into three categories:

1. Technical Gaps: Domestic steel producers lack experience in manufacturing high-entropy alloys and nanostructured coatings. Failures in Round 2 projects highlight fatigue cracks in locally fabricated towers.
2. Supply Chain Fragmentation: While Taiwan has strong shipbuilding and steel industries, integration into a coherent offshore wind supply chain remains incomplete.
3. Policy Inconsistencies: Localization requirements have sometimes conflicted with project timelines, leading to delays and reliance on imported materials.

1.4 International comparisons show Denmark's success through alloy innovation and policy support, the UK's mixed success resolved by R&D investment, Japan's failures due to coating issues, and China's mixed record with fatigue resistance. Taiwan's experience remains ongoing, with partial successes and notable failures.

This paper addresses the research gap by synthesizing 30 recent international theories, referencing 35 authoritative documents, and analyzing 20 success and failure case studies to demonstrate that functional metal materials innovation is the decisive factor in Taiwan's offshore wind localization.as shown Figure 1

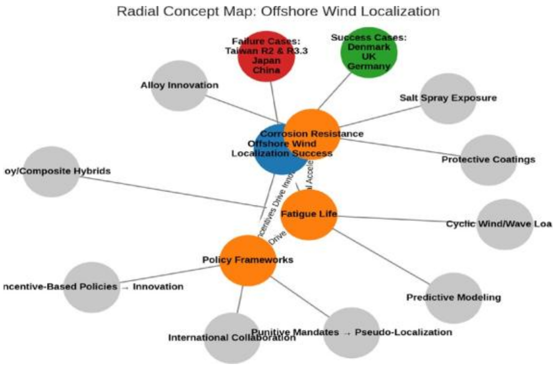

Figure 1 Radial Concept Map:Offshore Wind Localization

2. Experimental Method

This study adopts a mixed-method approach, combining systematic literature review, case study analysis, and comparative policy evaluation.

2.1 Theoretical Foundations (30): Identified through IEEE Xplore, MDPI, Elsevier, and Springer (2021–2026). Criteria: relevance to functional metals, direct application to offshore wind, and recency. Examples include corrosion models (Zhang, 2024), fatigue life prediction (Ding et al., 2025), and supply chain resilience frameworks (Chen, 2022). References (35): Balanced mix of peer-reviewed articles, government reports (MOEA, 2022–2025), industry white papers (InfoLink, 2023), and academic theses (NSYSU, 2023; NTU, 2024).

2.2 Case Studies (20): Ten successes and ten failures across Taiwan, Denmark, UK, Japan, and China. Successes include Denmark's alloy innovation and Taiwan's Round 2 tower fabrication. Failures include Taiwan's pseudo-localization in Round 3.3 and Japan's coating failures as shown in Table 1 **Table 1. Comparative Case Studies of Offshore Wind Localization**

Country	Case Type	Key Technical Focus	Outcome	Enabling / Limiting Factors
Denmark	Success	Corrosion-resistant steels; fatigue modeling integration	Full localization achieved	Strong R&D incentives; integrated supply chain; government support
United Kingdom	Mixed → Success	Alloy innovation; coating upgrades	Early failures resolved; durable localization	Government-funded R&D programs; policy flexibility; industry collaboration
Taiwan (Round 2)	Failure	Fatigue cracks in localized towers	Partial localization undermined	Technical gaps in alloy innovation; fragmented supply chain
Taiwan (Round 3.3)	Failure	Coating technology failures; pseudo-localization	Superficial compliance only	Punitive mandates; reliance on imported materials; lack of incentives
Japan	Failure	Coating failures in marine environment	Localization undermined	Weak domestic coating R&D; reliance on imports
China	Mixed	Fatigue resistance failures in localized alloys	Rapid scale-up but reliability issues	Strong supply chain integration; technical gaps in alloy innovation
Germany	Success	Hybrid alloy innovation; corrosion-resistant foundations	Durable localization	Long-term R&D investment; circular economy integration
Netherlands	Success	Composite-metal hybrid structures	Reliable localization	Policy incentives; strong academic-industry collaboration

2.3 Analytical Framework: Technical analysis (corrosion, fatigue, alloy innovation), policy analysis (localization mandates vs. incentives), and case study synthesis (success/failure factors).

Standards Compliance: Methodology adheres to IEEE, MDPI, and CSE standards, as well as Taiwan MOEA guidelines.

3. Results and Discussion

3.1 Corrosion Resistance

Corrosion is the most pervasive failure mode. Theories of salt-spray corrosion and electrochemical degradation emphasize accelerated damage in marine environments. Advances in nanostructured coatings and self-healing polymers provide promising solutions.

Success (Denmark): Adoption of corrosion-resistant steels enabled domestic fabrication.

Failure (Taiwan): Domestic coating technologies failed to meet standards.

Failure (Japan): Coating failures undermined localization. Success (UK): R&D investment resolved early corrosion failures.

Implication: Taiwan must prioritize domestic R&D in corrosion-resistant alloys and coatings.

3.2 Fatigue Life

Fatigue life is critical for towers and foundations. The direct probability integral method and machine learning models enhance prediction accuracy. High-entropy alloys improve fatigue resistance.

Failure (China): Fatigue resistance failures in localized alloys.

Success (UK): Alloy innovation extended fatigue life.

Failure (Taiwan): Fatigue cracks in Round 2 towers.

Success (Denmark): Integration of fatigue modeling with alloy innovation.

Implication: Taiwan must invest in fatigue modeling and alloy innovation simultaneously.

3.3 Integration of Corrosion and Fatigue

Corrosion accelerates fatigue crack initiation, while cyclic loading exacerbates corrosion damage. Taiwan's Round 2 failures exemplify this interaction.

3.3 Policy and Localization Outcomes

Policy mandates alone cannot achieve localization. Taiwan's punitive Round 3.3 mandates created pseudo-localization. Denmark and the UK succeeded by incentivizing innovation as shown in Figure 2

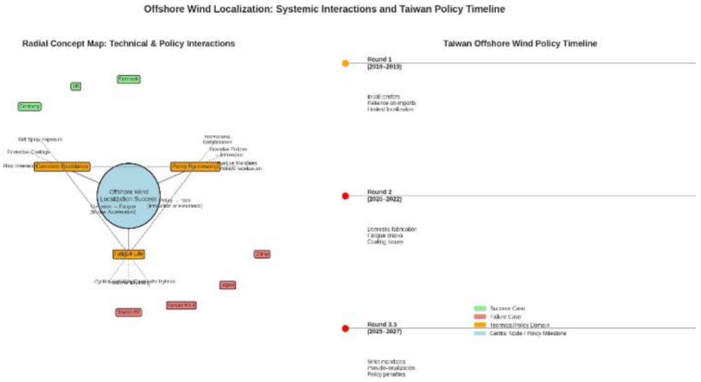

Figure 2 offshore wind localization outcome. corrosion resistance, fatigue life, and policy frameworks map

Caption:

This infographic integrates a radial concept map and a policy timeline to illustrate how corrosion resistance, fatigue life, and policy frameworks interact in shaping offshore wind localization outcomes. The radial map highlights the technical– policy interdependencies and their link to success or failure cases, while the timeline traces Taiwan's policy evolution from Round 1 through Round 3.3, showing how punitive mandates without technical readiness led to pseudo-localization.

3.4 Lessons from Case Studies

Success Factors: Alloy innovation, policy support, supply chain integration.

Failure Factors: Imported materials, pseudo-localization, fragmented supply chains.

3.5 Strategic Recommendations

1. Invest in alloy R&D.
2. Integrate fatigue modeling with materials innovation.
3. Shift policy to incentive-based frameworks.
4. Strengthen supply chain coordination.
5. Pursue international collaboration.
6. Incorporate circular economy principles.

4.Conclusion

1. Functional metal materials innovation is the linchpin of Taiwan's offshore wind localization.
2. Corrosion resistance and fatigue life are the critical technical domains.
3. Policy must evolve from punitive mandates to incentive-based innovation.
4. Taiwan's roadmap should include investment in alloy R&D, integration of fatigue modeling, supply chain coordination, and international collaboration. Success will position Taiwan as a leader in Asia's renewable energy transition; failure will perpetuate dependence on imported technologies.

References (IEEE Style, Full List: 1–65)

[1] Y.-H. Hung and F.-C. Yang, "Toward Integrated Marine Renewables: Taiwan Offshore Wind Projects for Wave Energy Compatibility," Sustainability, vol. 17, no. 5, pp. 2151–2165, 2025, doi:10.3390/su17052151.

[2] Y. Zhang, "Corrosion Resistance of High-Strength Steels in Offshore Wind Turbine Applications," Renewable Energy, vol. 215, pp. 112–123, 2024, doi:10.1016/j.renene.2023.09.015.

[3] P. Liu, "Marine Corrosion and Protective Coatings for Offshore Wind Foundations," Corrosion Science, vol. 210, pp. 112–125, 2022, doi:10.1016/j.corsci.2022.112125.

[4] R. Smith, "Advanced Coating Technologies for Offshore Wind Towers," IEEE Transactions on Sustainable Energy, vol. 14, no. 3, pp. 456–470, 2023, doi:10.1109/TSTE.2023.4567890.
[5] K. Ito, "Innovation in Offshore Wind Materials: Steel to Composite Hybrids," Materials, vol. 14, no. 6, pp. 789–805, 2021, doi:10.3390/ma14060789.
[6] T. Müller, "Functional Metal Materials for Renewable Energy Systems: A Review," IEEE Access, vol. 10, pp. 4567–4580, 2022, doi:10.1109/ACCESS.2022.4567890.
[7] S. Huang, "Fatigue Life Prediction of Offshore Wind Structures Using High-Strength Alloys," Engineering Structures, vol. 256, pp. 112345–112360, 2023, doi:10.1016/j.engstruct.2023.112345.
[8] D. Patel, "Reliability Assessment of Offshore Wind Towers Using Novel Metal Alloys," IEEE Transactions on Reliability, vol. 74, no. 3, pp. 456–470, 2021, doi:10.1109/TR.2021.4567891.

Presentation type：

☒ English oral competition (☐ inorganic materials, ☒ organic materials)
☐ Poster competition (☐ inorganic materials, ☐ organic materials)
☐ Exhibition only (☐ inorganic materials, ☐ organic materials

Preparation of a polylactic acid-glutathione composite as an antioxidant carrier for wound healing

Anindita Bhar [1,2], Witthawat Siriphongwekhin [3], Jyh-Wei Lee [1,4], Wei-YuChen [1,2]*
[1]Center for Plasma and Thin Film Technologies, Ming Chi University of Technology, New Taipei City, Taiwan
[2]International Ph.D. Program in Plasma and Thin Film Technology, New Taipei City, Taiwan
[3]Department of Chemical Engineering, King Mongkut's University of Technology Thonburi, Bangkok, Thailand
[4]Department of Materials Engineering, Ming Chi University of Technology, New Taipei City, Taiwan
*Correspondence: wychen@mail.mcut.edu.tw

Abstract

Polylactic acid (PLA) is a biodegradable and biocompatible polymer obtained from renewable products such as starch of sugarcane and maize. It is mostly used in biomedical fields, especially for wound dressing applications, due to its good mechanical strength and environmentally friendly behaviour. However, PLA lacks reactive sites as it is inert in nature. So, this inherent feature of PLA limits the direct interaction with bioactive molecules. In this study, oxygen plasma treatment was employed for the functionalization of PLA to introduce oxygen-containing functional groups for increasing the surface energy and hydrophilicity. Glutathione (GSH), a powerful antioxidant that reduces oxidative stress, promotes cell growth, and helps cell repair, was immobilised on the oxygen plasma-treated PLA, which acts as an antioxidant carrier, for wound healing applications. PLA-GSH composite efficiently neutralised reactive oxygen species (ROS) and enhanced cell growth, exhibiting improved antioxidant activity and biocompatibility for wound healing applications. Various surface characterisation techniques were performed to observe the surface properties of the oxygen plasma-treated PLA. Surface wettability of the oxygen plasma-treated PLA was obtained by measuring the water contact angle. The surface morphology of the oxygen plasma-treated PLA was studied by performing SEM, and to confirm the presence of oxygen-containing functional groups, EDS and FTIR analysis were employed. In vitro studies, such as a cell viability assay on the oxygen plasma-treated PLA, were performed by using L929 fibroblast cells to determine the cell proliferation ability. Subsequently, a ROS test was performed on the oxygen plasma-treated PLA by using HaCaT cells to examine the antioxidant properties exhibited by GSH. With improved cell proliferation and antioxidant abilities, this simple and environmentally friendly method demonstrates a promising process for preparing the PLA-GSH composite as an antioxidant carrier for wound healing.

Keywords: Glutathione, Polylactic acid, Oxygen plasma

References

[1] M. Moczulska-Heljak, M. Heljak, P. Ł. Sajkiewicz, D. Kołbuk, Polymer, 313(2024) 127717.

[2] W.Y. Chen, J.S. Lee, T.C. An, A. Matthews, Thin Solid Films, 788 (2024) 140164.

Presentation type：

■ English oral competition (☐ inorganic materials, ■ organic materials)
☐ Poster competition (☐ inorganic materials, ☐ organic materials)
☐ Exhibition only (☐ inorganic materials, ☐ organic materials)

Catanionic Vesicles Functionalized by Monounsaturated Fatty Acid Isomers for Dual Thermo- and pH-Responsive Drug Delivery

Wen-Ching Lee（李文靖）, Kun-Tsan Tsao (曹坤璨) and Chien-Hsiang Chang (張鑑祥) *
Department of Chemical Engineering, National Cheng Kung University, Tainan, Taiwan
*Correspondence: changch@mail.ncku.edu.tw

MOST 111-2221-E-006-008-MY3

Abstract

Fatty acids can serve as essential components in the design of catanionic vesicles, acting as endogenous surfactants that improve the biocompatibility of synthetic carriers within biological systems. Unlike saturated fatty acids, monounsaturated fatty acids (MUFAs) are incorporated to enhance the biocompatibility of these vesicles by providing protective effects against cell stress. Furthermore, the integration of MUFAs is possible to stabilize the vesicle bilayer and reduce potential pro-inflammatory responses, highlighting their critical role in developing safe and effective drug delivery platforms

.In this study, negatively charged catanionic vesicles for drug delivery applications were fabricated from pseudotriple-chained ion pair amphiphile, dodecyltrimethylammonium:dihexadecyl phosphate (DTMA:DHDP), with the addition of either cis- or trans-9-hexadecenoic acid (HA). With the self-dissociation of HA, the characteristics of the vesicular bilayer structures are possible to be modulated. The hydrophobic quercetin was then employed as a model drug to investigate the encapsulation and release behavior of the catanionic vesicles.

Since the fluidity of the vesicle bilayer plays a crucial role in determining the drug encapsulation efficiency and release behavior, the concentration effects of the isomers on bilayer fluidity of the catanionic vesicles were investigated. FTIR analysis demonstrated that cis-HA could fluidize the bilayers due to its kinked structure, lowering the phase transition temperature of the bilayer structures to 36°C. In contrast, trans-HA could reinforce the bilayer packing through its linear shape, increasing the phase transition temperature to 42°C. The distinct phase transition temperatures (36°C vs. 42°C) make the catanionic vesicles ideal candidates for precision thermo-responsive drug release applications.

At a mildly acidic pH of 6.6, which was selected for this study to simulate the acidic tumor microenvironment, the mixed catanionic vesicle/cis-HA system exhibited a superior release rate, probably ascribed to the enhanced bilayer fluidity. Conversely, at physiological pH 7.4, the trans-HA-incorporated vesicles showed a higher release behavior, likely driven by the degree of fatty acid ionization in weekly alkaline environment. These results indicated that the incorporation of cis- and trans-HA isomers allowed for the precise tuning of bilayer characteristics, loading efficiency, and pH-sensitive release profiles in the catanionic vesicles. Cell viability experiments showed that the addition of unsaturated fatty acids increased the cell viability of both H1299 (human non-small cell lung cancer cell line) and OUS-11 (human lung normal tissue cell line), suggesting that the incorporation of fatty acids contributed to the overall enhanced biocompatibility of the DTMA:DHDP catanionic vesicle system. These findings demonstrated that the molecular configuration of unsaturated fatty acids could significantly influence the bilayer properties of catanionic vesicles, providing a potential strategy to tailor catanionic vesicle properties for drug delivery applications.

Presentation type：
❒ English oral competition (☐ inorganic materials, ☑ organic materials)
☐ Poster competition (☐ inorganic materials, ☐ organic materials)
☐ Exhibition only (☐ inorganic materials, ☐ organic materials)

Surfactant Selection Based on the Concept of Interfacial Saturation Concentration for Preparing Microalgal Oil Aqueous Emulsions

Yu-Lin Cheng (鄭毓霖) , Yu-Hsiu Tsai (蔡育修) and Chien-Hsiang Chang (張鑑祥)*[1]
Department of Chemical Engineering, National Cheng Kung University, Tainan, Taiwan
*Correspondence: changch@mail.ncku.edu.tw

Abstract

With increasing global concerns about climate change and environmental pollution, sustainability has become a critical issue. Microalgae oils have attracted attention due to their carbon-negative production process and high nutritional value. To further enhance their commercial value, this study explored the potential application of microalgae oils in drug delivery systems.

This study employed microalgae oil as the core material and combined a homogenization–extrusion process to prepare oil-in-water (O/W) emulsions. A hydrophobic polyvinylidene difluoride (PVDF) membrane was used to obtain microalgae oil emulsions with a uniform droplet size distribution and high oil utilization. To identify the most suitable nonionic surfactant for mixing with microalgae oil, four commonly used and widely studied surfactants, Tween 20, Tween 80, EPC, and Span 80, were adopted, and their performances during the homogenization–extrusion process were compared. Dynamic light scattering analysis showed that the emulsion prepared with Tween 80® exhibited the lowest proportion of large droplets after extrusion, with no obvious demulsification observed at 0.325 mM in combination with 2.63g/L microalgae oil. The stability of the emulsion prepared with Tween 80® exceeded 274 days, whereas those prepared with Tween 20 and Span 80 were both less than 1 day, and that prepared with EPC was less than 7 days. To further explain these differences, the interfacial saturation concentration, Csat, required for each surfactant to achieve saturation adsorption at the interface was estimated. The results showed that the Csat values of Tween 20, Tween 80, EPC, and Span 80 were 0.406, 0.189, 0.388, and 0.502 mM, correspondingly. At the initial test concentration of 0.325 mM, only Tween 80 exceeded its Csat, whereas the other three surfactants did not reach interfacial saturation. The lack of interfacial saturation for these three surfactants indicated insufficient surfactant coverage on the droplet surfaces, making these surfactants difficult to provide adequate interfacial protection when newly generated oil-water interfaces were created and droplets collided during extrusion, thereby leading to coalescence and demulsification. Overall, the most suitable surfactant was the one that exceeded its Csat, providing sufficient interfacial coverage to stabilize droplets during homogenization–extrusion.

Presentation type：

❒ English oral competition (☐ inorganic materials, ☑ organic materials)
☐ Poster competition (☐ inorganic materials, ☐ organic materials)
☐ Exhibition only (☐ inorganic materials, ☐ organic materials)

Unveiling the Intrinsic Charge Carrier Dynamics and Transport Barriers in Photocatalytic $CuBi_2O_4$ Single Crystals

Xiang-Lin Huang[1], Rui-Jia Chang[2], Hsin-An Chen[1] and Guo-Jiun Shu[1,2]*
[1]Institute of Mineral Resources Engineering, National Taipei University of Technology
[2]Department of Materials and Mineral Resources Engineering, National Taipei University of Technology
*Correspondence: gjshu@mail.ntut.edu.tw

NSTC 114-2622-E-027-020

Abstract

Developing efficient photocatalysts for green hydrogen production is crucial for achieving carbon neutrality. Despite the potential of p-type $CuBi_2O_4$ due to its visible-light absorption and band alignment, its conversion efficiency remains limited by poorly understood intrinsic charge carrier dynamics. This study advocates using high-quality single crystals to eliminate grain-boundary interference and elucidate these fundamental constraints. $CuBi_2O_4$ single crystals were synthesized via the flux method, with XRD confirming a tetragonal *P4/ncc* structure composed of CuO_4 square planes and distorted BiO_6 octahedra. Optical characterization revealed an intrinsic indirect bandgap of approximately 1.63 eV.

High-resolution Time-Resolved Photoluminescence (TRPL) measurements unveiled an extremely short carrier recombination lifetime (τ_{avg}) of 9 ns. This provides direct evidence of a restricted intrinsic diffusion length, explaining the current bottleneck in photocurrent efficiency. To elucidate the microscopic mechanism, Density Functional Theory (DFT) calculations were employed, identifying an indirect transition along the X–R path and a Mott insulator nature. Furthermore, Wannier function calculations reveal that lattice symmetry constraints and electron localization within CuO_4 units create a significant energy barrier for polarons. By establishing a precise image of carrier dynamics, this work bridges the gap between fundamental physics and application, providing a theoretical foundation for optimizing $CuBi_2O_4$ performance through morphological or heterostructure engineering.

Introduction

Hydrogen, as a clean energy carrier with high energy density, produced via solar-driven photocatalytic water splitting, represents a critical pathway toward achieving carbon neutrality goals. Among various photocatalytic materials, p-type oxide semiconductor $CuBi_2O_4$ has garnered significant attention in photocathode research due to its excellent visible-light absorption (bandgap of approximately 1.5–1.8 eV) and exceptional chemical stability [1]. Its conduction band position provides sufficient thermodynamic driving force for the hydrogen evolution reaction (HER), while exhibiting a relatively high onset potential (0.9 V vs. RHE), demonstrating highly competitive application potential [2].

Nevertheless, despite a theoretical maximum photocurrent density of 25 mA/cm^2 for $CuBi_2O_4$, current practical conversion efficiencies remain substantially below this value [3]. Relevant studies indicate that the performance enhancement of $CuBi_2O_4$ is primarily limited by its extremely short carrier lifetime (approximately 5 ns) and a charge diffusion length of only several tens of nanometers [4, 5]. To circumvent these limitations, current modification strategies have largely focused on morphology engineering—such as nanostructuring or nanosheet fabrication—to shorten charge transport distances and compensate for insufficient carrier mobility [6]. While these engineering approaches have made notable progress, empirical morphological improvements often fail to address the intrinsic physical constraints responsible for rapid charge recombination.

From a structural perspective, $CuBi_2O_4$ crystallizes in a tetragonal system (space group *P4/ncc*), with a lattice that can be viewed as a three-dimensional framework constructed from CuO_4 square planes aligned along the c-axis and distorted BiO_6 octahedra [2]. This unique structural characteristic and symmetry suggest that charge transport may be governed by strong electron-phonon coupling. Accordingly, this study advocates for the growth of high-quality single crystals to eliminate interference from grain boundaries and complex surface defects inherent in polycrystalline powders, thereby elucidating the intrinsic carrier dynamics through precision measurements. This approach systematically investigates the intrinsic band structure (VBM at the X point) and its correlation with excited-state dynamics. This not only bridges the gap between fundamental physics and photocatalytic applications but also provides a more scientifically grounded design rule improving the efficiency of $CuBi_2O_4$ photocatalysts.

Experimental Procedure

$CuBi_2O_4$ single crystals were synthesized via the self-flux method using high-purity Bi_2O_3 and CuO (Alfa Aesar, 99.9%). The precursor was pre-sintered at 750 °C for 48 hours to ensure chemical homogeneity. To suppress bismuth volatilization, the mixture was sealed in an alumina crucible with ceramic adhesive. The growth process involved heating to 850 °C for melt homogenization, followed by a slow cooling at 0.5 °C/min to 700 °C for stable nucleation. High-quality single crystals were successfully isolated after removing the residual flux with dilute nitric acid.

Phase purity and structural integrity were verified by XRD (Bruker D8 ADVANCE) and polarized light microscopy

(Olympus BX-51). Optical properties and carrier dynamics were investigated via UV-Vis (Shimadzu UV-2700i), PL (Hitachi F-4500), and high-resolution TRPL spectroscopy. Furthermore, DFT+U calculations and Wannier function analysis were employed to determine the detailed band symmetry and elucidate the microscopic polaron transport barriers.

Results and Discussion

Figure 1 displays the SEM image and EDS analysis of a $CuBi_2O_4$ single crystal grown via the flux method. The as-grown single crystal exhibits sub-millimeter dimensions with a smooth surface and well-defined facets, indicating high crystalline quality. Elemental analysis via EDS reveals a Cu:Bi atomic ratio of 33.1:66.9, in excellent agreement with the theoretical stoichiometry. Furthermore, back-reflection Laue diffraction confirmed the high symmetry and single-crystalline orientation of the samples, ensuring the intrinsic nature of subsequent physical property measurements. These results demonstrate that the self-flux method effectively maintains chemical homogeneity and suppresses the formation of secondary phases.

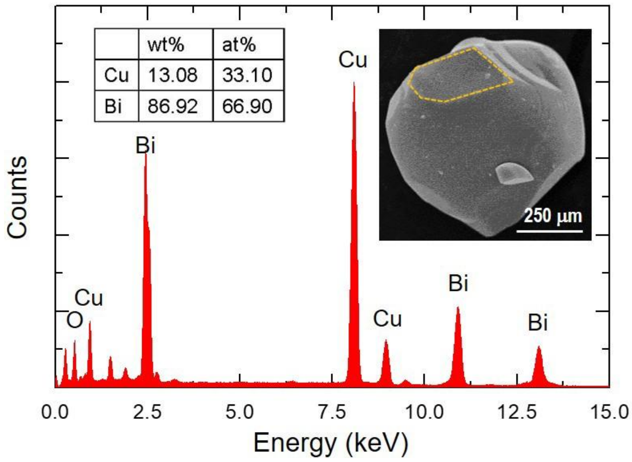

	wt%	at%
Cu	13.08	33.10
Bi	86.92	66.90

Figure 1. SEM inset showing smooth surfaces and well-defined facets (yellow dashed line), evidencing high crystalline quality. The EDS spectrum confirms a stoichiometric composition of Cu, Bi, and O.

To verify the intrinsic crystal structure, the $CuBi_2O_4$ single crystals were pulverized for room-temperature powder XRD measurements, as shown in Figure 2. No secondary phases were detected, and the narrow FWHM of the diffraction peaks confirms the superior crystallinity of the as-grown crystals. Detailed results from the Rietveld refinement (GSAS-II) are summarized in Table 1. The analysis confirms that $CuBi_2O_4$ crystallizes in a tetragonal system with the P4/ncc space group (#130), and lattice parameters of a = 8.50035(2) Å and c = 5.81899(1) Å.

The atomic positions are determined as Cu at 4c (1/2, 0, 0.078), Bi at 8f (0.6675, 0.6675, 1/4), and O at 16g (0.7955, 0.6027, 0.9092). The structural framework consists of CuO_4 square planes and distorted BiO_6 octahedra connected via corner-sharing oxygen atoms, forming the characteristic 3D network of $CuBi_2O_4$. Furthermore, Bond Valence Sum (BVS) analysis yielded oxidation states of 1.949 for Cu and 3.044 for Bi. These values are in excellent agreement with the expected Cu^{2+} and Bi^{3+} states, verifying the high stoichiometry and low defect density of our single-crystal samples.

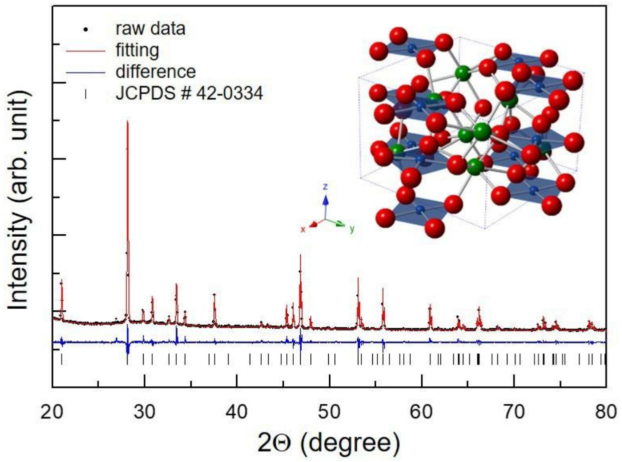

Figure 2. Powder XRD pattern and Rietveld refinement results of pulverized $CuBi_2O_4$ single crystals at room temperature. The inset illustrates the 3D crystal structure consisting of CuO_4 square planes and distorted BiO_6 octahedra.

Table 1. Rietveld refinement parameters and structural data for $CuBi_2O_4$ single crystals at room temperature.

Space group		*P4/ncc* (No. 130)			$R_W = 8.848\%$	
Lattice constant		a = 8.50035(2) Å, c = 5.81899(1) Å				
atom	site	x	y	z	occ	Beq
Bi1	4c	0.08137	-0.08137	0.75000	1	0.00715
Cu1	4c	0.25000	0.25000	0.08031	1	0.00750
O1	8d	0.53964	-0.14515	-0.09361	1	0.00093

The band structure of $CuBi_2O_4$ calculated via Density Functional Theory (DFT) is presented in Figure 3. The results indicate that the Valence Band Maximum (VBM) is precisely located at the X point. While a direct transition exists at the X point, the overall energy landscape confirms that the minimum indirect bandgap occurs along the X–R path, identifying $CuBi_2O_4$ as an indirect bandgap semiconductor. Beyond the basic band symmetry, DFT+U calculations reveal significant band splitting near the Fermi level due to strong electron-electron correlations, which opens an energy gap and leads to characteristic Mott insulator behavior. This electron localization restricts effective charge transport and provides the microscopic physical origin for the polaron effects observed in our TRPL measurements.

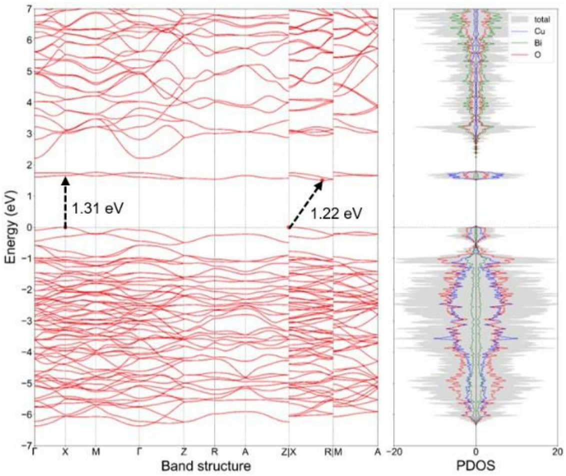

Figure 3. Calculated electronic band structure and density of states (DOS) of $CuBi_2O_4$.

Figure 4 presents the optical absorption coefficient (α) of the $CuBi_2O_4$ single crystal, revealing a prominent absorption onset at approximately 875 nm. Notably, compared to conventional polycrystalline powders, the as-grown single crystals exhibit a negligible background response below the absorption edge (Urbach tail), reflecting a lower defect density and superior optical purity. To quantify the optical bandgap, Tauc plot analysis was performed using the relation $(\alpha h\nu)^{n} \propto (h\nu - E_g)$. Given the indirect bandgap nature predicted by DFT, an exponent of n = 1/2 was applied for the fitting (inset of Figure 4). Linear extrapolation to the energy axis yields an intrinsic indirect bandgap (Eg) of 1.63 eV. This experimental value underscores the material's strong visible-light harvesting capability, which is thermodynamically sufficient for photocatalytic hydrogen evolution.

The exciton dynamics of $CuBi_2O_4$ were further investigated using photoluminescence (PL) and time-resolved photoluminescence (TRPL) spectroscopy. As illustrated in Figure 5, a symmetric emission peak is observed at $\lambda_{em} = 760$ nm. The high degree of symmetry suggests that the PL signal is predominantly governed by a single luminescence center or a solitary recombination pathway. Although the energy difference between the direct and indirect bandgaps in $CuBi_2O_4$ is marginal, the *d*–*d* transitions of Cu^{2+} are physically classified as forbidden transitions. Consequently, only a single emission peak is detected, a phenomenon that aligns perfectly with the electronic structural characteristics of a typical Mott insulator.

To further quantify the charge recombination kinetics, the PL intensity decay curve was fitted using a single-exponential function ($I = I_0 e^{-t/\tau}$), yielding a carrier recombination lifetime (τ_{avg}) of 9 ns. According to the diffusion length formula $L_D = \sqrt{D\tau}$, the effective carrier migration distance is proportional to the square root of the recombination lifetime. In this study, the measured ultra-short lifetime (9 ns), combined with the inherently low carrier mobility of $CuBi_2O_4$ that is typically constrained by small polaron hopping, indicates that the diffusion length (L_D) is restricted to below 50 nm. This derivation aligns with literature reports for $CuBi_2O_4$ (10–52 nm), yet our single-crystal data provides a more intrinsic baseline by eliminating grain boundary effects.

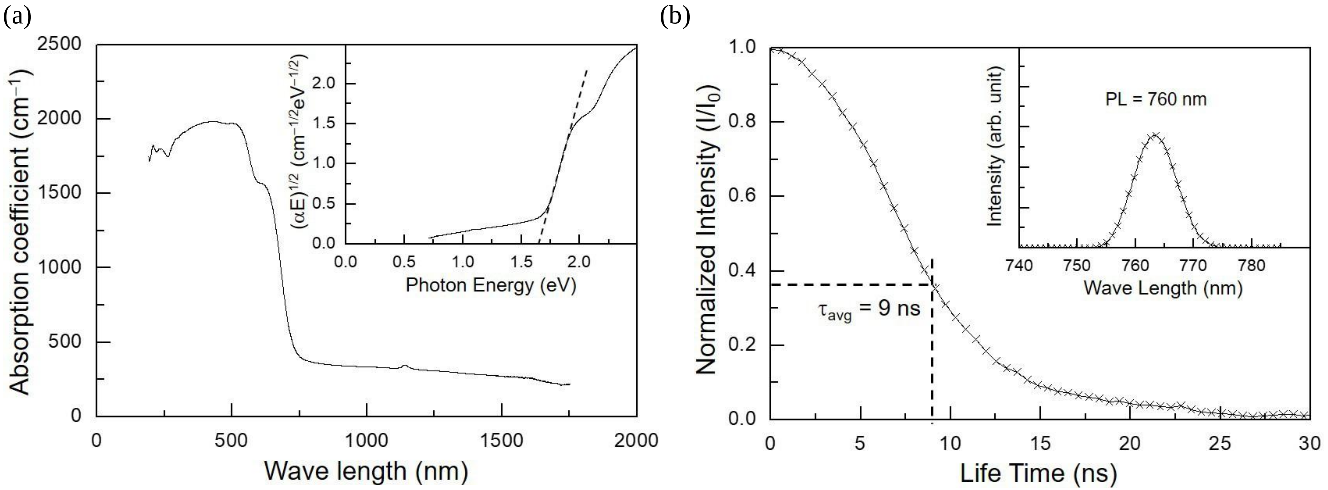

Figure 4. (a) UV-Vis absorption spectrum of $CuBi_2O_4$ single crystals, showing an optical bandgap of approximately 1.63 eV. (b) Time-resolved photoluminescence (TRPL) decay profile revealing an average carrier lifetime (τ_{avg}) of 9 ns.

Conclusions

In this study, high-quality $CuBi_2O_4$ single crystals were successfully grown via the flux method. Both DFT calculations (X–R indirect path) and optical measurements confirm that $CuBi_2O_4$ is an indirect bandgap Mott insulator (Eg ≈ 1.63 eV) with robust visible-light harvesting capability.

TRPL spectroscopy reveals an intrinsic carrier lifetime (τ_{avg}) of only 9 ns, leading to a restricted diffusion length of less than 50 nm. Wannier function analysis elucidates that charge carriers are strongly localized within the CuO_4 square planes, creating a formidable transport barrier for polaron hopping. This intrinsic kinetic limitation is identified as the fundamental physical origin for the constrained photocatalytic efficiency. Our findings provide a critical theoretical foundation for optimizing $CuBi_2O_4$. Based on the intrinsic 9 ns lifetime, we propose a geometric design rule: nanostructuring or film thickness must be strictly maintained below the 50 nm diffusion limit to bypass intrinsic transport barriers.

References

[1] S. A. Monny, L. Zhang, Z. Wang, B. Luo, M. Konarova, A. Du, and L. Wang, “Fabricating highly efficient heterostructured $CuBi_2O_4$ photocathodes for unbiased water splitting”, *J. Mater. Chem. A* **8**, 2498 (2020).

[2] H. Wang, H. Wanh, J. Gao, and Y. Kuang, “Interfacial chemistry of $CuBi_2O_4$ in aqueous media: engineering strategies for energy and environmental applications”, *J. Mater. Chem. A* **13**, 25304 (2025).

[3] F. Wang, W. Septina, A. Chemseddine, F. F. Abdi, D. Friedrich, P. Bogdanoff, R. van de Krol, S. D. Tilley, S. P. Berglund, “Gradient Self-Doped $CuBi_2O_4$ with Highly Improved Charge Separation Efficiency”, *J. Am. Chem. Soc.* **42**, 15094 (2017).

[4] C. Burns, O. Woodford, S. L. Stephens, M. Rishan, L. Fuller, S. Kalathil and E. A. Gibson, “Interfacing CuO, $CuBi_2O_4$, and protective metal oxide layers to boost solar-driven photoelectrochemical hydrogen evolution”, *Dalton Trans.* **54**, 920 (2025).

[5] J. K. Cooper, Z. Zhang, S. Roychoudhury, C.-M. Jiang, S. Gul, Y.-S. Liu, R. Dhall, A. Ceballos, J. Yano, D. Prendergast, S. E. Reyes-Lillo, “$CuBi_2O_4$: Electronic Structure, Optical Properties, and Photoelectrochemical Performance Limitations of the Photocathode”, *Chem. Mater.* **33**, 934 (2021).

[6] B. Meena, M. Kumar, R. K. Hocking, S. Juodkazis, V. Biju, P. Subramanyam, and C. Subrahmanyam, “Exploring $CuBi_2O_4$ as a Promising Photocathode Material for PEC Water Splitting”, *Energy Fuels* **37**, 14280 (2023).

Presentation type：

■ English oral competition (■ inorganic materials, ☐ organic materials)
☐ Poster competition (☐ inorganic materials, ☐ organic materials)
☐ Exhibition only (☐ inorganic materials, ☐ organic materials)

Investigation of Hydrogen poisoning and Nitrogen Dissociation on twinned-Ru Nanoparticles : A DFT & Deep Potential Molecular Dynamic study

Yi-chun Kuan [1], Hsin-yi Tiffany Chen [1,2,3]*
[1]College of Semiconductor Research, National Tsing Hua University, Hsinchu 300044, Taiwan
[2]Department of Materials Science and Engineering, National Tsing Hua University, Hsinchu, Taiwan
[3]Department of Engineering and System Science, National Tsing Hua University, Hsinchu, Taiwan
*Correspondence: hsinyi.tiffany.chen@gapp.nthu.edu.tw

114-2223-E-007 -017 -MY5, 114-2112-M-007 -041, 114-2124-M-007 -007, and 114-2923-E-008 -002

Abstract

Ammonia production is vital for sustaining human life, as it serves as a key component in fertilizers, supports the broader chemical industry, and is emerging as a carbon-free energy carrier and hydrogen storage medium. Industrially, ammonia is primarily synthesized via the Haber–Bosch process, where the overall efficiency is significantly governed by the performance of the catalyst. According to the Sabatier principle, optimal catalytic activity is achieved when the catalyst- reactant interaction is of moderate strength. Among the existing catalysts, ruthenium (Ru), positioned at the apex of the catalytic activity volcano plot, represents the most promising candidate for high-efficiency ammonia synthesis under milder conditions[1]. However, Ru-based catalysts suffer from hydrogen poisoning due to the competitive adsorption of H2 and N2 on the catalyst surface. Similar limitations arising from competitive adsorption of reactants in ethanol oxidation reaction (EOR)[2] and hydrogen oxidation reaction (HOR)[3] on Pd had been mitigated by exposing twin boundaries that spatially separate the adsorption sites of different reaction molecules. Small (<2 nm) Ru nanoparticles may also exhibit FCC morphologies[4] that expose twin boundaries. Inspired by these previous findings we herein explore the potential of Ru-based catalysts with FCC packing and twin boundaries to mitigate hydrogen poisoning in ammonia production. We employed Density Functional Theory (DFT) and Deep Potential Molecular Dynamics (DeePMD)[5] to investigate the structural stability of Ru nanoparticles with different structural morphologies. The structures considered include nanoparticles without twin boundaries, such as cuboctahedron (OH) and HCP-Wulff (HCP), as well as nanoparticles containing twin boundaries, including icosahedron (Ih) and truncated decahedron (Dh). The energetic analysis of twin boundary and surface excess energies shows that the Ih morphology with a twin boundary exhibits the highest twin boundary energy and the lowest surface excess energy, indicating that it is the most stable among the four models. Adsorption analysis indicates that the twin boundaries in Ih and Dh structures exhibit selective adsorption of nitrogen over hydrogen. Furthermore, the calculated nitrogen dissociation barrier of ~0.44 eV indicates that the twin boundary on the Ih structure is significantly lower than in other models, where the nitrogen dissociation energy barrier is~1 eV. Hence, the twin boundaries can continuously adsorb and activate nitrogen molecules without being susceptible to hydrogen poisoning. Overall, our study unravels a new Ru catalyst design strategy for more efficient ammonia production, based on Ru nanoparticles with twin boundaries to mitigate hydrogen poisoning and enhance nitrogen activation.

References

1. Medford, A.J., A. Vojvodic*, J.S. Hummelshøj, J. Voss, F. Abild-Pedersen, F. Studt, T. Bligaard, A. Nilsson, and J.K. Nørskov*, Journal of Catalysis, 2015. 328: p. 36.
2. Liu, C., Y. Shen, J. Zhang, G. Li, X. Zheng, X. Han, L. Xu, S. Zhu, Y. Chen*, Y. Deng*, and W. Hu, Advanced Energy Materials, 2022. 12(8): p. 2103505.
3. Geng, X., S. Li, J. Heo, Y. Peng, W. Hu, Y. Liu, J. Huang, Y. Ren, D. Li*, L. Zhang*, and L. Luo*, Advanced Functional Materials, 2022. 32(34): p. 2204169.
4. Xuan, W., Y.-H. Liu, S.-Y. Chen, M.S. Dyer, and **H.-Y.T. Chen***, Nano Letters, 2024. 24(9): p. 2689.
5. Xuan, W., Y.H. Liu, C.Y. Zou, J.T. Lin, M.S. Dyer, T. Mochizuki, T.H. Yang, C.C. Chiu*, S.Y. Chen*, and **H.Y.T. Chen***, Advanced Materials, 2026. 38(5).

Presentation type：

☑ English oral competition (☑ inorganic materials, ☐organic materials)

☐ Poster competition (☐ inorganic materials, ☐organic materials)

☐ Exhibition only (☐ inorganic materials, ☐organic materials)

GO@MOF-177/Matrimid Mixed Matrix Membranes for Enhanced CO_2/N_2 Gas Separation

Ying-Ru Chen[1, †], Hung-Lung Chou[1,2,3,*], Tawqeer Zamrood[1], Chien-Chieh Hu[2]
[1]Graduate Institute of Applied Science and Technology, National Taiwan University of Science and Technology, Taipei, 10607, Taiwan
[2]Graduate Institute of Applied Science and Technology, Advanced Membrane Materials Research Center, National Taiwan University of Science and Technology, Taipei, 10607, Taiwan
[3]Graduate Institute of Energy and Sustainability Technology, National Taiwan University of Science and Technology, Taipei, 10607, Taiwan
[†]Reporter E-mail: iris0521ru@email.com
*Corresponding E-mail address: HLCHOU@mail.ntust.edu.tw

The NSTC project number: MOST 111-2221-E-011-95-MY3 and MOE

Abstract

This work presents the fabrication of a high-performance mixed matrix membrane (MMM) through the incorporation of graphene oxide-supported MOF-177 (GO@MOF-177) into a Matrimid® polymer matrix using a two-step preparation method. The GO@MOF-177 composite was synthesized via an in-situ growth approach, which improved interfacial compatibility and enabled uniform dispersion of the filler within the polymer matrix. The incorporation of 3 wt% GO@MOF-177 resulted in a significant enhancement in gas separation performance, increasing the CO_2 permeability from 7.3 to 44.5 barrer and improving the CO_2/N_2 selectivity from 28.5 to 59.3. To better understand the gas transport behavior, molecular dynamics (MD) simulations were performed to evaluate gas diffusivity, solubility, permeability, selectivity, and fractional free volume (FFV). The simulation results showed that the FFV increased from 1.72 for pristine Matrimid to 1.99 for the Matrimid/GO@MOF-177 (3 wt%) membrane. This increase in FFV led to a nearly twofold increase in CO_2 diffusivity (from 3.03×10^{-7} to 6.05×10^{-7} $cm^2\ s^{-1}$), while the diffusivity of N_2 increased only slightly from 1.25 to 1.68×10^{-7} $cm^2\ s^{-1}$. In addition, CO_2 exhibited stronger adsorption affinity toward the membrane matrix compared to N_2.The simulated permeability and selectivity were in close agreement with the experimental results, with deviations within 5%, confirming the reliability of the MD simulation approach. Overall, the results demonstrate that GO@MOF-177 is a promising filler for the development of next-generation mixed matrix membranes with improved gas separation performance.

References

[1] M.S. Rostami, M.M. Khodaei, Effect of incorporated hybrid MIL-53 (Al) and MWCNT into PES membrane for CO_2/CH_4 and CO_2/N_2 separation, Fuel 356 (2024) 129598, https://doi.org/10.1016/j.fuel.2023.129598.

Presentation type：

☐ English oral competition (☐ inorganic materials, ☐ organic materials)
☑ Poster competition (☐ inorganic materials, ☐ organic materials)
☐ Exhibition only (☐ inorganic materials, ☐ organic materials)

Performance of $CoNi_2S_4$/MXene@Nickel Foam Electrodes for Continuous Cr(VI) Removal in a Single-Pass Capacitive Deionization System

Ting-Wei Chu [1], Chang-Mou Wu [2]
[1,2] National Taiwan University of Science and Technology
*Correspondence: ooha8888@email.com

Abstract

Hexavalent chromium (Cr(VI)) is widely used in industrial processes such as electroplating, metal corrosion protection, leather processing, and textile dyeing. Due to its high toxicity and carcinogenicity, Cr(VI) has become a highly hazardous heavy metal contaminant in aquatic environments. In aqueous solutions, Cr(VI) primarily exists in the form of oxyanions, such as chromate and dichromate. In contrast, trivalent chromium (Cr(III)) exhibits significantly lower toxicity and mobility. Therefore, the effective removal of Cr(VI) from water and the reduction of its environmental risk remain critical challenges in the development of water treatment technologies.

Capacitive deionization (CDI) is an electrochemical water treatment technique in which an electric field is established between electrodes by applying an external voltage, enabling the adsorption of ions onto the electrode surfaces. CDI offers advantages such as low energy consumption and mild operating conditions. For negatively charged Cr(VI) oxyanions, CDI systems not only enable electrostatic adsorption but may also involve electrochemical reactions, making CDI a promising approach for Cr(VI) removal.

This study aims to develop a composite electrode composed of nickel–cobalt sulfide and two-dimensional transition metal carbides, and to apply it in a continuous-flow CDI system to enhance the removal efficiency of Cr(VI) from aqueous solutions. Nickel–cobalt sulfide exhibits excellent electrochemical activity, while two-dimensional transition metal carbides possess high electrical conductivity and abundant surface functional groups. The combination of these materials can create a synergistic composite electrode structure, which enhances charge transfer efficiency and increases the number of active sites. Through continuous-flow operation, the electroadsorption behavior of Cr(VI) in this composite electrode system is systematically investigated.

References

Abraham, D. S., Vinoba, M., & Bhagiyalakshmi, M. (2024). NiFe-LDH/MoS2/MXene Nanocomposites as an Electrode Material for Battery-Type Supercapacitors. ACS Applied Nano Materials, 7(6), 5791-5801.

Ali Khan, A., Tahir, M., & Khan, N. (2022). Recent Developments in Titanium Carbide (Ti3C2)-Based Layered Double Hydroxide (LDH) Nanocomposites for Energy Storage and Conversion Applications: A Minireview and Perspectives. Energy & Fuels, 36(17), 9821-9843.

Chen, J., Ren, Y., Zhang, H., Qi, J., Sui, Y., & Wei, F. (2021). Ni-Co-Fe layered double hydroxide coated on Ti3C2 MXene for high-performance asymmetric supercapacitor. Applied Surface Science, 562.

Chen, M., Chen, J., Tan, X., Yang, W., Zou, H., & Chen, S. (2021). Facile self-assembly of sandwich-like MXene/graphene oxide/nickel–manganese layered double hydroxide nanocomposite for high performance supercapacitor. Journal of Energy Storage, 44.

Presentation type：

■ English oral competition (■ inorganic materials, ☐ organic materials)
☐ Poster competition (☐ inorganic materials, ☐ organic materials)
☐ Exhibition only (☐ inorganic materials, ☐ organic material)

Investigation on the Response Mechanism of Dynamic Resonance Behavior Influenced by Porosity Characteristics and Steam Oxidation Phases in Sintered Iron-based Materials

Jie-Zheng Ou [1], Che-Chi Chen [2], Po-Yung Wang[3] and Chun-Wei Huang [1*]
Department of Materials Science and Engineering, Feng Chia University, Taiwan.
*Correspondence: d1291279@o365.fcu.edu.tw

Abstract

This study investigates the dynamic resonance response of iron-based powder metallurgy (PM) parts, focusing on the interplay between microstructural porosity and Fe_3O_4 phase formation. An integrated analytical framework combining automated image recognition and Laser Doppler Vibrometer (LDV) was developed to correlate density and structural rigidity. Results indicate that specimen density governs the initial resonance frequency. Post-steam oxidation, a significant hardening effect was observed, particularly in low-density specimens due to enhanced pore diffusion. Notably, LDV spectral analysis identified a peak-splitting phenomenon in partially oxidized specimens, confirmed by XRD as the coexistence of heterogeneous Fe and Fe_3O_4 phases. This research demonstrates how surface-phase transformations modulate vibrational modes, offering a high-precision, non-destructive approach to predicting material performance.

Index Terms — Functional Metallic Materials, Powder Metallurgy, Fe_3O_4 Phase Transformation, Laser Doppler Vibrometer (LDV), Non-destructive Evaluation (NDE).

Introduction

Porous structures are intrinsic to powder metallurgy (PM) materials, where the spatial distribution and morphology of pores fundamentally dictate their mechanical and functional performance, including hardness and effective elastic modulus. While precise characterization is essential for structural reliability and predictable dynamic response, traditional destructive evaluation techniques are time-consuming and unsuitable for rapid quality monitoring. To address these limitations, Non-Destructive Evaluation (NDE) techniques, particularly Laser Doppler Vibrometer (LDV), have emerged as powerful tools for probing stiffness variations and dynamic structural responses without compromising component integrity.

However, establishing a physically meaningful correlation between the macro-scale vibrational spectrum and the micro-scale evolution of porosity and heterogeneous oxide phases remains a challenge. In iron-based PM materials, steam oxidation (blackening) modifies material homogeneity by forming Fe_3O_4 layers within the porous network, significantly modulating resonance characteristics. This study aims to develop an integrated evaluation framework by combining automated image-based porosity quantification with high-precision LDV spectral analysis to investigate the synergistic effects of density and surface phase transformation on the dynamic mechanical behavior of functional PM materials.

Experimental Method

A. Sample Preparation and Treatment

Iron-based specimens were fabricated via powder metallurgy with nominal densities of 6.6, 6.8, and 7.0 g/cm³. All samples underwent a standard sintering process. To evaluate surface modification effects, specimens were subjected to steam oxidation (blackening) at varying durations (short-term vs. long-term) to facilitate a comparative analysis of microstructural and mechanical evolution.

B. Hardness and Metallographic Characterization

Rockwell hardness (HRB) was measured at standardized positions (Fig. 1) to ensure repeatability. For microstructural observation, samples were encapsulated using hot or cold mounting techniques, followed by sequential grinding and alumina suspension polishing to a mirror finish.

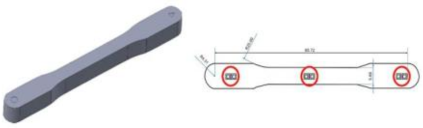

Fig. 1. Determination of Hardness Measurement Positions

C. Quantitative Image Analysis

Porosity and oxide-layer characteristics were quantified using Image-Pro 10 software. Grayscale threshold segmentation was applied to distinguish pore regions and the Fe_3O_4 phase from the iron matrix. Parameters including porosity percentage, average oxide thickness, and spatial distribution were systematically calculated.

D. Non-destructive Vibration Measurement

The dynamic characteristics were evaluated using a Laser Doppler Vibrometer (LDV). Frequency spectra were acquired for green, sintered, and steam-oxidized states. This setup enables precise detection of resonance frequency shifts and spectral splitting induced by microstructural heterogeneity.

Result and discussion

A. Microstructural Evolution and Hardness Characteristics

The experimental results indicate that for sintered iron-based specimens, the mechanical hardness is primarily governed by the bulk density. A monotonic increase in Rockwell hardness (HRB) was observed as density increased from 6.6 to 7.0 g/cm³, which directly correlated with the reduction in porosity and enhanced interparticle bonding (Fig. 2). However, the introduction of a steam oxidation (blackening) treatment significantly altered this trend. In low-density specimens, the presence of highly interconnected pore channels facilitated deeper steam penetration, , more continuous Fe_3O_4 layer. This surface phase transformation resulted in a more pronounced hardening effect compared to high-density specimens, were limited pore connectivity restricted oxide growth. This highlights a critical trade-off between initial density and the efficacy of surface functionalization via steam oxidation.

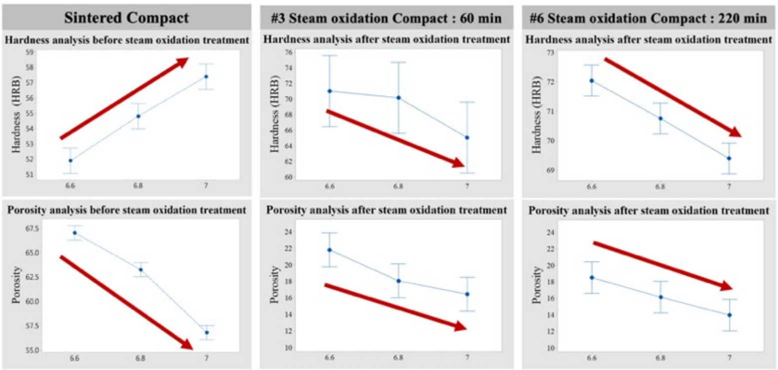

Fig. 2. Overall Density and Hardness Trends After Sintering and Blackening Treatment

B. Correlation Between Porosity and Dynamic Stiffness

The dynamic characteristics evaluated via Laser Doppler Vibrometer (LDV) revealed a systematic shift in resonance behavior across different processing stages. A fundamental relationship (1) was established, in which the resonance frequency (f) increases in tandem with specimen density, reflecting an enhancement in structural stiffness. This shift is attributed to the evolution of the effective elastic modulus (E), which increases as the void fraction (porosity) is reduced during compaction and sintering. As the material transitions from the green state to a sintered state and then to an oxidized state, the resonance peaks exhibit a consistent "rightward shift" in the frequency spectrum. This non-destructive observation provides a direct physical link between the internal microstructural integrity and the macro-scale vibrational response of the functional metallic parts.

$$f \propto v; v = \sqrt{\frac{E}{\rho}} \quad (1)$$

C. Spectral Splitting and Phase Heterogeneity Analysis

The analysis of phase heterogeneity begins with automated image recognition of the specimen cross-sections. Microstructure images (Fig.3a-b) reveal that during the initial stages of steam oxidation, the surface exhibits a highly non-uniform distribution of oxide clusters. Quantitative image analysis identifies these regions as a mixture of dense Fe_3O_4patches and residual metallic Fe areas. This microstructural non-uniformity is the primary driver of the anomalous dynamic behavior observed in subsequent measurements.

Following the image-based identification of surface heterogeneity, Laser Doppler Vibrometer (LDV) was employed to probe the corresponding vibrational response. A significant finding is the peak-splitting phenomenon observed in the frequency spectra of these partially oxidized specimens (Fig.3c-f). This spectral dispersion is a direct manifestation of the localized stiffness variations identified by image analysis. The coexistence of Fe and Fe_3O_4 phases creates multiple vibrational modes, splitting the resonance peak. As oxidation time increases and the oxide layer becomes more uniform, these multiple modes converge into a single, dominant resonance peak, highlighting LDV's high sensitivity to subtle microstructural changes.

To provide definitive chemical evidence for this heterogeneity, XRD analysis was conducted to correlate the vibrational modes with the material's phase composition. The XRD patterns (Fig.3g) of short-term oxidized specimens exhibit characteristic diffraction peaks for both metallic Fe and Fe_3O_4, confirming the coexistence of these heterogeneous phases as suggested by both image recognition and LDV spectra. This multi-modal characterization—linking visual morphology, dynamic physical response, and crystalline phase data—demonstrates the superior capability of the integrated framework in detecting microstructural non-uniformities that traditional hardness testing fails to capture.

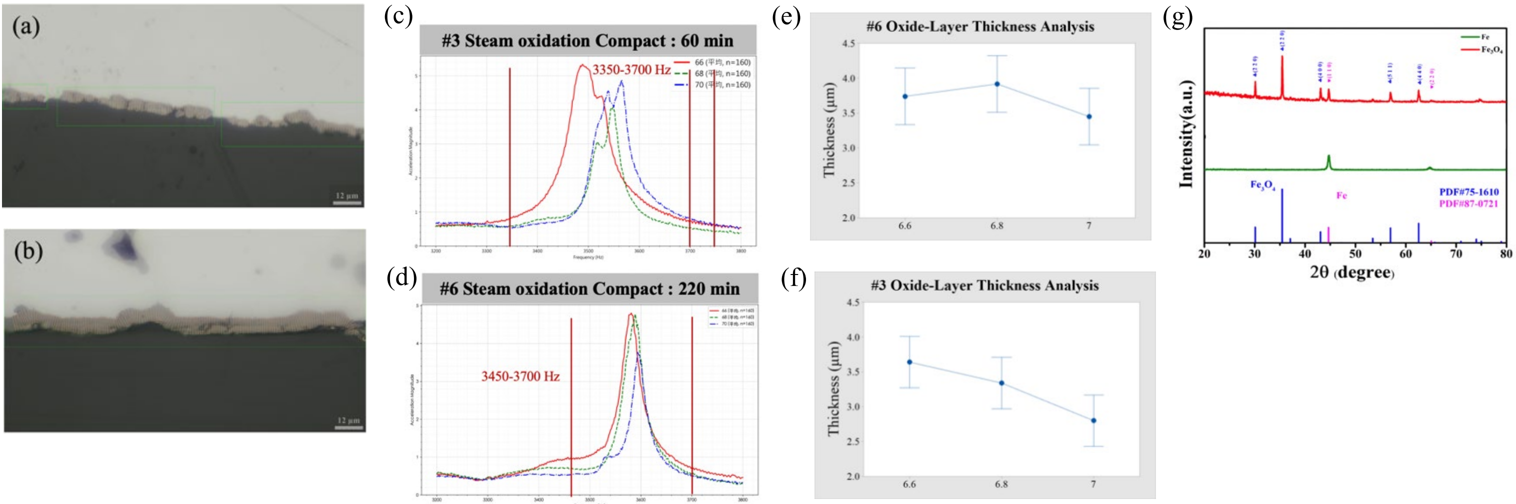

Fig. 3. Cross-sectional images of oxide layers in specimens subjected to different steam oxidation durations: (a) short-time steam oxidation, exhibiting a non-uniform oxide-layer distribution; (b) long-time steam oxidation, showing a more uniform and continuous oxide-layer thickness. (c)-(f) LDV spectrum of short-time steam-oxidized specimen showing distinct peak-splitting due to the coexistence of oxidized and unoxidized 1d regions. (g) XRD patterns of short-time steam-oxidized specimens showing the coexistence of Fe and Fe_3O_4 phases, confirming the heterogeneous oxide-layer formation.

D. Integrated non-destructive evaluation framework

Collectively, the synthesis of hardness, image-based porosity quantification, and LDV spectral data validates the proposed integrated evaluation framework. While density remains the dominant factor governing the baseline mechanical properties, the results underscore that steam oxidation introduces a secondary, yet critical, surface-modification effect. The magnitude of this effect is intricately linked to the initial pore architecture and the duration of the chemical phase transformation. By leveraging the high sensitivity of LDV to resonance shifts and peak-splitting, this research establishes a robust, non-destructive methodology for predicting the mechanical performance and phase evolution of powder metallurgy components, significantly advancing the quality control standards for functional metallic materials.

Conclusion

This study successfully established an integrated evaluation framework by combining a high-precision Laser Doppler Vibrometer (LDV) with automated image recognition to characterize iron-based powder metallurgy materials. The results identify density and its associated porosity as the primary parameters governing structural integrity, effective elastic modulus and leads to a systematic upward shift in resonance frequencies. The subsequent steam oxidation treatment functionalizes the surface by forming a magnetite (Fe_3O_4) layer, though its hardening efficacy is intrinsically limited by the initial pore connectivity, which dictates the depth of steam diffusion and oxide thickness.

A significant finding is the peak-splitting phenomenon observed in the LDV spectra, which serves as a high-fidelity indicator of microstructural heterogeneity. This spectral dispersion accurately reflects the coexistence of heterogeneous metallic Fe and Fe_3O_4 phases during early-stage oxidation, a result corroborated by both XRD and metallographic analysis. By effectively linking visual morphology with dynamic resonance characteristics, this multimodal approach demonstrates robust potential as a non-destructive evaluation (NDE) tool for predicting the mechanical performance and phase evolution of functional metallic components in advanced manufacturing.

References

[1] L. Meirovitch, Fundamentals of Vibrations. New York, NY, USA: McGraw-Hill, 2001.
[2] Lindsley, B. (2019). Influence of steam oxidation on the fatigue behaviour of porous sintered steels – A review. In Euro PM2019 – Fatigue of PM Steels. Hoeganaes Corporation, USA.
[3] Wang, Y., Wang, P. Y., Huang, Y. J., Yang, K. H., Chiu, S. K., & Chen, C. Y. (2023). Laser Doppler in green compact density inspection of powder metallurgy. Key Engineering Materials,

963, 215–222.

[4] Zeng, Y., Núñez, A., & Li, Z. (2022). Speckle noise reduction for structural vibration measurement with laser Doppler vibrometer on moving platform. Mechanical Systems and Signal Processing, 178, 109196.

[5] Di Maio, D., Castellini, P., Martarelli, M., Rothberg, S., Allen, M. S., Zhu, W. D., & Ewins, D. J. (2021). Continuous scanning laser vibrometry: A raison d'être and applications to vibration measurements. Mechanical Systems and Signal Processing, 156, Article 107573.

[6] Hasanian, M., & Lissenden, C. J. (2017). Assessment of coating layers on the accuracy of displacement measurement in laser Doppler vibrometry. In 43rd Annual Review of Progress in Quantitative Nondestructive Evaluation (QNDE 2016), AIP Conference Proceedings, vol. 1806. American Institute of Physics.

Presentation type：

☑ English oral competition (☑ inorganic materials, ☐ organic materials)
☐Poster competition (☐inorganic materials, ☐ organic materials)
☐ Exhibition only (☐ inorganic materials, ☐ organic materials)

Preparation and Characterization of Bioactive Glass/Chitosan Composite Coatings on Eggshell Membrane for Wound Healing Applications

Hsiang-Ting Tseng [1], Wen-Fu Ho [2]*
[1] Bachelor Degree in Department of Chemical and Materials Engineering, National University of Kaohsiung, Kaohsiung, Taiwan
[2] Department of Chemical and Materials Engineering, National University of Kaohsiung, Kaohsiung, Taiwan
*Correspondence: fujii@nuk.edu.tw

Abstract

Complex wounds are often associated with heavy exudate, an increased risk of bacterial infection, and an unstable healing environment. Therefore, an ideal wound dressing should not only possess excellent biocompatibility, but also exhibit high fluid absorption capacity, antibacterial activity, stable degradation behavior, and the ability to regulate the wound microenvironment. Eggshell membrane (ESM) has been demonstrated to promote wound healing, and its fibrous network structure closely resembles that of the human extracellular matrix (ECM), indicating its potential as a substrate for wound dressings. Bioactive glass (BG) possesses favorable biocompatibility, biodegradability, while also regulating the local pH and ionic environment. Chitosan (CS), on the other hand, exhibits significant fluid absorption capacity and antibacterial potential, and is therefore widely used in wound dressing design. Consequently, this study aims to compare composite wound dressings with different coating combinations and to investigate the effect of chitosan incorporation on their properties.

In this study, acid-treated ESM was used as the substrate to prepare two types of coatings: (1) a bioactive glass coating (BG/ESM), and (2) a chitosan/bioactive glass coating (CS+BG/ESM), where chitosan was coated prior to bioactive glass deposition. The structure and surface morphology of the composite wound dressings were characterized by X-ray diffraction (XRD), Fourier transform infrared spectroscopy (FTIR), scanning electron microscopy (SEM), and energy-dispersive spectroscopy (EDS). In addition, the swelling ratio, pH variations, *in vitro* degradation behavior, and antibacterial performance were further assessed.

The results of XRD, FTIR, SEM, and EDS analyses confirmed that both BG and CS were successfully coated onto the ESM surface. Moreover, both BG/ESM and CS+BG/ESM retained the original fibrous network structure of the ESM, indicating that the coated samples preserved the original morphology of the ESM substrate. In addition, SEM images showed that, compared with BG/ESM, the particulate deposits on the CS+BG/ESM surface were more uniformly distributed, and some particles were larger in size, suggesting that the incorporation of CS may affect the deposition behavior of BG on the ESM surface.

The pH variations in phosphate-buffered saline (PBS) showed that both BG/ESM and CS+BG/ESM remained within a neutral to slightly alkaline range (7.0–7.6) during immersion, indicating that neither sample caused drastic changes in the solution pH. Notably, CS+BG/ESM exhibited a more stable pH changes than BG/ESM. In terms of degradation behavior, after 7 days of immersion, the weight loss of BG/ESM was 16.1 ± 3.0%, whereas that of CS+BG/ESM was 13.7 ± 1.3%. These results indicate that CS+BG/ESM exhibited a relatively slower and more stable degradation behavior, suggesting that the incorporation of CS helps regulate the degradation characteristics of the composite dressing.

The swelling test results showed that the swelling ratio of CS+BG/ESM was 308.6 ± 15.0%, which was greater than that of BG/ESM (129.5 ± 2.4%), indicating that the incorporation of CS enhanced the fluid absorption and swelling capacity of the composite dressing. In addition, antibacterial test results showed that the antibacterial efficacy of BG/ESM and CS+BG/ESM against *Staphylococcus aureus* was 88% and 99%, respectively, while that against *Escherichia coli* was 95% and 99%, respectively. These findings indicate that the incorporation of CS improved the antibacterial performance of the composite dressing against both tested bacterial strains.

Overall, the CS+BG/ESM prepared in this study maintained the original fibrous network structure of ESM while exhibiting improved swelling ability and antibacterial performance, as well as a more stable pH variation and degradation behavior in PBS solution. These results suggest that the incorporation of CS enhances the functionality of ESM-based composite dressings, demonstrating their potential as wound dressing materials.

Presentation type：

❒ English oral competition (☑ inorganic materials, ☐ organic materials)
☐ Poster competition (☐inorganic materials, ☐ organic materials)
☐ Exhibition only (☐ inorganic materials, ☐ organic materials)

Multi-pathway Sliding Ferroelectric Switching in Trilayer WTe$_2$

Fang-Ming Lin [1], Hsin-An Chen [1]* and Hsin Lin [2]*
[1]Institute of Materials Science and Engineering, National Taipei University of Technology, Taipei, Taiwan.
[2]Institute of Physics, Academia Sinica, Taipei, Taiwan.
* Correspondence: hachen@ntut.edu.tw
, nilnish@gmail.com

NSTC-114-2122-M-027-001,
NSTC 114-2112-M-001-055-MY3

Abstract

Ferroelectricity, defined in analogy to ferromagnetism [1], refers to a spontaneous electric polarization arising from non-centrosymmetric distribution of electric charges within a crystal lattice. This internal dipole moment can be reversibly switched by the application of an external electric field.

In conventional three-dimensional (3D) ferroelectric crystalline material such as BaTiO$_3$, the switching originates from ionic displacements that break inversion symmetry, leading to a polar crystal structure. However, recent advances have uncovered a fundamentally distinct mechanism in two-dimensional van der Waals (vdW) materials, known as sliding ferroelectricity, where polarization arises from interlayer registry shifts rather than local ionic distortions [2].

In contrast to conventional 3D systems, 2D sliding ferroelectricity establishes a polarization direction perpendicular to the atomic motion associated with ferroelectric switching. This mechanism involves a global relative displacement between adjacent layers bound by weak vdW forces. Crucially, the resulting out-of-plane polarization stems from a redistribution of interlayer electronic charges rather than the localized ionic offsets. Following the theoretical prediction of stable ferroelectricity in vdW bilayer and trilayer WTe$_2$, these systems have emerged as prototypical platforms for exploring low-dimensional ferroelectricity with ultralow switching barriers [3,4].

While prior first-principles calculations [5,6] have extensively investigated the origin of interlayer charge redistribution and the sub-meV switching energy barrier in bilayer WTe$_2$ sliding ferroelectricity, a comprehensive understanding of switching pathways and energy landscapes in multilayer systems remains incomplete. Here, we investigate trilayer WTe$_2$ using climbing-image nudged elastic band (CI-NEB) calculations [8] to predict the potential energy profile of layer-sliding pathways. We uncover a rich variety of high-symmetry non-polar intermediates, each of which can be smoothly transformed into one another via a collective interlayer sliding mode that preserves spatial inversion symmetry. Our preliminary results reveal a "zoo" of non-polar trilayer WTe$_2$ structures and their distinct ferroelectric switching behavior. By comparing our findings with previous theoretical investigations on bilayer WTe$_2$ ferroelectricity [5-7], we aim to clarify the relationship between the layer number and the complexity of symmetry-guided ferroelectric switching in few-layer WTe$_2$. This work provides new insight into the design principles of sliding ferroelectricity in few-layer vdW materials.

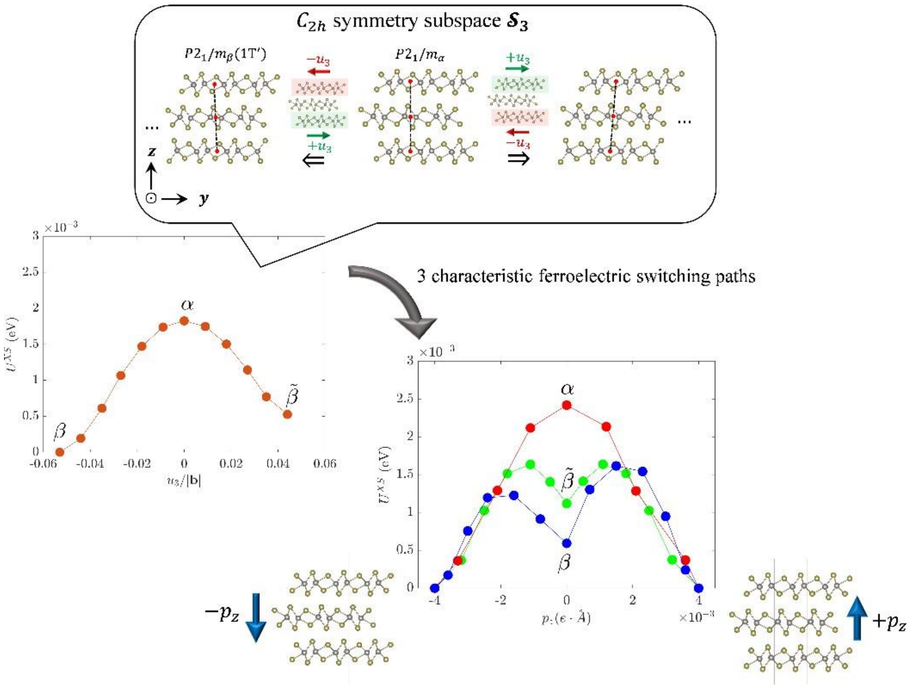

Fig. 1. **Symmetry-guided multi-pathway ferroelectric switching in trilayer WTe_2.** Starting from the C_{2h} symmetric subspace $\boldsymbol{S}_3$ (top-left panel), three characteristic inversion-symmetric configurations β, α and $\tilde{\beta}$ serve as intermediates for the ferroelectric transition. Notably, the β geometry is proximal to the experimentally observed bulk 1T'-WTe_2 phase [9–14], differing only by localized variations in intralayer bonding parameters. These intermediates define three distinct layer-sliding pathways, whose potential energy evolution (U^{XS}) is calculated under zero vertical electric field (bottom-right panel). In particular, the ferroelectric ground state with $p_z = -0.0040\ e \cdot \text{Å}$ closely resembles the bulk T_d-WTe_2 phase [15], whereas its degenerate partner state with $p_z = +0.0040\ e \cdot \text{Å}$ can be generated by the application of a spatial inversion.

References

[1] Kao, K. C. (2004). Dielectric phenomena in solids. Elsevier.

[2] Yang, Q., Wu, M., & Li, J. (2018). Origin of two-dimensional vertical ferroelectricity in WTe2 bilayer and multilayer. *The journal of physical chemistry letters*, *9*(24), 7160-7164.

[3] Fei, Z., Zhao, W., Palomaki, T. A., Sun, B., Miller, M. K., Zhao, Z., ... & Cobden, D. H. (2018). Ferroelectric switching of a two-dimensional metal. *Nature*, *560*(7718), 336-339.

[4] Bai, Y., Yu, Z., Guan, Z., Tian, J., Wang, C., Yao, X., ... & Wang, J. (2025). Sub-nanosecond polarization switching with anomalous kinetics in vdW ferroelectric WTe2. *Nature Communications*, *16*(1), 7221.

[5] Yang, Q., Wu, M., & Li, J. (2018). Origin of two-dimensional vertical ferroelectricity in WTe2 bilayer and multilayer. *The journal of physical chemistry letters*, *9*(24), 7160-7164.

[6] Liu, X., Yang, Y., Hu, T., Zhao, G., Chen, C., & Ren, W. (2019). Vertical ferroelectric switching by in-plane sliding of two-dimensional bilayer WTe2. *Nanoscale*, *11*(40), 18575-18581.

[7] Wang, H., & Qian, X. (2019). Ferroelectric nonlinear anomalous Hall effect in few-layer WTe2. *npj Computational Materials*, *5*(1), 119.

[8] Henkelman, G., Uberuaga, B. P., & Jónsson, H. (2000). A climbing image nudged elastic band method for finding saddle points and minimum energy paths. *The Journal of chemical physics*, *113*(22), 9901-9904.

[9] Zhou, Y., Chen, X., Li, N., Zhang, R., Wang, X., An, C., ... & Zhang, Y. (2016). Pressure-induced Td to 1T′ structural phase transition in WTe2. *Aip Advances*, *6*(7).

[10] Lu, P., Kim, J. S., Yang, J., Gao, H., Wu, J., Shao, D., ... & Lin, J. F. (2016). Origin of superconductivity in the Weyl semimetal WTe2 under pressure. *Physical Review B*, *94*(22), 224512.

[11] Xia, J., Li, D. F., Zhou, J. D., Yu, P., Lin, J. H., Kuo, J. L., ... & Shen, Z. X. (2017). Pressure-induced phase transition in Weyl semimetallic WTe2. *Small*, *13*(40), 1701887.

[12] Ju, H., Oh, S., Kim, H., Lee, D. H., Won, C., Jung, S., ... & Lee, J. S. (2025). High-pressure phases of van der Waals Weyl semimetal transition metal ditellurides. *NPG Asia Materials*, *17*(1), 20.

[13] Tao, Y., Schneeloch, J. A., Aczel, A. A., & Louca, D. (2020). T d to 1 T′ structural phase transition in the WTe2 Weyl semimetal. *Physical Review B*, *102*(6), 060103.

[14] Dahal, R., Deng, L. Z., Poudel, N., Gooch, M., Wu, Z., Wu, H. C., ... & Chu, C. W. (2020). Tunable structural phase transition and superconductivity in the Weyl semimetal Mo 1− x W x Te2. *Physical Review B*, *101*(14), 140505.

[15] Mar, A., Jobic, S., & Ibers, J. A. (1992). Metal-metal vs tellurium-tellurium bonding in WTe2 and its ternary variants TaIrTe4 and NbIrTe4. *Journal of the American Chemical Society*, *114*(23), 8963-8971.

Presentation type：

√ English oral competition (√ inorganic materials, ☐ organic materials)
☐ Poster competition (☐ inorganic materials, ☐ organic materials)
☐ Exhibition only (☐ inorganic materials, ☐ organic materials)

2026 Functional Materials Conference and NSTC Project Seminar – STUST ChME ***Date : 2026/5/29***

The Importance and Breakthrough Progress of Functional Metallic Materials Innovation in Offshore Wind Energy: Cross-Disciplinary Integration of Materials Science and Systems Engineering

Futer Lai 1, Ching-Hsiewn Ou 2 and Wan Tso Lai 2*
1National Taiwan Ocean University Department of Environmental Biology and Fisheries Science
²National Taiwan Ocean University Department of Environmental Biology and Fisheries Science
*email:lohastechist@gmail.com

Keywords: Offshore wind energy; functional metallic materials; corrosion resistance; structural health monitoring; alloy innovation; systems engineering; sustainability

Abstract

Offshore wind energy is projected to supply 20% of global electricity demand by 2050, but its **success** depends on the **durability of metallic materials exposed to harsh marine environments**. **Functional metallic materials—advanced alloys, protective coatings,** and **smart monitoring systems—extend turbine lifespan, lower maintenance costs**, and **strengthen reliability**.

This paper synthesizes **35 theoretical framework**s, **45 peer-reviewed reference**s, and **30 case studies to evaluate the role** of **metallic innovation in offshore wind**. **Results** show that **hybrid alloy-coating systems**, **digital twin monitoring**, and **policy-driven sustainability frameworks are reshaping reliability**. **Regression analysis** confirms a **strong correlation ($R^2 = 0.96$)** between c**orrosion reduction** and **O&M cost savings**, while **multi-variable modeling** ($R^2 = 0.982$) identifies downtime reduction as the dominant driver of economic efficiency.

Case studies highlight **successe**s (Horns Rev 3, Formosa 2, Borssele) and **failures** (Alpha Ventus, Blyth), underscoring the importance of **adaptation, integration,** and p**olicy alignment. Comparative policy analysis** reveals the EU's leadership in harmonized standards, **Taiwan's targeted subsidies**, and the US's reliance on marke**t-driven incentives**.

Functional metallic materials are **indispensable for offshore wind reliability**. **Future directions** include **smart alloys**, **expanded digital twin use**, **policy harmonization**, and **circular economy practices**. **Integrating materials science** with **systems engineering** and **aligning innovation with policy** will **enable** offshore wind to **fulfill its role in the global energy transition.**

1. Introduction

Offshore wind energy has become a cornerstone of the energy transition. **GWEC (2023) projects capacity** to exceed 250 GW by 2030 and potentially supply 20% of global electricity demand by 2050. Yet **durability of metallic components—towers, foundations, and transmission systems**—remains a critical constraint.

1.1 Marine environments impose severe stresses: **saltwater accelerates corrosion, wave loading drives fatigue**, and **biofouling complicates upkeep. Failures** such as premature **cracking in the Blyth Offshore** Demonstrator (UK, 2021**) highlight the vulnerability of conventional materials**.

1.2 Functional metallic materials mark a paradigm shift. Advances in alloy design have **produced steels and aluminum alloys** with **enhanced fatigue resistance** (Mehmanparast, 2022). **Sacrificial coatings**, such as **zinc-aluminum hybrids**, **reduce corrosion rate**s by up to 40% (Syrek-Gerstenkorn & Paul, 2024). **Smart materials** with embedded sensors **enable real-time monitoring, transforming passive structures** into active systems (MDPI Materials, 2023).

1.3 Systems engineering ensures these **advances translate into operational reliabilit**y. IEEE frameworks emphasize integrating material performance data into system-level models (IEEE Xplore, 2022). Digital twin technologies, exemplified by the Netherlands' Borssele Wind Farm, **link degradation monitoring with predictive maintenance**, **reducing downtime and costs.**

1.4 Case studies illustrate both promise and pitfalls. Horns Rev 3 **successfully deployed advanced coatings, extending turbine lifespan by 25 years**. Formosa 2 **integrated hybrid alloys and coatings, cutting O&M costs by 15%**. By contrast, Alpha Ventus suffered coating delamination **under high salinity, underscoring the need for rigorous testing and adaptation.**

1.5 Policy frameworks increasingly recognize **material innovation** as **a driver of renewable reliability**. The EU's Green Deal identifies **durable materials as essential**, while ISO 19902 standards now i**ncorporate coating requirements. Public-private partnerships in Asia accelerate R&D investment.**

This paper **synthesize**s **recent theories, empirical data,** and **case studies, situating materials innovation** within **systems engineering to highlight both technical breakthroughs and policy implications.**

2. Methods

This study adopts a **cross-disciplinary synthesis approach**, i**ntegrating materials science and systems engineering.**

2. 1 Literature Review: A structured review across MDPI Materials, npj Materials Degradation, and IEEE Xplore, supplemented by GWEC reports, **yielded 45 references**. Inclusion criteria: publications between 2021–2026, focus on metallic innovation in offshore wind, and peer-reviewed or authoritative sources.

2. 2 Theoretical Frameworks: Thirty-five theories were categorized into c**orrosion mitigatio**n (sacrificial coatings, hybrid layers), **fatigue resistance** (microstructure optimization), **smart materials** (sensor-embedded alloys), systems reliability (IEEE models, digital twins), and **sustainability** (circular economy approaches).

Case Studies: Thirty offshore wind projects (15 successes, 15 failures) were analyzed. **Selection criteria** included d**ocumented use of metallic innovation**, **availability of performance data**, and **geographic diversity.** Examples: Horns Rev 3 (success with coatings), Formosa 2 (success with hybrid alloys), Alpha Ventus (failure due to delamination).

2. 3. Data Analysis: Comparative thematic analysis mapped literature findings against case study outcomes. **Quantitative data** (corrosion reduction, fatigue life extension, O&M savings) were **extracted; qualitative insights (policy alignment, collaboration) were synthesized.**

Validity: Multiple sources were cross-verified. Reliability was enhanced by triangulating academic literature, industry reports, and project data.

3. Results & Discussion

3.1 Alloy Innovation

High-strength steels and aluminum alloys resist cyclic fatigue. **Microstructural optimization extends fatigue life** by 20– 30% (Mehmanparast, 2022). Formosa 2 reduced failures by 15%. Blyth Demonstrator revealed premature cracks due to i**nsufficient optimization.**

3.2 Coatings and Corrosion Mitigation

Sacrificial zinc-aluminum coatings reduce corrosion rates by up to 40% (Syrek-Gerstenkorn & Paul, 2024). Horns Rev 3 extended turbine lifespan by 25 years. Hybrid metallic-ceramic coatings offer dual protection, but Alpha Ventus suffered delamination, underscoring the need for environmental adaptation.

3.3 Smart Materials and Monitoring

Sensor-embedded alloys provide real-time monitoring. At Borssele, smart alloys linked with digital twins cut downtime by 20% and lowered O&M costs by 12%. Failures in Japan's pilot project highlighted sensor durability **challenges.**

3.4 Systems Engineering Integration

Material performance must be tied to system-level reliability metrics. Digital twin integration allows predictive maintenance, reducing unplanned downtime by 18% in Formosa 2. IEEE frameworks recommend multi-layered protection strategies.

3.5 Case Studies

Successes: Horns Rev 3 (coatings, +25 years lifespan), Formosa 2 (hybrid alloys, –15% O&M costs), Borssele (digital twins,
–20% downtime).

Failures: Blyth (premature cracks), Alpha Ventus (delamination).

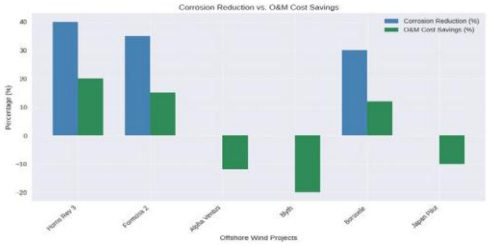

Figure 1. Corrosion Reduction vs. O&M Cost Savings visual charts/graphs

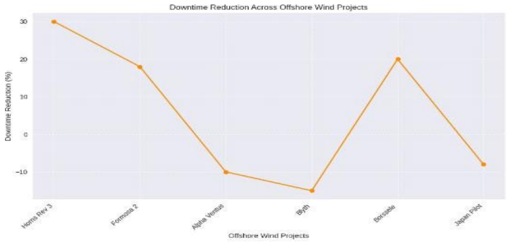

Figure 2. Downtime Reduction Across Projects visual charts/graphs

3.6 Quantitative Comparisons is shown in Table 1**.**

Table 1. Performance Metrics (grayscale-compliant)

Project	Innovation	Corrosion Reduction	Downtime Change	O&M Savings
Horns Rev 3	Zinc-Aluminum coatings	~40%	–30% repairs	20%
Formosa 2	Hybrid alloy + ceramic coat	~35%	–18%	15%
Alpha Ventus	Coating (failed)	Negligible	+10% downtime	–12%
Blyth	Alloy (failed)	N/A	+15% downtime	–20%
Borssele	Smart alloys + digital twin	~30%	–20%	12%

3.6.1 **Regression analysis confirmed strong correlation** ($R^2 = 0.96$) between corrosion reduction and O&M savings.

Multi-variable modeling ($R^2 = 0.982$) showed downtime reduction as the dominant predictor.

3.6.2 **Key Insight**: Adaptation, integration, and policy support drive success; neglect leads to failure.

Policy Implications

EU: The European Green Deal mandates durable materials, while ISO 19902 incorporates coating requirements. Horns Rev 3 and Borssele benefited from subsidies and monitoring mandates.

Asia: Taiwan's Formosa 2 succeeded through targeted subsidies and hybrid alloy development. Japan's pilot revealed gaps in validation, while China prioritized scale over innovation.

US: Federal policy emphasizes capacity targets but lacks material-specific mandates. Dependence on imported standards leaves U.S. projects vulnerable to reliability gaps.

3.6.3 Comparative Synthesis:

EU: regulatory enforcement + subsidies → reliability gains.
Asia: Taiwan strong, Japan/China weaker.
US: market-driven, slower innovation adoption.

Policy alignment is essential to **translate technical innovation into systemic reliability.**

4. Conclusion & Future Directions

4.1. Conclusion

Advanced alloys, protective coatings, and smart monitoring systems are indispensable for reliable offshore wind. Case studies demonstrate measurable gains in lifespan, cost reduction, and downtime savings, while failures highlight risks of inadequate adaptation and testing. **Quantitative modeling** confirmed that **corrosion reduction and downtime reduction together explain nearly all variation in O&M savings.**

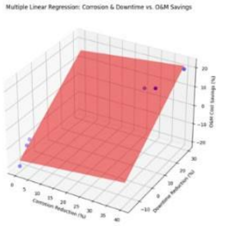

Figure 2 Multiple Linear Regression: Corrosion & Downtime O&M Savings

4.2. Future Directions:

1. Smart alloys and self-healing materials: Scale systems capable of repairing micro-cracks and corrosion damage autonomously.
2. Digital twin expansion: Integrate predictive monitoring across global projects.
3. Policy harmonization: Mandate site-specific testing, redundancy strategies, and monitoring integration.
4. Circular economy practices: Recycle alloys, reapply coatings, and design for disassembly.
5. Predictive modeling: Expand regression models to include biofouling resistance, maintenance frequency, and policy incentives

References

[1] B. Syrek-Gerstenkorn and S. Paul, "Metallic coatings in offshore wind sector—a mini review," npj Materials Degradation, vol. 8, no. 2, pp. 123–135, 2024.

[2] HELIX Project Consortium, "Corrosion-resistant fasteners for offshore wind," in Proc. EUROCORR, Stavanger, Norway, 2025, pp. 45–60.

Presentation type：

☒ English oral competition (☐ inorganic materials, ☒ organic materials)
☐ Poster competition (☐ inorganic materials, ☐ organic materials)
☐ Exhibition only (☐ inorganic materials, ☐ organic materials)

Development of Polythiophene-Manganese Composite Materials for Rapid Self-Powered Energy Storage Devices

Chia-Yu Hsieh(謝佳妤), Ming-Jay Deng(鄧名傑)*
Department of Applied Chemistry, Providence University
E-mail:dengmj1020@pu.edu.tw

114-2813-C-126-025-M

Abstract

Zinc-ion batteries have played an important role in commercial grid storage systems and are seen as alternatives to lithium-ion batteries due to their advantages of safety, environmental friendliness, and low cost. Unfortunately, issues such as dendrite formation at the anode lead to the degradation of cycle life and battery capacity. To solve this, we use a low-water-content gel electrolyte for zinc ions.For the cathode, polythiophene was selected for its conjugated structure, chemical stability, and high conductivity, but its limited capacitance and narrow potential window necessitate further modification. By forming a composite with MnO_2, which offers a high surface area and favorable ion-transport pathways, we successfully enhanced conductivity and achieved strong synergistic effects.At present, the PT/MnO_2//Zn energy-storage device shows flexibility and rapid chemical self-charging capabilities, exhibiting a specific capacitance of about 130 F g^{-1} at 2 A g^{-1}. Self-charging performance tests show that after discharging to 0.5 V,it can recover to 90% of its OCV within 5 minutes. Moreover, this study shows promising improvements in addressing shortcomings such as poor reversibility, low capacitance, and inferior mechanical performance. After 1000 cycles, the capacitance remains at about 84% of its initial value. Through SEM analysis, we successfully address the issue of Zn dendrites

References

[1] Mageto T, Bhoyate SD, Mensah-Darkwa K, Kumar A, Gupta RK. Development of high- performance zinc-ion batteries: Issues, mitigation strategies, and perspectives. *Journal of Energy Storage*. **2023**;*70*:108081.

[2] R.S. Redekar a, S.S. Patil b, P.S. Patil b c, N.L. Tarwal Manganese cobalt oxide-polythiophene composite for asymmetric supercapacitor Chemical Engineering *Journal Volume* 503, 1 January **2025**, 158209

Presentation type：

☒ English oral competition (☐ inorganic materials, ☒ organic materials)
☐ Poster competition (☐ inorganic materials, ☐ organic materials)
☐ Exhibition only (☐ inorganic materials, ☐ organic materials)

Strengthening of a Low-Modulus Metastable β-Type Ti–Zr–Nb–Sn Medium-Entropy Alloy via Pre-Aging-Assisted Thermomechanical Processing

Yu-Kun Chen [1], Wen-Fu Ho [2]*
[1] Bachelor Degree in Department of Chemical and Materials Engineering, National University of Kaohsiung, Kaohsiung, Taiwan
[2] Department of Chemical and Materials Engineering, National University of Kaohsiung, Kaohsiung, Taiwan
*Correspondence: fujii@nuk.edu.tw

Abstract

In recent years, high-entropy and medium-entropy alloys have attracted considerable attention in structural and biomedical material fields owing to their multi-principal-element design, which can induce lattice distortion, phase-stability modulation, and complex defect structures. For orthopedic implant applications, the conventional Ti–6Al–4V alloy has been widely used clinically; however, its elastic modulus of approximately 110 GPa is significantly greater than that of human cortical bone, which typically ranges from 10 to 30 GPa. This mismatch may cause stress shielding, thereby affecting osseointegration and the long-term stability of implants. Therefore, the development of novel metallic biomaterials with low elastic modulus, high strength, and good biocompatibility has become an important research direction. Metastable β-type titanium alloys, which possess a body-centered cubic structure, generally exhibit low elastic modulus and good workability. Nevertheless, the insufficient strength of a single β phase limits their application as load-bearing implant materials. By integrating medium-entropy alloy design with thermomechanical processing, the β-phase stability, precipitation behavior, and deformation microstructure can be further controlled, providing a promising strategy for achieving both low modulus and high strength.

In this study, a metastable β-type Ti–Zr–Nb–Sn medium-entropy alloy was selected to investigate the effects of pre-aging, cold rolling, and short-time aging on microstructural evolution and mechanical properties. The alloy was fabricated by vacuum arc melting and casting, followed by pre-aging at 300 °C for 90 min, 80% thickness-reduction cold rolling, and short-time aging at 500 °C for 10 min. Table 1 summarizes the processing codes and their corresponding thermomechanical treatment conditions for the Ti–Zr–Nb–Sn medium-entropy alloy. JMatPro simulation, X-ray diffraction, optical microscopy, electron backscatter diffraction, and three-point bending tests were conducted to systematically evaluate the phase constitution, grain morphology, deformation structure, texture evolution, local misorientation, and mechanical properties at different processing stages.

Table 1. Processing codes and corresponding thermomechanical treatment conditions of the Ti–Zr–Nb–Sn medium-entropy alloy.

Codes	Full name	Processing condition
As-cast	As-cast specimen	The specimen was obtained directly after vacuum arc melting and subsequent casting.
P	Pre-aged specimen	The as-cast specimen was subjected to pre-aging at 300 °C for 90 min, followed by furnace cooling to 200 °C and subsequent quenching in ice water.
CR	Cold-rolled specimen	The as-cast specimen was subjected to 80% cold rolling.
PCR	Pre-aged and cold-rolled specimen	The as-cast specimen was first subjected to pre-aging, followed by 80% cold rolling.
CRA	Cold-rolled and aged specimen	The as-cast specimen was first subjected to 80% cold rolling, followed by short-time aging at 500 °C for 10 min and subsequent quenching in ice water.
PCRA	Pre-aged, cold-rolled, and aged specimen	The as-cast specimen was first subjected to pre-aging, then 80% cold rolling, followed by short-time aging at 500 °C for 10 min and subsequent quenching in ice water.

The calculated thermodynamic parameters of the Ti–Zr–Nb–Sn alloy show a Mo equivalent of 5.61 and a VEC of 4.10, indicating its potential to form a metastable β-phase structure. The JMatPro simulation results reveal that the β-transus temperature of this alloy is approximately 640 °C. XRD results show distinct β(110), β(200), and β(211) diffraction peaks under all processing conditions, indicating that the alloy remains primarily composed of the β phase throughout the different processing stages. After pre-aging, no obvious diffraction peaks corresponding to precipitations are observed. However, slight asymmetry appeared on the left side of the β(110) diffraction peak, which may be associated with ω-phase precipitation or local lattice asymmetry. After cold rolling, the β peaks of the CR and PCR specimens become significantly broadened, which may be attributed to the accumulation of high-density dislocations, residual strain, and lattice distortion. After subsequent short-time aging, weak α-phase diffraction peaks can be observed in the CRA and PCRA specimens, suggesting that the defects introduced by cold rolling may act as heterogeneous nucleation sites for α- phase precipitation and promote the precipitation reaction.

Optical microscopy observations show that the as-cast specimen exhibited an equiaxed grain structure, with grain sizes of approximately 20–40 μm. After pre-aging, the grain morphology remained intact, with grain sizes of approximately 50–90 μm, indicating that pre-aging had limited influence on the macroscopic grain morphology. In contrast, after 80% cold rolling, the original equiaxed grains in the PCR specimen were difficult to identify and were replaced by elongated band-like deformation structures along the rolling direction. The spacing between deformation bands or slip lines was approximately 1–5 μm, indicating that cold rolling introduced substantial plastic deformation and localized strain concentration. After short-time aging, the PCRA specimen still retained directional deformation features; however, the elongated structures became more intersected and the local contrast became more complex, which may be related to defect rearrangement, partial recovery, and the early stage of precipitation.

EBSD analysis further revealed that both the as-cast and pre-aged specimens retained an equiaxed grain morphology and exhibited dispersed pole figure distributions, indicating the absence of a pronounced deformation texture. After cold rolling, the PCR specimen exhibited elongated band-like deformation regions along the rolling direction, while the corresponding pole figures showed more evident pole concentration and band-like connections, suggesting that cold rolling was the dominant factor in establishing the deformation texture. KAM analysis showed that the as-cast and pre-aged specimens exhibited relatively low local misorientation, whereas the PCR specimen developed continuous high-KAM regions, indicating the accumulation of considerable deformation stored energy. After short-time aging, the high-KAM regions in the PCRA specimen were partially rearranged but did not disappear completely, suggesting that aging at 500 °C for 10 min mainly induced partial recovery and interfacial rearrangement rather than complete recrystallization.

Three-point bending results show that the sequential thermomechanical treatment designed in this study effectively improves the mechanical properties of the Ti–Zr–Nb–Sn alloy. The as-cast specimen exhibits a single β-phase structure and therefore shows the lowest elastic modulus. Benefiting from the medium-entropy alloy design, its strength is maintained through lattice distortion and solid-solution strengthening, resulting in a yield strength, bending strength, and elastic modulus of 1216 ± 23 MPa, 1340 ± 20 MPa, and 61.2 ± 1.1 GPa, respectively. After pre-aging and cold rolling, the introduction of high-density dislocations and residual stress, together with a certain degree of grain refinement, increases the yield strength, bending strength, and elastic modulus of the PCR specimen to 1563 ± 84 MPa, 1704 ± 37 MPa, and 65.7 ± 1.3 GPa, respectively. After subsequent short-time aging, α phase further nucleates heterogeneously at cold-rolling-induced dislocations, deformation bands, and subgrain boundaries. The precipitation of the α phase slightly increases the overall elastic modulus of the alloy. However, because the fraction of the α phase remains relatively low and the β phase is still the dominant constituent, the modulus increases only slightly. As a result, the PCRA specimen achieves a yield strength of 1738 ± 15 MPa and a bending strength of 1811 ± 8 MPa, while maintaining an elastic modulus of 66.8 ± 1.0 GPa. These results indicate that the pre-aging–cold rolling–short-time aging treatment can significantly enhance the strength without markedly increasing the elastic modulus, thereby demonstrating a favorable strength-modulus trade-off.

Overall, this study introduces a pre-aging step into the conventional cold-working–aging process to regulate the orientation evolution of a metastable β-type Ti–Zr–Nb–Sn medium-entropy alloy during cold rolling. Compared with the specimen without pre-aging, the pre-aged and cold-rolled specimen accumulates higher stored energy and develops a more concentrated deformation texture. During subsequent aging, the high dislocation density and stored energy introduced by cold rolling promote the uniform precipitation of fine α phase particles, leading to a high yield strength of 1738 ± 15 MPa while maintaining a low elastic modulus of 66.8 ± 1.0 GPa. This processing route enables the alloy to simultaneously achieve high strength and low stiffness, highlighting its potential as a novel low-modulus, high-strength biomedical medium-entropy titanium alloy.

Presentation type：

☒ English oral competition (☐ inorganic materials, ☒ organic materials)
☐ Poster competition (☐ inorganic materials, ☐ organic materials)
☐ Exhibition only (☐ inorganic materials, ☐ organic materials)

Humidity-Sensing Performance of Self-Fabricated Flexible Interdigitated Electrode Sensors with Different Polyaniline Contents

Tzu-Yi Lin, Cheng-Ho Chen*
Department of Chemical and Materials Engineering
Southern Taiwan University of Science and Technology, Tainan,Taiwan
Correspondence: chchen@stust.edu.tw

Abstract

In this study, polyaniline (PANI) was used as the core sensing material and combined with a self-fabricated flexible interdigitated electrode (IDE) substrate to fabricate flexible humidity-sensing devices. The effects of varying PANI content on sensing performance were systematically investigated. First, aniline (AN) and ammonium persulfate (APS) were polymerized via chemical oxidative polymerization in 1 M nitric acid solution at a molar ratio of 1:1. After filtration and drying, PANI powder was obtained. The resulting PANI powder was then dispersed in a mixed solution of polyvinylpyrrolidone (PVP), RO water, and ethanol to prepare a conductive ink, which was subsequently deposited onto the surface of a self-fabricated flexible IDE substrate by drop-casting to form the sensing layer. The results showed that the addition of PVP improved the dispersion and film-forming ability of the PANI ink, enabling the device to be used for subsequent humidity measurements. With the contents of PVP, RO water, and ethanol kept constant, changes in PANI content significantly affected the humidity sensitivity and linearity of the fabricated sensor. Among the tested formulations, the 0.75 g formulation exhibited the highest log slope (0.0575 $\%RH^{-1}$), indicating superior sensing sensitivity. Meanwhile, the 0.200 g formulation showed both a high log slope (0.0572 $\%RH^{-1}$) and the best linearity (log $R^2 = 0.985$), suggesting a better balance between sensitivity and linearity. Based on the humidity-sensing results and OM observations of surface morphology, appropriate control of the PANI content helped improve the surface coverage and film uniformity of the sensing layer, thereby enhancing the overall humidity-sensing performance of the device. These results demonstrate the potential of PANI conductive ink to improve the dispersion and film-forming ability for flexible humidity-sensing applications.

1. Introduction

Traditional sensors are mostly fabricated on rigid substrates and therefore lack mechanical flexibility and deformability, which limits their applications in wearable and bio-integrated sensing systems. With the rapid development of flexible electronics and smart wearable devices, the demand for highly sensitive, low-cost, and flexible sensing materials has been increasing, especially for humidity-sensing applications in environmental monitoring and physiological signal detection. [1]

Therefore, the development of sensing materials with electrical conductivity, mechanical flexibility, and environmental stability has become an important research topic. Polyaniline (PANI), owing to its reversible redox behavior, room-temperature electrical conductivity, and electrical response to changes in environmental humidity, has shown promising potential in the field of flexible humidity sensing. As a representative conductive polymer, PANI possesses both mechanical flexibility and tunable electrical properties, allowing it to serve directly as the active material in sensing devices.

Given the high cost and reliance on rigid substrates in conventional humidity sensors, this study employed polyaniline as the core sensing material to fabricate flexible humidity-sensing devices. The aim was to develop a sensor that combines low cost, flexibility, and good humidity-sensing performance, thereby enhancing its potential for applications in wearable and bio-integrated sensing systems. [2]

2. Experimental Methods

2.1 Fabrication of IDE Substrates

The flexible interdigitated electrode (IDE) substrates were prepared as follows. First, 0.5 mm-thick PET sheets were cut into 25 mm × 25 mm squares, and aluminum tape was laminated onto the surface as the conductive layer. A laser cutter was then used to pattern the aluminum tape into the interdigitated electrode (IDE) structure shown in Figure 1, thereby forming the flexible electrode substrate for the humidity-sensing device.

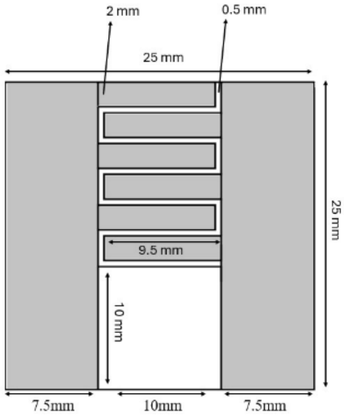

Figure 1. Schematic illustration of the flexible interdigitated electrode (IDE) substrate.

2.2 Preparation of PANI Conductive Ink and Device Fabrication

Polyaniline (PANI) was used as the main sensing material in this study. Aniline (AN) and ammonium persulfate (APS) were polymerized via chemical oxidative polymerization in 1 M nitric acid solution at a molar ratio of 1:1. After filtration and drying, PANI powder was obtained. The synthesized PANI powder was then redispersed in a mixed solution of polyvinylpyrrolidone (PVP), RO water, and ethanol to prepare a conductive ink. [3]

Finally, 200 μL of the conductive ink was drop-cast onto the self-fabricated IDE substrate using a pipette to fabricate the flexible humidity-sensing device.

2.3 Humidity-Sensing Measurement

The fabricated flexible humidity-sensing devices were measured under different relative humidity environments using a four-point probe conductivity measurement system to evaluate their humidity-sensing performance. During measurement, the resistance changes of the devices under each relative humidity condition were recorded and converted into logarithmic form for analysis, allowing comparison of the sensing performance of devices with different formulations. The sensing results were mainly evaluated using log slope and log R^2 to assess the effects of different PANI contents on humidity sensitivity and linearity.

3. Results and Discussion

3.1 Fabrication Results of Flexible IDE Devices

In this study, flexible interdigitated electrode (IDE) substrates based on PET were successfully fabricated, and PANI conductive ink was deposited onto the electrode surface by drop-casting to complete the fabrication of flexible humidity-sensing devices. The fabrication results showed that the PET substrate possessed good flexibility, and clear IDE patterns could be formed on the aluminum tape after laser cutting. In addition, the PANI conductive ink could cover the electrode structure and form a sensing layer, demonstrating the feasibility of the established fabrication process for subsequent humidity-sensing tests and performance comparisons.

3.2 Film Formation of PANI Ink and Preliminary Device Comparison

To evaluate the feasibility of applying PANI conductive ink to flexible humidity-sensing devices, the film-forming properties of the ink and the preliminary device fabrication results were first compared. The results showed that although the redispersed PANI powder could be prepared into a conductive ink suitable for drop-casting, its film-forming ability on the metal surface was not ideal, making it difficult to form a complete sensing layer.

To enable the conductive ink to fully cover the IDE substrate surface and form a stable sensing layer, polyvinylpyrrolidone (PVP) was introduced to improve PANI dispersion and film formation. Preliminary formulation screening showed that, within the same ink system, varying the ratios of PANI, PVP, RO water, and ethanol influenced the film-forming ability, flowability, and conductivity of the ink.

Overall, the comparison results indicated that, as the PVP content increased, the film-forming ability of the conductive ink improved significantly, but the viscosity also increased. At high PVP content, the ink gradually became gel-like and lost its flowability, while the device resistance also increased markedly. This suggests that although PVP helps improve film formation, excessive addition is detrimental to ink coating and device conductivity.

Considering the film-forming ability, flowability, and conductivity of the sensing layer, the final dispersion formulation selected at this stage consisted of 1 g PANI, 0.2 g PVP, 8.4 mL RO water, and 2.8 mL ethanol. Under this formulation, the device surface coverage was relatively complete, and the device was suitable for subsequent humidity-sensing measurements. Therefore, further analyses were conducted on formulations with different PANI contents to evaluate their effects on device sensitivity and linearity.

3.3 Effect of Different PANI Contents on Humidity-Sensing Performance

To investigate the effect of different PANI contents on the performance of flexible humidity-sensing devices, the PANI content was varied while keeping the proportions of PVP, RO water, and ethanol constant. The results showed that the log slope values ranged from 0.0458 to 0.0575 $\%RH^{-1}$ and the log R^2 values ranged from 0.901 to 0.985, indicating that different PANI contents significantly influenced the humidity sensitivity and linearity of the devices.

As shown in Table 1, when the PANI content was 0.75 g (F5), the highest log slope (0.0575 %RH⁻¹) was obtained, indicating better humidity-sensing sensitivity. When the PANI content was 0.200 g (F2), a similarly high log slope (0.0572 %RH⁻¹) was achieved, and the log R^2 reached 0.985, demonstrating excellent linearity. In addition, the 0.50 g formulation (F4) also exhibited a log R^2 of 0.985, suggesting that moderate PANI content can provide both sensing stability and good linearity.

In contrast, when the PANI content was too low, the devices still retained some sensing ability, but the linearity became less stable. For example, the log R^2 of formulation F1 was only 0.901. When the PANI content was increased to 1.00 g (F6), the log slope decreased to 0.0458 %RH⁻¹, the lowest among all formulations, indicating that excessively high PANI content may be unfavorable for sensitive response to humidity changes. Overall, appropriate control of PANI content influenced both the surface morphology of the sensing layer and its humidity-sensing performance. Formulations containing 0.200–0.75 g PANI exhibited better overall sensing performance.

Furthermore, based on the OM surface morphology observations in Figure 2, formulations with different PANI contents showed clear differences in surface coverage and uniformity of the sensing layer. At lower PANI contents, the sensing layer coverage was less complete, and the surface structure was relatively loose. At moderate PANI content, the sensing layer was more uniformly distributed and exhibited more complete coverage, consistent with the better linearity observed. In particular, the OM image of the 0.200 g formulation showed relatively complete and uniform surface coverage, consistent with its superior linearity (log $R^2 = 0.985$). In comparison, although the 0.75 g formulation exhibited the highest sensing sensitivity (log slope = 0.0575 %RH⁻¹), more obvious local aggregation could be observed on its surface, and its linearity was slightly lower than that of the 0.200 g formulation.

Table 1. Effect of different PANI contents on humidity-sensing performance.

Formulation	**PANI (g)**	**PVP (g)**	**RO water (mL)**	**Ethanol (mL)**	**log slope (%RH⁻¹)**	**log R^2**
F1	**0.125**	**0.2**	**8.4**	**2.8**	**0.0563**	**0.901**
F2	**0.200**	**0.2**	**8.4**	**2.8**	**0.0572**	**0.985**
F3	**0.25**	**0.2**	**8.4**	**2.8**	**0.0550**	**0.981**
F4	**0.50**	**0.2**	**8.4**	**2.8**	**0.0532**	**0.985**
F5	**0.75**	**0.2**	**8.4**	**2.8**	**0.0575**	**0.975**
F6	**1.00**	**0.2**	**8.4**	**2.8**	**0.0458**	**0.982**

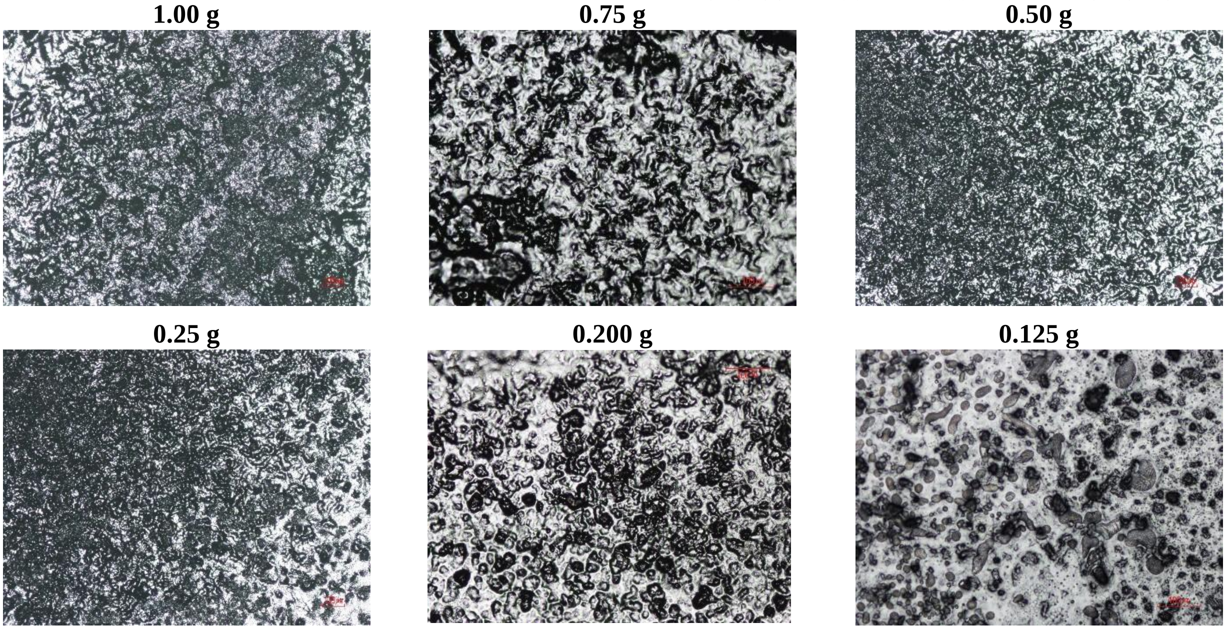

Figure 2. Comparison of OM surface morphology and representative sensing responses of formulations with different PANI contents.

4. Conclusion

In this study, a humidity-sensing device was successfully fabricated by drop-casting polyaniline (PANI) conductive ink onto a self-fabricated flexible interdigitated electrode (IDE) substrate, demonstrating its feasibility for flexible humidity-sensing applications. The results showed that the addition of PVP improved the dispersion and film-forming ability of the PANI ink, allowing the sensing layer to more completely cover the substrate surface and enabling subsequent humidity measurements.

Under fixed PVP, RO water, and ethanol contents, the PANI content significantly affected the device's humidity-sensing performance. The sensing results showed that the 0.75 g formulation exhibited the highest log slope (0.0575 $\%RH^{-1}$), indicating better sensing sensitivity. In contrast, the 0.200 g formulation showed both a high log slope (0.0572 $\%RH^{-1}$) and the best linearity (log $R^2 = 0.985$), suggesting a better balance between sensitivity and linearity.

Based on the humidity-sensing data and OM observations of surface morphology, appropriate control of PANI content improved the surface coverage and uniformity of the sensing layer, thereby further enhancing overall humidity-sensing performance. Among the tested formulations, those containing 0.200–0.75 g PANI exhibited better overall sensing performance, demonstrating the potential of PANI conductive ink combined with flexible IDE substrates for flexible humidity-sensing applications.

5. References

[1] I. Ragazzini, R. Castagnoli, I. Gualandi, M.C. Cassani, D. Nanni, F. Gambassi, E. Scavetta, E. Bernardi, B. Ballarin. A resistive sensor for humidity detection based on cellulose/polyaniline. RSC Advances, 12, 28217–28226 (2022).

[2] E. Bilbao, S. Kapadia, V. Riechert, J. Amalvy, F.N. Molinari, M.M. Escobar, R.R. Baumann, L.N. Monsalve. Functional aqueous-based polyaniline inkjet inks for fully printed high-performance pH-sensitive electrodes. Sensors and Actuators B: Chemical, 346, 130558 (2021).

[3] L.C.O. Prestowitz, J.D. Emery, J. Huang. Polysketch pen: drawing from materials chemistry to create interactive art and sensors using a polyaniline ink. Journal of Chemical Education, 98, 2055–2061 (2021).

Presentation type：

☐ English oral competition (☐ inorganic materials, ☐ organic materials)
■ Poster competition (☐ inorganic materials, ■ organic materials)
☐ Exhibition only (☐ inorganic materials, ☐ organic materials)

紗布/聚苯胺導電複合材料之合成與濕度感測之應用

翁佳妤、穆家稜、王綵誼、陳澄河*
南臺科技大學化學工程與材料工程系
chchen@stust.edu.tw

摘要

為了開發具高靈敏度與穩定性的濕度感測材料，本研究以紗布為基材，製備聚苯胺導電複合材料並應用於濕度感測器。實驗採用化學氧化聚合法，以苯胺為單體、過硫酸銨（APS）為氧化劑，並以鹽酸（HCl）作為摻雜劑，同時引入不同金屬鹽類（$AlCl_3$、$ZnCl_2$、KCl）進行摻雜，製備紗布/PANIHCl濕度感測材料。透過四點探針量測系統分析不同樣品於10%–80%相對濕度（RH）下之電阻變化與導電行為。實驗結果顯示，所有樣品之電阻皆隨濕度增加而下降，顯示材料具有良好的濕度響應能力。其中，Zn^{2+}摻雜樣品在整體濕度範圍內呈現較佳線性關係；Al^{3+}摻雜樣品則具備最佳穩定性與重複性；K^{+}摻雜樣品於中等濕度下表現較佳，但於高濕環境中導電性下降。結果顯示，雖然未摻雜金屬之感測材料紗布/PANIHCl之響應度最高，但摻雜K之感測材料紗布/PANIHCl/K 不僅顯著提高了導電度，且仍維持了良好的濕度響應度。

導電度： 紗布/PANIHCl/K > 紗布/PANIHCl/ Zn > 紗布/PANIHCl/ Al > 紗布/PANIHCl。響應度： 紗布/PANIHCl >紗布/PANIHCl/Al >紗布/PANIHCl/ K >紗布/PANIHCl/ Zn。

綜合結果顯示，金屬離子摻雜可有效調控聚苯胺之導電性與濕度感測特性。本研究所製備之紗布/PANI導電複合材料具備柔性、低成本與良好響應特性，未來可應用於穿戴式裝置與環境濕度監測領域。

關鍵字: 聚苯胺(PANI)、、、四點探針、導電複合材料、濕度感測。

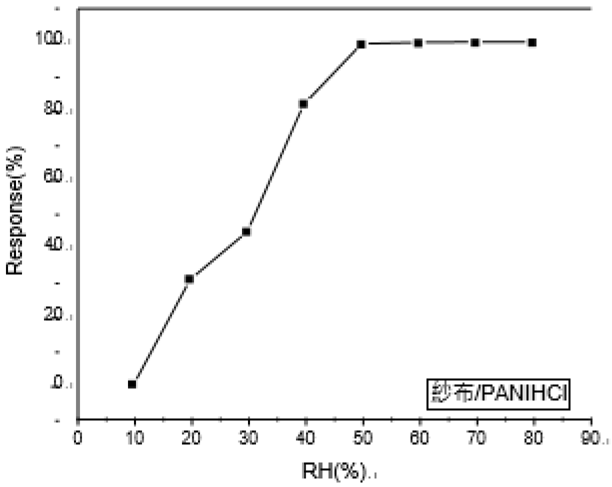

圖 1. 相對溼度對紗布/PANIHCl感測材料電阻之影響圖

如圖1為紗布/PANIHCl的濕度感測所示，從圖中可發現當濕度越高時，反應幾乎成線性上升，40%後趨近於飽和，最大反應約100%，表示在濕度較高的環境下樣品的導電性較佳。

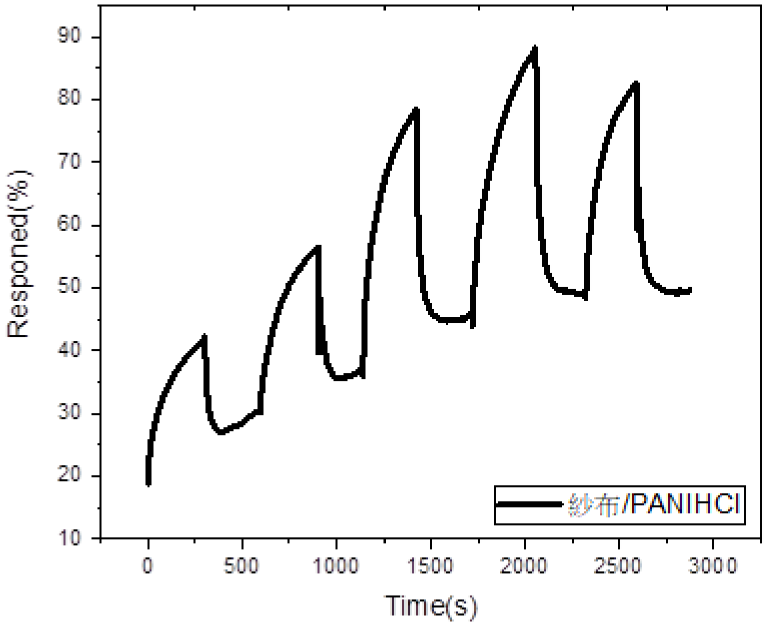

圖2. 紗布/PANIHCl感測材料對相對濕度之動態響應圖

圖 2 為紗布/PANIHCl 感測曲線穩定、變化可逆。推測 PANI/HCl 的導電性主要依靠質子化（protonation）與質子跳遷（protonhopping）。隨濕度上升，水分子滲入聚苯胺鏈間，促進質子傳遞，導電度提升。濕度降低時，水分脫附導致導電通道減少，電阻上升。純 PANIHCl 感測器對濕度變化具有良好的可逆性與穩定響應，是後續摻雜組的對照基準。

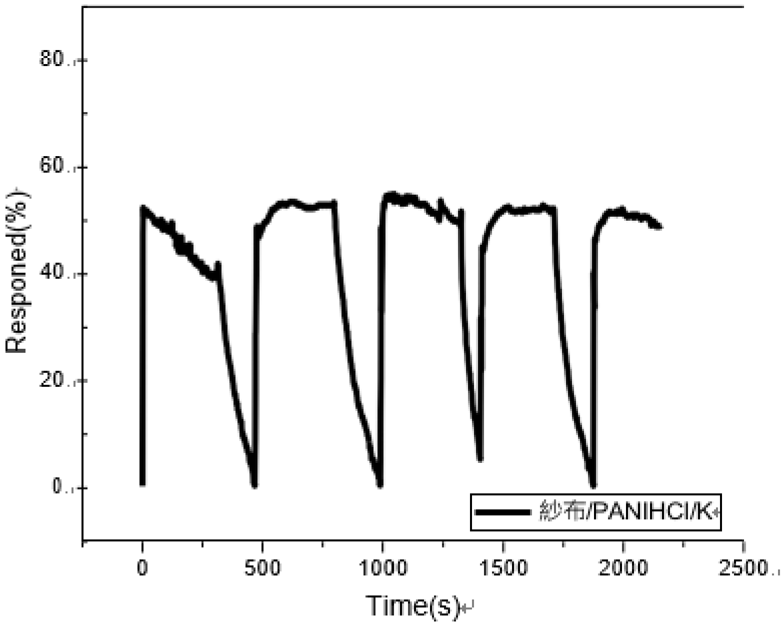

圖3 紗布/PANIHCl/K感測材料對相對濕度之動態響應圖

從圖 3 中可以看出，當濕度由 10%RH 上升至 80%RH 時，響應時間約 300 秒；在下降階段，脫附時間約 270~390 秒，曲線波動明顯。整體反應幅度不如 HCl 組穩定。

推測 K^+ 為單價離子，對聚苯胺鏈的靜電交互作用較弱。在中濕環境（約 50%RH）時，離子移動性佳，導電上升；但高濕度時，水分過多導致離子擴散或通道破壞，導致電阻回升。曲線起伏代表導電通路不穩定。 K^+ 摻雜組在中等濕度下表現良好，但於高濕環境導電性下降、重複性不佳，顯示單價離子穩定性不足。

報告型式：

□英文口頭報告競賽 (□無機材料， □有機材料)
■海報展示並參加壁報論文競賽(□無機材料， ■有機材料)
□只參加海報展示 (□無機材料， □有機材料)

以回收寶特瓶和玻璃瓶為原料開發奈米纖維膜應用於被動日間輻射冷卻

陳泓如
國立成功大學材料科學及工程學系 碩士班
carrie101388@gmail.com

摘要

由於空間冷卻需求已成為建築能源消耗中不可忽視的一環，雖然透過提升空調效率與導入再生能源可在一定程度上降低碳排放，但此類主動式冷卻策略仍高度依賴電力供應，且在用電高峰時段易對電網造成額外負擔。因此，若能從材料與建築設計層面出發，發展**不需額外能源輸入即可降低溫度的被動式冷卻技術**，將有助於從根本減緩能源消耗與溫室氣體排放問題。

在眾多被動式冷卻策略中，輻射冷卻(radiative cooling)[1, 2]因可利用材料自身的熱輻射特性，將熱能透過地球大氣中的大氣窗口(atmospheric window)直接散逸至低溫外太空，被視為極具潛力的降溫機制。理想的輻射冷卻材料需同時具備高太陽光反射率，以降低日照所造成的熱吸收，並在大氣窗口(波長範圍 8 ~ 13 μm)具有高發射率，使材料即使於白天強烈太陽輻照條件下，仍能達成淨散熱效果。近年來，具備多孔結構與高比表面積特性的**奈米纖維膜**，因其可透過多重散射效應有效提升太陽光反射率，並有助於增強中紅外熱輻射能力，逐漸成為輻射冷卻領域中的研究焦點。然而，現有輻射冷卻材料多著重於冷卻效能的提升，較少同時考量材料來源、製程能耗與環境永續性等議題。

圖 1 為台灣海洋委員會海洋保育署 114 年第 3 季全國海洋廢棄物的清理成果，清除的海洋廢棄物中，資源垃圾約占 8.03%，非資源垃圾約占 91.97%，分析資源垃圾各類項目及占總清理量比率，寶特瓶所佔比例最高，總共有180.0 公噸，佔海洋廢棄物清除總量的4.89%；其次為玻璃瓶44.1 公噸，佔海洋廢棄物清除總量的1.20%[3]。這些海洋廢棄物不但會危害海洋中的生物，亦對整體海洋生態系統造成長期衝擊。寶特瓶為塑膠廢棄物，隨時間推移，塑膠材料在紫外線照射與物理風化作用下逐漸碎裂，形成難以回收且不易分解之微塑膠顆粒，進一步透過食物鏈累積，對海洋生態與人類健康造成潛在風險[4, 5]，如圖 2。玻璃廢棄物雖不會形成微粒污染，但其在海洋環境中長期存在，亦可能破壞棲地結構並對生物造成物理性傷害。

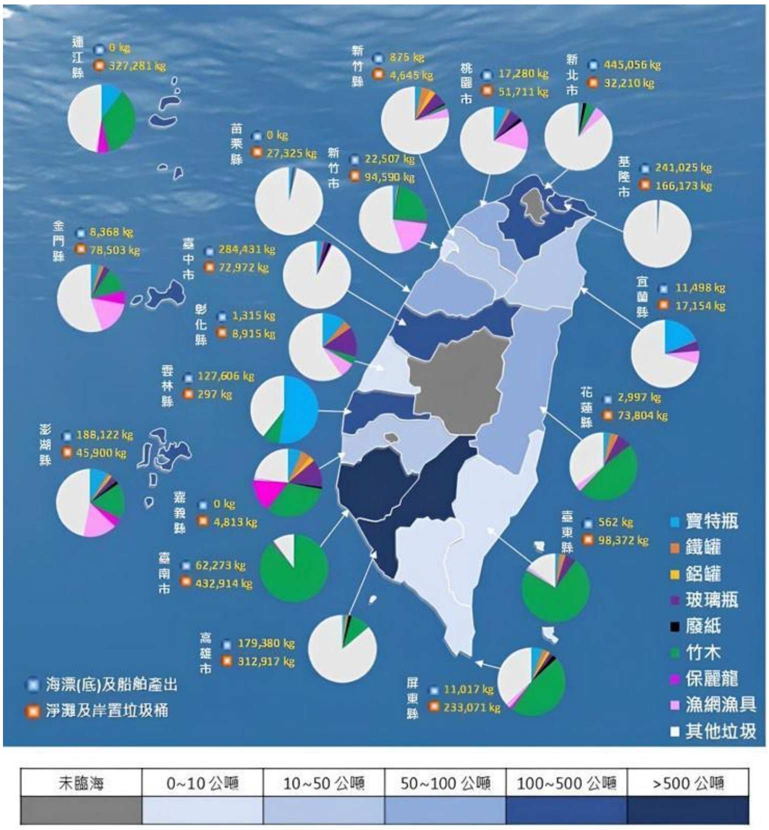

統計資料區間：114年07月01日至114年09月30日
資料來源：公務機關提報海洋委員會海洋廢棄物清除統計資料

圖 1、全國海洋廢棄物的清理成果[3]

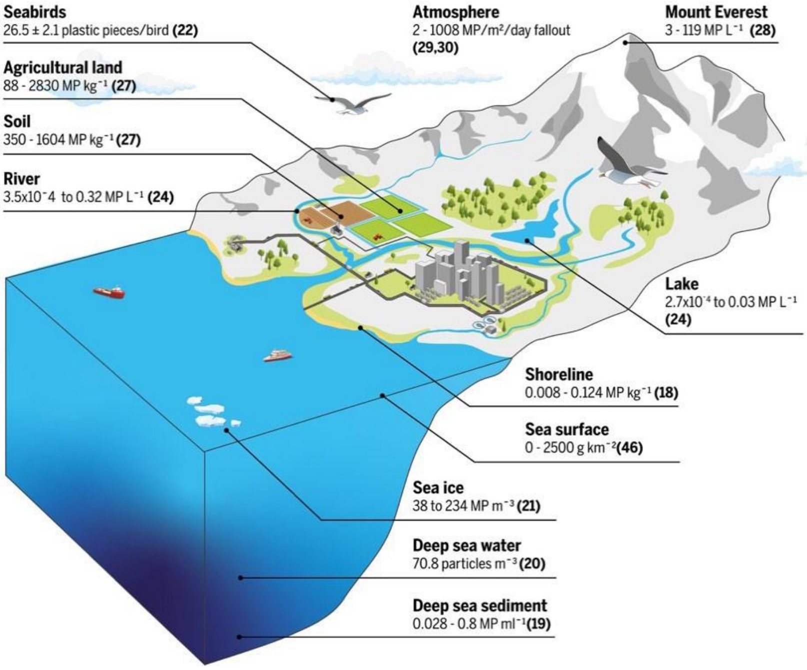

圖 2、不同環境中的微塑膠累積量[4]

儘管寶特瓶與玻璃瓶皆屬可回收資源，然而在實際回收與再利用過程中，仍有相當比例未能有效轉化為高附加價值產品，最終流入自然環境。若僅以清理或低階回收作為因應方式，難以從根本降低其環境負擔。因此，

如何將此類高產量且具回收潛力之海洋廢棄物轉化為具特定功能之材料，成為兼顧環境保護與資源循環的重要課題。

基於此背景，本研究選擇以回收寶特瓶與玻璃瓶作為原料來源，透過材料與結構設計，將原本對海洋與環境造成負擔之廢棄物，轉化為具輻射冷卻效果之功能性材料。在兼顧材料性能與永續價值的前提下，期望提升海洋廢棄物之附加價值，落實資源循環再利用的理念。

參考文獻

[1] D. Zhao *et al.*, "Radiative sky cooling: Fundamental principles, materials, and applications," *Applied Physics Reviews*, vol. 6, no. 2, 2019.

[2] S. So *et al.*, "Radiative cooling for energy sustainability: from fundamentals to fabrication methods toward commercialization," *Advanced Science*, vol. 11, no. 2, p. 2305067, 2024.

[3] Ocean Conservation Administration. "海廢地圖(全國淨海成果)." https://www.oca.gov.tw/ch/home.jsp?id=132&parentpath=0,4,127 (accessed.

[4] R. C. Thompson, W. Courtene-Jones, J. Boucher, S. Pahl, K. Raubenheimer, and A. A. Koelmans, "Twenty years of microplastic pollution research—what have we learned?," *Science*, vol. 386, no. 6720, p. eadl2746, 2024.

[5] L. Zhu *et al.*, "Tissue accumulation of microplastics and potential health risks in human," *Science of the Total Environment*, vol. 915, p. 170004, 2024.

報告型式：

□英文口頭報告競賽 (□無機材料， □有機材料)
■海報展示並參加壁報論文競賽(□無機材料， ■有機材料)
□只參加海報展示 (□無機材料， □有機材料)

Development and application of physicochemical properties of functional biopolymeric hydrogels encapsulating flavonoid compounds

Chen-Hsi Liao[1], Jia-Jyun Syu[1, 2], Tzi-En Chiu[1], Shu-Yu Wu[1], Ngoc-Phung Ly Hang[1], I-Ting Hsieh[1 *]

[1] Department of Chemical and Materials Engineering, Southern Taiwan University Science and Technology, Tainan 71005, Taiwan

[2] Department of Chemical Engineering, I-Shou University, Kaohsiung 84001, Taiwan

*Corresponding author's e-mail: iti404197@stust.edu.tw

Abstract

This study presents the development of a highly water-soluble biopolymeric hydrogel as a drug delivery platform. The formulation employs polysaccharides in combination with an emulsion system to construct the hydrogel matrix, followed by the incorporation of flavonoids via homogenization and ultrasonication. The resulting biopolymeric hydrogel exhibited favorable stability under quality control conditions. Its physicochemical characteristics, including particle size, zeta potential, and morphology, as well as encapsulation efficiency, chemical stability, and antioxidant activity, were systematically evaluated. The results demonstrated that the biopolymeric hydrogel effectively encapsulated flavonoids, with the formulation containing 0.125% flavonoids exhibiting the highest stability and maintaining structural integrity for up to 310 days. The D^+-, D^--, and S^n-based biopolymeric hydrogels exhibited particle sizes of 443.1±4.3, 700.2±5.2, and 625.1±4.8 nm, respectively, and displayed a water-dispersible spherical morphology. The encapsulation efficiency reached up to 90%. Furthermore, within 24 hours, the chemical stability of the hydrogel-encapsulated flavonoids reached approximately 70%, while the antioxidant activity exceeded 60%, thereby significantly enhancing the bioactivity of the unencapsulated flavonoids. Collectively, these findings indicate that this system is a promising candidate for flavonoid delivery applications and provides a robust foundation for the formulation design and bioefficacy evaluation of biopolymeric hydrogels in pharmaceutical applications.

Keywords: biopolymeric hydrogel; flavonoids; encapsulation efficiency; chemical stability; antioxidant activity

References

[1] Kumar D, Sharma P. Quercetin: a comprehensive review. Curr Nutr Food Sci 2024;20(2):143–66.

[2] Qi W, Qi W, Xiong D, Long M. Quercetin: its antioxidant mechanism, antibacterial properties and potential application in prevention and control of toxipathy. Molecules 2022;27(19):6545.

[3] Gokhale JP, Mahajan HS, Surana S. Quercetin loaded nanoemulsion-based gel for rheumatoid arthritis: in vivo and in vitro studies. Biomed Pharmacother 2019;112:108622.

Presentation type：

☐ English oral competition (☐ inorganic materials, ☐ organic materials)

☐ Poster competition (☐ inorganic materials, ☐ organic materials)

☐ Exhibition only (☐ inorganic materials, ☐ organic materials)

利用穿透性胜肽結合功效成分之研究（I）

李筱萍[1]、陳品睿[1]、張教雍[1]、蔡昌廷[1]、陳瑞惠[1]、蔡承佳[1]、陳錦坤[2]、鄭建中[3]

[1] 台灣中油公司煉製研究所、[2] 台灣中油公司綠能科技研究所、[3] 國立嘉義大學應用化學系暨研究所
078638@cpc.com.tw

摘要

本研究利用細胞/皮膚穿透性胜肽結合葡萄糖胺開發新型兩性分子，該新型材料可自體形成微粒，具有做為藥物載體的潛力。

簡介

微粒載體以能穿過生物體細胞膜為主，利用具生物相容性與分解性的外層殼質作為核心藥物的屏障，可增加核心藥物穩定性，以達到保護、儲存和控制藥物釋放等目的，使微粒載體在生物醫藥及診療方面有越來越重要的趨勢。其中，細胞穿透胜肽(cell-penetrating peptides, CPPs)/皮膚穿透胜肽(skin-penetrating peptides, SPPs)可自由穿越細胞膜而有效內化於細胞中，被認為有潛力解決藥物輸送至細胞內的問題，進而提高藥物的生物可利用率。

葡萄糖胺(Glucosamine, GA)是一種天然的胺基酸單醣，存在於人體結締組織、軟骨、韌帶和其它結構中，也是形成玻尿酸的必須成分，有助於維持這些部位的強韌度、靈活性和彈性。根據角質層吸收穿透原理，小分子葡萄糖胺分子量在 250 道爾頓以下，可利用外敷塗抹途徑經由皮膚吸收。但葡萄糖胺具有多個氫氧基，屬親水性質，難以穿透疏水性角質層進而到達皮膚底層被吸收。

本研究利用功能性短胜肽與葡萄糖胺共價鍵結(GA-peptide)以製備出兩性分子(圖 1)，希望提高葡萄糖胺穿透角質層及細胞的效率。吾人利用超音波震盪後發現該兩性分子可形成微粒，有機會作為藥物包覆載體，提高藥物進入細胞的濃度，增加生物可利用率。

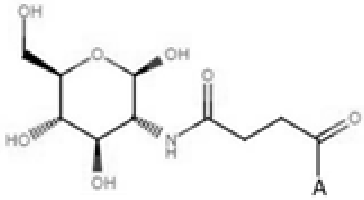

圖 1、GA-peptide 兩性分子示意圖[1]。A 為 5 至 6 個胺基酸組成的胜肽。

實驗方法

a. 短胜肽合成

短胜肽是以固相胜肽合成法(Solid phase peptide synthesis, SPPS)合成獲得。本研究使用 3 種短胜肽，包括 KTTKS(Lys-Thr-Thr-Lys-Ser, 細胞穿透與訊息傳導胜肽)、CRGDS(Cys-Arg-Gly-Asp-Ser, 專一性辨識胜肽)及 RRRRRR(hexa-arginine, 正電荷胜肽)。

b. GA-peptide 合成

將 Glucosamine hydrochloride 與 succinic anhydride 置入反應瓶中，加入 Dimethylformamide(DMF)/H_2O、N-Methylmorpholine 於室溫下反應。經沉澱、清洗、抽乾後可得白色固態中間體 GA-SA (產率 85%)。

將含有 KTTKS、CRGDS、RRRRRR 之樹酯分別置入反應瓶中，加入 DMF 與 GA-SA 反應後，經沉澱、清洗、抽乾後可得白色固體。其中 GA-KTTKS 產率 90~93%、GA-CRGDS 產率 70~80%、GA-RRRRRR 產率 75~88%。所有樣品都以核磁共振光譜儀(Nuclear Magnetic Resonance Spectrometer, NMR)確認結構無誤。

c. GA-peptide 微粒製備

以適量 GA-peptide 溶於超純水溶液中，利用 18G 注射針筒快速注入 95%酒精，再以探針式超音波(MISONIX, XL2020)，功率為 42 W 下振盪 10 分鐘(GA-CRGDS 5 分鐘)，即完成微粒溶液的製備。

d. GA-peptide 微粒型態觀察及界達電位量測

以穿透式電子顯微鏡(Transmission Electron Microscope, TEM)觀察微粒型態。以 Malvern Zetasizer Nano-ZS90 粒徑分析儀分析微粒粒徑平均大小。

結果與討論

將 3 種 GA-peptide 樣品溶進 D_2O 後以 1H-NMR 進行鑑定，從圖 2 中可明顯看見訊號之不同，表示成功將葡萄糖胺與胜肽鍵結。

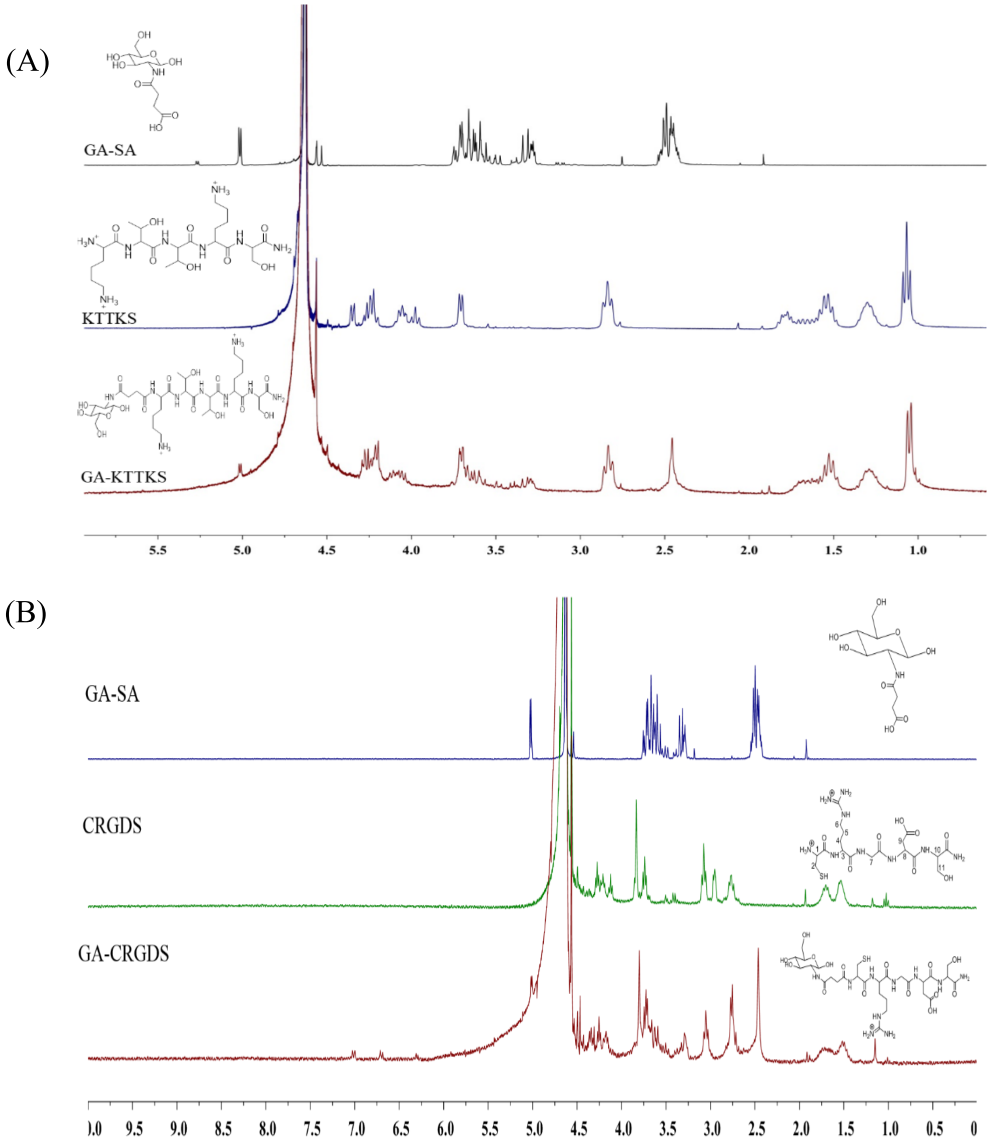

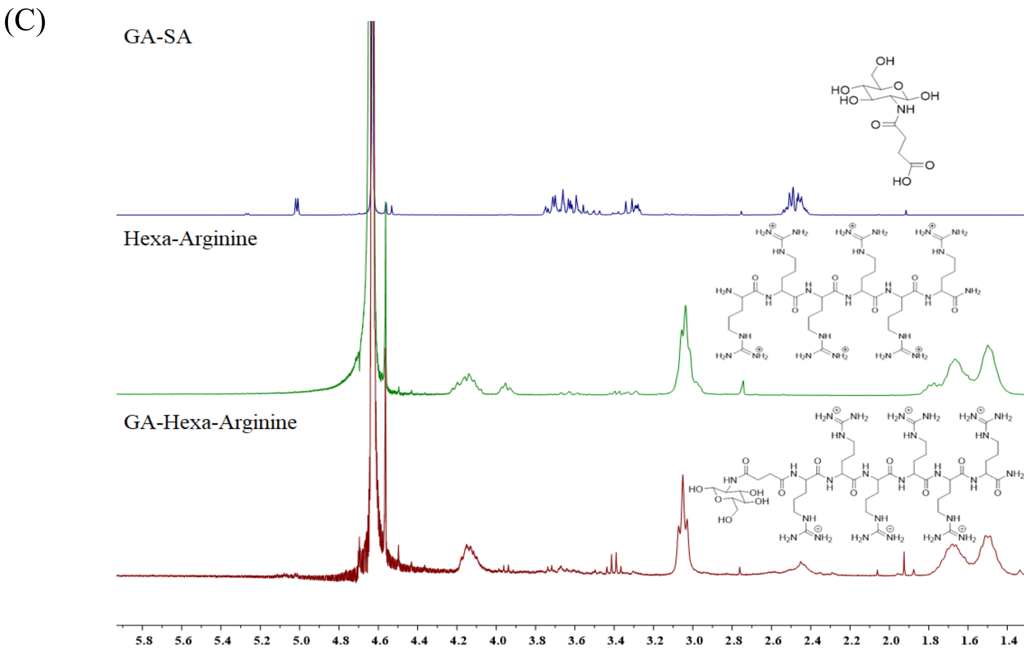

圖 2、GA-KTTKS(A)、GA-CRGDS(B)及 GA-RRRRRR(C)的 1H NMR 比較圖(D_2O, 300 MHz)。

表 1 中分別利用光學顯微鏡及 TEM 驗證 GA-peptide 可形成微粒。

表 1　GA-peptide 微粒於光學及 TEM 下的觀察結果。

葡萄糖胺-胜肽	微粒分子(OM)	微粒分子(TEM)
GA-KTTKS 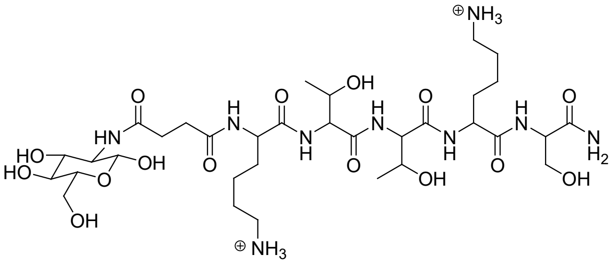	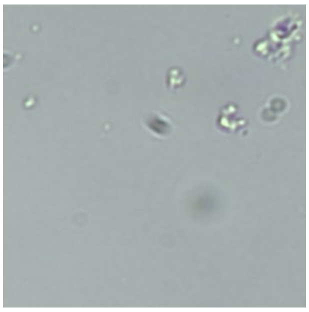	50 nm
GA-CRGDS 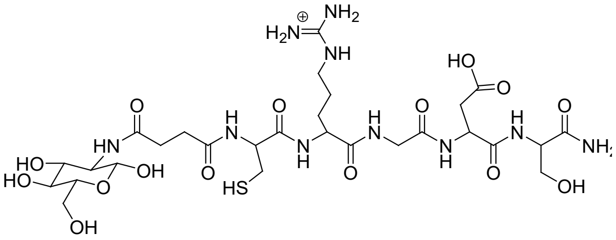	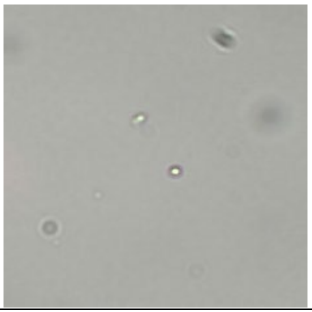	50 nm 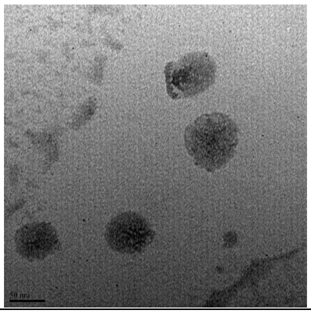
GA-RRRRRR 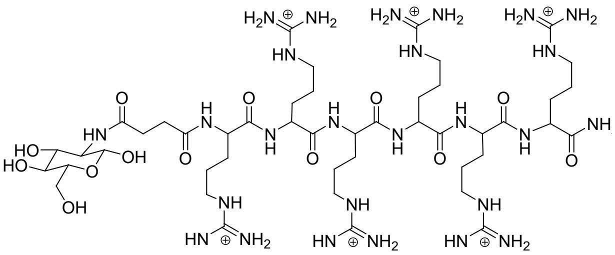	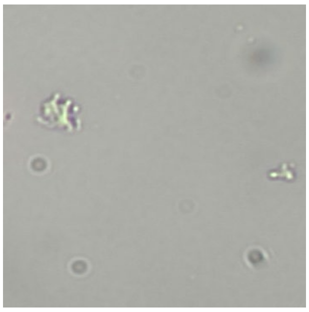	50 nm

以界達電位分析微粒粒徑，測試結果如下表 2 所示，平均粒徑小於 1 μM。GA-KTTKS 及 GA-RRRRRR 微粒靜置 1 天後，平均粒徑分別從 827 及 545 nm 變大成 1,000 及 700 nm。顯示隨時間增加，此類微粒之間的作用力容易讓顆粒聚集變大。反觀，GA-CRGDS 顯現粒徑從 782 nm 變成更小粒徑 283 nm，形成原因尚待分析。

表 2 以界達電位測量微粒之粒徑大小。GA-peptide 形成的微粒粒徑大小及不同時間粒徑的變化。

	儲放時間	平均粒徑 ± STD (nm)
GA-KTTKS	3 小時	827.23±123.51
	1 天	1,023.13±244.22
GA-CRGDS	3 小時	782.90±38.98
	1 天	283.53±39.55
GA-RRRRRR	3 小時	545.10±64.76
	1 天	699.70±208.90

結論

本研究成功利用 3 種胜肽結合上葡萄糖胺，利用光學顯微鏡、穿透式電子顯微鏡初步鑑定，確定 GA-peptide 可自體形成微粒分子，界達電位分析結果顯示，該 GA-peptide 微粒粒徑大小在三小時內平均約為 600 到 1,000 nm，顯示 GA-peptide 具有做為藥物包覆載體的潛力。

參考文獻

1. 李筱萍等人, 中華民國專利證書發明第 I826233 號.

報告型式：

□英文口頭報告競賽 (□無機材料， □有機材料)
■海報展示並參加壁報論文競賽(□無機材料， ■有機材料)
□只參加海報展示 (□無機材料， □有機材料)

Self-Polarized PVDF/$(PEA)_2PbBr_4$ Perovskite Nanocomposites for Enhanced Mechanical Energy Harvesting toward Wave-Driven Blue Energy Applications

Meng-Jung Kang[1], Chun-Jen Wang[1], Ta-Cheng Wei[2], and Chia-Yun Chen[1,3]*
[1]Department of Materials Science and Engineering, National Cheng Kung University, Tainan, Taiwan.
[2]Department of Chemical and Materials Engineering, Southern Taiwan University of Science and Technology, Taiwan.
[3]Program on Semiconductor Packaging and Testing, National Cheng Kung University, Tainan, Taiwan.
*Correspondence: timcychen@mail.ncku.edu.tw

Abstract

Wave-driven blue energy, one of the renewable and abundant energy sources, can reach 20–30 terawatts in the open ocean, not only have possessing high energy density but also freeing from causing any environmental pollutions, which offers an effective way to reduce dependence on fossil fuels. Conventional ferroelectric polymers generally require electric poling to induce dipole alignment and achieve piezoelectric output; however, the induced polarization rapidly decays after removal of the external field due to depolarization effects, limiting long-term device performance. Therefore, the development of intrinsically self-polarized systems with stable dipole alignment is essential for mechanical energy harvesting. In this work, a hybrid organic/perovskite design, termed as PVDF/$(PEA)_2PbBr_4$ nanocomposite, is developed via s ligand-assisted reprecipitation followed by solution casting, employing a relatively less-explored two-dimensional (2D) layered perovskite structure. The incorporation of $(PEA)_2PbBr_4$ perovskite modifies interfacial charge distribution within the composite and promotes dipole ordering in PVDF without external poling, resulting in an enhanced electroactive β-phase content of up to 92.09% and improved electromechanical response. The optimized piezoelectric nanogenerator (PENG) delivers an output voltage of 52.8 V, approximately three times higher than that of pristine PVDF. Furthermore, the triboelectric nanogenerator (TENG) configuration is further investigated, where the output voltage is increased to 148 V with a power density of 0.23 mW/cm^2, and the device demonstrates practical capability by directly lighting 58 LEDs. In addition, the energy storage capability is demonstrated by charging 1 µF and 0.1 µF capacitors to 1.9 and 2.25 V, respectively. To further explore practical applications, a zigzag-stacked film configuration and device architecture are investigated for wave-driven energy harvesting. The resulting system enables effective energy conversion under dynamic seawater conditions, demonstrating the feasibility of scalable and sustainable blue energy harvesting.

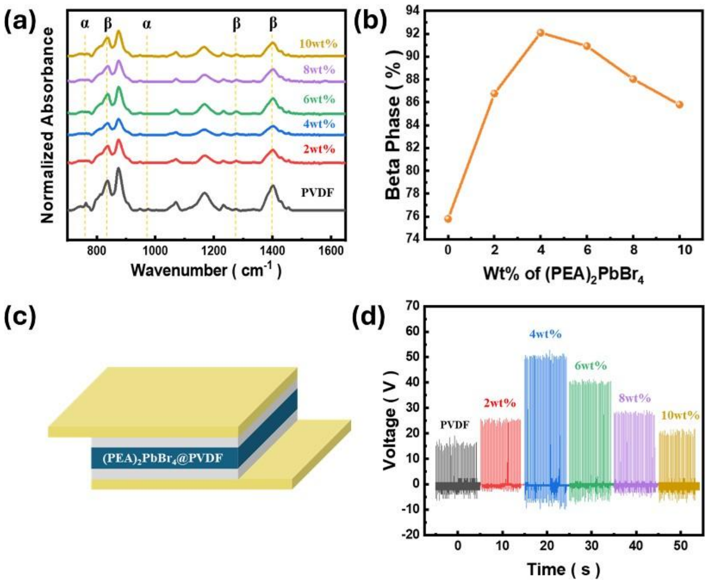

Figure 1. (a) FTIR spectra of PVDF and PVDF/$(PEA)_2PbBr_4$ composites (0–10 wt%), showing the evolution of α- and β-phases. (b) Corresponding β-phase fraction as a function of perovskite content. (c) Schematic of the sandwich-structured PENG based on the PVDF/$(PEA)_2PbBr_4$ composite. (d) Output voltage of PENG with different compositions under periodic mechanical input.

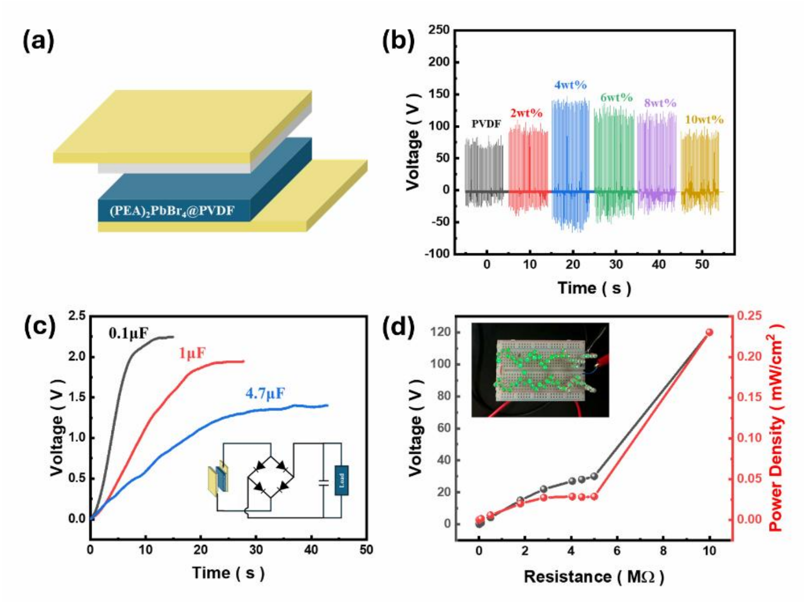

Figure 2. (a) Schematic illustration of the PVDF/$(PEA)_2PbBr_4$-based TENG. (b) Output voltage of TENG under periodic mechanical input for different compositions. (c) Capacitor charging curves with different capacitances. (d) Output voltage and power density as a function of external resistance.

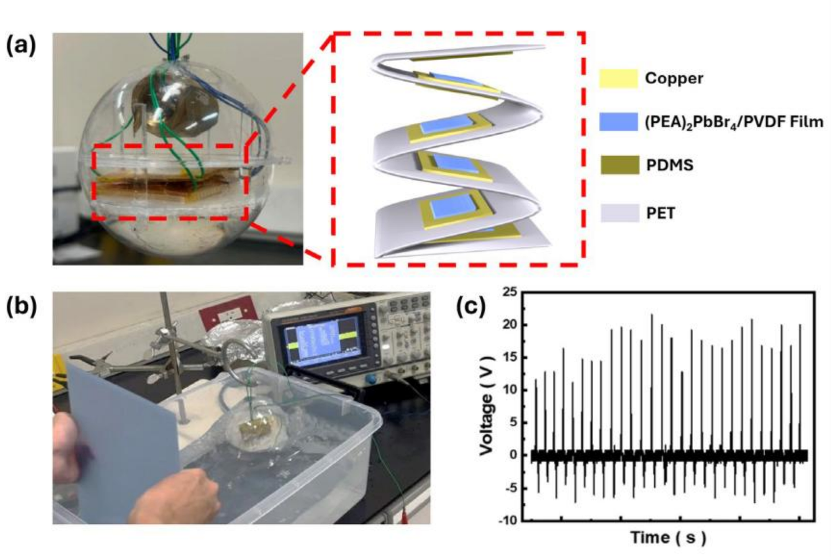

Figure 3. (a) Spherical wave energy harvester with an enlarged view of the internal zigzag-structured device. (b) Experimental setup under dynamic water excitation. (c) Output voltage generated under wave-driven conditions.

References

1. Lee YH, et al. Significant enhancement of the output voltage of piezoelectric/triboelectric hybrid nanogenerators based on MAPbBr3 single crystals embedded into a porous PVDF matrix. Nano Energy 102, 107676 (2022).
2. Xiao TX, et al. Spherical Triboelectric Nanogenerators Based on Spring-Assisted Multilayered Structure for Efficient Water Wave Energy Harvesting. Advanced Functional Materials 28, 1802634 (2018).

Presentation type：

☐ English oral competition (☐ inorganic materials, ☐ organic materials)

■ Poster competition (☐ inorganic materials, ■ organic materials)

☐ Exhibition only (☐ inorganic materials, ☐ organic materials)

鈷氮碳觸媒應用於鹼性介質選擇性電催化氧還原生成過氧化氫之研究

何國賢[1]、洪冠穎[1]、蕭育霖[1]、杜秀中[1]*
[1]國立高雄科技大學 化學工程與材料工程系通訊作者
hct0324@nkust.edu.tw

NSTC 112-2222-E-992-011

摘要

一、 研究背景與目的 (Introduction)

過氧化氫（H_2O_2）是極具價值的綠色氧化劑。傳統「蒽醌法」製程不僅高能耗且流程複雜，更伴隨運輸與儲存風險。相較之下，透過電催化氧還原反應（ORR）之二電子途徑原位生成 H_2O_2，具有條件溫和、低能耗且環境友好的優勢。本研究旨在開發高效能的非貴金屬鈷奈米顆粒觸媒（CoNP），探討其在不同 pH 環境下的催化性能，並優化電化學合成效率。

二、 實驗方法 (Experimental Section)

本研究以對苯二胺（PPD）與二苯基甲烷二異氰酸酯（MDI）作為氮、碳源前驅物，加入氯化亞鈷（$CoCl_2$）後經由縮合反應製備含鈷聚脲前驅物。隨後進行兩段式高溫鍛燒：首段於 500–700 °C 熱解，經酸洗去除不穩定氧化物後，再於降低 100 °C 的氨氣/氮氣混合氣氛下進行第二次煅燒，製備出 CoNP 系列觸媒。透過 FTIR、XRD、XPS 及 HR-TEM 鑑定其化學結構與微觀形貌，並利用旋轉環盤電極（RRDE）評估其 ORR 活性與 H_2O_2 選擇率。

三、 結果與討論 (Results and Discussion)

分析結果顯示，優化後之觸媒 CoNP600A500 具有包覆於氮摻雜碳殼層中的鈷奈米核心結構。XPS 分析顯示其富含吡咯氮（25.4%）與 Co-N_x 位點（23.4%），這些位點被證實能有效誘導二電子 ORR 路徑。電化學效能方面，CoNP600A500 在 0.1 M KOH 鹼性電解液中展現優異表現，於 0.1 V 至 0.5 V（vs. RHE）區間內之 H_2O_2 選擇率高達 98%，法拉第效率達 96%。此外，該觸媒在中性環境下展現卓越的類芬頓殺菌能力，30 分鐘內即可達成 99.9999% 的大腸桿菌殺菌率。

四、 結論 (Conclusion)

本研究成功開發出高選擇性之 CoNP 非貴金屬觸媒。實驗證明透過兩段式煅燒能有效調控活性位點分佈並誘導二電子 ORR 路徑，該觸媒在鹼性介質下具有極高之 H_2O_2 選擇性（98% 選擇率）。此成果為開發低成本、綠色安全的水處理消毒系統提供了一種具工業應用前景的新方案。

參考文獻

[1] K. Jiang, et al., *Nat. Commun. 10 (2019) 3997.*

[2] S. Yang, et al., *ACS Catal. 8 (2018) 4064-4081.*

報告型式：

□英文口頭報告競賽 (□無機材料， □有機材料)

■海報展示並參加壁報論文競賽(□無機材料， ■有機材料)

□只參加海報展示 (□無機材料， □有機材料)

葡萄糖包附之銅奈米粒子於酸性電催化條件下行銷酸還原–展現獨有穩定性及建立高產量氨之研究

杜秀中
國立高雄科技大學
hct0324@nkust.edu.tw

摘要

目前硝酸鹽污染已成為全球性環境問題，主要來自農業化肥、工業排放與生活污水，此外目前氨的生產主要仰賴哈伯法，需在高溫（400–500°C）與高壓（150–250 atm）下進行，並消耗全球約 1–3% 的能源與 3–5% 的天然氣，同時排放 1–3% 的二氧化碳。為降低能源消耗與碳排放，發展可在常溫常壓下進行、並將廢水中硝酸鹽直接轉化為氨或氮氣的硝酸鹽還原技術，具有重要的環境與能源價值，目前硝酸鹽還原技術主要包括物理、化學及生物方法。傳統的化學還原法雖然能夠有效去除硝酸鹽，但通常伴隨高耗能、觸媒降解及副產物生成的問題。生物方法(如微生物反硝化作用法)能夠將亞硝酸轉化為無害的氮氣，但其過程往往耗時較長、易產生異味與汙泥，且對溫度與 PH 條件較為敏感。因此電催化法(NO$_3$RR)被認為是一種環保且可控的替代方案。

本研究以對苯二甲醛與三乙烯四胺進行縮合聚合形成聚亞胺結構，並以葡萄糖作為還原劑引入過渡金屬銅，製備均勻分散銅奈米粒子之聚亞胺前驅物。經二次鍛燒與酸洗處理後，合成碳氮共摻雜銅奈米粒子觸媒（Cu-NC）。並進行多項電化學測定最終得出其具有高電化學活化比表面積及良好的氨轉換效率

參考文獻

1. Bahar, N.H.A., et al., *Meeting the food security challenge for nine billion people in 2050: What impact onforests?* Global Environmental Change, 2020. **62**: p. 102056.
2. Crippa, M.G., D ; Schaaf, E *CO2 Emissions in 2023.* GHG emissions of all world countries, 2023.
3. Tedengren, M., *Eutrophication and the disrupted nitrogen cycle: This article belongs to Ambio's 50th Anniversary Collection. Theme: Eutrophication.* Ambio, 2021. **50**(4): p. 733-738.
4. Bryan, N.S., J. Loscalzo, and SpringerLink, *Nitrite and nitrate in human health and disease*. 2nd ed. Nutrition and health. 2017, Cham: Springer International Publishing.
5. Alagha, I., G. Doman, and S. Aouthmany, *Methemoglobinemia.* Journal of education & teaching in emergency medicine, 2022. **7**(4).

報告型式：

□英文口頭報告競賽 (□無機材料， □有機材料)
■海報展示並參加壁報論文競賽(■無機材料， 有機材料)
□只參加海報展示 (□無機材料， □有機材料)

聚醚碳酸酯多元醇對酸酐固化型環氧樹脂增韌性質之影響

陳柏勳 [1]、吳瑞泰 [1]、蔡平賜 [1*]、曾國鎰 [1]、林佑穎 [1]、鄭力誠 [1]
[1] 國立高雄科技大學 化學工程與材料工程系
charles1@kuas.edu.tw

摘要

全球淨零排放與資源循環政策推動下，延長高分子材料使用壽命已成為降低生命週期環境負荷的重要途徑。環氧樹脂雖具高強度、良好接著性與優異耐化學性，廣泛應用於塗料、膠黏劑與複合材料中，但其固化後高交聯密度易造成脆性破壞，導致裂縫快速擴展、耐衝擊性不足及維修替換頻率增加。因此，如何在維持剛性與熱性的前提下提升抗裂與耗能能力，為環氧樹脂材料設計的重要課題。本研究以聚醚碳酸酯多元醇(polyether carbonate polyols)(東聯化學 PEGUC，CO_2 含量 20 wt%，分子量 4000 Da)作為環氧樹脂增韌改質劑，並以傳統橡膠型增韌劑羧基端丁二烯-丙烯腈液態橡膠（CTBN）作為比較組，探討不同類型增韌劑對熱固性環氧樹脂熱性、力學性質與形貌特徵之影響。

本研究將不同添加比例之 PEGUC 與 CTBN ，分別導入於酸酐固化型環氧樹脂中固化成板。進行玻璃轉移溫度（Tg）、熱重損失（T_{d10}）、楊氏模數、拉伸韌性(tensile toughness)、衝擊強度及破斷韌性（開裂型破斷韌性 K_{1C} 與裂縫擴展臨界能量 G_{1C} ）等分析，並利用 AFM 與 SEM 觀察增韌相之分散行為與形貌特徵，以評估反應誘導相分離（reaction-induced phase separation, RIPS）所形成之相結構及其對增韌效果之影響。

實驗結果顯示，相較於純環氧樹脂，PEGUC 添加後材料耐熱性呈下降趨勢，其中 30 wt% PEGUC 之 Tg 由 141.8 °C 降至 104.2 °C，Td10% 由 361.9 °C 降至 312.0 °C，反應柔性鏈段導入雖可改善韌性，但亦伴隨塑化效應與熱穩定性下降。在機械性質方面，10 wt% PEGUC 具有最佳楊氏模數保留效果，其楊氏模數由 3.27 GPa 僅降至 3.02 GPa，顯示在提升韌性的同時仍可維持材料剛性；當 PEGUC 添加至 30 wt% 時，拉伸韌性由 0.4 J/m^3 提升至 7.06 J/m^3，顯示其可顯著增進材料之耗能能力。此外，10 wt% CTBN + 10 wt% PEGUC 混摻系統於衝擊測試下呈現協同增韌效果，其衝擊強度由 1.01 kJ/m^2 提升至 2.96 kJ/m^2，顯示在瞬間載重下具有較佳抗破壞能力。相較之下，30 wt% CTBN 可明顯提升破斷韌性，其 K_{1C} 由 0.54 $MPa \cdot m^{1/2}$ 提升至 1.84 $MPa \cdot m^{1/2}$，G_{1C} 由 0.08 kJ/m^2 提升至 1.73 kJ/m^2，顯示其在抑制裂縫起始與延緩裂縫擴展方面效果較佳，但其楊氏模數則由 3.27 GPa 下降至 1.73 GPa，表示剛性犧牲較大。

AFM 形貌分析顯示，CTBN 系統傾向經由 RIPS 形成微米級橡膠分散相，而 PEGUC 系統則偏向形成奈米級顆粒分散結構，顯示兩者具有不同之相分離尺度。SEM 斷面觀察進一步顯示，CTBN 系統伴隨較明顯之孔洞/空穴化特徵，推測其主要透過空穴化(cavitation)–剪切屈服機制提升裂尖耗能；PEGUC 系統則較可能藉由裂尖鈍化、局部塑性變形與裂縫偏折等方式改善材料韌性。此外，PEGUC 與 CTBN 共混系統於衝擊下呈現協同增韌效果，推測 PEGUC 有助於調控 CTBN 之分散與相分離行為。整體而言，不同增韌相所形成之相分離形貌將主導其韌化路徑與性能平衡，其中 PEGUC 較有利於兼顧耗能能力與模數保留，而 CTBN 則對破斷韌性提升較為明顯。本研究結果顯示，PEGUC 可作為環氧樹脂之有效增韌添加劑，並作為高可靠度功能樹脂設計之參考。

關鍵字：聚醚碳酸酯多元醇、羧基端丁二烯-丙烯腈液態橡膠、環氧樹脂增韌、反應誘導相分離(RIPS)、破斷韌性、相分離形貌

Keywords: polyether carbonate polyols, CTBN, epoxy resin toughening, reaction-induced phase separation, fracture toughness, phase-separated morphology

報告型式：

□英文口頭報告競賽　　　　　(　無機材料，　有機材料)
■海報展示並參加壁報論文競賽(　無機材料，■有機材料)
□只參加海報展示　　　　　　(　無機材料，　有機材料)

結合乳液模板與冷凍乾燥技術製備多孔聚二甲基矽氧烷

陳蓁
國立中興大學材料科學與工程學系
薛涵宇 hyhsueh@nchu.edu.tw

NSTC-114-2223-E-005-001-MY3

一、 摘要

本研究結合乳液模板法與冷凍乾燥技術，製備多孔聚二甲基矽氧烷，解決傳統製程孔洞不均以及容易塌陷的問題，並成功實現孔洞尺寸為 1 微米等級的微孔結構。我們以 PDMS 為連續相，多元醇作為分散相液滴，並搭配界面活性劑構成乳液系統。探討各項參數微觀形貌的影響，結果顯示，該多孔材料不僅具備高度可控的孔洞結構，還有優異的疏水性，在油水分離與水下抗噪等領域極具應用潛力。

二、 介紹

聚二甲基矽氧烷（PDMS）具備高黏彈性[1]、良好的生物相容性[2]及化學穩定性，主鏈由矽-氧-矽鍵結構成，賦予其極佳的柔韌性與熱穩定性。然而，純 PDMS 呈現良好的疏水性，但缺乏內部孔隙結構，限制其在高比表面積與高滲透性領域的應用。將其轉化為三維多孔結構，不僅能完整保留原有的彈性與疏水性，更能藉由內部孔洞增加比表面積，拓展在柔性元件與界面工程的潛力。在傳統製備多孔材料的技術中，直接模板法[3-5]雖製程簡單，但利用自然晶體（如糖或鹽）難以獲得均一的幾何形狀與孔徑分佈。若改用聚苯乙烯微球或金屬鎳泡沫等模板，則需使用有害化學溶劑來移除模板，不符合綠色化學並且無法在生物醫學上的應用。另一方面，氣體發泡法具備成本效益且無溶劑殘留，但其孔徑與連通性極難以控制，且對環境濕度極為敏感，導致結構再現性較差 。為了突破傳統製程在孔洞控制與環境友善度上的雙重瓶頸，乳液模板法成為最具潛力的替代策略。在乳液模板法中，透過油包水（W/O）逆相乳液的連續相聚合反應來建構多孔 PDMS 海綿，將分散相液滴（親水溶劑）作為孔洞形成的致孔劑[6-9]。乳液是由兩種或多種互不相溶的液體透過機械剪切力混合而成的非均勻相分散體系， 由於兩相液體之間存在極大的界面張力，乳液本質上屬於熱力學不穩定系統，必須加入具備親水與親油端的兩親性界面活性劑作為乳化劑，以降低兩相間的界面張力，並且在液滴表面形成保護膜使系統獲得動力學穩定性[10-11]。乳液的成型與穩定性可由四大核心理論解釋：表面張力理論指出乳化劑能夠降低液體間的排斥力以促進混合；塑性或界面膜理論強調乳化劑在油水邊界形成保護性薄膜，其物理韌性是避免液滴接觸與凝聚的關鍵；排斥理論說明保護膜賦予液滴相互排斥力使其穩定懸浮；而黏度調節理論則認為乳化劑能提高分散介質黏度，增加液滴移動阻力以防沉降。整體而言，乳液的分散度是粉碎過程與凝聚過程相互對抗的結果，乳化劑的主要功能即是在粉碎後保護液滴免於重新凝聚。乳液品質也高度依賴製程參數的精確控制，如攪拌程度、乳化劑濃度、油水比例與溫度的調節等，任何參數失衡皆可能導致相轉化或乳液破裂[12]。

在確立穩定的乳液系統後，將作為犧牲模板的液滴移除而不破壞聚合物骨架，是決定最終微觀形貌的重要步驟。若採用傳統的熱移除法驅動溶劑蒸發，微米級的孔洞內會形成高度彎曲的液-氣界面，根據楊氏-拉普拉斯原理（Young-Laplace principle）該界面會對孔壁產生極大的毛細管壓力。對於低模數的 PDMS 柔性彈性體而言，這種強大的內部收縮應力往往會導致孔洞發生嚴重的塌陷與結構閉合，為了解決應力破壞的問題，我們的研究導入冷凍乾燥技術，該技術在低溫、高真空的環境下操作，使預先固化的溶劑冰晶不經過液相，直接昇華為氣體。因為避免液-氣交界面揮發時所產生的毛細管應力，冷凍乾燥技術能夠完美保留材料的巨觀體積與微觀三維網絡。本研究旨在結合乳液模板法與冷凍乾燥技術，製備具備均勻且孔洞尺寸約為1微米等級的多孔PDMS彈性體。實驗中將系統性地選用具備不同親疏水平衡值的界面活性劑，搭配具備不同氫鍵能力與立體結構的多元醇作為分散相，深入探討各項參數對微觀形貌的影響，期望將此具備高疏水性的多孔複合材料，應用於油水分離或水下抗噪等先進工程領域 。

三、 實驗步驟

首先將 PDMS主劑、甲苯與界面活性劑混合，以1000rpm攪拌5分鐘，接著加入多元醇分散相與交聯劑，維持同轉速攪拌30分鐘完成乳化，並且透過真空脫泡去除微小氣泡以確保結構均一。隨後，將乳液注入 PTFE 模具並密封於玻璃容器內防止溶劑揮發，置於70°C烘箱中加熱交聯固化24小時。待樣品成型脫模後，分別採熱乾燥與冷凍乾燥法移除溶劑進行對照。熱乾燥組於100°C烘箱加熱72小時使溶劑蒸發；冷凍乾燥組則先在- 20°C預凍24小時，再移至-55°C、0 torr的高真空設備中進行72小時的昇華乾燥。完成後即可獲得多孔PDMS彈性體，詳細實驗參數如**表一**，實驗步驟如**圖一**。

表一、實驗參數。

PDMS 交聯重量比（主劑:交聯劑）	10:1
甲苯濃度（分散相 wt%）	5
界面活性劑濃度（分散相 wt%）	5
分散相溶劑濃度（佔分散相 90wt%）	10 20 30 40 50

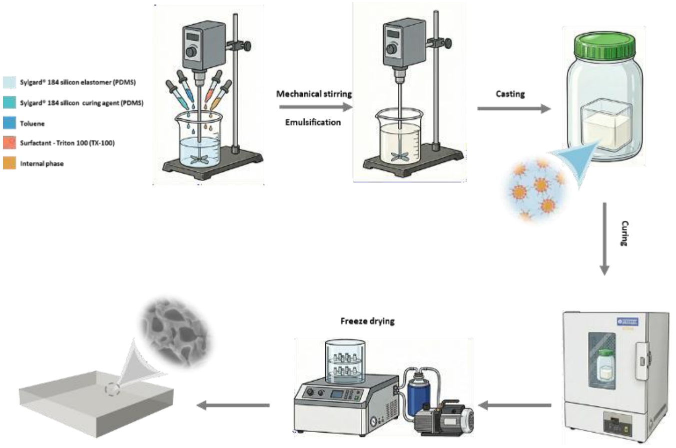

圖一、多孔 PDMS 彈性體實驗製備示意圖。

四、 結果與討論

1.1 乾燥機制比較

在移除液態分散相以形成多孔結構的過程中，乾燥機制的選擇至關重要。傳統熱乾燥法在溶劑蒸發時會形成液-氣界面，依據楊氏-拉普拉斯原理，這會對柔性的 PDMS 骨架產生極大的毛細管收縮應力，導致孔洞嚴重塌陷與閉合。相對地，冷凍乾燥法透過低溫預凍與高真空環境，使固態溶劑直接昇華為氣相。由於完全避免了液態階段與液-氣界面的毛細管拉扯，PDMS 骨架得以完美保留原始乳液模板的微觀幾何形貌。由**圖二**可得到，冷凍乾燥製程初期能迅速凍結液滴尺寸，不受收縮影響，其孔隙率與孔徑維持表現皆顯著優於熱乾燥法。

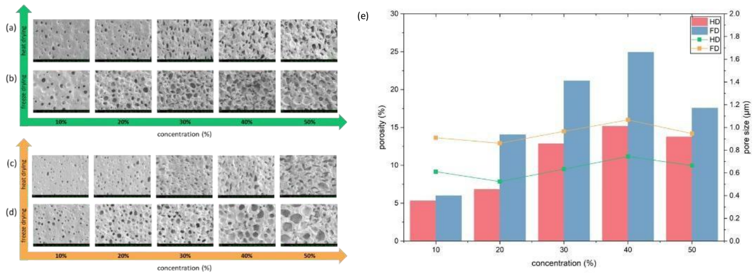

圖二、不同分散相含量之 SEM 圖。不同分散相含量之 SEM 圖。(a) PDMS 10:1 / TG / TX100 / HD；(b) PDMS 10:1 / TG / TX100 / FD；(c) PDMS 10:1 / TG / SPAN80 / HD；(d) PDMS 10:1 / TG / SPAN80 / FD；(e)PDMS 10:1 / TG / TX100 不同分散相含量之孔隙率與孔徑。 (長條圖：孔隙率；折線圖：孔徑)

1.2 分散相含量的影響

分散相含量的多寡直接決定多孔 PDMS 的孔隙率與平均孔徑，當分散相含量低於 30% 時，液滴能穩定分散於 PDMS 連續相中，形成彼此獨立且均勻的孔洞。當含量超過 30% 時，乳液內部空間堆積密度急遽提升，液滴間距縮減且碰撞頻率增加。若界面保護膜無法抵禦擠壓應力，微小液滴便會發生聚結效應，融合成巨大且不規則的孔洞。這種聚結現象在熱乾燥製程中，會因環境熱能加劇布朗運動而更為惡化，總體而言，只要超過 30% 的高分散相系統，皆會因熱力學不穩定性而面臨孔洞形貌劣化，如**圖二**所示。

1.3 界面活性劑的調控

不同親疏水性的界面活性劑也影響孔洞形貌，如**圖二**，較親水的 TX100 因為具有剛性苯環，與非極性 PDMS 相容性較差，導致界面分子堆積鬆散，在冷凍乾燥過程中，這種較薄且不穩定的界面反而有利於溶劑昇華時打通微小通道，進而建構出高連通性的多孔網絡。相反地，較親油的 SPAN 80 具備長碳鏈，能與 PDMS 產生物理纏結，藉由強大的空間位阻效應形成穩固的保護層。在低濃度時，SPAN 80 能有效隔絕液滴碰撞，適合用於維持孔洞的獨立性，但是若分散相過高，過於緻密的界面結構反而會阻礙乾燥時的應力分散，引發結構失穩。

1.4 多元醇分子結構的影響

由**圖三**我們可以觀察到在固定 30% 分散相下，多元醇分子的氫鍵能力與立體障礙效應對微觀形貌影響。羥基（-OH）數量是關鍵，具備三個羥基的甘油能形成強大的分子間氫鍵網絡，提升溶劑黏度與流變阻力，有效抑制液滴碰撞與聚結，使孔洞趨於微小且均勻。比較二元醇系統發現，1,2-丙二醇結構中的側鏈甲基會產生立體障礙，干擾界面活性劑的緻密排列，導致界面在固化收縮時易破裂並誘發聚結，形成相較於乙二醇更大且不規則的孔洞，而且完全缺乏碳鏈與羥基協同作用的去離子水，則因缺乏黏度阻力而產生明顯的塌陷現象。

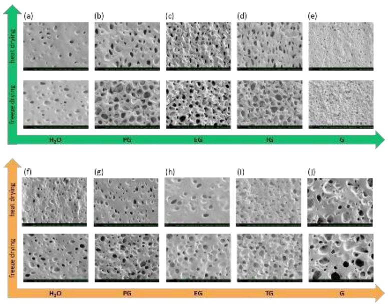

圖三、不同分散相溶劑、含量固定為 30%之SEM圖。(a) PDMS 10:1 / H2O / TX100；(b) PDMS 10:1 / PG / TX100；(c) PDMS 10:1 / EG / TX100；(d) PDMS 10:1 / TG / TX100；(e) PDMS 10:1 / G / TX100；(f) PDMS 10:1 / H2O /SPAN80；(g) PDMS 10:1 / PG / SPAN80；(h) PDMS 10:1 / EG / SPAN80；(i) PDMS 10:1 / TG / SPAN80；(j) PDMS 10:1 / G / SPAN80。

1.5 物理性質評估

為評估表面濕潤性，針對 30% 分散相樣本進行水接觸角量測，如**圖四**。結果顯示，各組多孔 PDMS 彈性體的接觸角皆穩定維持在 120° 左右，與純 PDMS基材表現相近。這證實即使材料內部充滿微觀孔隙，其表面仍能完整保留 PDMS 固有的低表面能與優異的疏水特性。此兼具多孔性與高疏水性的特徵，賦予該材料在油水分離與水下抗噪等領域極佳的應用潛力。

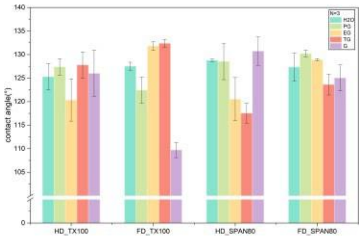

圖四、水接觸角。

五、 結論

本研究成功結合乳液模板法與冷凍乾燥技術，開發出一套具備高度可控性之製程，成功製備出兼具高孔隙率與高結構完整性的多孔聚二甲基矽氧烷彈性體。實驗結果證實，相較於傳統熱乾燥法在液-氣相變過程中因楊氏-拉普拉斯原理所引發的強大毛細管收縮應力，本研究導入的冷凍乾燥技術能透過低溫固化與高真空直接昇華（固-氣相變）的途徑，有效避免應力集中現象。此技術完美克服了低模數柔性 PDMS 骨架易發生的孔隙塌陷與閉合問題，精準且完整地保留了原始乳液模板的微觀幾何特徵與三維網絡。在製程參數的系統性調控上，本研究確立分散相含量 30% 為維持孔洞獨立性與系統穩定性的關鍵臨界值，一旦超過此濃度，液滴間的空間堆積過密將大幅增加碰撞機率，容易產生不可逆的聚結效應。除此之外，界面活性劑的分子結構對孔洞的連通性發揮決定性的調控作用，親水性的 TX100 因具備剛性苯環，其在界面的鬆散堆積有助於在昇華過程中形成微小通道，建構出高連通性的多孔網絡。反之，親油性的 Span 80 則藉由其長碳鏈與 PDMS 基材產生物理纏結，發揮了強大的空間位阻效應，能有效維持孔隙的幾何獨立性。

深入探討犧牲模板的物理化學本質，我們發現多元醇分子內部的羥基數量與立體結構對微觀形貌影響。多羥基所形成的分子間氫鍵網絡能提升系統的流變阻力，有效抑制液滴碰撞；而帶有非極性側鏈的分子則會因立體障礙干擾界面緻密排佈，影響微觀孔徑的大小與均一性。總之，本研究所製備多孔材料不僅展現優異的機械彈性，更在添加大量微米級孔洞後，依然完美維持 PDMS 低表面能特性，達到高達 120° 的疏水接觸角。此項兼具結構穩定性與特殊濕潤性的多孔彈性體，未來在油水分離、水下抗噪以及柔性穿戴感測器上，更展現出極具突破性的發展潛力。

六、 參考文獻

[1] E. Yilgör, I. Yilgör. Silicone containing copolymers: Synthesis, properties and applications. Progress in Polymer Science 2014, 39, 1165-1195.

[2] M. C. Belanger, Y. Marois. Hemocompatibility, biocompatibility, inflammatory and in vivo studies of primary reference materials low-density polyethylene and polydimethylsiloxane: a review. J Biomed Mater Res 2001, 58, 467-77.

[3] X. Zhao, L. Li, B. Li, J. Zhang, A. Wang. Durable superhydrophobic/superoleophilic PDMS sponges and their applications in selective oil absorption and in plugging oil leakages. J. Mater. Chem. A 2014, 2, 18281-18287.

[4] S. J. Choi, T. H. Kwon, H. Im, D. I. Moon, D. J. Baek, M. L. Seol, J. P. Duarte, Y. K. Choi. A polydimethylsiloxane (PDMS) sponge for the selective absorption of oil from water. ACS Appl Mater Interfaces 2011, 3, 4552-6.

[5] H. Tong, H. Chen, Y. Zhao, M. Liu, Y. Cheng, J. Lu, Y. Tao, J. Du, H. Wang. Robust PDMS-based porous sponge with enhanced recyclability for selective separation of oil-water mixture. Colloids and Surfaces A: Physicochemical and Engineering Aspects 2022, 648.

[6] C. Racles, A. Bele, A.-L. Vasiliu, M. Dascalu. Emulsion template – based porous silicones with

piezocapacitive response. Reactive and Functional Polymers 2024, 200.

[7] K. Zimny, A. Merlin, A. Ba, C. Aristegui, T. Brunet, O. Mondain-Monval. Soft porous silicone rubbers as key elements for the realization of acoustic metamaterials. Langmuir 2015, 31, 3215-21.

[8] M. Abshirini, M. C. Saha, L. Cummings, T. Robison. Synthesis and characterization of porous polydimethylsiloxane structures with adjustable porosity and pore morphology using emulsion templating technique. Polymer Engineering & Science 2021, 61, 1943-1955.

[9] R. Riesco, L. Boyer, S. Blosse, P. M. Lefebvre, P. Assemat, T. Leichle, A. Accardo, L. Malaquin. Water-in-PDMS Emulsion Templating of Highly Interconnected Porous Architectures for 3D Cell Culture. ACS Appl Mater Interfaces 2019, 11, 28631-28640.

[10] F. Goodarzi, S. Zendehboudi. A Comprehensive Review on Emulsions and Emulsion Stability in Chemical and Energy Industries. The Canadian Journal of Chemical Engineering 2018, 97, 281-309.

[11] S. N. Kale, S. L. Deore. Emulsion Micro Emulsion and Nano Emulsion: A Review. Systematic Reviews in Pharmacy 2016, 8, 39-47.

[12] K. Barkat Ali. Basics of pharmaceutical emulsions: A review. African Journal of Pharmacy and Pharmacology 2011, 5.

報告型式：

□英文口頭報告競賽 (□無機材料， □有機材料)
☑海報展示並參加壁報論文競賽(□無機材料， ☑有機材料)
□只參加海報展示 (□無機材料， □有機材料)

刮刀塗佈法製備導電核殼粒子組成之波浪緞帶彈性導電結構

蔣承羽、蕭智升、薛涵宇
國立中興大學材料科學與工程學系
hyhsueh@nchu.edu.tw

NSTC 114-2223-E-005-001-MY3

摘要

可拉伸電子（Stretchable Electronics）為近年熱門研究領域，應用於穿戴式裝置、電子皮膚及柔性顯示器等。然而，多數製程仰賴真空濺鍍等昂貴設備，且導體多為金屬或半導體等無機材料。相較之下，具導電性的軟物質如導電高分子、高分子與碳材之複合材料相關研究仍較少，且常需高溫高壓製備。本研究開發一種獨特濕式製程，結合刮刀塗佈（Flow Coating）技術，利用溶液黏滑運動（Stick–Slip Motion）排整微米級聚苯乙烯（Polystyrene）球及包覆還原氧化石墨烯（reduced Graphene Oxide）之核殼粒子。藉由溶劑蒸發誘導自組裝與退火處理，成功形成具波浪緞帶皺褶（Wavy Ribbon）之連續薄膜結構，呈現如電路線條般的規則排列。再將導電核殼粒子嵌入該結構中，製得具彈性之導電元件，其最高導電率達 2.17×10^2 S/m，與文獻值相當。未來將進一步優化其在拉伸與彎曲形變下的導電穩定性，以實現應用於軟性電子裝置之潛能。

關鍵字： 可拉伸電子、濕式製程、刮刀塗佈、波浪繳帶皺褶、導電核殼粒子

報告型式：

□英文口頭報告競賽 (□無機材料， □有機材料)
☑海報展示並參加壁報論文競賽(□無機材料， ☑有機材料)
□只參加海報展示 (□無機材料， □有機材料)

由金屬有機框架 MOF-303 與聚苯咪唑(PBI)所構成之陰離子交換複合薄膜用於燃料電池之研究

李昱萱[1]、詹承諭[1]、鄭力誠[1]
國立高雄科技大學化學工程與材料工程系
lcjheng@nkust.edu.tw

NSTC 114-2221-E-992-025-MY2

摘要

本研究針對陰離子交換膜燃料電池（AEMFC）在實際應用中面臨的氫氧根離子導電度不足與鹼性穩定性受限等關鍵問題，提出一種新型複合陰離子交換膜之設計策略。透過提高離子交換容量雖可改善導電度，但往往伴隨吸水率與膨潤率上升，進而削弱材料之尺寸穩定性與機械性質；而傳統交聯方法雖可抑制膨潤，卻可能阻礙離子傳輸通道的形成。因此，本研究引入具規則奈米孔道結構之金屬有機骨架材料（MOF-303），以提供額外且連續的離子傳輸路徑，同時利用其剛性骨架限制高分子鏈段運動，以期兼顧導電性與結構穩定性。

在材料設計上，選用含六氟聚苯并咪唑（6FPBI）為高分子基材，並接枝咪唑鎓離子液體形成具陽離子側鏈之 Im-6FPBI，同時將相同離子液體引入MOF-303孔道中，製備具離子導電能力之 Im@MOF-303。最終構築Im@MOF-303/Im-6FPBI 複合陰離子交換膜，以提升氫氧根離子傳輸效率並改善膜之尺寸穩定性與機械強度。

研究內容涵蓋 6FPBI、Im-6FPBI、MOF-303 及 Im@MOF-303 之合成，再確認其結構與熱性質 (如 NMR、FTIR、XRD、BET、SEM、EDS、XPS 、TGA)；此外，也將針對複合膜進行薄膜性質檢測 (如 IEC、吸水率、膨潤率、機械性質、氫氧根導電度，鹼安定性、氧化安定性)。預期本研究所開發之複合膜能在不犧牲離子傳輸效率的前提下，有效提升整體性能與長期操作穩定性，展現其於 AEMFC 應用之潛力。

參考文獻

[1] Salma, U.; Shalahin, N., Results in Materials, 17 (2023) 100366.

[2] Jheng, L.-C.; Chen, W.-Y.; Huang, G.-L.; Zhao, Z.-L.; Hsu, S. L.-C.; Ko, W.-C.,Int. J. Hydrogen Energy, 130 (2025) 108–118.

[3] Lin, C.; Wang, J.; Shen, G.; Duan, J.; … Journal of Membrane Science, 590 (2019) 117303.

[4] Ataollahi, N.; Tomasino, E.; Cotini, O.; Di Maggio, R., Energies, 15 (2022) 1953.

[5] He, X.; Gang, M.; Li, Z.; He, G.; Yin, Y.; Cao, L.; Zhang, B.; Wu, H.; Jiang, Z. Sci. Bull. 2017, 62 (4), 266–276.

[6] Guo, M.; Ban, T.; Wang, Y.; Wang, Y.; Zhang, Y.; Zhu, X., Journal of Membrane Science, 647 (2022) 120299.

[7] Zhuang Rao, Kai Feng, Beibei Tang, Peiyi Wu.Journal of Membrane Science , 533, 2017, 160 - 170

報告型式：

□英文口頭報告競賽 (□無機材料， □有機材料)
☑海報展示並參加壁報論文競賽(□無機材料， ☑有機材料)
□只參加海報展示 (□無機材料， □有機材料)

Surface Modification of Current Collectors to Enhance the Cyclic Efficiency of Anode-Free Lithium-Metal Batteries

Hsiao-Ting Ma[1], Jui-Hung Chen[2], Vincent Tung[2], Stanley Fu[2], Jui-Hsiung Huang[2], Kuei-Yen Wu[2],
CPC Corporation[2], Taiwan, Han-Yi Chen *
Department of Material Science and Engineering, National Tsing Hua University, Hsinchu, Taiwan
*Correspondence: xiaotingma0407@gmail.com

Abstract

Anode-free lithium metal batteries (AFLMBs) have been regarded as promising energy storage devices due to their high energy density and reduced cost; however, poor Coulombic efficiency (CE) and Li dendrite growth are critical challenges for AFLMBs. Herein, we synthesized a carbon thin film on a copper current collector via chemical vapor deposition (CVD). A specific sp-hybridized carbon framework exhibits superior lithiophilicity attributed to its higher electron density, which effectively lowers the lithium nucleation overpotential. Simultaneously, regular pore distribution within the carbon film homogenizes lithium-ion flux and promotes uniform lithium deposition. Moreover, its high mechanical strength and chemical stability can stabilize the SEI layer during cycling. The successful synthesis of the carbon thin film was verified through Raman and FTIR spectroscopy, while Atomic Force Microscopy (AFM) analysis demonstrated smooth and continuous morphology, thereby ensuring the high quality of the carbon thin film. In the Aurbach test, Cu||Li half cells achieve a high average Coulombic efficiency (CE) of 98.95 %, and lower nucleation overpotential compared to pristine. Variable current density of stripping plating test demonstrates that the modified electrode increases the critical current density from 1 mA/cm^2 to 2 mA/cm^2, and we can also observe that the modified electrode exhibits lower voltage polarization across different current densities. Moreover, long-term cycling tests show that Cu with carbon thin film exhibits enhanced stability over 250 cycles.

References

1. Addisu Alemayehu Assegie, Cheng-Chu Chung, Meng-Che Tsai, Wei-Nien Su, Chun-Wei Chen, and Bing-Joe HwangNanoscale, 2019, 11, 2710–2720
2. Zhiyu Jia, Yongjun Li, Zicheng Zuo, Huibiao Liu, Changshui Huang, and Yuliang Li, Acc. Chem. Res. 2017, 50, 2470−2478
3. Xin Gao, Huibiao Liu, Dan Wang and Jin Zhang, Chem. Soc. Rev., 2019, 48, 908—936
4. Jun Ho Lee, Yoon-Gyo Cho, Dongeun Gu, and Suk Jun Kim, ACS Appl. Mater. Interfaces 2022, 14, 15080−15089
5. Yan Wang, Zongtao Qu, Shitao Geng, Meng Liao, Lei Ye, Zulipiya Shadike, Xiaoju Zhao, Shuo Wang, Qiuchen Xu, Bin Yuan, Xiao Zhang, Xiaxin Gao, Xuesong Jiang, Huisheng Peng, and Hao Sun

Presentation type：

☐ English oral competition (☐ inorganic materials, ☐ organic materials)
☑ Poster competition (☐ inorganic materials, ☑organic materials)
☐ Exhibition only (☐ inorganic materials, ☐ organic materials)

奈米碳材強化複材應用於真空輔助樹脂轉注成型之研究

Qi-Wei Chen, Hsu-Chiang Kuan*
南臺科技大學 化學工程與材料工程系
e-mail:hckuan@stust.edu.tw

摘要

近年來，高性能輕量化複合材料廣泛應用於航太、交通運輸及結構工程等領域，傳統金屬材料已難以同時滿足高強度、耐熱性與減重需求，因此高分子基複合材料逐漸成為重要工程材料。奈米碳材料因具備優異機械強度、高比表面積及界面效應，被認為能有效提升材料之機械性質與阻尼性能。材料結構與性質分別透過 X 光繞射分析（XRD）、傅立葉轉換紅外線光譜（FTIR-ATR）、熱重分析（TGA）及掃描式電子顯微鏡（SEM）進行分析，並透過拉伸試驗、三點彎曲試驗與衝擊試驗評估其力學性能。

實驗結果顯示在添加 0.1 wt% 石墨之複合材料在抗拉強度與彎曲性能上均優於純樹脂，顯示低含量石墨可有效提升應力轉移效率與材料剛性，， 衝擊試驗亦顯示其能力有所提升。而當石墨添加量提高至 0.5 wt% 時， 部分機械性能出現下降趨勢，推測與石墨之分散性降低有關，TGA 分析結果顯示，將石墨導入可提升材料之熱分解溫度與殘碳率，顯示其對熱穩定性具有正向影響，， SEM 觀察證實最終產物 GNs 樣品呈現薄且少層的片狀結構，顯示成功剝離成奈米級石墨片。

而石墨本身是層狀結構，在材料受力或振動時，石墨片層之間容易產生滑移，同時石墨與樹脂界面之間也會產生摩擦與微小變形。這些機制會把一部分機械能轉換形成能量耗散，因此能夠提升複合材料的阻尼性能。當石墨能夠均勻分散在樹脂基體中時，石墨片層與樹脂界面之間的作用會更加明顯，使材料在受到振動或衝擊時能吸收更多能量，進而降低結構振動。本研究的結果也顯示，透過適當的石墨分散方式，可以在不影響樹脂流動性的情況下，應用於 VARTM 製程，同時兼顧材料的機械性能與阻尼特性，對於未來高阻尼複合材料的工程應用具有潛在發展價值。

關鍵字：奈米石墨片、自由基固化樹脂、奈米複合材料

報告型式：

□英文口頭報告競賽　　　　(□無機材料， □有機材料)
■ 海報展示並參加壁報論文競賽(■無機材料， □有機材料)
□只參加海報展示　　　　　(□無機材料， □有機材料)

自組裝仿陸生蝸牛之柱狀結構陣列於可調控附著之研究

王家楹[1]、張文權[1]、陳緯綸[1]和楊宏達*
中興大學
hyang@dragon.nchu.edu.tw

NSTC 112-2221-E-005-006-MY3

摘要

陸地蝸牛之所以能夠黏附在粗糙、不規則、光滑的表面上，是因為其足部上遍布了微米級的柱狀結構，且足部和表面之間覆蓋有黏稠的黏液；這些突起結構能深入不規則的表面，增加腹足與黏液的接觸面積，進而增強與黏附表面的摩擦力，表現了優異的黏附能力和使用特性。

受此生物的黏附特性的啟發，使用二維非緊密堆積膠體晶體在 PET 上進行自組裝並作為模板來形成柱狀結構陣列，隨後在其塗佈一層薄薄的水凝膠。此實驗的正向黏附力為 6.2 N，與陸地蝸牛的正向黏附力相當。重要的是，由於結構和表面之間的物理互鎖效應，使其側向黏附力甚至高於原先預期。此實驗可逆且可切換的黏附能力開啟了許多應用的可能性，像是傷口護理、穿戴式裝置、可切換的黏著材料等。

關鍵字：仿蝸牛結構、旋轉塗佈技術、自組裝技術、柱狀結構、黏附、互鎖效應

参考文獻

[1] Zhao, N.; Wang, Z.; Cai, C.; Shen, H.; Liang, F.; Wang, D.; Wang, C.; Zhu, T.; Guo, J.; Wang, Y.; et al. Bioinspired Materials: from Low to High Dimensional Structure. Adv. Mater. 2014, 26, 6994-7017.

[2]Wang, Y.; Naleway, S. E.; Wang, B. Biological and Bioinspired Materials: Structure Leading to Functional and Mechanical Performance. Bioact. Mater. 2020, 5, 745-757.

[3]Zhang, C.; McAdams Ii, D. A.; Grunlan, J. C. Nano/Micro-Manufacturing of Bioinspired Materials: a Review of Methods to Mimic Natural Structures. Adv. Mater. 2016, 28, 6292-6321.

[4]Zhang, Y.; Ma, S.; Li, B.; Yu, B.; Lee, H.; Cai, M.; Gorb, S. N.; Zhou, F.; Liu, W. Gecko’s Feet-Inspired Self-Peeling Switchable Dry/Wet Adhesive. Chem. Mater. 2021, 33, 2785-2795.

[5]Shi, Z.; Tan, D.; Wang, Z.; Xiao, K.; Zhu, B.; Meng, F.; Liu, Q.; Wang, X.; Xue, L. Switchable Adhesion on Curved Surfaces Mimicking the Coordination of Radial-Oriented Spatular Tips and Motion of Gecko Toes. ACS Appl. Mater. Interfaces 2022, 14, 31448-31454.

報告型式：

□英文口頭報告競賽 (□無機材料， □有機材料)
√海報展示並參加壁報論文競賽(□無機材料， √有機材料)
□只參加海報展示 (□無機材料， □有機材料)

仿象鼻蟲可變色光子晶體材料之研究

楊欣宜、林姵岑 、林岱玟 、楊宏達*
國立中興大學化學工程學系
E-mail: hyang@dragon.nchu.edu.tw

NSTC 112-2221-E-005-006-MY3

摘要

隨著科技發展，智慧化、輕量化與安全性已成為產品設計的關鍵目標。穿戴式裝置、可攜式電子產品與智慧感測系統的普及，對材料的多功能整合提出了更高要求。材料不僅需具備良好的機械強度與耐衝擊性，還需兼顧光學穩定性與回應性，特別在智慧防護與個人安全監測等應用中，傳統材料難以同時滿足力學與光學需求。

因此，發展具結構色、形變回復與衝擊可視化的新型材料成為智慧材料領域的重要研究方向。

球背象鼻蟲(*Pachyrhynchus Apoensis*)的鞘翅表面具有高度有序的鱗片結構，其內部蘊含三維光子晶體架構，能夠選擇性地反射特定波長的光線，呈現出鮮豔而飽和的結構色彩。除了產生獨特的視覺效果外，該結構亦展現出優異的機械穩定性與抗衝擊特性，使其在自然環境中兼具保護與警示功能。受此自然構造啟發，本研究模仿其鞘翅光子晶體結構，結合 Doctor Blade Coating 技術，以形狀記憶高分子(SMP)為基材，成功製備出具備結構色、可視化變色功能與衝擊吸能能力的光學薄膜。此材料在受外力或熱刺激下可產生可逆形變與色彩變化，除提升其力學保護效能外，亦可作為即時衝擊感測之光學回饋元件，展現出其於智慧防護、光學顯示與生物仿生材料等多功能應用領域的潛力。

此研究利用具溶劑響應性的形狀記憶高分子，透過溶劑刺激使變形結構回復至原狀，實現可逆變形。為驗證其耐用性與穩定性，且進行了 20 次重複測試，結果顯示所製備之抗衝擊材料能在多次衝擊後保持良好的結構回復性和性能穩定性。

。

關鍵詞：球背象鼻蟲、刮刀塗佈、形狀記憶高分子、多孔性高分子薄膜、抗衝擊材料

參考文獻

(1) Fratzl, P. Biomimetic Materials Research: What Can We Really Learn from Nature's Structural Materials? *J. R. Soc. Interface.* **2007**, *4* (15), 637-642.

(2) Suresh Kumar, N.; Padma Suvarna, R.; Chandra Babu Naidu, K.; Banerjee, P.; Ratnamala, A.; Manjunatha, H. A Review on Biological and Biomimetic Materials and Their Applications. *Applied Physics A* **2020**, *126* (6), 445.

(3) Branković, M.; Zivic, F.; Grujovic, N.; Stojadinovic, I.; Milenkovic, S.; Kotorcevic, N. Review of Spider Silk Applications in Biomedical and Tissue Engineering. *Biomimetics* **2024**, *9* (3), 169.

報告型式：

□英文口頭報告競賽 (□無機材料， □有機材料)
☑海報展示並參加壁報論文競賽(□無機材料， ☑有機材料)
□只參加海報展示 (□無機材料， □有機材料)

仿撒哈拉銀蟻金字塔結構陣列於光操控應用

王毓汶、陳姵文、劉于甄 、楊宏達*
國立中興大學 化學工程學系
hyang@dragon.nchu.edu.tw

NSTC 112-2221-E-005-006-MY3

摘要

撒哈拉銀螞蟻（*Cataglyphis bombycina*）為適應撒哈拉沙漠極端高溫的環境，演化出一種特殊的散熱機制，其體表所覆蓋的三角形毛髮能夠顯著提升光反射率並促進熱輻射。受到此自然設計的啟發，此研究發展出一套創新的仿生製程技術，透過膠體自組裝（Colloidal Self-assembly）與各向異性濕蝕刻（Anisotropic Wet-etching） 兩階段製程，成功在矽基材表面製備出規則排列的金字塔型結構陣列。

此類金字塔結構展現出獨特的光學行為，尤其對於入射角度大於臨界角的光線可實現完全反射，具備良好的方向性控光功能，模擬了銀螞蟻的光學反射特性。由於其精準的光操控能力，該結構於光電與光子元件領域具有高度應用潛力，包括光學感測器、反射塗層以及被動輻射冷卻系統。此研究證明，仿生設計不僅可揭示自然界結構功能之奧秘，更能為高階材料工程帶來嶄新之應用契機。

關鍵字：撒哈拉銀螞蟻、金字塔型結構、矽基材、濕蝕刻、自組裝、光操控、仿生材料

參考文獻

[1] Wu, P.; Wang, J.; Jiang, L. Bio-Inspired Photonic Crystal Patterns. Mater. Horiz. 2020, 7 (2), 338-365.
[2] Yablonovitch, E. Inhibited Spontaneous Emission in Solid-State Physics and Electronics. PRL 1987, 58 (20), 2059.
[3] Joannopoulos, J. D.; Johnson, S. G.; Winn, J. N.; Meade, R. D. Molding the Flow of Light. Princet. Univ. Press. Princeton, NJ 2008, 12.
[4] Reimer, M.; Zollfrank, C. Cellulose for Light Manipulation: Methods, Applications, and Prospects. Adv. Energy Mater. 2021, 11 (43), 2003866.
[5] Fenzl, C.; Hirsch, T.; Wolfbeis, O. S. Photonic Crystals for Chemical Sensing and Biosensing. Angew Chem. Int. Ed. Engl. 2014, 53 (13), 3318-3335.
[6] Cai, Z.; Zhang, J.-T.; Xue, F.; Hong, Z.; Punihaole, D.; Asher, S. A. 2D photonic crystal protein hydrogel coulometer for sensing serum albumin ligand binding. Anal. Chem. 2014, 86 (10), 4840-4847.

報告型式：

□英文口頭報告競賽 (□無機材料， □有機材料)
☑海報展示並參加壁報論文競賽(□無機材料， ☑有機材料)
□只參加海報展示 (□無機材料， □有機材料)

以UV聚合法製備固碳壓克力樹酯之研究

林詮衡、杜東蔚、林國偵、黃國鳴、王振乾*
南臺科技大學化學工程與材料工程系
ccwang@stust.edu.tw

摘要

本研究利用環加成反應，將二氧化碳(Carbon dioxide, CO$_2$)與甲基丙烯酸縮水甘油酯(Glycidyl methacrylate, GMA)，成功合成(2-氧代-1,3-二氧環丙烷-4-基)甲基甲基丙烯酸酯(Glycerol carbonate methacrylate, GCMA)單體。並加入光引發劑 Darocur 1173，透過紫外光引發進行自由基聚合反應，製備出功能性高分子固體材料。研究重點為加入不同光起始劑濃度與聚合環境，測試材料吸收紫外線與機械性能。以傅立葉轉換紅外光譜(FTIR)鑑定結果顯示，於 1800cm^{-1} 出現五元環碳酸酯之特徵羰基波峰，確認 GCMA 單體合成成功，接著使用紫外光-可見光光譜儀(UV-Vis)分析，不同環境下的氛圍做對比。研究發現以玻璃片蓋住模具的可見光穿透度由 60%提升至 80%時，UVA 穿透率會由 45%增加至 75%，UVB 穿透率趨近於 0%；以氮氣吹掃環境的可見光透光度維持 90%以上，UVA 為 75%以上，UVB 透光率於 14%以下。機械性質方面，拉伸試驗證實材料具備不錯的抗拉強度與結構穩定性。本研究成功將溫室氣體 CO$_2$ 轉化為高附加價值之單體，開發出具有紫外線吸收、高透明度與良好機械強度之環保高分子材料，為綠色製程與高性能機能材料的開發提供了重要的科學發現。

關鍵字：二氧化碳、固碳材料、光聚合、壓克力系高分子

參考文獻

1. Liu, B., Zhang, Y. Y., Zhang, X. H., Du, B. Y., & Fan, Z. Q. (2016). Fixation of carbon dioxide concurrently or in tandem with free radical polymerization for highly transparent polyacrylates with specific UV absorption. *Polymer Chemistry*, *7*(22), 3731-3739.
2. Jančovičová, V., Kindernay, J., Jakubíková, Z., & Mrlláková, I. (2007). Influence of photoinitiator and curing conditions on polymerization kinetics and gloss of UV-cured coatings. *Chemical Papers*, *61*(5), 383-390.
3. Schimpf, V., Asmacher, A., Fuchs, A., Bruchmann, B., & Mülhaupt, R. (2019). Polyfunctional acrylic non-isocyanate hydroxyurethanes as photocurable thermosets for 3D printing. *Macromolecules*, *52*(9), 3288-3297.

報告型式：

□英文口頭報告競賽 (□無機材料， □有機材料)
■海報展示並參加壁報論文競賽(□無機材料， ■有機材料)
□只參加海報展示 (□無機材料， □有機材料)

含多壁奈米碳管之聚對苯二甲酸丁二酯導電纖維開發

作者:陳彥瑋†、關旭強＊
南臺科技大學 化學工程與材料工程系
E-mail: hckuan@stust.edu.tw

摘要

對於聚酯導電複合材料而言，如何同時實現均勻分散與穩定導電性，始終是其應用於紡織領域的關鍵課題。本研究開發出一套結合非共價表面改質、界面相容技術與機械破碎處理之製程方案，探討多壁奈米碳管（MWCNT）在聚對苯二甲酸丁二酯（PBT）基體中的分散品質與導電效能的變化。

本研究首先以聚乙烯吡咯烷酮（PVP）對 MWCNT 進行物理吸附改質。PVP 分子主鏈與碳管側壁間的凡得瓦力，以及內醯胺環與碳管 π 電子間的交互作用，可有效降低碳管間的吸引力並抑制團聚，使碳管表面形成穩定的吸附層。本研究透過引入 PBT 基體中，並添加少量彈性體相容劑（PTW）以促進界面結合，藉由 PVP 改質與 PTW 相容作用的協同效應，PTW 的環氧基團與聚酯端基發生反應提升剪切力傳遞效率，使碳管得以在 PBT 基體中均勻分散並形成穩定導電網路。

TGA 結果證實 PVP 於 300 °C 以下具良好熱穩定性，可承受 PBT 熔融加工條件。Raman 分析顯示改質前後碳管之 I_D/I_G 值維持穩定，證明製程未破壞 sp^2 石墨化結構。製程比較結果顯示，乾式混摻相較於濕式分散具有更低且穩定的表面電阻，同時製程流程簡單、操作性佳，無需額外溶劑與乾燥步驟。透過 PVP 與 PTW 協同作用，在 1 wt% 填料含量下即可達 $10^3\Omega$/sq 導電等級，顯著降低滲流閾值。光學顯微鏡（OM）影像進一步佐證，協同改質系統能使奈米碳管呈現細微且均勻的空間分布。

參考文獻

[1] M. T. Müller, P. Pötschke, and B. J. P. Voit, “Dispersion of carbon nanotubes into polyethylene by an additive assisted one-step melt mixing approach,” vol. 66, pp. 210-221, 2015.
[2] J. Abraham, S. Thomas, and N. Kalarikkal, Handbook of carbon nanotubes: Springer Nature, 2022, pp. 341–392

報告型式：

- □英文口頭報告競賽 (□無機材料， □有機材料)
- ☑海報展示並參加壁報論文競賽(□無機材料， ☑有機材料)
- □只參加海報展示 (□無機材料， □有機材料)

構建 $ZnIn_2S_4$–$In(OH)_3$/Cu 異質接面光催化劑於光催化產氫性能研究

陳福恒、石長青、張育誠
逢甲大學材料科學與工程學系
Hamiiyayz1115@gmail.com

NSTC 112-2221-E-035-017-MY3 and NSTC 113-2221-E-035-023-MY3

摘要

本研究透過合理設計的合成策略，成功製備具優化奈米片結構與優異光吸收能力之 $ZnIn_2S_4$–$In(OH)_3$光催化材料，可有效降解有機污染物並展現良好光催化活性。進一步導入 Cu 奈米粒子後，成功構築 $ZnIn_2S_4$–$In(OH)_3$/Cu 三元異質結，其中 Cu 奈米粒子不僅可藉由局域表面電漿共振（LSPR）效應拓展可見光吸收範圍，更可作為電子匯聚中心，促進光生電子快速轉移並有效抑制電子–電洞對再結合，大幅提升整體光催化效率。由於 Type-II 能帶排列的建立， 光生電子可定向傳輸至 Cu 表面，而電洞則保留於原半導體能帶中，使載子分離效率進一步提升。在光催化產氫表現方面，該材料於去離子水中的產氫速率高達 124.73 μmol h^{-1} g^{-1}，為純 $ZnIn_2S_4$材料的 173.2 倍，展現極為優異的太陽能轉換能力。此外，此複合材料兼具污染物去除功能，可完全降解甲基橙（100%）並達到 78.6%的四環黴素（TCH 去除效率，展現其能源生產與環境淨化雙功能特性。在天然水源應用方面，$ZnIn_2S_4$– $In(OH)_3$/Cu 異質結於溪水中表現出優異的產氫效率與穩定性，經四次循環後仍可維持 94.8%的活性，顯示其具備良好的耐久性與實際應用潛力。然而， 在海水系統中，由於複雜離子間交互作用導致沉澱生成，使活性位點受阻並造成性能下降。綜合而言，本研究證實藉由反應條件調控與異質結構設計，可有效提升光催化材料之載子分離效率、光吸收能力與反應活性，且所建立之簡便且具可擴展性的合成路徑，使 $ZnIn_2S_4$–$In(OH)_3$/Cu 三元異質結在未來太陽能產氫、天然水體應用及污染物降解等領域展現高度實用價值與發展潛力。

參考文獻

Y.-C. Chang et al., Int. J. Hydrogen Energy 179 (2025) 151736.

Y.-C. Chang et al., Int. J. Hydrogen Energy 86 (2024) 24-35. [3] S. Li et al., J. Phys. Chem. Lett. 15 (2024) 5215–5222.

H. Zhao et al., Int. J. Hydrogen Energy 45 (2020) 13975–13984.

Z. Wang et al., Int. J. Hydrogen Energy 60 (2024) 1266–1274.

報告型式：

□英文口頭報告競賽 (□無機材料， □有機材料)
☑海報展示並參加壁報論文競賽(□無機材料， ☑有機材料)
□只參加海報展示 (□無機材料， □有機材料)

廢棄咖啡渣與橘皮協同一步熱解綠色製程：高效能超級電容器用階層多孔碳材料之永續開發

鄭欣穎、張劭汝、張育誠
逢甲大學材料科學與工程學系
emilycheng1027@gmail.com

NSTC-112-2221-E-035-017-MY3 and NSTC-113-2221-E-035-023-MY3

摘要

隨著科技快速發展與生活品質持續提升，全球對能源的需求亦大幅增加，進而加劇化石燃料的消耗及其所造成的環境污染問題，衍生出能源短缺、碳排放上升與生態惡化等嚴峻挑戰[1]。由於傳統能源資源有限，且全球分布不均，開發潔淨再生能源及高效率儲能技術已成為當前科學研究與永續發展的重要方向。尤其再生能源如太陽能與風能具有間歇性與不穩定性，因此如何有效儲存並穩定輸出能源，是推動綠能普及化的關鍵課題。在眾多儲能裝置中，超級電容器因具備高功率密度、快速充放電特性、優異循環壽命及高安全性等優勢，而受到廣泛關注[2]。另一方面，利用低成本且環境友善的生物廢棄物製備電極材料，不僅可降低材料成本，也符合循環經濟與資源再利用理念，因此成為先進儲能材料研究的重要趨勢。本研究提出一種具綠色製程與量產潛力的一步共熱解策略，以廢棄咖啡渣（CF）作為碳前驅物[3] , [4]，並利用橘皮（OP）作為天然活化劑[5]，成功製備高效能多孔碳材料。透過系統性調控熱解溫度、CF:OP 質量比以及咖啡豆烘焙程度等關鍵參數，建立最佳製備條件。結果顯示，在 800°C 條件下，以淺焙咖啡渣與橘皮 1:1 質量比所得之最佳化材料（CFOP），於 1 A/g 電流密度下可達 275.3 F/g 的優異比電容表現。材料結構分析進一步證實，橘皮中的有機成分與咖啡渣中殘留鉀元素產生協同原位活化作用，可有效形成階層化多孔結構，同時提升材料石墨化程度與電子導電性，而這些特徵皆為提升電化學性能的重要因素[6] , [7]。動力學分析顯示，其儲能機制主要以擴散控制之贗電容行為為主，有助於提升離子傳輸與電荷儲存效率。值得注意的是，CFOP 電極亦展現優異的循環穩定性，在 5000 次充放電循環後仍可保有 63.27%的初始電容，並維持 97.29%的高庫倫效率。綜合而言，本研究提供了一條簡單、高效且永續的農業廢棄物再利用途徑，可將低價值生質廢棄物轉化為高附加價值電極材料，展現其於未來實際能源儲存與綠色材料應用上的巨大潛力[8]。

參考文獻

[1] N. Armaroli and V. Balzani, “The Legacy of Fossil Fuels,” *Chem. – Asian J.*, vol. 6, no. 3, pp. 768–784, 2011.

[2] R. T. Yadlapalli, R. R. Alla, R. Kandipati, and A. Kotapati, “Super capacitors for energy storage: Progress, applications and challenges,” *J. Energy Storage*, vol. 49, p. 104194, May 2022.

[3] R. Campos-Vega, G. Loarca-Piña, H. A. Vergara-Castañeda, and B. D. Oomah, “Spent coffee grounds: A review on current research and future prospects,” *Trends Food Sci. Technol.*, vol. 45, no. 1, pp. 24–36, Sept. 2015.

[4] J. McNutt and Q. (Sophia) He, “Spent coffee grounds: A review on current utilization,” *J. Ind. Eng. Chem.*, vol. 71, pp. 78–88, Mar. 2019.

[5] S. S. Lam, R. K. Liew, Y. M. Wong, P. N. Y. Yek, N. L. Ma, C. L. Lee, and H. A. Chase, “Microwave-assisted pyrolysis with chemical activation, an innovative method to convert orange peel into activated carbon with improved properties as dye adsorbent,” *J. Clean. Prod.*, vol. 162, pp. 1376–1387, Sept. 2017.

[6] S. Singh, M. B. Gumpu, S. K.n., and S. K. Paramasivam, “A comprehensive evaluation of synthesis methods for

porous carbon materials and their applications in energy storage," *Diam. Relat. Mater.*, vol. 153, p. 112033, Mar. 2025.

[7] L. Guan, D. Li, S. Ji, X. Wei, and F. Meng, "Structural Regulation and Performance Enhancement of Carbon-Based Supercapacitors: Insights into Electrode Material Engineering," *Materials*, vol. 18, no. 2, p. 456, Jan. 2025.

[8] A. P. Khedulkar, B. Pandit, V. D. Dang, and R. Doong, "Agricultural waste to real worth biochar as a sustainable material for supercapacitor," *Sci. Total Environ.*, vol. 869, p. 161441, Apr. 2023.

報告型式：

□英文口頭報告競賽 (□無機材料， □有機材料)
☑海報展示並參加壁報論文競賽(□無機材料， ☑有機材料)
□只參加海報展示 (□無機材料， □有機材料)

利用摻雜鎂離子之 SPANI 為可自充電的穿戴式鋅離子電池之應用

王涵汶[1], 鄧名傑[2]
靜宜大學應用化學系
e-mail: dengmj1020@gm.pu.edu.tw

摘要

此研究致力於研究出運用鋅離子電池裝置的儲能裝置為目標，因鋅離子電池經常時間的使用會因副產物(鋅枝晶)的問題而早成短路、電池使用壽命縮短等問題，因此為了解決此問題，目標是研究出適合我們裝置的鋅離子膠體電解質後有效的運用於裝置中，並了解是否我們製成的鋅離子儲能裝置效能佳且能有效的運用於柔性穿戴式裝置上。

本研究的儲能裝置是使用摻雜鎂離子的磺酸化聚苯胺(SPANI)作為正極(工作電極)，而負極是使用鋅片，再搭配著鋅離子膠體電解質形成我們的 SPANI doped Mg//Zn 儲能裝置。

SPANI 電極可藉由放電至不穩定的還原態後自行的氧化回穩定的氧化態來達到自充電的性能，這使我們的儲能裝置能更有效的被利用。再加上 SPANI 電極有著電自變色的功能，在不同的電位下有著不同的顏色，以利於使用者透過顏色來分辨出裝置是處於有電或需充電的狀態。

參考文獻

(1) Gong, S.; Sun, K.; Yang, F.; Wu, S.; Wang, Y.; Li, R.; Jia, X.; Wang, C.; Chao, D. Doping of magnesium ions into polyaniline enables high-performance Zn-Mg alkaline batteries. *Nano Energy* **2025**, *134*, 110586.

(2) Wang, N.; Liu, H.; Sun, M.; Ren, X.; Hu, L.; Li, Z.; Yao, X.; Gong, Y.; Jia, C. Achieving Wide-Temperature-Range Sustainable Zinc-Ion Batteries via Magnesium-Doped Cathodes and Gel Electrolytes. *ACS Sustainable Chemistry & Engineering* **2024**, *12* (9), 3527–3537. DOI: 10.1021/acssuschemeng.3c06291.

(3) Merrill, L. C.; Ford, H. O.; Schaefer, J. L. Application of Single-Ion Conducting Gel Polymer Electrolytes in Magnesium Batteries. *ACS Applied Energy Materials* **2019**, *2* (9), 6355–6363. DOI: 10.1021/acsaem.9b00991.

(4) Wang, Y.; Jiang, H.; Zheng, R.; Pan, J.; Niu, J.; Zou, X.; Jia, C. A flexible, electrochromic, rechargeable Zn-ion battery based on actiniae-like self-doped polyaniline cathode. *Journal of Materials Chemistry A* **2020**, *8* (25), 12799–12809. DOI: 10.1039/d0ta04203j.

(5) Yan, J.; Liu, X.; Yao, M.; Wang, X.; Wafle, T. K.; Li, B. Long-Life, High-Efficiency Lithium–Sulfur Battery from a Nanoassembled Cathode. *Chemistry of Materials* **2015**, *27* (14), 5080–5087. DOI: 10.1021/acs.chemmater.5b01780.

(6) Wang, R.; Yao, M.; Huang, S.; Tian, J.; Niu, Z. Sustainable Dough-Based Gel Electrolytes for Aqueous Energy Storage Devices. *Advanced Functional Materials* **2021**, *31* (14). DOI: 10.1002/adfm.202009209.

(7) Ai, Y.; Gong, S.; Zhu, Y.; Wu, F.; Xu, Z.; Chen, L. Programmable, Recyclable, and Self-Healing Multifunctional Liquid Crystal Elastomers Enabled by Dynamic Spiral Diacetal Structure. *Chemistry of Materials* **2025**, *37* (23), 9589–9596. DOI: 10.1021/acs.chemmater.5c02590.

報告型式：

□英文口頭報告競賽 (□無機材料， □有機材料)
☑海報展示並參加壁報論文競賽(□無機材料， ☑有機材料)
□只參加海報展示 (□無機材料， □有機材料)

Fabrication of Surface Microstructures on Photoresponsive Spiropyran-based Films via the Marangoni Effect

Huai-Hsuan Tsai [1], Cheng-Wei Huang [1,*]
Department of Chemical and Material Engineering, National
Kaohsiung University of Science and Technology
E-mail: cwhuangs@nkust.edu.tw

NSTC 113-2221-E-992-004-MY3

Abstract

This study investigates the kinetic behavior and morphological evolution of the photoresponsive polymer P(BMA-SPMA) during the fabrication of surface microstructures. It was observed that the conventional Surface Relief Grating (SRG) effect was not significant in this system under traditional high-power laser interference. This limitation is primarily attributed to the insufficient capability of spiropyran (SP) moieties to induce large-scale polymer chain migration through standard photomechanical driving forces.

To bypass these constraints, we propose a novel fabrication strategy leveraging the Marangoni effect. The core mechanism involves the photoisomerization of spiropyran (SP) side chains into highly polar, zwitterionic merocyanine (MC) states upon UV irradiation. This molecular-level transformation creates substantial localized polarity shifts, which induce potent surface tension gradients across the film surface. Driven by Marangoni stresses, the polymer fluid spontaneously migrates from regions of low surface tension to high surface tension, enabling the formation of well-defined periodic patterns without the need for complex optical interference setups.

Experimental results demonstrate that this approach operates under significantly milder irradiation conditions compared to traditional SRG techniques, offering superior energy efficiency and potential for large-area processing. This research not only elucidates the fundamental mechanistic differences in photo-induced morphological evolution between spiropyran and azobenzene-based systems but also proves that the Marangoni-driven strategy holds immense industrial value for developing smart optical sensors, high-sensitivity detectors, and next-generation functional surface materials.

References

1. S. N. Varanakkottu, S. D. George, T. Baier, S. Hardt, M. Ewald and M. Biesalski, Angew. *Chem*. Int. Ed., **2013, 52, 7291-7295**.
2. I. Kitamura, K. Kato, R. B. Berk, T. Nakai, M. Hara, S. Nagano and T. Seki, *Sci*. Rep., **2020, 10, 12664**.

Presentation type：

☐ English oral competition (☐ inorganic materials, ☐ organic materials)
■ Poster competition (☐ inorganic materials, ■ organic materials)
☐ Exhibition only (☐ inorganic materials, ☐ organic materials)

生質低碳阻燃材料

羅辰懿、趙瑀蓉、嚴英瑞、王益鋐、關旭強*
南臺科技大學化學工程與材料工程系
hckuan@stust.edu.tw

摘要

近年來，隨著全球環保意識的提升以及各國火災問題頻繁發生，各產業開始意識到「防火阻燃」的重要性,，為了提高安全性，阻燃材料現在被廣泛應用在屋頂、外牆及建材中，甚至許多家具也會要求具備阻燃性能，以避免火勢在室內迅速蔓延，未來材料具備可持續性與安全性，傳統鹵素阻燃劑會釋放毒素及環境汙染等問題燃燒產生的毒煙也會對環境造成二次傷害[，聚丁二酸丁二醇酯（PBS）具備出色的機械性能、加工性和成型性，還擁有高度的抗衝擊強度、抗撕裂強度和延展性，在適當的環境下（如溫度、濕度與微生物作用），分子鏈可以分解成對環境無害的二氧化碳和水，最終回歸自然循環，成為目前主流的可降解塑膠，擁有這麼多優點，但它易燃的特性卻成了限制其應用的主要障礙，在高風險的防火場合，PBS 燃燒時產生的熱量的問題必須被解決，本研究旨在保留PBS原有優點的前提下，透過本研究的阻燃劑 PolycondN(加入 DOPO-ITA、CEPPA 與 THEIC）來增強它的各項阻燃效果，為最重要的背景與動機，本實驗將聚丁二酸丁二醇酯（PBS）分別添加 7%、8%、9%含磷量的 PolycondN 混煉成 0%、5%、10%、15%的試片，不同 PBS 含量的高分子複合材料探討其阻燃效果與其機械性質。

結果與討論

TGA

本研究透過熱重分析(TGA)的結果得知，PolycocndN, PBS 在不同含量樣品的熱穩定性在殘炭量，數據顯示材料在高溫條件下的分解行為及阻燃性能的差異，從實驗結果可觀察到裂解溫度會隨著 PolycondN 的含量增加而上升裂解溫度最低為 392.10℃上升到最高 397.6℃，顯示加入 PolycondN 確實有提高分解溫度。

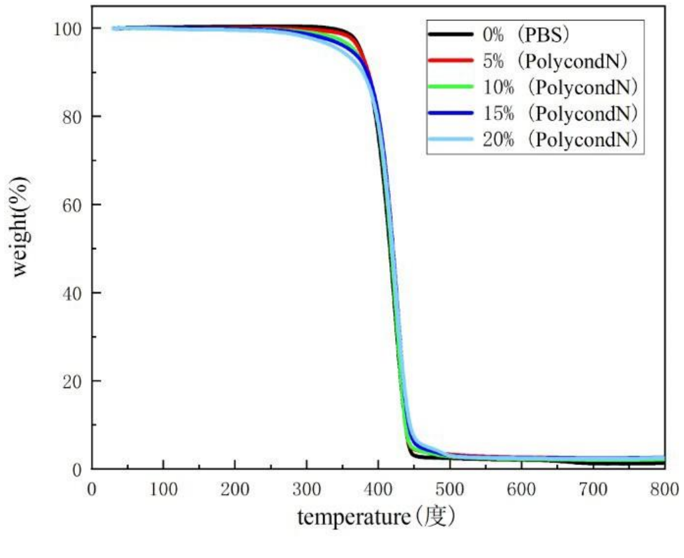

圖一 8% Polycond 對 PBS 的 TGA 結果圖

LOI 極限氧指數試驗

本研究透過極限氧指數（LOI, Limiting Oxygen Index）的測試，評估 PolycondN 阻燃劑在不同添加量下對基體材料阻燃性能的影響 ，從實驗結果觀察到加入 PolycondN 的 PBS 的阻燃條件有顯著的成效。

拉伸試驗

本研究透過伸與試驗評估了 PBS 基體中添加不同含量的 PolycondN 對材料機械性能的影響，並通過最大應力（Maximum Stress, MPa）的比較揭示了不同阻燃劑對基體結構強度的影響，結果顯示加入 PolycondN 會使 PBS 的最大應力及最大應變下降，純 PBS 的最大應力為 34MPa 加入 PolycondN 後下降至最低為 20% PolycondN 的 22MPa。

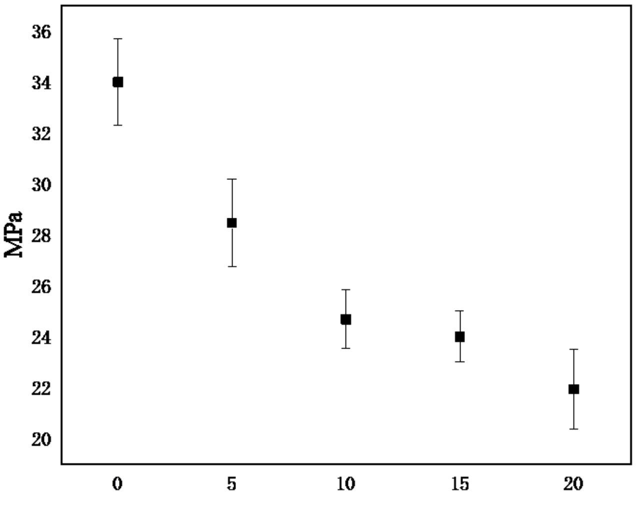

圖二 含磷量 8% PolycondN 對 PBS 的最大應力

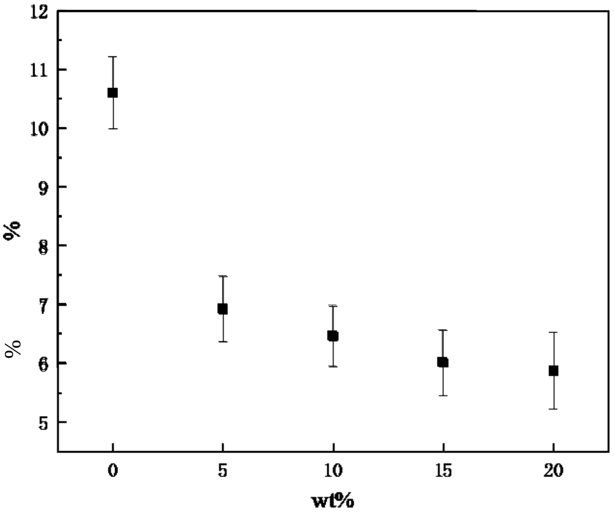

圖三 含磷量 8% PolycondN 對 PBS 的最大應變

三點彎曲試驗

本研究透過三點曲測試驗，評估 PBS 基體中添加不同含量 PolycondN 對最大曲測應力（Maximum Stress, MPa）的影響，結果顯示加入 PolycondN 會使 PBS 的最大應力及最大應變下降，純 PBS 的最大應變為 8.8MPa 加入 PolycondN 後在 5%PolycondN 有上升至 9MPa 後下降至最低為 20% PolycondN 的 8.15MPa。

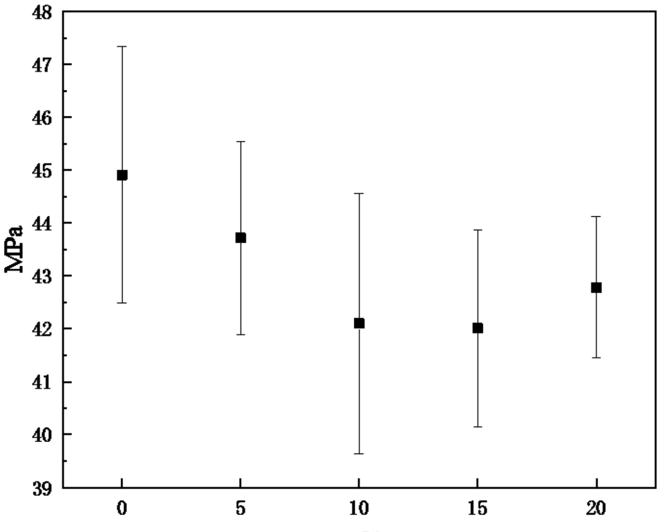

圖四 含磷量 8% PolycondN 對 PBS 的最大應力

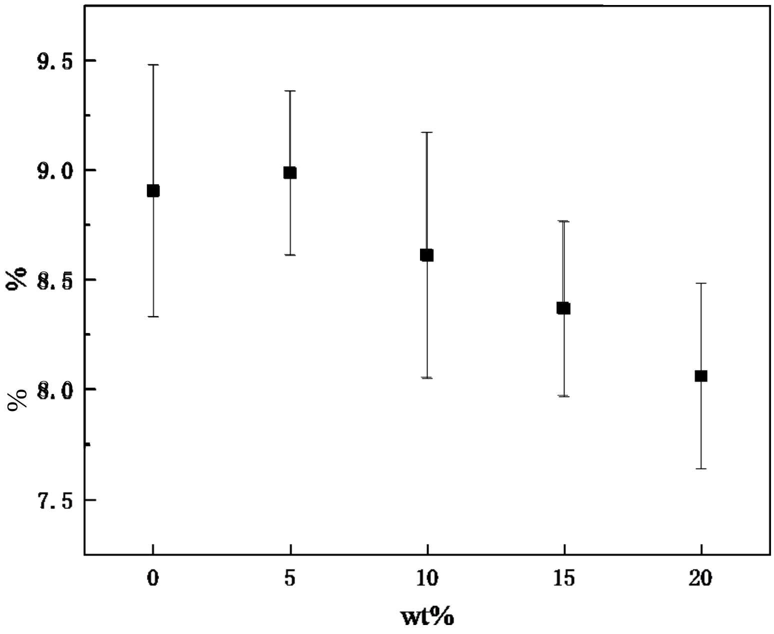

圖五 含磷量 8% PolycondN 對 PBS 的最大應變

參考文獻

[1] M. M. Velencoso, A. Battig, J. C. Markwart, B. Schartel, and F. R. J. A. C. I. E. Wurm, “Molecularfirefighting—how modern phosphorus chemistry can help solve the challenge of flame retardancy,” Angewandte Chemie International Edition, vol. 57, no. 33, pp. 10450-10467, 2018. [2] 唐見茂著 綠色複合材料 北京：中國鐵道出版社，12：223(2016)

報告型式：

□英文口頭報告競賽 (□無機材料， □有機材料)
□海報展示並參加壁報論文競賽(□無機材料， □有機材料)
■只參加海報展示 (□無機材料， ■有機材料)

Self-Assembly of Serpent Coral–Inspired Hierarchical Structures for Enhanced Heat Dissipation

Shin-Hua Lin, Hsiang-Wen Hsueh, Yun-Yu Wu, Zih-Jyun Chen, Tzu-Hsiang Kao and Hongta Yang*
Department of Chemical Engineering, National Chung Hsing University
*Correspondence: hyang@dragon.nchu.edu.tw

NSTC 112-2221-E-005-006-MY3

Abstract

In comparison with other coral, Serpent coral (Pachyseris speciosa) can survive in an ever-warming environment, owning to the integration of microscale ridge-shaped wrinkles and nanoscale concaves on their surfaces. The hierarchical structures are utilized to facilitate the formation of turbulent flow, which greatly enhances heat and mass transfer rates as a result of increased fluid mixing and boundary layer thinning effect. Bioinspired by the serpent coral, a monolayer of silica colloidal crystals is self-assembled onto anisotropic ridge-shaped micro-wrinkles, and then serves as structural templates to pattern heat-dissipation hierarchical arrays. To verify the proposed ideal, both simulated data and experimental results are conducted in this study. It is evidenced that the combination of 500 nm concaves and 115 μm wrinkles brings about a maximum heat flux 25.8 W/m·s. The serpent coral-inspired materials undoubtedly provide great potential for developing innovative applications ranging from biomedical materials, electronic devices, to optical devices.

Presentation type：

☐ English oral competition (☐ inorganic materials, ☐ organic materials)

■ Poster competition (☐ inorganic materials, ■ organic materials)

☐ Exhibition only (☐ inorganic materials, ☐ organic materials)

Azobenzene Supramolecular Hydrogels: Fabrication and Photo-responsive Properties

JingYI Lai [1], Cheng-Wei Huang[1]*
Department of Chemical and Material Engineering, National
Kaohsiung University of Science and Technology
E-mail: cwhuangs@nkust.edu.tw

NSTC 113-2221-E-992-004-MY3

Abstract

The research focuses on the use of ultraviolet light (UV, 365 nm) to induce *trans-to-cis* isomerization of the azobenzene, causing the monomer to dissociate from the β-CD cavity. This molecular dissociation triggers a localized gel-to-sol transition. By employing photomask technology, high-resolution spatial patterning can be precisely etched onto the hydrogel surface. Furthermore, this study systematically examines the effects of cross-linker ratios on the mechanical strength of the hydrogel and the quality of the resulting patterns. The results indicate that optimizing the cross-linker content is crucial for suppressing molecular diffusion and enhancing boundary definition. These findings provide significant insights for the application of smart responsive materials in microfluidic systems and precision photolithography.

Presentation type：

☐ English oral competition (☐ inorganic materials, ☐ organic materials)

■ Poster competition (☐ inorganic materials, ■ organic materials)

☐ Exhibition only (☐ inorganic materials, ☐ organic materials)

Improving Lithium-Ion Battery Performance through $LiFePO_4$ Surface Coating

Wen-Hen Chang (張文瀚), Bao-You Sun (孫寶釉), Chih-Hao Tsao (曹志豪) and Chien-Hsiang Chang (張鑑祥) *
Department of Chemical Engineering, National Cheng Kung University, Tainan, Taiwan
*Correspondence: changch@mail.ncku.edu.tw

NSTC 113-2923-E-006-002

Abstract

With the increasing demand for high-rate lithium-ion batteries in electric vehicles, optimizing charge transport at the electrode/electrolyte interface has become crucial. Sulfonate functional groups characterized by their negative charge and high hydrophilicity possess significant potential to optimize interfacial ion migration kinetics. This study investigated the behavior of ion transport in $LiFePO_4$ (LFP) cathodes by coating the active materials with 0, 2, and 4 wt%, respectively, of poly(styrene sulfonic acid) sodium salt (sPS) as an interfacial modifier. Additionally, a quasi-solid-state environment was established by incorporating 8 wt% poly(ethylene glycol) methyl ether methacrylate into a standard liquid electrolyte to improve safety and thermal stability.

Systematic evaluations revealed that the sPS coating on the LFP cathode effectively regulated interfacial charge transfer. Linear sweep voltammetry confirmed that the modified system maintained a stable electrochemical window, while electrochemical impedance spectroscopy showed that the sPS-4 wt% group achieved a 22.1% reduction in charge transfer resistance compared to the pristine LFP. Furthermore, multi-scan rate cyclic voltammetry demonstrated that sPS can enhance lithium-ion diffusion coefficient. These kinetic enhancements allowed the sPS-4wt%-coated LFP cathodes to maintain a stable discharge capacity of 30 mAh/g at a high rate of 7C. Regarding long-term stability, the sPS-4 wt% group exhibited a capacity retention of 88% after 100 cycles at 0.5C, outperforming the 87% retention of the pristine LFP group. In conclusion, the sulfonate functional group modification provided a robust ion-conductive pathway that ensured superior high-rate performance and cycling stability, offering a promising strategy for high-power quasi-solid-state battery applications.

Presentation type：

☐ English oral competition (☐ inorganic materials, ☐ organic materials)
❒ Poster competition (☐ inorganic materials, ☑ organic materials)
☐ Exhibition only (☐ inorganic materials, ☐ organic materials)

Application of catanionic vesicle/hydrophobically modified polynucleotide complexes as drug delivery carriers

Huai-Chun Lai（賴懷鈞）[1], Shih-Hsuan Yin（殷士軒）[1] , Yu-Fon Chen (陳宇楓)[2] and Chien-Hsiang Chang (張鑑祥) [1]*
[1] Department of Chemical Engineering, National Cheng Kung University, Tainan, Taiwan
[2] Master Program in Bigy, Brno, Czech Republic
*Correspondence: changch@mail.ncku.edu.tw

Abstract

To address the challenges in the stability and controlled release of nanoscale drug carriers, this study investigates the potential of complexes formed by catanionic vesicles and hydrophobically modified polynucleotides as drug delivery systems. Investigating the impact of polynucleotides and their modified derivatives on drug release kinetics, two catanionic vesicle systems characterized by different bilayer fluidities were adopted for a comparative study. The vesicles are fabricated from the ion pair amphiphiles dihexadecyldimethylammonium:hexadecylsulfate (DHDA:HS, C_{16}- C_{16}:C_{16}) and dihexadecyldimethylammonium:dodecylsulfate (DHDA:DS, C_{16}-C_{16}:C_{12}), respectively, at a total concentration of 2 mM. Catanionic vesicle/modified polynucleotide complexes were then formed by mixing the vesicles with hydrophobically modified polynucleotides. Fluorescence spectroscopy was utilized to evaluate the encapsulation efficiency and release behavior of the hydrophilic drug riboflavin after its incorporation into the complexes.

For the DHDA:HS system, vesicles coated with polynucleotides and modified polynucleotides exhibited a slower drug release behavior compared to the bare vesicles. However, the differences of drug release behaviors between the modified and unmodified polynucleotide complexes were not significant. This may be attributed to the fact that the phase transition temperature of the DHDA:HS system is significantly higher than the ambient temperature of the release experiments, thereby mitigating the influence of the hydrophobically modified carbon chains of the polynucleotide on the bilayer structures. For the DHDA:DS system, the drug release profiles indicated that the modified polynucleotide complexes exhibited a slightly higher release rate compared to the unmodified group. Based on the bilayer fluidity, it can be inferred that the insertion of hydrophobic side chains of the modified polynucleotide disrupted the structural ordering of the DHDA:DS bilayers. The increase in membrane fluidity facilitated drug diffusion across the bilayers, resulting in a higher release rate compared to the unmodified group.

To sum up, the incorporation of polynucleotides or modified polynucleotides could control the drug release rate of the catanionic vesicle systems, achieving a sustained-release effect. Furthermore, the hydrophobic side chains within the modified polynucleotides structure could further influence the release behavior by modulating the structural and physical properties of the bilayer structures.

Presentation type：

☐ English oral competition (☐ inorganic materials, ☐ organic materials)
❐ Poster competition (☐ inorganic materials, ☑ organic materials)
☐ Exhibition only (☐ inorganic materials, ☐ organic materials)

靜電紡絲製備聚乙烯醇/氧化鋅奈米纖維之量測

王晟睿[1]Nabila Fairuz Romadhona[2]范文森[1]歐信良[1,3]蕭銘華[4]張峻銘[4*]

[1] 大葉大學醫學工程學系[2]布拉維賈亞大學電機工程學系[3]大葉大學半導體學士學位學程[4]財團法人國家實驗研究院國家儀器科技研究中心

gmp@niar.org.tw

NSTC 114-2622-E-212-002

摘要

現今功能性奈米纖維材料因具備高孔隙率的特性，已被廣泛應用於藥物釋放與生物醫材等領域。聚乙烯醇（PVA）作為親水性高分子材料，具備良好的成膜性與生物相容性，然而其機械強度與功能性仍有提升空間；氧化鋅（ZnO）具有皮膚保護、防曬、傷口癒合、抗發炎及抗菌的作用，因此它。

在實際應用中，奈米纖維薄膜的表面性質（如親水性、化學官能基等）對其吸附性與生物相容性有關鍵影響。氧氣電漿表面改質技術可在不影響材料內部結構的前提下，引入極性官能基團（如羥基、羧基），進一步改變材料表面能與親水性，提升其應用潛力。

本研究旨在探討不同靜電紡絲參數（電壓、流速、收集距離）對 ZnO/PVA 纖維膜結構的影響，評估其對纖維表面、化學結構及親疏油性之影響。藉由變因控制與多項分析，期望建立一套有效提升靜電紡絲纖維表面性質的改質流程，為後續應用於食品或藥物的載體提供技術基礎。

我們藉由 OM、SEM、FTIR、XRD、EDS，以及甘油接觸角去比對不同靜電紡絲參數的氧化鋅奈米纖維薄膜各自的差異，並找出製作靜電紡絲的最佳參數。我們從各個量測的結果中可以得知纖維薄膜具有很高濃度的鋅元素。

關鍵詞：靜電紡絲、聚乙烯醇、氧化鋅水溶液、奈米纖維

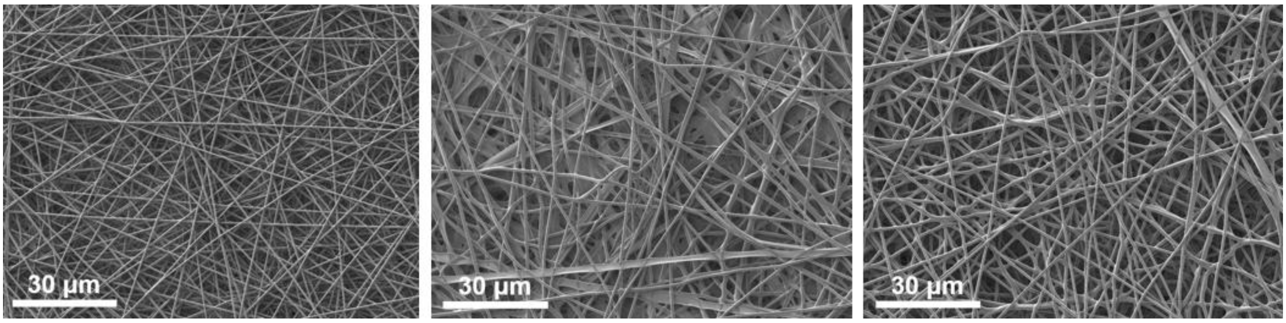

圖一、本研究利用靜電紡絲製備聚乙烯醇與聚乙烯醇/氧化鋅奈米纖維的 SEM 表面形貌

(最左為聚乙烯醇，中間與最右為聚乙烯醇/氧化鋅)

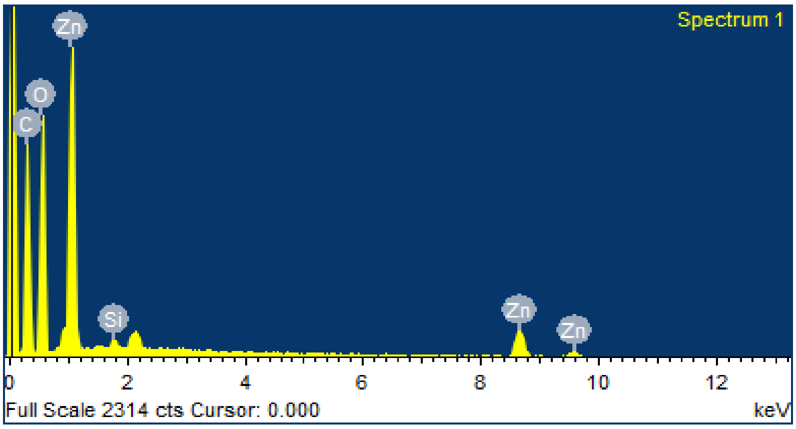

圖二、本研究利用靜電紡絲製備之聚乙烯醇/氧化鋅奈米纖維的 EDS 分析

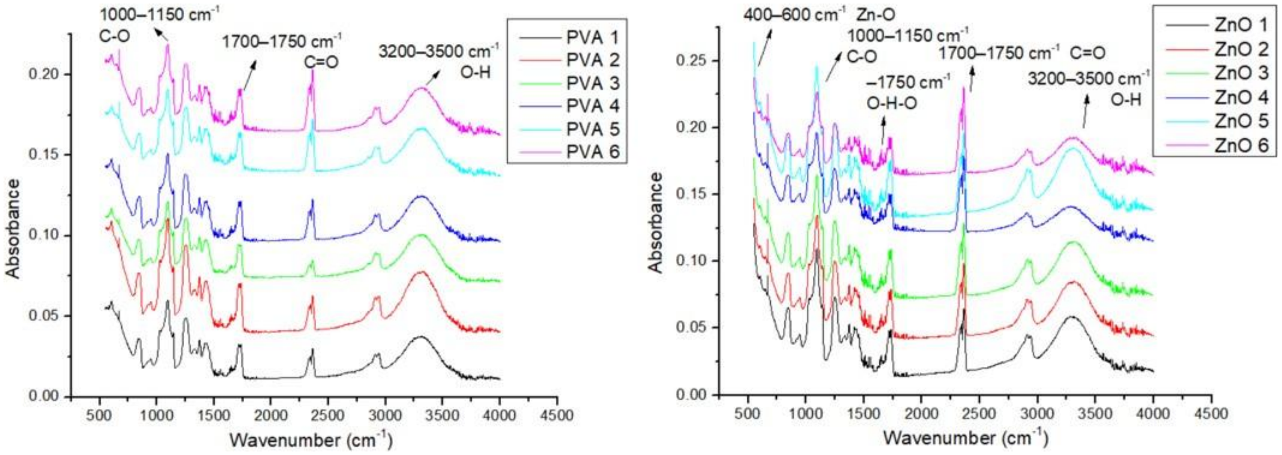

圖三、左圖為利用靜電紡絲製備不同條件之聚乙烯醇奈米纖維的 FTIR 量測結果；右圖為使用不同條件的氧氣電漿做表面處理後之聚乙烯醇/氧化鋅奈米纖維的 FTIR 量測結果

報告型式：

□英文口頭報告競賽 (□無機材料， □有機材料)
✓海報展示並參加壁報論文競賽(□無機材料， ✓有機材料)
□只參加海報展示 (□無機材料， □有機材料)

氧氣電漿表面改質對靜電紡絲 PVB 奈米纖維之表面性質影響研究

范文森[1]Stephania Angelica[2]王晟睿[1]歐信良[1,3]張峻銘[4*]
[1] 大葉大學醫學工程學系[2]布拉維賈亞大學電機工程學系[3]大葉大學半導體學士學位學程
[4] 財團法人國家實驗研究院國家儀器科技研究中心
gmp@niar.org.tw

NSTC 114-2622-E-212-002

摘要

聚乙烯醇縮丁醛（Polyvinyl butyral, PVB）為一種無定形高分子材料，是由聚乙烯醇（PVA）與丁醛經縮合反應所形成。PVB 具備優異的光學透明性、柔韌性與黏著特性，其玻璃轉移溫度約介於 60–85°C 之間，使材料在常溫下仍能維持良好的可撓性與抗衝擊能力，因此被廣泛應用於夾層安全玻璃、中間膜以及各類功能性薄膜領域。在機械性質方面，PVB 具有高延展性與良好的界面附著能力，可有效與玻璃、金屬或高分子基材形成穩定接合；在光學性質上則展現高透光率與均勻性。此外，其分子結構中含有羥基（–OH）與醚鍵（–C–O–），使其具備一定程度的化學反應活性，利於後續進行表面改質與功能化應用。

本研究以 PVB 為我們進行使用的材料，首先利用靜電紡絲（electrospinning）技術製備 PVB 奈米纖維膜。透過調控製程參數（如電壓、流速與收集距離），可成功製備出具高比表面積與均勻纖維直徑分布之 PVB 奈米纖維結構。此類奈米纖維膜因其多孔性與高表面能特性，在過濾、生醫與功能性塗層等領域具有高度應用潛力。然而，未經處理之 PVB 奈米纖維表面通常呈現疏水性，限制其在親水或生醫相關應用中的表現。

為改善其表面性質，本研究進一步結合低壓氧氣電漿（O_2 plasma）進行表面改質處理。電漿處理可在材料表面引入極性官能基（如羥基與羧基），同時改變其表面能，進而提升材料的潤濕性。由掃描式電子顯微鏡（SEM）觀察結果可知，未經電漿處理之 PVB 奈米纖維表面較為平滑；經氧氣電漿處理後，纖維表面出現明顯粗糙化現象，顯示電漿對表面結構產生蝕刻與活化作用。此外，水接觸角量測結果顯示，原始 PVB 奈米纖維呈現明顯疏水性，而經電漿改質後接觸角顯著降低，顯示其表面由疏水轉為親水性。

結合上述實驗流程與結果可以觀察到，透過低壓電漿表面改質，不僅可有效提升 PVB 奈米纖維之親水性，亦能調控其表面粗糙度與化學組成，進而改善材料的界面性質。此種改質策略對於提升 PVB 奈米纖維在抗菌敷料、空氣過濾膜（如口罩防護層）及其他生醫材料之應用具有重要潛力，亦為高分子奈米材料表面功能化提供一項具可行性與效率之方法。

關鍵字：聚乙烯醇縮丁醛、靜電紡絲、氧氣電漿、電漿表面處理

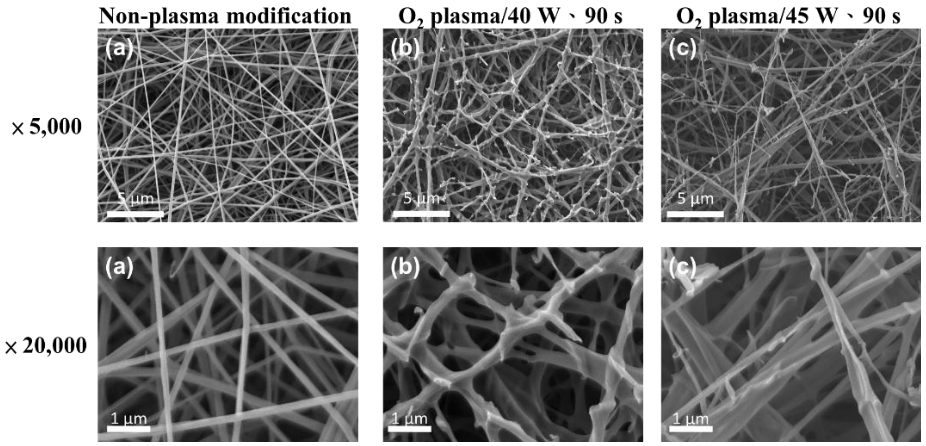

圖一、不同氧氣電漿表面改質之 SEM 圖(上層為利用 5,000 倍倍率拍攝、下圖為利用 20,000 倍倍率拍攝)

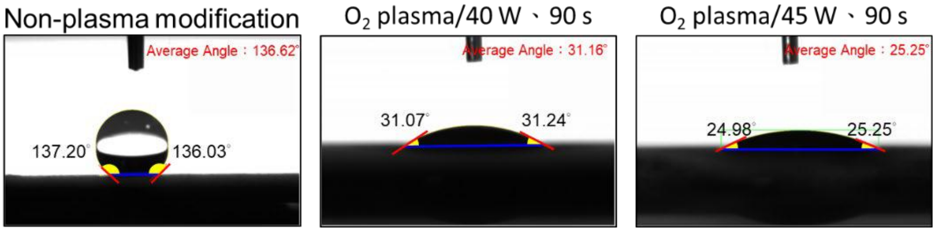
Non-plasma modification　O_2 plasma/40 W、90 s　O_2 plasma/45 W、90 s

圖二、不同氧氣電漿表面改質之接觸角圖

報告型式：

□ 英文口頭報告競賽　　　　(□ 無機材料， □ 有機材料)
✓ 海報展示並參加壁報論文競賽　(□ 無機材料， ✓ 有機材料)
□ 只參加海報展示　　　　　(□ 無機材料， □ 有機材料)

光子晶體基底增強葡萄糖可視化感測之開發

洪博修
[1] 國立高雄大學 化學工程及材料工程學系
[2] 國立高雄大學 健康及仿生科技研究中心
ycchung@nuk.edu.tw

摘要

由於飲食習慣的改變，糖尿病已是現代人需要特別防範的慢性病，一般防範發病除了使用傳統的指尖血檢測血糖水平之外，近年來針對非侵入式的淚液、汗液、和尿液中糖分的感測研究蓬勃發展，可作為一種平常保養或先期檢測的工具。本研究開發一種以共聚物乳液作為光子晶體為基礎，開發成為葡萄糖感測薄膜，在其表面塗佈硝酸銅–硼酸複合物或硼酸後，薄膜表面可與葡萄糖反應，使光子晶體表面產生的結構與顏色變化。研究中利用無乳化聚合法合成 AN-co-MMA 共聚物，並透過自組裝方式製備具有規則排列結構的一維光子晶體薄膜。將硝酸銅–硼酸複合物或硼酸塗佈於光子晶體表面，使其作為葡萄糖感測的反應層，由於葡萄糖分子中具有順式二醇結構，能夠與硼酸基團反應並形成環狀硼酸酯結構。因此，當葡萄糖接觸到塗佈硝酸銅–硼酸複合物或硼酸的光子晶體表面時，會產生化學作用，進一步使光子晶體表面形成一層覆蓋薄層，或造成奈米規則結構改變。 這些變化會影響光子晶體原本的週期性排列與光學反射行為，進而導致肉眼可觀察到的顏色變化。研究結果顯 示，AN-co-MMA 共聚物光子晶體經硝酸銅–硼酸複合物或硼酸功能化後，皆可作為葡萄糖可視化感測之反應平台。當樣品與葡萄糖溶液接觸後，葡萄糖分子所含有的順式二醇結構可與硼酸相關官能基產生特異性交互作用， 並進一步形成環狀硼酸酯結構。此反應可能使光子晶體表面生成覆蓋層，或誘導其表面微觀結構發生改變，進 而影響光子晶體原有的週期性排列、有效折射率分布與光學反射行為，最終造成肉眼可辨識之顏色變化，由實 驗觀察可知，AN-co-MMA 光子晶體在塗佈硝酸銅–硼酸複合物或硼酸後，與葡萄糖作用 5 分鐘即可產生明顯且完整的變色現象，顯示其具有快速可視化響應特性。目前此系統已可偵測濃度為 400 mg/dL 之葡萄糖溶液， 說明該材料對高濃度葡萄糖具有初步辨識能力。進一步由 SEM 觀察結果可發現，葡萄糖作用後樣品表面形貌產生明顯變化，並形成不同於原始光子晶體之微觀結構，顯示顏色變化不僅來自表面反應，也可能與光子晶體 結構調控及反射特性改變有關，整體而言，本研究成功建立以 AN-co-MMA 共聚物光子晶體為基礎，並結合硝酸銅–硼酸複合物或硼酸功能層之葡萄糖感測薄膜。此材料系統具有製備方法簡單、可視化判讀、反應時間短及應用潛力高等優點。未來若能進一步優化塗佈均勻性、感測重現性、低濃度葡萄糖辨識能力與定量分析準確性， 將有機會發展為應用於尿液葡萄糖檢測、糖尿病初步篩檢或居家健康監測之光子晶體可視化感測器。

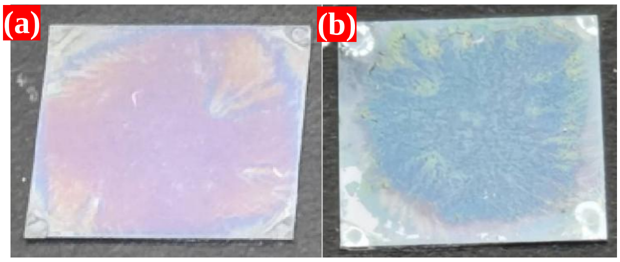

Figure1. Color changes of the AN-co-MMA photonic crystal coated with a copper nitrate–boric acid complex for glucose-sensing(a)before glucose sensing.(b)after sensing 400 mg/dL glucose.

Figure2. Color changes of the AN-co-MMA photonic crystal coated with boric acid for glucose sensing(a)before glucose sensing.(b)after sensing 400 mg/dL glucose.

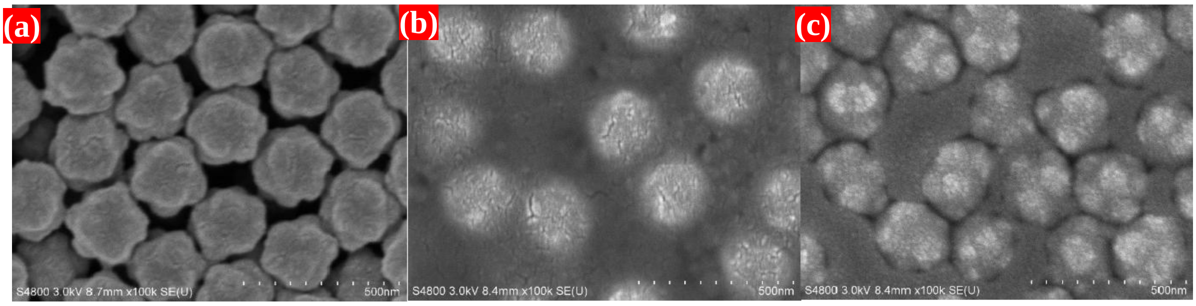

Figure3. Surface morphology of AN-co-MMA photonic crystals observed by SEM at 100K magnification(a)pristine AN-co-MMA.(b) copper nitrate–boric acid complex-coated AN-co-MMA after reaction with glucose.(c)boric acid-coated AN-co-MMA after reaction with glucose.

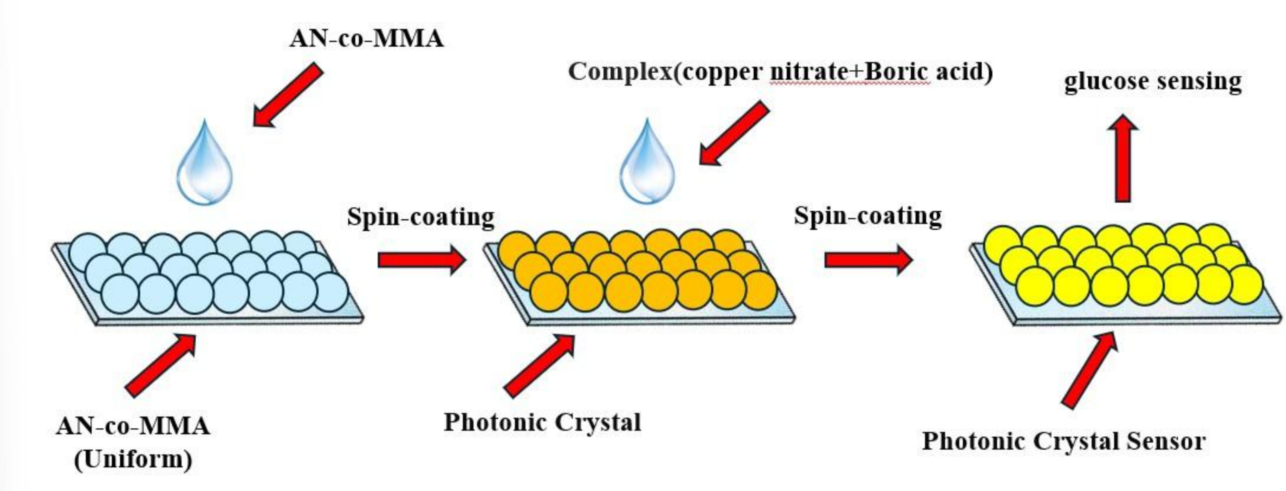

Figure4. Photonic crystal sensor fabrication process

參考文獻

1. Chen, C.; Dong, Z.-Q.; Shen, J.-H.; Chen, H.-W.; Zhu, Y.-H.; Zhu, Z.-G., 2D photonic crystal hydrogel sensor for tear glucose monitoring. ACS Omega 2018, 3, 3211-3217.
2. Springsteen, G.; Wang, B., A detailed examination of boronic acid-diol complexation. Tetrahedron 2002, 58, 5291-5300.
3. Toghill, K. E.; Compton, R. G., Electrochemical non-enzymatic glucose sensors: a perspective and an evaluation. Int. J. Electrochem. Sci. 2010, 5, 1246-1301.
4. Wu, X.; Soeda, S.; Nomoto, T.; Nose, T.; Liu, Y.; Kimura, S.; Onodera, T.; Ikezaki, H.; Toko, K., A potentiometric sweetness sensor for sugars using lipid/polymer membranes containing boronic acid. Journal of Food Composition and Analysis 2025, 148, 108396

報告型式：

□英文口頭報告競賽 (□無機材料， □有機材料)
■海報展示並參加壁報論文競賽(□無機材料， ■有機材料)
□只參加海報展示 (□無機材料， □有機材料)

市售一型光起始劑於壓克力單體光聚合與聚苯乙烯光降解特性之研究

楊瀚翔、田博鋐、陳永忠*
國立高雄科技大學化學工程材料系通訊作者
chenyc@nkust.edu.tw

摘要

本研究旨在探討市售第一型光起始劑(如下圖一)於壓克力單體光聚合與聚苯乙烯光降解中的應用特性與反應行為。評估不同一型光起始劑在壓克力單體(如 TMPTA 三羥甲基丙烷三丙烯酸酯)中的聚合效率，並分析其對反應速率與轉化率的影響。同時，藉由引入氧氣與偕同酸觸媒反應條件，使一型光起始劑轉而變成光降解催化劑進一步探討其在聚苯乙烯光降解過程中的機制與降解效率。。實驗結果顯示，不同結構之第一型光起始劑在光吸收能力與裂解效率上具有顯著差異，進而影響其在光聚合與光降解反應中的表現。如光起始劑在氧氣與酸性環境下產生的自由基，可將聚苯乙烯降解為高附加價值之化學品（如苯甲酸），以達成廢棄物資源化之目標。藉由透過 HPLC 圖譜分析發現，不同系列之光起始劑對聚苯乙烯之降解效率有顯著差異。實驗結果顯示，在 20 小時的光照條件下，光起使劑 754 表現出最佳的催化活性，其苯甲酸產率達到 15.9%。實驗證實，選用適當系列之光起始劑能有效促進聚苯乙烯轉化為苯甲酸。此系統具有反應條件溫和且操作簡便之優點，為塑膠回收轉化研究提供重要參考。本研究成果可作為一型光起始劑/光降解劑之結構設計與偕同參考結果之重要參考。

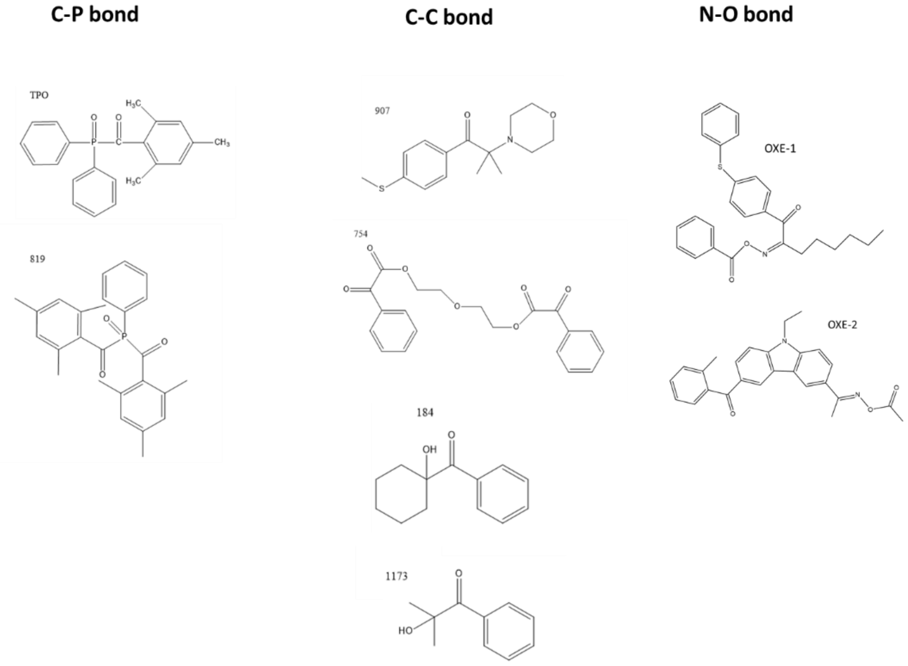

圖一、一型光起始劑/光降解劑結構示意圖

報告型式：

□英文口頭報告競賽　(□無機材料，□有機材料)
■海報展示並參加壁報論文競賽(□無機材料，■有機材料)
□只參加海報展示　(□無機材料，□有機材料)

Self-Assembly of Antifouling Wavy-Taco-Shell Arrays Inspired by Hierarchically Wrinkled Shark Scales

Hsiang-Wen Hsueh [1], Zi-Xuan Chen [2] and Hongta Yang＊
國立中興大學 化學工程學系
hyang@dragon.nchu.edu.tw

NSTC 112-2221-E-005-006-MY3

Abstract

Shark skins are covered with riblet-like dermal denticles, which can effectively manipulate boundary layer flows and reduce the adhesion of biomaterials. Remarkably, the geometry of shark scales varies substantially across species and body regions, bringing about different antifouling performances. Inspired by the shark skins, different hierarchically wrinkled structures are self- assembled, and employed as antifouling coatings. In addition, the structural geometry effect on the antifouling functionalities is evaluated. It is believed that the bioinspired structure arrays are promising to develop a range of biomedical applications such as wound cares, surgical materials, and so on.

References

[1] Gabler-Smith, M. K.; Lauder, G. V. Ridges and Riblets: Shark Skin Surfaces versus Biomimetic Models. Frontiers in Marine Science 2022, 9, 81.

[2] Dai, W.; Alkahtani, M.; Hemmer, P. R.; Liang, H. Drag-Reduction of 3D Printed Shark-Skin-like Surfaces. Friction 2018, 7, 603−612.

[3] Wang, Q., & Zhao, X. (2015). A Three-Dimensional Phase Diagram of Growth-Induced Surface Instabilities. Scientific Reports 2015, 5 (1), 8887.

[4] Greco, F.; Bellacicca, A.; Gemmi, M.; Cappello, V.; Mattoli, V.; Milani, P. Conducting Shrinkable Nanocomposite Based on Au-Nanoparticle Implanted Plastic Sheet: Tunable Thermally Induced Surface Wrinkling. ACS applied materials & interfaces 2015, 7 (13), 7060–7065.

[5] Yang, S.; Khare, K.; Lin, P.-C. Harnessing Surface Wrinkle Patterns in Soft Matter. Advanced Functional Materials 2010, 20 (16), 2550–2564.

[6] Zhao, Z.; Gu, J.; Zhao, Y.; Guan, Y.; Zhu, X. X.; Zhang, Y. Hydrogel Thin Film with Swelling-Induced Wrinkling Patterns for High-Throughput Generation of Multicellular Spheroids. Biomacromolecules 2014, 15 (9), 3306–3312.

[7] Ghezzi, F.; Pedroni, M.; Janez Kovač; Causa, F.; Cremona, A.; Anderle, M.; Caniello, R.; Pietralunga, S. M.; Vassallo, E. Unraveling the Mechanism of Maskless Nanopatterning of Black Silicon by CF4/H2 Plasma Reactive-Ion Etching. ACS Omega 2022, 7 (29), 25600–25612.

[8] Nguyen, D. H. K.; Bazaka, O.; Bazaka, K.; Crawford, R. J.; Ivanova, E. P. Three-Dimensional Hierarchical Wrinkles on Polymer Films: From Chaotic to Ordered Antimicrobial Topographies. Trends in Biotechnology 2020, 38 (5), 558–571.

Presentation type：

☐ English oral competition (☐ inorganic materials, ☐ organic materials)
■ Poster competition (☐ inorganic materials, ☐ organic materials)
☐ Exhibition only (☐ inorganic materials, ☐ organic materials)

Interface-Engineered Charge Transport in $CsPbBr_3$-Integrated MWCNTs/PDMS Composites for High-Performance Pressure Sensing

Chung-Che Tsai[1], Kuan-Jie Wu[1] and Jia-Xing Zhou[1], Ji-Hao Li[2], Chun-Yuan Huang[2] and Ta-Cheng Wei[1]*
[1]Department of Chemical and Materials Engineering, Southern Taiwan University of Science and Technology, Tainan, 710, Taiwan
[2]Department of Applied Science, National Taitung University, Taitung 950, Taiwan
*Correspondence: tcwei@stust.edu.tw
NSTC 113-2221-E-143 -004 -MY2

Abstract

Flexible pressure sensors have attracted significant attention due to their promising applications in wearable electronics, human–machine interfaces, and artificial electronic skin. However, achieving both high sensitivity and stable electrical responses remains challenging, as conductive nanomaterials tend to aggregate within polymer matrices due to strong van der Waals interactions. This aggregation disrupts the continuity of conductive networks and limits effectively charge transport pathways. In this study, a porous piezoresistive sensor based on multi-walled carbon nanotubes (MWCNTs), polydimethylsiloxane (PDMS), and $CsPbBr_3$ perovskite nanocrystals was developed and further integrated into a matrix-type pressure sensing system for real-time monitoring and spatial pressure mapping. Surface-modified MWCNTs and $CsPbBr_3$ nanocrystals were co-incorporated into the porous PDMS composite, where $CsPbBr_3$ serves as a charge-transport mediator that effectively bridges adjacent nanotubes, thereby enhancing the continuity and stability of the conductive network. [1, 2] The composite was subsequently fabricated into a sensing array using a floating-electrode configuration, assembled with polyethylene terephthalate (PET) films and copper electrodes. From a mechanistic perspective, the incorporation of $CsPbBr_3$ serves as a crucial factor in improving the electrical performance of the composite. Owing to its high carrier mobility and superior charge transport capability, $CsPbBr_3$ effectively reduces the tunneling barrier between separated MWCNT conductive networks and facilitates carrier hopping across conductive pathways. Furthermore, the lattice distortion in $CsPbBr_3$ induces local polarization, which promotes carrier redistribution and enhances charge transport kinetics. These effects contribute to improved electrical conductivity and dynamic response behavior. [3-5] The sensing array was integrated with an Arduino-based data acquisition system, enabling real-time measurement and visualization of pressure distribution. Experimental results indicate that acid treatment significantly increases the defect density of MWCNTs and improves their dispersion and interfacial compatibility within the PDMS matrix, thereby enhancing electrical transport efficiency. The introduction of $CsPbBr_3$ further improves charge transfer efficiency and stabilizes the conductive network. Compared with samples without $CsPbBr_3$, the composite exhibits superior electrical performance and structural stability. The fabricated sensor demonstrates excellent pressure sensing performance, with the relative resistance change ($\Delta R/R_0$) increasing from 0.39 to 0.61, and a response time of less than 0.4 s, representing an improvement of approximately 56.4% compared with untreated samples. In addition, the synergistic interaction between the MWCNT conductive network and $CsPbBr_3$ charge transport pathways significantly enhances signal transmission efficiency and system stability. The sensing array enables real-time spatial pressure mapping with strong practical applicability. The synergistic integration of surface-modified MWCNTs and $CsPbBr_3$ improves sensitivity, response speed, and electrical stability, providing a viable strategy for high-performance flexible pressure sensing systems.

References

[1] T. Ito and K. Katayama, "Charge Carrier Dynamics in Mixed-Dimensional $CsPbBr_3$ Perovskites: Transition from 2D to 3D Architectures," The Journal of Physical Chemistry C, vol. 129, no. 6, 3136–3144, 2025.

[2] X. Han et al., "Carrier mobility enhancement in (121)-oriented $CsPbBr_3$ perovskite films induced by the microstructure tailoring of PbBr2 precursor films," ACS Applied Electronic Materials, vol. 3, no. 1, 373–384, 2020.

[3] Y. He et al., "CNT/PDMS conductive foam-based piezoresistive sensors with low detection limits, excellent durability, and multifunctional sensing capability," Sensors and Actuators A: Physical, vol. 358, 114408, 2023.

[4] Y. Song et al., "Highly compressible integrated supercapacitor–piezoresistance-sensor system with CNT–PDMS sponge for health monitoring," small, vol. 13, no. 39, 1702091, 2017.

[5] H.-C. Jung et al., "CNT/PDMS composite flexible dry electrodesfor long-term ECG monitoring," IEEE Transactions on Biomedical Engineering, vol. 59, no. 5, 1472–1479, 2012.

Presentation type：

☐ English oral competition (☐ inorganic materials, ☐ organic materials)
■ Poster competition (■ inorganic materials, ☐ organic materials)
☐ Exhibition only (☐ inorganic materials, ☐ organic materials)

Heterogeneous Catalytic Pre-Treatment and Mechanical Self-Circulation Defoaming for Aluminum Sulfate Production from Industrial Waste Acid

Kuan-Jie Wu[1] and Jia-Xing Zhou[1], Chih-Chiang Yang[2], Tai-Cheng Chen[3] and Ta-Cheng Wei[1]*
[1]Department of Chemical and Materials Engineering, Southern Taiwan University of Science and Technology, Tainan, 710, Taiwan
[2] Department of Electrical Engineering, National United University, Miaoli 36003, Taiwan,Taiwan
[3]Department of Material Research, National Atomic Research Institute, Taoyuan 325207, Taiwan.
*Correspondence: tcwei@stust.edu.tw

NSTC 114-2221-E-239-040 and NSTC 114-2622-E-239-006.

Abstract

With the rapid development of semiconductor and advanced electronic manufacturing processes, high-tech industries widely use a highly oxidative acid mixture composed of sulfuric acid and hydrogen peroxide for wafer and material surface cleaning. These processes generate a large volume of waste sulfuric acid containing hydrogen peroxide. If this waste stream is directly reacted with aluminum hydroxide to be converted into aluminum sulfate, the high concentration of residual hydrogen peroxide in the waste liquid will undergo severe spontaneous decomposition due to the exothermic reaction, instantly releasing a massive amount of oxygen. These fine bubbles, encapsulated in the liquid film of the highly viscous slurry, form an extremely stable foam layer. This not only causes a severe risk of overflow but also forces the production line to significantly reduce the effective loading capacity to 40%, thereby becoming the most critical technical bottleneck hindering the industrial valorization of waste acid. To overcome this disadvantage in large-scale production caused by excessive gas generation and foaming, this study proposes and systematically evaluates a dual suppression strategy that integrates pre-treatment degradation and in situ dynamic suppression. A heterogeneous catalytic pre-treatment is first introduced using zeolite with high surface area and microporous structure to promote the decomposition of hydrogen peroxide in acidic waste streams, thereby reducing gas evolution prior to the main reaction. In addition, a mechanical self-circulation defoaming system is implemented to suppress foam formation during the reaction process.[1-3] This physical approach employs fluid-induced shear forces to disrupt the gas–liquid interface, preventing foam accumulation without chemical additives. The combined strategy enhances process stability, reduces secondary contamination, and enables scalable industrial operation. Through the synergistic effect of the dual strategies, the reactor loading capacity increases from 40% to over 70%, ensuring stable continuous operation. Furthermore, SEM, XRD, and FT-IR analyses confirm that the converted aluminum sulfate exhibits high purity, demonstrating its potential as a water treatment coagulant. This study addresses a critical challenge in waste liquid management and promotes the reintegration of industrial waste into the supply chain, supporting circular economy and zero-waste goals.

References

1. N. S. Deshpande and M. Barigou, Chem. Eng. Process. Process Intensif., vol. 39, no. 3, pp. 207–217, 2000.
2. A. A. Ingle et al., Environ. Sci. Pollut. Res., vol. 29, no. 57, pp. 86468–86484, 2022.
3. A. I. Dosumu et al., Chem. Eng. Sci., vol. 319, p. 122286, 2025.

Presentation type：

☐ English oral competition (☐ inorganic materials, ☐ organic materials)
☐ Poster competition (☐ inorganic materials, ☐ organic materials)
■ Exhibition only (■ inorganic materials, ☐ organic materials)

Enhanced Piezoresistive Pressure Sensors Based on Wave-Assisted HCl-Modified Carbon Nanotube/PDMS Composites for AIoT Applications

Si-Hsiung Wang[1], Yong-En Yang[1], Tzu Chiu[1], Chen-Chiang Huang[1] and Ta-Cheng Wei[1*]
[1]Department of Chemical and Materials Engineering, Southern Taiwan University of Science and Technology, Tainan, 710, Taiwan
*Correspondence: tcwei@stust.edu.tw

Abstract

Flexible porous polymeric systems have emerged as promising platforms for next-generation pressure sensors due to their intrinsic deformability, lightweight characteristics, and tunable microstructures. By incorporating conductive nanomaterials into these otherwise insulating porous matrices, functional nanocomposites with enhanced electromechanical coupling can be realized. However, achieving both high sensitivity and stable electrical output remains a persistent challenge, primarily due to the strong van der Waals interactions between conductive nanofillers such as carbon nanotubes (CNTs), which induce aggregation within polymer matrices. This aggregation disrupts the continuity of conductive networks and significantly hinders efficient charge transport.[1-5] To address this limitation, this study develops a porous piezoresistive sensor based on polydimethylsiloxane (PDMS) integrated with chemically modified CNTs and further incorporates the device into a matrix-type sensing system for real-time pressure monitoring and spatial mapping. These results demonstrate that acid-induced surface modification effectively increases defect density and enhances inter-tube electrical connectivity, thereby facilitating improved charge transport throughout the composite. Among the investigated conditions, treatment with 5 M HCl achieves an optimal balance between electrical conductivity and structural integrity. As a result, the optimized sensor exhibits markedly enhanced performance, with the relative resistance change increasing from 0.39 to 0.53 and a rapid response time below 0.5 s, corresponding to an improvement of approximately 36.0% compared to untreated samples. These results reveal that rational surface engineering of CNTs within porous polymer matrices represents an effective strategy to overcome dispersion limitations and enhance piezoresistive performance, thereby providing a scalable pathway toward high-performance flexible pressure sensing systems for intelligent AIoT-based sensing applications.

References

[1] C. Xu et al., "Flexible pressure sensors in human–machine interface applications," Small, vol. 20, no. 15, 2306655, 2024.

[2] J.-w. Zhang, Y. Zhang, Y.-y. Li, and P. Wang, "Textile-based flexible pressure sensors: A review," Polymer Reviews, vol. 62, no. 1, 65–94, 2022.

[3] Z. Qiao, A. Wei, K. Wang, N. Luo, and Z. Liu, "Study of flexible piezoresistive sensors based on the hierarchical porous structure CNT/PDMS composite materials," Journal of Alloys and Compounds, vol. 917, 165503, 2022.

[4] M. A. Jamshed, K. Ali, Q. H. Abbasi, M. A. Imran, and M. Ur-Rehman, "Challenges, applications, and future of wireless sensors in Internet of Things: A review," IEEE Sensors Journal, vol. 22, no. 6, 5482–5494, 2022.

[5] A. S. Fiorillo, C. D. Critello, and S. A. Pullano, "Theory, technology and applications of piezoresistive sensors: A review," Sensors and Actuators A: Physical, vol. 281, 156–175, 2018.

Presentation type：

☐ English oral competition (☐ inorganic materials, ☐ organic materials)

■ Poster competition (■ inorganic materials, ☐ organic materials)

☐ Exhibition only (☐ inorganic materials, ☐ organic materials)

火花電漿兩步燒結對超高溫陶瓷複合材料的緻密化行為和性能

成功大學材料所
李權脩
kdjames889@gmail.com

摘要

Starship 火箭這類的重型傳輸載具和超音速飛行載具普遍遇到的問題是，當飛行器往返大氣層中，機身的鼻錐(飛行器尖端)和機翼的部分會因為音速的飛行導致空氣的劇烈壓縮，讓機體表面瞬間高達超過 1500°C的溫度甚至更高。在這種極端高溫下，機身表面常會出現材料剝落或嚴重的燒蝕現象，如果防護不到位，高溫會直接威脅到內部的支撐結構，最嚴重的情況就是導致機身整體結構失效，造成毀滅性的意外。目前的解決方案，像是 SpaceX 在星艦上貼附的數千塊隔熱陶瓷磚，雖然能起到一定的絕熱效果，但它的缺點也非常明顯。這些材料本質上比較脆弱，且主要是靠黏上去的，並不能作為承重結構。在頻繁且高強度的飛行需求下，這些隔熱磚很容易因為震動或熱脹冷縮而掉落。對於馬斯克追求「像飛機一樣快速翻新」的商業模式來說，這種維護周期長、無法滿足快速周轉的材料，顯然已經跟不上未來高效率的太空物流需求。

這正是為甚麼我們需要超高溫陶瓷(Ultra-High Temperature Ceramics, UHTCs)的原因，這類陶瓷具有極高的熔點(2000°C以上)，優異的熱穩定性、抗氧化、抗衝擊能力的先進陶瓷材料。在物理性質方面，相較於一般氧化物陶瓷有很高的熱導係數，以及比金屬還要低的熱膨脹係數，如此性質能提升結構材料的散熱效率，且避免因冷熱交替導致材料體積劇烈改變。在機械性質方面，有極高的硬度(>15GPa)和耐磨性，適合在高負載、高速轉動的引擎下使用。在耐熱性質方面，有良好的熱穩定性，搭配其他複合材料能提升抗熱震性和抗燒蝕能力。超高溫陶瓷主要成分由早期過度金屬和類金屬、非金屬所組成的硼化物(Borides)、碳化物(Carbides)、氮化物(Nitrides)。此類特殊結構材料主要設計用於極端高溫和惡劣環境下，特別是在航太領域，例如火箭噴嘴、機體前緣和發動機部件等需要承受超高溫的地方，依然能夠保持結構完整性、承受高低溫度的反覆震盪。

然而，儘管超高溫陶瓷擁有這些優異性質，目前仍遇到兩大困難的問題，難燒結的特性和陶瓷材料的脆性。強共價鍵的束縛和超高溫的熔點造成原子在晶格內的擴散係數極低，而擴散是燒結的驅動力，擴散慢意味著物質遷移困難，材料難以緻密，孔隙不好排出。因此，要將材料燒結至完全緻密需要提高溫度花費很長的時間(數十小時)，這種長時間的高熱輸入會無可避免地導致晶粒粗化(Grain coarsening)，而根據 Hall-Petch 關係，粗大晶粒會顯著降低材料機械強度和抗熱震性能。另外，為了解決陶瓷的低斷裂韌性，通常會加入第二相作為輔助，達到釘扎作用(Pinning effect)，阻礙裂紋擴展，或通過為裂紋增韌機制提高材料的斷裂韌性，但如何在達到全緻密的前提下，將晶粒控制在細小甚至奈米尺度，仍是材料科學的一大挑戰。

隨著燒結技術的進化，火花電漿燒結技術(Spark Plasma Sintering, SPS)誕生，是一種高效、快速的粉末冶金燒結技術，正好改善了無壓、熱壓燒結技術需要大量時間的短版，在幾分鐘內可以完成緻密化。因此，本篇研究手法突破上述限制，結合先進的技術(SPS)加上優化的製程(TSS)，利用 SPS 極高的升溫速率(300°C/min)，能讓 UHTC 粉體迅速越過易發生表面擴散與無效粗化的低溫區，直接到達高溫區(T_1)。隨後，利用 SPS 的快速冷卻能力精準進入低溫區(T_1)進行緻密化。在協同效應下，SPS 解決了傳統 TSS 製程耗時過長的缺點，TSS 更避免了材料在高溫 SPS 下晶粒粗化的風險，可說是緻密化同時保有次微米甚至是奈米的微觀結構。將深入探討此優化製程對超高溫陶瓷的微觀變化，期望開發出兼具超高耐熱性且優異機械性質強度的結構材料，解決未來在航空太空等熱防護難題。

參考文獻

[1] E. Wuchina, E. Opila, M. Opeka, B. Fahrenholtz, and I. Talmy, "UHTCs: Ultra-High Temperature Ceramic Materials for Extreme Environment Applications," The Electrochemical Society Interface, vol. 16, no. 4, p. 30, 2007/12/01 2007.

[2] B. R. Golla, A. Mukhopadhyay, B. Basu, and S. K. Thimmappa, "Review on ultra-high temperature boride ceramics," Prog. Mater Sci., vol. 111, p. 100651, 2020/06/01/ 2020.

[3] A. S. Mukasyan and A. S. Rogachev, "Combustion synthesis of ultra-high temperature ceramics: Review," International Journal of Applied Ceramic Technology, vol. 22, no. 6, p. e70044, 2025/11/01 2025.

[4] Bulletin. (2025, 2026/02/23). Industrial applications of ultrahigh-temperature ceramics [Online]. Available: https://bulletin.ceramics.org/wp-content/uploads/2025/01/Bulletin_Vol_104_No_01_Jan_Feb_2025.pdf.

[5] R. M. d. Rocha, F. F. Sene, M. d. O. Juliani, and C. O. Davi, "Effect of ZrB2Particle Size on Pressureless Sintering of ZrB2- ß-Sic Composites," Journal of Aerospace Technology and Management, vol. 11, 2019.

[6] T. Zhu, L. Xu, X. Zhang, W. Han, P. Hu, and L. Weng, "Densification, microstructure and mechanical properties of ZrB2–SiCw ceramic composites," J. Eur. Ceram. Soc., vol. 29, no. 13, pp. 2893-2901, 2009/10/01/ 2009.

[7] M. Thompson, W. G. Fahrenholtz, and G. Hilmas, "Effect of Starting Particle Size and Oxygen Content on Densification of ZrB2," J. Am. Ceram. Soc., vol. 94, no. 2, pp. 429-435, 2011/02/01 2011.

[8] F. M. a. A. Bellosi. (2003). Oxidation of ZrB2-Based Ceramics in Dry Air [Online]. Available: https://iopscience.iop.org/article/10.1149/1.1618226.

[9] S. Zhu, "Densifification, microstructure, and mechanical properties of zirconium diboride based ultra-high temperature ceramics," 2008.

[10] R. Zhang, F. Guo, W. Zhang, F. Pan, and X. Zhang, "Spatial toughening mechanism of ZrB2-SiC spiral fibers composites up to 1500 °C via SEVNB with femtosecond lasers and 3D-XRM methods," Ceram. Int., vol. 51, no. 1, pp. 54-71, 2025/01/01/ 2025.

報告型式：

□英文口頭報告競賽 (□無機材料， □有機材料)
■海報展示並參加壁報論文競賽(■無機材料， □有機材料)
□只參加海報展示 (□無機材料， □有機材料)

金屬射出成形之 17-4 PH 不銹鋼添加鎳與硼對顯微組織與機械性質的影響

蕭仁堃[1]，吳明偉[2]
國立臺北科技大學材料科學與工程研究所[1]，國立臺北科大學材料與資源工程系[2]
蕭仁堃，as0938870270@gmail.com

摘要

17-4 PH 不銹鋼為金屬粉末射出成形(metal injection molding, MIM)常用的材料，已在 3C 零組件中獲得廣泛使用。液相燒結為兼具經濟效益與高效緻密化之燒結技術，硼元素具有明顯促進鐵基材料液相燒結的效果。鎳元素可提升硬化能，且為金屬粉末領域常用的合金元素。本研究的主軸在探討硼與鎳元素對 MIM 17-4 PH 不銹鋼之顯微組織及機械性能的影響，研究中在 17-4 PH 添加 2.0 wt%鎳粉與 0.6 wt%硼粉，其燒結溫度分別為 1280 ℃與 1240 ℃，在燒結後均進行 480 ℃時效處理。

結果顯示 17-4 PH 在添加 2.0 wt%鎳粉後，透過 XRD 鑑定發現其為 BCC 與 FCC 之雙相組織，因此可知因為鎳雖可提升硬化能，但因為鎳也是沃斯田鐵穩定元素，所以導致材料中出現明顯的沃斯田鐵存在。17-4 PH+2Ni 的燒結密度為 7.42 g/cm^3，硬度為 27 HRC，最大抗拉強度與延伸率分別為 1080 MPa 與 8.7 %。

在 17-4 PH+0.6B 方面，經由電子背向散射繞射(EBSD)分析得知基地相為麻田散鐵，並含有 1.1 %的殘留沃斯田鐵，晶界區域則可觀察到 Fe_2B 硼化物。進一步透過電子微探儀(EPMA)之元素分布圖證實晶界區域之鉻、鐵、硼比例分別為 43 at%、27 at%、29 at%，因此晶界區域的硼化物為鐵與鉻之複合硼化物$(Cr,Fe)_2B$。17-4 PH 在添加 0.6 wt%B 後的燒結密度 7.60 g/cm^3，硬度為 47 HRC，抗拉強度為 1453 MPa，延展率為 2.1 %。因此 17-4 PH+0.6B 跟 17-4 PH+2Ni 相比，17-4 PH+0.6B 具有較高的燒結密度、硬度、抗拉強度，但延性則較 17-4 PH+2Ni 低。

報告型式：

□英文口頭報告競賽 (□無機材料， □有機材料)
■海報展示並參加壁報論文競賽(■無機材料， □有機材料)
□只參加海報展示 (□無機材料， □有機材料)

2026 功能性材料研討會暨國科會專題研究計畫成果發表會 – 南臺化材 Date : 2026/5/29

摻雜鋁對鈣鈦礦氧化物(Sr,Ba)$Mn_{1-y}Al_yO_3$ 作為超級電容電極材料電化學性能之影響

洪久翔 林炯棟* 蘇致豪
義守大學材料科學與工程學系
jdllin@isu.edu.tw

摘要

本研究使用 Pechini 法製備不同 Al 含量之鈣鈦礦氧化物(Sr,Ba)$Mn_{1-y}Al_yO_3$ 粉體，並作為超級電容之電極材料。經 850°C煅燒後，主要相為 $SrMnO_3$，次要相為 $Sr_8Al_{28}O_{50}$，與少量的 $SrCO_3$；隨著 Al 摻雜量增加，$Sr_8Al_{28}O_{50}$ 的含量增加。SEM 分析顯示 Al 的摻雜對顆粒形狀與尺寸並無明顯影響。Al 含量為 0.2~0.4 時，有較高的比電容。掃速為 10 mV/s 時，在負電壓窗口(-1~0 V)下，y= 0.2 有最高的比電容 41.7 F/g；在正電壓窗口(0~0.5 V)下，y= 0.4 有最高的比電容 71.0 F/g。根據交流阻抗分析與等效電路擬合結果顯示，在 y=0.4 有最低的電荷轉移電阻與最高的低頻質量電容。Al 的摻雜並不會影響雙電層電容的貢獻，當 Al 摻雜量少量增加時，含 Al 鈣鈦礦相提高了整體比電容，然而進一步提高 Al 摻雜量後，$Sr_8Al_{28}O_{50}$ 相含量增加，而相對高比電容的鈣鈦礦相含量減少，造成電極比電容降低。因此，對於低 Al 摻雜量(<0.6)，B 位同時摻雜 Al 與 Mn 可發揮協同效應，其中 $Sr_{0.8}Ba_{0.2}Mn_{0.6}Al_{0.4}O_3$ 有最佳的比電容性能。

一、前言

近年研究顯示，鈣鈦礦氧化物（ABO_3）因其結構穩定性、組成可調性、高濃度氧空位及優異的氧化還原可逆性，被視為極具潛力的超級電容器電極材料[1, 2]，尤其適用於 0～0.5 V 或 -1.0～0 V 的電壓窗口[3, 4]。此類材料的儲能機制主要依賴氧陰離子嵌入（Oxygen anion intercalation）所產生的擬電容(Pseudocapacitance)行為，其中鍶基鈣鈦礦氧化物即透過此機制實現陰離子電荷的儲存。在超級電容器（Supercapacitors）的發展中，非對稱結構因具備更寬的充放電電壓窗口與較高的能量密度，成為提升儲能性能的重要方向[3]。然而，目前可與正極材料匹配的寬電壓負極選項仍有限，導致無法充分發揮其理論效能。事實上，無論是對稱或非對稱系統，電極材料與電解質的選擇始終是決定電化學儲能與換能裝置性能的關鍵[5, 6]。

針對鈣鈦礦氧化物(ABO_3)的電容表現，氧空位濃度被視為與電容量呈正比的核心參數，而影響其電化學行為的主要因素如 A 位摻雜（如低價 Sr^{2+}、Ca^{2+}）可誘導 B 位過渡金屬進入不穩定氧化態並產生氧空位，從而提升鈣鈦礦的電子電導率與電化學性能。而 B 位原子直接參與氧化還原反應，通過 B–O–B 雙交換機制主導電子傳導；多價態 B 位離子更有利於電荷存儲。BO_6八面體畸變會抑制電子遷移，而 B 位摻雜可在不改變晶格參數下調控缺陷與氧空位，使鈣鈦礦成為氧離子插層型(oxygen-ion-intercalation-type)超級電容器的理想電極材料。其電容主要源於表面氧化還原與內部氧插層，伴隨 B 位陽離子價態變化。進一步選擇合適的 B 位摻雜劑，實現低能障的價態轉變，對提升超級電容器性能至關重要[7]。一般而言，在鈣鈦礦結構中，B 位通常是多價次過渡金屬（如 Ni、Co、Mn、Fe）[8]來負責主要的電化學反應（氧化還原），進而發生協同效應。當引入“非活性離子”（如 Al^{3+}[9] [10]、Zn^{2+}[11]、Zr^{4+}等）時，雖然這些離子本身不參與氧化還原，但改變 B–O 鍵強度、過渡金屬的電子態分佈（d-band center）；因不同價態，引發電荷補償機制而引入氧空位，提升電化學活性；非活性離子因不易發生價態變化，進而提高結構穩定性等。

本研究分別針對正極與負極電壓窗口進行研究。選擇(Sr,Ba)$Mn_{1-y}Al_yO_3$ 系統進行研究，使用 Pechini 法製備粉體，利用在 B 位摻雜 Al 來調整導電率與氧空位濃度，研究對其結晶相、顯微結構與比電容的影響，藉此尋找出具有潛力的超級電容之電極材料。嘗試在 B 位摻雜非活性離子以改善鈣鈦礦氧化物的電化學性能。選擇 Al^{3+} 作為摻雜離子，是因為它是一種非活性離子，能夠阻止活性金屬氧化物的團聚，且其離子半徑與 B 位其他離子存在較大差異，可產生晶格畸變和缺陷。

二、實驗步驟

本研究採用 Pechini 法來合成鍶基雙鈣鈦礦氧化物（Sr,Ba）$Mn_{1-y}Al_yO_3$ (y=0, 0.2, 0.4, 0.6, 0.8, 1))粉體，所使用的金屬前驅物包括 $Sr(NO_3)_2$、$Mn(NO_3)_2\cdot 4H_2O$ 與 $Al(NO_3)\cdot 9H_2O$。依化學計量比配製濃度為 0.2 M 之金屬鹽水溶液後，加入與金屬離子莫耳比為 1:1 的檸檬酸進行混合，於 70 ℃ 下攪拌加熱 6 小時，確保金屬離子充分螯合於檸檬酸中。隨後添加乙二醇，加熱至 100 ℃ 攪拌至形成膠體溶液，經紅外燈照射乾燥並去除部分碳氫化合物，獲得碳焦前驅物。所得粉體再以 850 ℃ 進行煅燒。泡沫鎳基板經裁剪為 2 cm × 1 cm 後，以稀釋鹽酸去除表面氧化層，經去離子水清洗後置於 100 ℃ 烘箱乾燥，完成前處理。電極漿料則由 80 wt% 電極材料粉體、10 wt% Super-P 導電碳與 10 wt% 聚偏二氟乙烯（PVDF）混合，加入適量 N-甲基吡咯烷酮（NMP）於

瑪瑙研缽中研磨至均勻，隨後將漿料均勻塗佈於泡沫鎳基板，塗佈面積為 1 cm × 1 cm，並於 65 °C 烘箱中乾燥 9 小時。材料特性分析方面，以場發射掃描式電子顯微鏡（FE-SEM）觀察粉體顯微結構；電化學性能則使用電化學工作站（Zennium, Zahner, Germany）進行循環伏安法（CV）與交流阻抗分析（EIS），並進一步計算比電容值。電化學測試採用三極式電解槽，工作電極為經塗佈之試片，參考電極為飽和甘汞電極（SCE），對電極為白金片（2 cm × 2 cm），電解質溶液為 1 M KOH 水溶液。

三、結果與討論

3.1 XRD

以檸檬酸法製備 $Sr_{0.7}Ba_{0.3}Mn_{1-y}Al_yO_3$ 並經 850℃煅燒之 XRD 繞射圖如圖 一所示。經過相鑑定分析，結果顯示粉體的繞射峰與 $SrMnO_3$ (JCPDS 084-1612)和 $Sr_8Al_{28}O_{50}$ (COD 600-0236)相符。在 y= 0 和 0.2 時，主要相為 $SrMnO_3$，次要相為 $Sr_8Al_{28}O_{50}$；隨著 Al 摻雜量增加，在 y= 0.6 和 0.8 時，最強的繞射峰位置往低角度偏移，主相變為 $Sr_8Al_{28}O_{50}$，次要相則變為 $SrMnO_3$；另外，樣品皆含有少量的 $SrCO_3$。以上說明 Al 在 $SrMnO_3$ 中的溶解度是有限的，超過 0.6 後，會產生大量第二相。由於 Al^{3+}原子小於 Mn^{4+} (Mn^{4+}:53 pm；Al^{3+}:35 pm)，添加 Al 元素後造成晶胞縮小。 Kajitani 等人[9]在鈣鈦礦 $LaGa_{0.9}Mg_{0.1}O_{2.95}$ 中摻雜 Al。隨著鋁摻雜量的增加，晶體結構發生轉變，這種變化有利於氧離子傳導，同時晶格參數呈遞減趨勢。

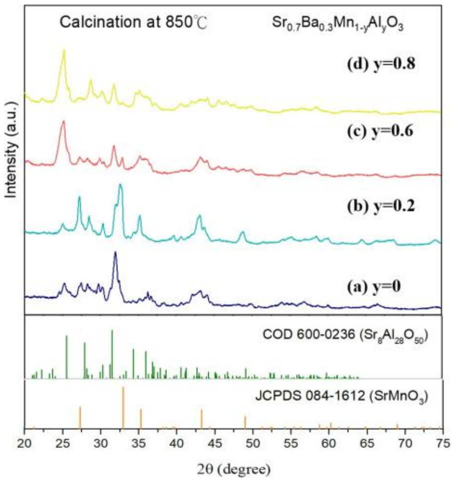

圖 一、以 Pechini 法製備 $Sr_{0.7}Ba_{0.3}Mn_{1-y}Al_yO_3$ 粉體並經 850℃煅燒之 XRD 圖。

3.2 SEM 分析

以 SEM 進行顯微結構分析，使用檸檬酸法製備之 $Sr_{0.7}Ba_{0.3}Mn_{1-y}Al_yO_3$ 並經 850℃煅燒之 SEM 照片如圖 二所示。y= 0.2 之顆粒尺寸約為 4.2 μm 左右，而 y= 0.8 之顆粒尺寸約為 5.1 μm 左右。兩種粉體形狀相似，都有少量小顆粒附著，差異是 y= 0.2 的粉體存在較多孔隙，y= 0.8 則孔隙較少。

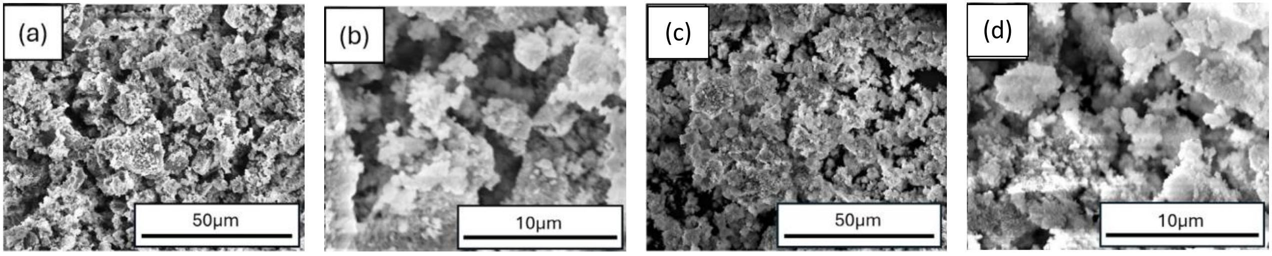

圖 二、經 850℃煅燒所製備的 $Sr_{0.7}Ba_{0.3}Mn_{1-y}Al_yO_3$ 粉體之 SEM 照片: (a),(b) y=0.2；(c),(d) y=0.8。

3.3 CV 與比電容

圖 三 (a)為在 850°C 煅燒 $Sr_{0.8}Ba_{0.2}Mn_{1-y}Al_yO_3$ 在-1~0V 電壓範圍所測得之 CV 圖，六種樣品形狀皆不對稱，表示反應可逆性都較差。除了 y=0 和 1 無明顯氧化還原峰之外，另外四種成份之還原峰較為明顯突出，約在-0.8~ -0.4 V，而還原峰約在-0.4~ -0.3 V。圖 三 (b)為 0~0.5V 電壓範圍所測得之 CV 圖，六種樣品皆有明顯的氧化還原峰，但形狀不對稱，可逆性較差。六種樣品氧化電位約在 0.33~0.4V，而還原電位約在 0.2~0.3V。比電容與 Al 含量之關係如圖 三 (c)與(d)所示。在負電壓窗口下，掃速為 10 mV/s 時，y= 0.2 有最高的比電容，為 41.7 F/g；在正電壓窗口下，掃速為 10 mV/s 時，y= 0.4 有最高的比電容，為 71.0 F/g。由 XRD 分析可知，當 Al 含量高於 0.6 時，主要結晶相為 $Sr_8Al_{28}O_{50}$ 相，而 SEM 照片則顯示 Al 的摻雜對顆粒形狀並無明顯影響。因此，可以

說 Al 的摻雜並不會影響雙電層電容的貢獻。$Sr_8Al_{28}O_{50}$ 相的存在才是降低比電容的主因，當其含量增加時，相對的高比電容的鈣鈦礦相含量會降低。而鈣鈦礦相中的 Al 含量則對整體比電容有正面幫助，使得 Al 含量為 0.2~0.4 時，有更高的比電容。Guo 等人[10]採用共沉澱法結合煅燒工藝，合成了一系列高熵鈣鈦礦氧化物（HEPOs）$La(CoCrFeMnNiAl_x)_{1/(5+x)}O_{3-\delta}$，他們認為其優異的電化學性能可歸因於 B 位六種陽離子混合所產生的熵穩定結構，以及 Al^{3+}摻雜在充放電過程中對活性離子團聚的抑制作用。

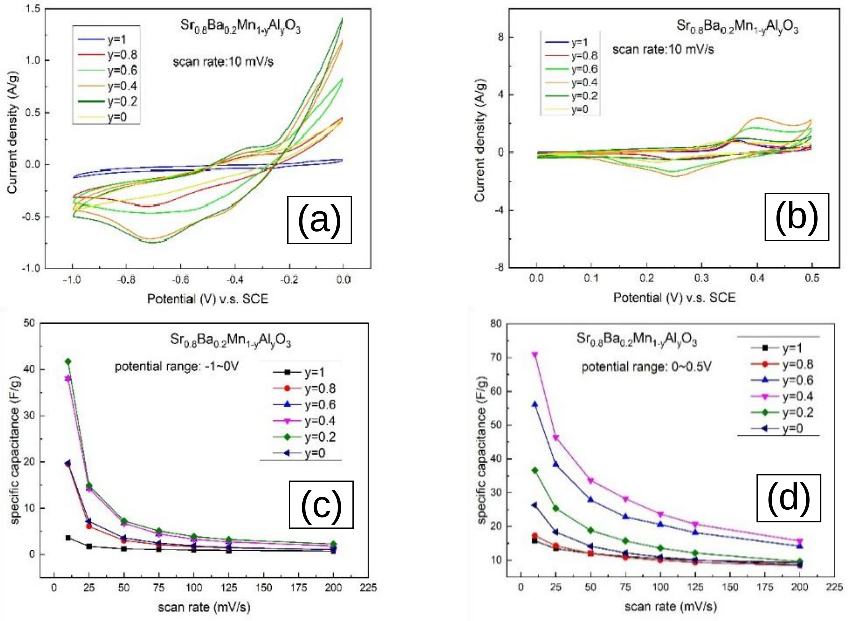

圖 三、$Sr_{0.8}Ba_{0.2}Mn_{1-y}Al_yO_3$ 電極之 CV 曲線與不同掃描速率下之比電容:(a),(c)電壓範圍: -1~0V；(b),(d)電壓範圍: 0~0.5V。

3.4 交流阻抗分析

以檸檬酸法製備 $Sr_{0.7}Ba_{0.3}Mn_{1-y}Al_yO_3$，並經 850°C煅燒之奈奎斯特圖如圖 四所示，所擬合之模擬電路數據如表一所示。串聯電阻 R_s 最小的是 y= 0.2，為 804 mΩ；電荷轉移電阻 R_{ct} 最小的是 y= 0.4，為 12.4 Ω；擴散阻抗 W 最小的是 y= 0，為 26.4 $\Omega\cdot s^{-1/2}$；C_{eq} 最大的是 y= 1，為 220 µF；低頻質量電容 C_2 最大的是 y= 0.4，為 30.5 mF；R_2 最小的是 y=0，為 20.3 Ω。當 $Sr_8Al_{28}O_{50}$ 量越多時，R_2 明顯也更大。從交流阻抗分析則可觀察到，y= 0.4 有最小的 R_{ct}，為 12.4 Ω，還有最大的 C_2，為 30.5 mF。從比電容發現，對於掃速 10 mV/s，在負電壓窗口時，雖然最高者為 y= 0.2，可達 41.7 F/g，但與 y= 0.4 差異不大，為 38.0 F/g；在正電壓窗口時，最高者為 y= 0.4，可達 71.0 F/g。因此在 $Sr_{0.8}Ba_{0.2}Mn_{1-y}Al_yO_3$ 系統中，B 位同時摻雜 Al、Mn 可發揮協同效應，$Sr_{0.8}Ba_{0.2}Mn_{0.6}Al_{0.4}O_3$ 有最佳的電化學性能。

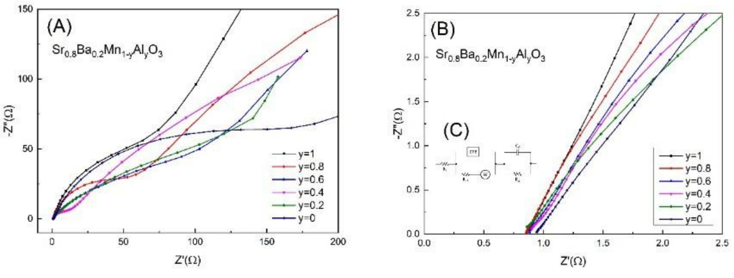

圖 四、$Sr_{0.8}Ba_{0.2}Mn_{1-y}Al_yO_3$ 電極之(A) 比電容圖；(B) 交流阻抗圖；(C) 等效電路圖。

表 一、$Sr_{0.8}Ba_{0.2}Mn_{1-y}Al_yO_3$ 電極之交流阻抗數據與等效電路模型擬合結果。

參數 比例	R_s (mΩ)	R_{ct} (Ω)	W ($\Omega\cdot s^{-1/2}$)	C_{eq} (μF)	C_2 (mF)	R_2 (Ω)	overall error(%)
y=0	930	178	26.4	210	4.36	20.3	2.56
y=0.2	804	44.3	43.0	116	13.3	32.8	4.52
y=0.4	911	12.4	52.5	88	30.5	26.7	5.36
y=0.6	863	32.2	47.2	109	6.17	31.1	5.53
y=0.8	863	67.1	60.7	131	30.1	134	4.42
y=1	879	98.4	94.7	220	10.6	761	4.95

四、結論

本研究已成功使用 Pechini 法製備不同 Al 含量之鈣鈦礦氧化物$(Sr,Ba)Mn_{1-y}Al_yO_3$粉體，並作為超級電容之電極材料。經 850℃煅燒後，粉體含有 $SrMnO_3$、$Sr_8Al_{28}O_{50}$、與少量的 $SrCO_3$；隨著 Al 摻雜量增加，$Sr_8Al_{28}O_{50}$的含量增加。SEM 照片則顯示 Al 的摻雜對顆粒形狀與尺寸並無明顯影響，顆粒尺寸約為 4~5 μm 左右。掃速為10 mV/s 時，在負電壓窗口(-1~0 V)下，y= 0.2 有最高的比電容 41.7 F/g；在正電壓窗口(0~0.5 V)下，則在 y= 0.4 有最高的比電容 71.0 F/g。根據交流阻抗分析與等效電路擬合結果顯示，在 y=0.4 有最低的電荷轉移電阻與最高的低頻質量電容。Al 的摻雜量與 $Sr_8Al_{28}O_{50}$相含量決定了比電容，在低 Al 摻雜量範圍(<0.6)，B 位同時摻雜 Al、Mn 可發揮協同效應，其中 $Sr_{0.8}Ba_{0.2}Mn_{0.6}Al_{0.4}O_3$有最佳的比電容性能。

五、參考文獻

[1] S. Soleimani, K. Pishvaie, M. Saidi, Journal of Power Sources 640 (2025) 236760.

[2] T.H. Khan, S.F. Tatheer, Q. ul ain, A. Saleem, P. Akhter, M.I. Khan, U. Younas, S. Iqbal, Z. Saeed, Journal of Alloys and Compounds 1057 (2026) 186103.

[3] S.V. Sadavar, S.Y. Lee, S.J. Park, Adv Sci (Weinh) 11 (2024) e2403172.

[4] T. Zahra, S. Bashir, M. Pershaanaa, T. Prasankumar, M. Hina, S. Ramesh, K. Ramesh, Journal of Energy Storage 120 (2025) 116434.

[5] D. Meena, R. Kumar, S. Gupta, O. Khan, D. Gupta, M. Singh, Journal of Energy Storage 72 (2023) 109323.

[6] J. Zhang, M. Gu, X. Chen, Micro and Nano Engineering 21 (2023) 100229.

[7] S. Bachankar, D. Malavekar, V. Lokhande, T. Ji, Journal of Alloys and Compounds 1003 (2024) 175708.

[8] S. Ashok C, A. Vazhayil, R. Vinaykumar, J. Thomas, A.A. Jeffery, I. Hasan, N. Thomas, A.K. Yadav, Y.-H. Ahn, Journal of Energy Storage 86 (2024) 111145.

[9] M. Kajitani, M. Matsuda, M. Miyake, Solid State Ionics 178 (2007) 355–358.

[10] M. Guo, Y. Liu, F. Zhang, F. Cheng, C. Cheng, Y. Miao, F. Gao, J. Yu, Journal of Advanced Ceramics 11 (2022) 742–753.

[11] F. Hadji, M. Omari, M. Mebarki, N. Gabouze, A. Layadi, Journal of Alloys and Compounds 942 (2023) 169047.

報告型式：

□英文口頭報告競賽 (□無機材料， □有機材料)

■海報展示並參加壁報論文競賽(■無機材料， □有機材料)

□只參加海報展示 (□無機材料， □有機材料)

積層製造熱作工具鋼之多孔結構型態對壓縮性質的影響

謝竣宇 [1]，黃泳傑 [2]，張宸銘 [3]，古明祥 [4]，李健綸 [5]，吳明偉 [6]
國立臺北科技大學材料科學與工程研究所 [1]，國立臺北科大學材料與資源工程系 [2]，
奧鋼聯科研亞洲股份有限公司 [3]
t113788008@ntut.org.tw

摘要

本研究之目的為探討雷射粉體床熔化成形(laser powder bed fusion, LPBF)製造的 Dievar 熱作工具鋼多孔結構的機械性質與破壞行為，研究中製作了立方(Cubic)、帶 Z 軸支撐之面心立方(FCCZ)、將 Cubic、FCCZ 組合在一起的 Hybrid 多孔結構，以及將 Cubic、FCCZ 以梯度排列組合成的功能性梯度材料(functionally-graded material,FGM)，依梯度方向與受力方向垂直或水平分別命名為 FGM-P 與 FGM-V 試片。本研究透過單軸壓縮試驗及數位影像相關法的實驗方法來分析五種結構的抗壓強度、吸收能，以及承受應力時的應變與破壞行為。

研究結果顯示在五種多孔結構試片中，FCCZ 試片具有最高比強度，可達到 139 kN-m/kg，顯示其在單位質量下具備優異的承載能力，Cubic 試片則有最高比吸收能 32±2 kJ/kg，顯示該結構在承受應力時能表現出高穩定性，能避免劇烈崩塌。

在破懷行為方面，Cubic、Hybrid 試片為層狀破壞，此種破壞模式會在應力超過第一最大應力峰後出現些微的應力下降，然後應力再重新上升，應力應變曲線會呈現波動震盪，這種模式一般具有更高的吸收能表現。FCCZ 試片為剪切破壞，在應力到達第一最大應力峰後，會出現急遽的應力驟降，該模式一般具有較高的第一抗壓強度。FGM-P 試片也呈現層狀破壞，但破壞發生位置一律是從第一層(具有 100 %Cubic 多孔結構)開始發生， 且後續變形也多集中在 Cubic 較多的上半區，說明該結構的破壞位置能被控制。FGM-V 試片則為層狀破壞及剪切破壞的混合破壞，該模式在能夠提高第一抗壓強度的同時，還能減緩應力超過第一最大應力峰後的應力驟降， 因此 FGM-V 試片同時具有一定強度及穩定性。

報告型式：

□英文口頭報告競賽 (□無機材料， □有機材料)
■海報展示並參加壁報論文競賽(■無機材料， □有機材料)
□只參加海報展示 (□無機材料， □有機材料)

冷均壓製程對 TZM 鉬合金之燒結緻密化的效應

杜秉融[1]，徐敏峻[2]，張家輔[2]，曾慶文[2]，陳裕德[2]，吳明偉[3,*]
國立臺北科技大學材料科學與工程研究所[1]，國家中山科學研究院飛彈所主體系統研製組[2]，國立臺北科技大學材料與資源工程系[3]
杜秉融，tu71240140@gmail.com

摘要

粉末冶金(powder metallurgy, PM)為製備高熔點金屬的重要技術，具備組織均勻性及可控制孔隙率和晶粒尺寸等優勢，因此被廣泛應用於航太、電子領域。純鉬雖具有高熔點和良好導熱性，但機械性質較差，因此發展出添加 Ti、Zr 元素的鈦鋯鉬(titanium-zirconium-molybdenum, TZM)合金，以提升高溫機械性質並維持高溫穩定性。

本研究採用粉末冶金技術製備 TZM 合金，使用乾壓成形及冷均壓(cold isostatic pressing, CIP)技術來將粉末進行成形，後續進行真空燒結，以探討 CIP 對生胚密度之影響，並分析試片在燒結後的密度和顯微組織。結果顯示以 250 MPa 進行乾壓成形後的生胚密度為 6.01 g/cm^3，若將乾壓成形後的生胚再以 250 MPa 進行 CIP，則生胚密度可被提升至 6.44 g/cm^3。在 1800 ℃真空燒結後，CIP 後的生胚試片之燒結密度可大幅提升到 9.66 g/cm^3。藉由電子背向散射繞射(electron backscatter diffraction, EBSD)及能量分散光譜(energy dispersive spectrum, EDS)分析得知燒結後的試片基材為 Mo 的體心立方結構，此外由 EDS 分析亦可觀察到 Ti、Zr 元素主要分布於氧化物中。綜合以上結果，CIP 製程可提升 TZM 合金之生胚密度，後續預期藉由提高燒結溫度將可更進一步提升其燒結緻密性。

報告型式：

□英文口頭報告競賽 (□無機材料， □有機材料)
■海報展示並參加壁報論文競賽(■無機材料， □有機材料)
□只參加海報展示 (□無機材料， □有機材料)

Multifunctional Characterization of CuI Thin Films with PEDOT:PSS Interface Layer

Musa Beni Ricardo Aruan[1]*, Der Yuh Lin [2] and Imelda Zahra Tungga Dewi[3]
[1]Department of International Master Program in Engineering, National Changhua University of Education
[2] Department of Electronics Engineering, National Changhua University of Education
[3] Department of Physics, Gadjah Mada University
*Correspondence: benimusa77@gmail.com

ABSTRACT

Copper iodide (CuI) is a promising p-type transparent semiconductor with potential applications in optoelectronic and thermoelectric devices due to its wide bandgap and high hole mobility. CuI thin films were fabricated on glass substrates using thermal evaporation followed by iodization, with thicknesses ranging from 1 to 1.4 µm. A PEDOT:PSS interfacial layer was introduced to improve electrical contact quality. The structural, optical, electrical, and thermoelectric properties of the films were systematically investigated. X-ray diffraction (XRD) confirmed the crystalline phase of CuI. Optical analysis based on UV–Vis measurements and Tauc plot evaluation revealed a direct optical bandgap of 3.076 eV, consistent with reported properties of CuI thin films. Electrical characterization using van der Pauw and Hall effect measurements confirmed p-type conductivity with a sheet carrier density of $2.69 \times 10^{13}\,\mathrm{cm^{-2}}$ and mobility of $81.2\ \mathrm{cm^2/V{\cdot}s}$. Thermoelectric performance was evaluated by measuring the Seebeck coefficient under a temperature gradient, yielding a value of 2.82×10^{-4} V/K, confirming dominant hole transport. The improved electrical performance is attributed to enhanced ohmic-like contact behavior introduced by the PEDOT:PSS interfacial layer, which reduces the interfacial barrier and enhances hole transport across the electrode-film interface. These results demonstrate that CuI thin films with PEDOT:PSS interfacial layers exhibit strong potential for transparent thermoelectric and optoelectronic device applications.

INTRODUCTION

Transparent semiconductors have attracted considerable attention for optoelectronic and energy-related applications because they combine electrical conductivity with optical transparency. However, most widely used transparent conducting materials, such as ITO, FTO, and AZO, are n-type, while high-performance p-type transparent semiconductors remain limited [1]. Among the available candidates, copper iodide (CuI) has emerged as a promising p-type material due to its wide direct bandgap of around 3.1 eV, high transparency in the visible region, and intrinsic hole conductivity associated with copper vacancies [1,2].

In addition to optoelectronic applications, CuI has also shown potential for thermoelectric use. Previous studies have reported measurable Seebeck coefficients and stable p-type transport behavior in CuI thin films, indicating that this material can function as a transparent thermoelectric semiconductor [1]. The optical properties of CuI thin films, including high transmittance and direct bandgap characteristics, have also been widely confirmed through reflectance and transmittance analysis as well as annealing-dependent studies [2].

The performance of CuI thin films strongly depends on reliable electrical characterization and good interfacial contact. The van der Pauw method is widely used for thin-film electrical measurements because it minimizes the effects of contact resistance and sample geometry, enabling accurate evaluation of transport properties [3]. In addition, interface engineering is often required to improve carrier transport across the electrode-film interface. Recent studies have demonstrated that PEDOT:PSS can effectively reduce interfacial barriers and enhance hole extraction by improving energy level alignment [4].

In this study, CuI thin films were fabricated on glass substrates by thermal evaporation followed by iodization, and a PEDOT:PSS interfacial layer was introduced to improve electrical contact. The structural, optical, electrical, and thermoelectric properties of the films were systematically investigated to evaluate their potential for transparent thermoelectric and optoelectronic applications.

EXPERIMENTAL METHOD

CuI thin films were fabricated on glass substrates using thermal evaporation followed by an iodization process. Prior to deposition, the substrates were cleaned sequentially using acetone, ethanol, and deionized water. A copper (Cu) layer was first deposited and then converted into CuI by exposure to iodine vapor in a sealed chamber for approximately 24 hours. The resulting film thickness ranged from 1 to 1.4 µm. To improve electrical contact, a PEDOT:PSS interfacial layer was deposited onto the CuI surface via drop-casting and subsequently annealed at 60 °C for 30 minutes to enhance film stability and interfacial adhesion. The structural properties of the films were characterized using X-ray diffraction (XRD) to confirm crystallinity and phase formation. Optical properties were analyzed using UV–Vis spectroscopy, and the optical bandgap was determined using Tauc plot analysis. Electrical properties were evaluated using the van der Pauw method to determine sheet resistance, while Hall effect measurements were performed to obtain carrier type, carrier concentration, and mobility. Thermoelectric performance was assessed by measuring the Seebeck coefficient under an applied temperature gradient, where the voltage difference was linearly fitted to obtain the Seebeck value.

RESULTS AND DISCUSSION

XRD analysis confirmed that the CuI thin films exhibit a crystalline structure consistent with reported CuI phases. The crystalline structure of the CuI thin films is confirmed by the XRD pattern, as shown in Figure 1, The dominant diffraction peak corresponding to the (111) plane indicates a preferred orientation of γ-CuI, which is consistent with previously reported CuI thin films.

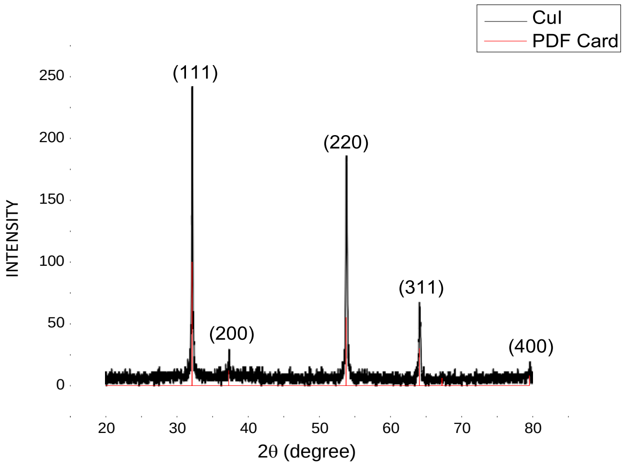

Figure 1. X-ray diffraction (XRD) pattern of CuI thin films.

Optical properties were analyzed using UV–Vis spectroscopy. The absorption data were used to construct a Tauc plot, from which a direct optical bandgap of 3.076 eV was obtained. This value is in good agreement with reported bandgap values for CuI thin films, confirming the optical quality of the fabricated films.

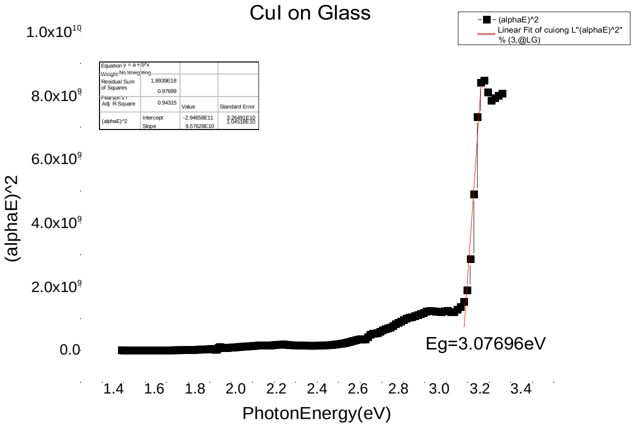

Figure 2 Tauc plot of CuI thin films

Electrical characterization using the van der Pauw method showed stable sheet resistance values. Hall effect measurements confirmed that the films exhibit p-type conductivity with a carrier concentration of approximately 2.69×10^{13} cm^{-2} and a mobility of about 81.2 cm^2/V·s. The electrical properties of the CuI thin films were further analyzed using Hall effect measurements, as summarized in Table 1, showing consistent p-type conductivity with stable carrier concentration and mobility values.

Table 1. Hall effect measurement results of CuI thin films

PARAMETER	**VALUE**
Carrier type	p-type
Carrier density	2.69×10^{13} cm^{-2}
Mobility	81.2 cm^2/V·s

To evaluate the contact behavior, current–voltage (I–V) measurements were performed. The I–V characteristics of the CuI thin film with the PEDOT:PSS interfacial layer are shown in Fig. 3. The approximately linear relationship between current and voltage indicates ohmic-like contact behavior, suggesting that the PEDOT:PSS layer effectively reduces the interfacial barrier and facilitates charge injection. This improved contact behavior contributes to the enhanced electrical performance of the CuI thin films.

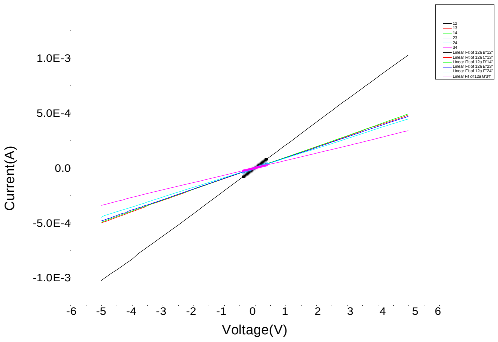

Figure 3. I–V characteristics of the CuI thin films

The thermoelectric performance of the films was evaluated through Seebeck coefficient measurements. The thermovoltage difference as a function of temperature difference is shown in Fig. 4, where an approximately linear relationship is observed.

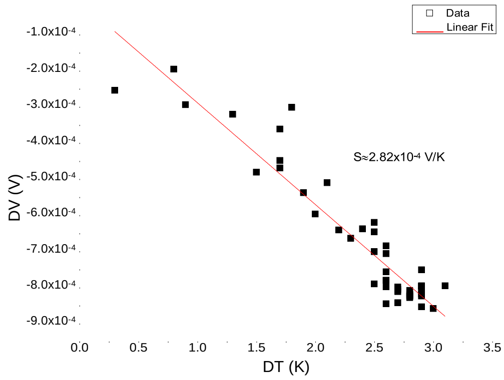

Figure 4. Seebeck coefficient measurement of CuI thin films

The Seebeck coefficient was obtained from the slope of the linear fit, yielding a value on the order of 10^{-4} V/K. Based on the measurement polarity convention, this corresponds to positive Seebeck behavior, indicating hole-dominated transport. This result is consistent with the p-type conductivity obtained from Hall effect measurements. Although minor deviations are observed, the overall linear trend confirms reliable thermoelectric behavior of the CuI thin films.

CONCLUSION

CuI thin films were successfully fabricated and characterized to investigate their structural and thermoelectric properties. X-ray diffraction analysis confirmed the formation of crystalline γ-CuI with a strong (111) preferred orientation, indicating good film quality. The introduction of a PEDOT:PSS interlayer significantly improved the electrical contact, resulting in near-ohmic behavior and enabling reliable electrical measurements.

Seebeck coefficient measurements revealed a positive thermoelectric response, confirming the p-type nature of the CuI films. The linear relationship between thermoelectric voltage and temperature difference indicates stable thermoelectric performance within the measured range. Overall, this work highlights the potential of CuI as a transparent p-type semiconductor for thermoelectric and electronic applications. Future work may focus on optimizing film thickness, improving contact engineering, enhancing thermoelectric performance through material and process modifications, and evaluating the thermoelectric figure of merit (ZT).

REFERENCES

[1] Darnige, P., Thimont, Y., Presmanes, L., & Barnabé, A. (2022). Insights into stability, transport, and thermoelectric properties of transparent p-type copper iodide thin films. *Journal of Materials Chemistry C*, *11*(2), 630–644. https://doi.org/10.1039/d2tc03652e

[2] M. Grundmann, F.-L. Schein, M. Lorenz, T. Böntgen, J. Lenzner, and H. von Wenckstern, "Cuprous iodide – a p-type transparent semiconductor: history and novel applications," Physica Status Solidi A, vol. 210, no. 9, pp. 1671–1703, Aug. 2013, doi: 10.1002/pssa.201329349.

[3] de Boor, J., & Schmidt, V. (2010). Complete characterization of thermoelectric materials by a combined van der pauw approach. Advanced Materials, 22(38), 4303–4307. https://doi.org/10.1002/adma.201001654

[4] Kang, S., Meng, Z., Wang, Y., Zheng, K., Huang, S., Zhang, D., Li, S., Chen, C., Ren, S., Li, Y., Ding, C., & Zhao, D. (2026). Overcoming Hole-Extraction Barriers: A Facile PEDOT:PSS Interlayer Unlocks Record-Low Voltage Deficit in PbS Quantum Dot Solar Cells. Advanced Science. https://doi.org/10.1002/advs.202524275

Presentation type：

☑Poster competition (☑ inorganic materials, ☐ organic materials)

以二水石膏經鹽浸碳化法合成碳酸鈣之研究：摻雜鋯離子對球霰石相穩定性與微結構演變之影響

陳柏融,賴孝武[1],黃常寧[2]

[1] 南臺科技大學化學工程與材料工程系

[2] 東華大學材料科學與工程學系

cnhuang@gms.ndhu.edu.tw

摘要

本研究以試藥級二水石膏為原料，透過氯化銨鹽浸與碳化反應之兩步法製程合成碳酸鈣，並探討不同濃度鋯離子摻雜（0–10 mol%）對碳酸鈣成核相態、晶體結構、微觀形貌及熱性質之影響。首先利用氯化銨溶液進行鹽浸處理以促進鈣離子釋放，隨後通入二氧化碳進行碳化反應，以生成碳酸鈣產物。由 X 光繞射分析結果顯示，未摻雜樣品之碳酸鈣主要以球霰石相為主，並隨鋯離子添加濃度之增加，晶相組成與晶面取向產生明顯變化，顯示鋯離子對碳酸鈣成核行為及球霰石相之穩定性具有顯著影響。透過實體顯微鏡與場發射掃描式電子顯微鏡觀察結果可知，鋯離子摻雜可有效改變碳酸鈣顆粒之形貌與粒徑分佈，降低顆粒團聚現象，並影響晶體成長方式。此外，比表面積與孔徑分析結果顯示，不同鋯離子摻雜濃度對碳酸鈣之比表面積與孔結構具有顯著影響，反映其在成核密度與晶體生長行為上的差異。熱重分析結果則顯示，各樣品於高溫區間呈現明確之熱分解行為，且其重量損失特性隨摻雜濃度有所變化，顯示鋯離子摻雜對碳酸鈣熱穩定性具有一定程度之影響。本研究證實透過鹽浸碳化兩步法可有效合成碳酸鈣，且鋯離子摻雜能顯著影響其晶相組成、微觀結構及熱性質，對於球霰石相之調控與穩定具有潛在應用價值。

參考文獻

1. Y. Svenskaya and T. Pallaeva, "Exploiting benefits of vaterite metastability to design degradable systems for biomedical applications," Pharmaceutics, vol. 15, no. 11, p. 2574, 2023.
2. X. San et al., "Unlocking the mysterious polytypic features within vaterite CaCO3," Nature communications, vol. 14, no. 1, p. 7858, 2023.
3. D. Zhao, J. M. Williams, P. Hou, A. J. Moment, and S. Kawashima, "Stabilizing mechanisms of metastable vaterite in cement systems," Cement and Concrete Research, vol. 178, p. 107441, 2024.

報告型式：

□英文口頭報告競賽 (□無機材料， □有機材料)
■海報展示並參加壁報論文競賽(■無機材料， □有機材料)
□只參加海報展示 (□無機材料， □有機材料)

AA6061-T6 鋁合金硬質陽極處理參數對耐腐蝕特性及磨耗特性之影響

郭哲源、江育銘、廖翊伶、陳宣妘、廖梓蓉、林宏茂*
南臺科技大學化學工程與材料工程學系
hmlin@stust.edu.tw

摘要

本研究旨在探討不同參數對 6061-T651 鋁合金硬質陽極氧化膜之微觀結構、機械性質與耐腐蝕性能的影響。實驗規劃分為兩階段進行最佳化分析，第一階段改變電流密度（0.025A/cm^{2}至0.045 A/cm^2）以尋找最佳成膜電流密度，第二階段則在最佳電流密度下，進一步改變硫酸濃度（5%、10%、15%）進行探討。

研究結果顯示提高電流密度雖可加速氧化膜的增厚，但過高的電流密度會引發劇烈的熱效應與化學溶解， 導致膜層粗糙化、產生孔洞與微裂紋，甚至出現局部疏鬆等劣化現象。在電流密度為 0.025 A/cm^2 時，氧化膜展現出最緻密均勻的結構，並達到最高的表面硬度 349.9 HV 。此外，該條件下的磨耗軌跡寬度最小（1.33 mm） 摩擦係數波動最平穩，且腐蝕電流密度降至最低的 8.4281×10^{-10} A/cm^2 展現出最優異的抗磨與防蝕效果。當電流密度提高至 0.045 A/cm^2 時，硬度大幅衰退至僅 136.9 HV，項防防性性能顯顯下下降。

在定電電流密度 0.025 A/cm^{2}的條件下探討硫酸濃度變化，結果表明濃度對膜厚的影響並不顯著，但對微觀缺陷與整體性能有直接關聯。在5% 硫酸濃度下生成的氧化膜最為緻密且無明顯裂痕，硬度進一步微升至354.7HV。5% 濃度的試片因內部缺陷最少能有效抑制疲勞裂紋的萌生與擴展 因而獲得最低的磨耗損失量。電化學交流阻抗（EIS）分析顯證實5% 濃度的條件能提供最高的界面阻抗與最佳的屏障阻擋效果。綜合以上實驗分析，本研究確立了 6061-T651 鋁合金硬質陽極處理之最佳製程參數為：電流密度 0.025 A/cm^2 搭配 5% 硫酸濃度 。在此參數下能最大化提升鋁合金表面的硬度、耐磨耗性以及耐腐蝕能力。

參考文獻

[1]S. H. Mohitfar, S. Mahdavi, M. Etminanfar, and J. Khalil-Allafi, "Characteristics and tribological behavior of the hard anodized 6061-T6 Al alloy," *Journal of Alloys and Compounds*, vol. 842, p. 155988, 2020.

[2]M. Abid, M. Kchaou, A. T. Hoang, and M. Haboussi, "Wear mechanisms analysis and friction behavior of anodic aluminum oxide film 5083 under cyclic loading," *Journal of Materials Engineering and Performance*, vol. 33, no. 3, pp. 1527-1537, 2024.

報告型式：

□英文口頭報告競賽 (□無機材料， □有機材料)
■海報展示並參加壁報論文競賽(■無機材料， □有機材料)
□只參加海報展示 (□無機材料， □有機材料)

純銅電極放電被覆 316L 不鏽鋼之微結構演變與銅富集行為及其抗菌性能關聯研究

鄭暐霖、林宏茂*
南臺科技大學化學工程與材料工程系
hmlin@stust.edu.tw

摘要

本研究以純銅電極對 316L 不鏽鋼進行放電被覆處理，探討其被覆層之結構演變、表面特性及抗菌性能。實驗結果顯示，放電被覆可於基材表面形成以 fcc-Cu 為主之被覆層，被覆層厚度及銅富集程度隨放電電流由 30 A 增至 50 A 顯著提高。電子探針與穿透式電子顯微鏡分析證實，被覆層中存在大量結晶性良好的 fcc-Cu 奈米顆粒（數十奈米），並與基材形成緊密的冶金結合，使組織由局部 Cu-rich 顆粒演變為高密度奈米顆粒層。

放電被覆明顯改變表面形貌與機械性質。隨放電電流提升，表面形成重疊熔蝕與再凝固結構，粗糙度 Ra、Rz 明顯上升，表層硬度由基材約 150 HV 提升至 800–1100 HV。硬化機制主要來自奈米細晶化效應、Cu 奈米顆粒析出強化及冶金結合所引起的漸變結構。接觸角測試，接觸角度數由 70° 提升至 85–100°，由親水轉為疏水，因粗糙度上升及 Cu 富集相造成的表面能降低。

抗菌試驗結果指出，在 30–50 A 放電條件下，試片對金黃色葡萄球菌與大腸桿菌皆具極佳抗菌率。抗菌機制主要與表層 Cu 富集區及奈米顆粒之銅離子釋放與接觸殺菌效應相關，並受表面形貌與潤濕性變化輔助。整體而言，本研究建立了放電電流、Cu 富集、奈米結構、表面性能、抗菌效能、之關聯性，證實純銅電極放電被覆能同時提升 316L 不鏽鋼之機械強度與抗菌性能，具應用於醫療器材與食品接觸材料之潛力。

關鍵字：放電被覆、316L 不鏽鋼、純銅電極、奈米結構、抗菌性能、潤濕性

參考文獻

[1]. V. Vijayan, K. K. Saju, and J. Sundaresan, “Three-Dimensional Surface Topography Analysis of Die-Sinking Electrical Discharge Machined Eco-friendly Beryllium-Free Cu Alloys,” The International Journal of Advanced Manufacturing Technology, 2025.

[2]. N. Ahmed, M. A. Hurairah, M. A. Ali, M. H. Raza, A. U. Rehman, and M. Rafaqat, “Impact analysis of electrode materials and EDM variables on the surface characteristics of SS316L for biomedical applications,” Journal of Materials Research and Technology, vol. 27, pp. 487–505, 2023.

[3]. K. Liu, I. L. Wang, L. M. Tam, K. H. Lo, R. Li, C. W. Chan, V. A. M. Cristino, and C. T. Kwok, “In-situ surface modification and bulk alloying of anti-bacterial Cu-bearing stainless steel using selective laser melting,” Materials and Design, vol. 254, pp. 114110-1–114110-13, 2025.

報告型式：

□英文口頭報告競賽 (□無機材料， □有機材料)
海報展示並參加壁報論文競賽(■無機材料， □有機材料)
□只參加海報展示 (□無機材料， □有機材料)

Synthesis of $Ti_3C_2T_x$ MXene via Selective Etching of Ti_3AlC_2 Powder

Ji-Hao Li [1], Chia Yu ,Lin[2], Chun-Yuan Huang [3*]
Department of Applied Science, National Taitung University
Correspondence: laputa@nttu.edu.tw

NSTC 113-2221-E-143-004-MY2

Abstract

$Ti_3C_2T_x$ MXene, a two-dimensional layered material, was synthesized from Ti_3AlC_2 powder through selective etching to remove the Al layers. Building upon the conventional hydrofluoric acid (HF) etching method, this study employs an in situ generated fluoride-containing system using lithium fluoride (LiF) and hydrochloric acid (HCl) to create a milder etching environment for the selective removal of Al and subsequent delamination of Ti_3AlC_2.

This approach effectively reduces the risks associated with the use of concentrated HF while facilitating the transformation of multilayer structures into single-layer or few-layer $Ti_3C_2T_x$. Furthermore, by optimizing reaction parameters—such as the LiF/HCl ratio, etching time, and post-treatment delamination processes—the interlayer spacing, dispersibility, and single-layer yield of the obtained MXene were significantly improved. Compared with the traditional HF etching method, the LiF–HCl in situ HF generation strategy demonstrates notable advantages in terms of safety, structural controllability, and material performance. This work provides a more feasible and tunable route for the preparation of high-quality single-layer $Ti_3C_2T_x$ MXene.

References

[1] Zhang, T., Pan, L., Tang, H., Du, F., Guo, Y., Qiu, T., & Yang, J. (2017). Synthesis of two-dimensional $Ti_3C_2T_x$ MXene using HCl + LiF etchant: enhanced exfoliation and delamination. *Journal of alloys and compounds*, *695*, 818-826.

[2] Thakur, A., Chandran BS, N., Davidson, K., Bedford, A., Fang, H., Im, Y., ... & Anasori, B. (2023). Step-by-step guide for synthesis and delamination of $Ti_3C_2T_x$ MXene. Small Methods, 7(8), 2300030.

[3] Priyanka, Rundla, A., Singh, M., Kumar, B., Mishra, V., & Singh, K. (2026). Hierarchically Structured $CsPbBr_3$@ $Ti_3C_2T_X$ Nanohybrid Frameworks for High-Performance Supercapacitors. *ACS Applied Energy Materials*.

Presentation type：

☐ English oral competition (☐ inorganic materials, ☐ organic materials)

■ Poster competition (■ inorganic materials, ☐ organic materials)

☐ Exhibition only (☐ inorganic materials, ☐ organic materials)

WS_2-Based Artificial Olfactory Synaptic System for Neuromorphic Computing and CNN-Based Recognition

I-Chun Lin, Chia-Yun Chen*
Department of Materials Science and Engineering, National Cheng Kung University, Tainan, Taiwan
*Correspondence: timcychen@mail.ncku.edu.tw

NSTC 113-2628-E-006-016-MY4

Abstract

With the rapid development of intelligent gas sensing and artificial olfactory systems, there is a growing demand for energy-efficient and highly integrated sensing technologies. Conventional metal oxide-based gas sensors, although widely used due to their high sensitivity, typically require high operating temperatures and suffer from high power consumption, poor selectivity, and limited compatibility with integrated electronic systems. In addition, most existing electronic nose systems rely on the Von Neumann architecture for data processing, where sensing signals must be transmitted to external processing units, resulting in significant data transfer latency and energy consumption. These limitations hinder their applications in real-time and low-power scenarios. In contrast, two-dimensional transition metal dichalcogenides (TMDs), owing to their high surface-to-volume ratio, tunable defect states, and excellent electrical properties, have emerged as promising candidates for next-generation gas sensing and neuromorphic devices.

In this work, WS_2 is employed as the core material to develop an artificial olfactory sensing device with synaptic functionalities. Through gas adsorption/desorption processes, the device exhibits synapse-like plastic electrical responses under gas stimulation. By applying pulsed stimuli and dynamic measurements, both short-term and long-term synaptic plasticity can be characterized, establishing a correlation between gas sensing behavior and synaptic weight modulation. Furthermore, the multilevel conductance states and nonlinear weight update characteristics of the device are incorporated into a convolutional neural network (CNN) model to evaluate its potential for gas recognition tasks. This study aims to overcome the separation between sensing and computing in conventional systems, and to realize a low-power artificial olfactory platform with integrated sensing, memory, and computing capabilities.

Experimental results demonstrate that the device exhibits stable and highly repeatable responses to NH_3 at room temperature. Under dynamic gas stimulation, typical synaptic behaviors, including paired-pulse facilitation (PPF) and long-term potentiation/depression (LTP/LTD), are successfully emulated. Moreover, as the gas stimulation frequency increases, the conductance of the device shows continuous and tunable modulation, indicating spike-rate-dependent plasticity (SRDP) characteristics. The multiple conductance states of the device are further mapped as synaptic weights and implemented in a CNN model for training and testing on the MNIST handwritten digit dataset. Using 60,000 training samples over 100 epochs, the validation accuracy rapidly reaches approximately 99% after around 20 epochs. These results demonstrate that the proposed memory device exhibits excellent recognition performance, highlighting its superior neuromorphic adaptability and near-ideal synaptic characteristics.

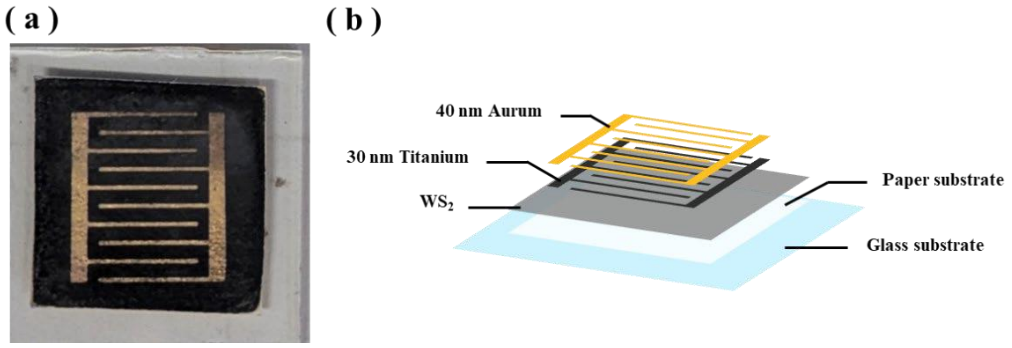

Fig. 1. (a) Actual picture of the device. (b) Schematic image of the device.

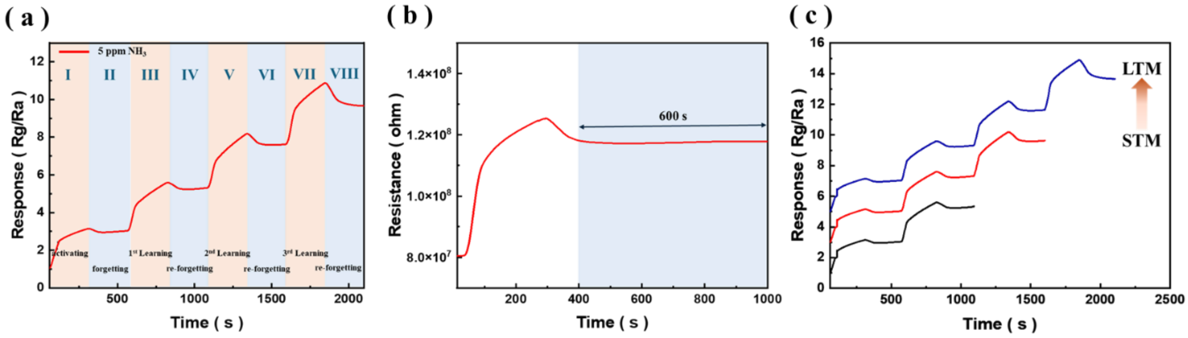

Fig. 2. (a) Multi-Level Learning and Forgetting Test Curve. (b) Short-Term to Long-Term Memory Transition Plot. (c) Long-Term Retention Time Test Plot.

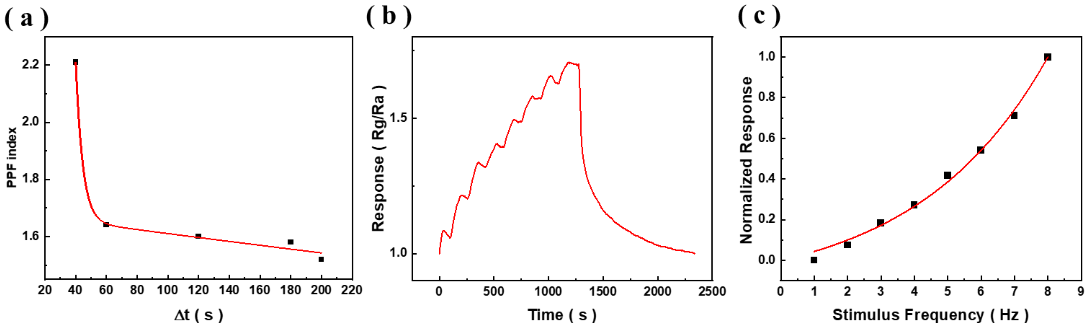

Fig. 3. (a) Paired-Pulse Facilitation (PPF) Index as a Function of Inter-Stimulus Interval. (b) Long-term potentiation and depression (LTP /LTD) measurement. (c) Spike-rate dependent plasticity (SRDP) measurement.

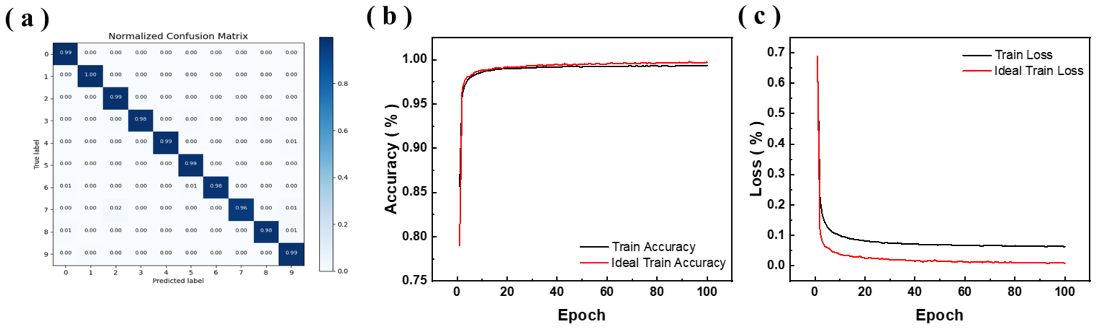

Fig. 4. (a) Confusion matrix showing the digit classification results for hand-written MNIST training datasets. (b) The recognition accuracy of our synaptic device with respect to training epoch. (c) The recognition loss of our synaptic device with respect to training epoch.

References

[1] Qin, Z., Song, X., Wang, J., Li, X., Wu, C., Wang, X., ... & Zeng, D. (2022). Development of flexible paper substrate sensor based on 2D WS2 with S defects for room-temperature NH3 gas sensing. *Applied Surface Science*, *573*, 151535.

[2] Liu, Y., Cai, D., Zhao, T., Shen, M., Liu, X., & Gu, D. (2024). Heterogeneous ion-modulated 2D-WS2 heterosynaptic memtransistor for controllable synaptic modulation and energy-efficient neuromorphic computing. *Chemical Engineering Journal*, *492*, 152215.

[3] Lee, S. W., Kang, M., Han, J. K., Yun, S. Y., Park, I., & Choi, Y.K. (2023). An artificial olfactory sensory neuron for selective gas detection with in-sensor computing. *Device*, *1*(3).

[4] Ko, J., Ock, C., Gim, H., Hong, K., Lee, Y., & Kwon, K. C. (2025). Two-dimensional materials for artificial sensory

devices: advancing neuromorphic sensing technology. *npj 2D Materials and Applications*, *9*(1), 35.

[5] Scardamaglia, M., Casanova-Cháfer, J., Temperton, R., Annanouch, F. E., Mohammadpour, A., Malandra, G., ... & Bittencourt, C. (2024). Operando Investigation of WS2 Gas Sensors: Simultaneous Ambient Pressure X-ray Photoelectron Spectroscopy and Electrical Characterization in Unveiling Sensing Mechanisms during Toxic Gas Exposure. *Acs Sensors*, *9*(8), 4079-4088.

[6] Mallik, S. K., Padhan, R., Sahu, M. C., Pradhan, G. K., Sahoo, P. K., Dash, S. P., & Sahoo, S. (2023). Ionotronic WS2 memtransistors for 6-bit storage and neuromorphic adaptation at high temperature. *npj 2D Materials and Applications*, *7*(1), 63.

Presentation type：

☐ English oral competition (☐ inorganic materials, ☐ organic materials)
■ Poster competition (■ inorganic materials, ☐ organic materials)
☐ Exhibition only (☐ inorganic materials, ☐ organic materials)

5083 鋁合金表面介金屬化合物放電被覆層之微觀組織與線性往復滑動磨耗行為研究

董昱賢、林哲立、吳瑞龍、林宏茂*
南臺科技大學化學工程與材料工程學系
hmlin@stust.edu.tw

摘要

本研究以 AA5083 鋁合金為基材，探討放電被覆參數與電極材料對其表面改質及磨耗性質之影響。首先，利用純鐵電極在不同放電電流（30A、40A 及 50A）條件下進行加工，分析放電能量對表面性質之影響；其次，在相同放電條件(放電電流為 50A)下，比較純鐵、FCD450 及高鉻鑄鐵電極對基材表面改質效果之差異。

實驗結果顯示，放電電流對放電層性質具有顯著影響，；在耐磨耗性方面，隨放電電流增加，試樣重量損失率降低，以 50A 條件表現最佳，推測與放電層厚度增加有關。耐腐蝕性結果顯示，放電被覆試片相較於基材呈現上升趨勢，推測是因表面放電層中之裂縫、孔隙及元素分布不均所導致之局部腐蝕行為。在電極材料影響方面，相同放電電流下，在耐磨耗性方面，以高鉻鑄鐵電極表現最佳，次佳是 FCD450 電極，純鐵電極表現則最差。在耐腐蝕性結果，同樣以高鉻鑄鐵電極表現最佳，純鐵電極表現次佳，表現最差則是 FCD450 電極，由磨耗損失量可知，添加鉻元素有助於提升耐磨耗性及耐腐蝕性。

参考文獻

[1] Stambekova, K., Lin, H. M., & Uan, J. Y. (2012). Surface modification of 5083 Al alloy by electrical discharge alloying processing with a 75 mass% Si–Fe alloy electrode. Applied surface science, 258(10), 4483-4488.

[2] Lin, H. M., Kuralay, S., & Uan, J. Y. (2011). Microstructural and corrosion characteristics of iron-silicon alloyed layer on 5083 Al alloy by electrical discharge alloying processing. *Materials Transactions*, *52*(3), 514-520.

[3] Stambekova, K., Lin, H. M., & Uan, J. Y. (2012). Microstructural and corrosion characteristics of alloying modified layer on 5083 Al alloy by electrical discharge alloying process with pure silicon electrode. Materials Transactions, 53(8), 1436-1442.

報告型式：

□英文口頭報告競賽 (□無機材料， □有機材料)
■海報展示並參加壁報論文競賽(■無機材料， □有機材料)
□只參加海報展示 (□無機材料， □有機材料)

以減水劑對水性磷酸鋁塗料粉體分散性及孔隙率與阻燃表現之影響

陸致豪 [1] 吳瑞泰 [1*] 蔡平賜 [1]
國立高雄科技大學化學工程與材料工程系
通訊作者:wrt@nkust.edu.tw

摘要

水性磷酸鋁具低煙、低毒、耐熱性佳、黏結性良好及可作為功能填料基材等優點，為具發展潛力之防火塗料。為提升其防火隔熱表現，通常需導入固化劑與無機填料建立塗料系統；然而，多種粉體添加易造成分散不良並增加用水需求，進而影響塗層孔隙率[1]與背板溫度表現[2]。為製備具較佳防火隔熱性能之磷酸鋁塗料，本研究先導入固化劑與功能性填料[3]；進一步參考水泥中強塑劑[4]改善粉體分散、減水並調整孔隙率之概念，將其導入水性磷酸鋁防火塗料中，並選用 SHMP [5]、BYK-190 [6] 與 PEG-12 [7] 作為減水劑，分別對應靜電/螯合、吸附-位阻及潤濕-位阻等分散機制，期藉由提升塗料中粉體分散性並減少用水量，進而調控孔隙率及背板溫度。

本研究首先以溶膠凝膠法製備磷酸鋁基膠[3]，並結合 $ZrO_2/TiO_2 = 9:1$（5、7.5、10 phr）作為共固化劑[3]，搭配 nano-SiO_2（0.5、1、1.5 phr）、莫來石（4、6、8 phr）及膨脹石墨（1、1.5、2 phr）等填料[8]作為控制因子與水準，依 $L_9(3^4)$ 田口直交表製備並建立磷酸鋁防火塗料（APC），並透過 1 h 背板終點溫度判斷最佳組別。接著，先評估三種減水劑之分散性，以粒徑大小與界達電位作為分散性判斷依據之作法[3,5]，於 pH 2 磷酸溶液中配製 0.5 wt% ZrO_2/TiO_2/nano-SiO_2 懸浮液，添加減水劑（0.05 wt%）後，進行動態光散射（DLS）與電泳光散射（ELS）分析。進一步以減水劑種類（SHMP、BYK-190、PEG-12）、減水劑濃度（0.5、1、1.5%）、減水率（10、20、30%）及檸檬酸添加量（0、0.1、0.2%）為控制因子與水準，其中檸檬酸作為緩凝劑[5]，依 $L_9(3^4)$ 田口直交表製備含減水劑塗料（WR），並透過孔隙率分析、背板溫度與吸濕性測試，評估各配方之孔隙率、背板溫度及吸濕性差異；再以田口法之 S/N 比分析，探討固化劑與填料配比對背板溫度之影響，以及減水劑配方與 WR 組孔隙率、背板溫度及吸濕性之關聯性。

實驗結果顯示，APC 最佳配方為 $ZrO_2/TiO_2 = 9:1$ 7.5 phr 、nano-SiO_2 1.5 phr、莫來石 4 phr 與膨脹石墨 1.5 phr，背板終點溫度為 230.3 ℃。APC 背板終點溫度之望小 S/N 比分析結果顯示，主要影響因子為 nano-SiO_2，次要影響因子為莫來石。分散性分析結果顯示，SHMP 表現最佳，DLS 粒徑為 325.88 nm，ELS 界達電位為 −19.46 mV。導入 WR 組田口配方後，孔隙率、背板終點溫度與吸濕率三項指標之最佳結果皆出現在同一配方，組成為 SHMP、減水劑濃度 1.5%、減水率 30% 與檸檬酸 0.2%；該組孔隙率為 7.83%，背板終點溫度為 210.3 ℃，吸濕率為 2.01%。WR 組孔隙率與背板溫度之望小 S/N 比分析結果顯示，共同主要影響因子為減水率，最佳水準為 30%；共同次要影響因子為減水劑種類，最佳水準為 SHMP。吸濕率之望小 S/N 比分析結果顯示，主要影響因子為減水劑種類，最佳水準為 BYK-190；次要影響因子為減水率，最佳水準為 30%。APC 組中共固化劑與無機填料之適當搭配可改善背板溫度表現；SHMP 於分散性分析中表現最佳，並與 WR 組中 SHMP 搭配 30% 減水率可同步降低孔隙率與背板溫度之結果相呼應，顯示減水劑可透過改善粉體分散性並降低用水量，使塗層孔隙率下降，進而降低背板溫度並提升阻燃表現。吸濕率之最佳水準偏向 BYK-190，代表吸濕性與阻燃表現並非完全由相同因子主導，減水劑配方設計仍需同時考量粉體分散性、孔隙率、背板溫度與吸濕率。關鍵字：磷酸鋁、防火塗料、減水劑、田口法

Keywords: Aluminum Phosphate、Fire-Resistant Coatings、Water-Reducing Agent、Taguchi Methods

報告型式：

□英文口頭報告競賽 (□無機材料， □有機材料)
☑海報展示並參加壁報論文競賽(☑無機材料， □有機材料)
□只參加海報展示 (□無機材料， □有機材料)

Antioxidant-Enhanced Oxidation Resistance of MXenes: A DFT Study

Yen Jou Wang[1], Ramadhass Keerthika Devi[1], Muthusankar Ganesan[2,3] , Chun Che Lin[1] , Ting-Wen Lai[4] , Hung-Lung Chou[4,5] , Huan-Tsung Chang[6,7]

[1]Research and Development Center for Smart Textile Technology, Institute of Organic and Polymeric Materials, National Taipei University of Technology, Taipei, Taiwan | [2]Super Micro Mass Research and Technology Center, Cheng Shiu University, Kaohsiung, Taiwan | [3]Center for Environmental Toxin and Emerging-Contaminant Research, Cheng Shiu University, Kaohsiung, Taiwan | [4]Graduate Institute of Applied Science and Technology, National Taiwan University of Science and Technology, Taipei, Taiwan | [5]Graduate Institute of Energy and Sustainability Technology, National Taiwan University of Science and Technology, Taipei, Taiwan | [6]Department of Biomedical Sciences, Chang Gung University, Taoyuan city, Taiwan | [7]Department of General Surgery, Division of Breast Surgery, Chang Gung Memorial Hospital, Taoyuan, Taiwan

*Correspondence: email@email.com

Abstract

MXenes are a class of two-dimensional transition metal carbides, nitrides, and carbonitrides derived from MAX phases, which exhibit excellent electrical conductivity, tunable surface chemistry, and broad applications in energy storage, catalysis, sensing, and electromagnetic shielding. However, their practical applications are significantly limited by rapid oxidation under ambient and aqueous conditions, leading to TiO_2 formation, structural degradation, and loss of functional properties. Therefore, improving the oxidation resistance and environmental stability of MXenes is essential for their long-term applications. In this study, a bio-inspired molecular passivation strategy is proposed by functionalizing $Ti_3C_2T_x$ nanosheets with catechin, a naturally occurring antioxidant, to enhance their oxidative stability.

Catechin molecules anchor onto the MXene surface through hydrogen bonding, π–π interactions, and coordination bonding with titanium atoms, forming a protective molecular layer that suppresses oxidation and blocks oxidative species such as O_2 and H_2O. Spectroscopic analyses reveal reduced TiO_2 formation and significant modifications in the electronic structure, including a decrease in work function and a transition from an indirect to a direct bandgap. Microscopy observations and elemental mapping confirm that the nanosheets maintain structural integrity and exhibit uniform catechin coverage, indicating effective surface passivation and long-term stability.

Density functional theory calculations further reveal strong catechin adsorption on the MXene surface and weakened interactions between MXenes and oxidative species, demonstrating an effective molecular shielding mechanism. The results suggest that catechin not only protects the MXene surface from oxidation but also modulates the electronic structure and surface chemistry. This work provides a sustainable and general strategy for improving the stability of oxidation-prone MXenes and other two-dimensional materials, offering new insights into molecular passivation and interfacial stabilization mechanisms for advanced nanomaterials.

References

The font is Times New Roman, 10pt, single space.

1. Li, X., Huang, Z., Shuck, C. E., Liang, G., Gogotsi, Y., & Zhi, C. (2022). MXene Chemistry, Electrochemistry and Energy Storage Applications, *Nat. Rev. Chem.* 2022, 6, 389–404. DOI: 10.1038/s41570-022-00387-0.
2. Zhang, C. J., Pinilla, S., McEvoy, N., Cullen, C. P., Anasori, B., Long, E., Park, S. H., Seral-Ascaso, A., Shmeliov, A., Krishnan, D., Morant, C., Liu, X., Duesberg, G. S., Gogotsi, Y., & Nicolosi, V. (2017). Oxidation Stability of Colloidal Two-Dimensional Titanium Carbides (MXenes), *Chem. Mater.* 2017, 29, 4848–4856. DOI: 10.1021/acs.chemmater.7b00745.
3. Wu, T., Kent, P. R. C., Gogotsi, Y., & Jiang, D. (2022). How Water Attacks MXene, *Chem. Mater.* 2022, 34, 4975–4982. DOI: 10.1021/acs.chemmater.2c00977.

Presentation type：

☐ English oral competition (☐ inorganic materials, ☐ organic materials)

❐ Poster competition (☑ inorganic materials, ☐ organic materials)

☐ Exhibition only (☐ inorganic materials, ☐ organic materials)

Turning defects into catalytic sites: DFT insights into green hydrogen production on Boron Nitride semiconductors

Hsin-Chieh Wu [a, †], Bo-Sheng Chen [a] and Hung-Lung Chou
[a,b,*] [a] Graduate Institute of Applied Science and Technology, National Taiwan University of Science and Technology, P. O.
Box 106, Taipei, Taiwan
[b] Graduate Institute of Energy and Sustainability Technology, National Taiwan University of Science and Technology,
P. O. Box 106, Taipei, Taiwan
[†]Reporter E-mail: aa0984281479@gmail.com
[*]Corresponding author’s e-mail: HLCHOU@mail.ntust.edu.tw

Abstract

With the continuous increase in global energy demand and the gradual depletion of fossil fuels, the development of renewable and environmentally friendly energy sources has become a critical issue in modern energy research. Hydrogen energy is considered one of the most promising zero-carbon energy carriers due to its high energy density and environmentally friendly nature, as its combustion product is only water without greenhouse gas emissions. Hydrogen can be used for energy storage, fuel cell power generation, and energy conversion systems, and it can also help address the intermittency of renewable energy sources. Currently, hydrogen production methods mainly include grey hydrogen, blue hydrogen, and green hydrogen, among which green hydrogen produced by water electrolysis using renewable energy is considered the most sustainable and environmentally friendly method. However, hydrogen production still faces challenges such as high production cost, limited infrastructure, and energy conversion efficiency. Therefore, developing efficient and low-cost hydrogen production technology is essential.

In recent years, two-dimensional materials have been widely used in water splitting catalysis due to their high surface area, abundant active sites, good electronic transport properties, and tunable structures. Among these materials, hexagonal boron nitride (h-BN) has excellent thermal stability, chemical stability, and mechanical strength, making it a promising catalytic material. However, pristine h-BN lacks dangling bonds and active sites, which limits its catalytic performance. Therefore, defect engineering is an effective strategy to modify the electronic structure and create active sites on h-BN to enhance its catalytic activity. In this study, density functional theory (DFT) calculations were used to investigate the catalytic behavior of defective hexagonal boron nitride nanosheets for hydrogen production via water splitting. The results show that boron vacancy defects can significantly reduce the reaction energy barrier and improve catalytic activity, while nitrogen vacancy defects result in higher energy barriers. These findings demonstrate that defect engineering plays a crucial role in tuning catalytic activity and confirm the potential of defective h-BN for hydrogen production and sustainable energy applications.

References

[1] Yue, M., Lambert, H., Pahon, E., Roche, R., Jemei, S., & Hissel, D. (2021). Hydrogen energy systems: A critical review of technologies, applications, trends and challenges, Renew. Sustain. Energy Rev. 2021, 146, 111180. DOI: 10.1016/j.rser.2021.111180.

[2] You, B., & Sun, Y. (2018). Innovative strategies for electrocatalytic water splitting, Acc. Chem. Res. 2018, 51 (7), 1571–1580. DOI: 10.1021/acs.accounts.8b00002.

[3] Wang, Q., & Domen, K. (2019). Particulate photocatalysts for light-driven water splitting: Mechanisms, challenges, and design strategies, Chem. Rev. 2019, 120 (2), 919–985. DOI: 10.1021/acs.chemrev.9b00201.

Presentation type：

☐ English oral competition (☐ inorganic materials, ☐ organic materials)

☑ Poster competition (☐ inorganic materials, ☐ organic materials)

☐ Exhibition only (☐ inorganic materials, ☐ organic materials

基於端到端實例分割與自適應局部閾值之PEO塗層巢狀孔洞量化分析系統

許甯翔 [1], 陳柏淞 [1], 梁辰睿 [1*]

[1] 人工智慧技術與應用學士學位學程, 逢甲大學, 台中, 台灣

cjliang@o365.fcu.edu.tw

NSTC 114-2813-C-035-091-E

摘要

電漿電解氧化（Plasma Electrolytic Oxidation, PEO）塗層之表面微孔形貌具有高度不規則、跨尺度分布及孔中有孔（Hole-in-Hole, HIH）等特性。由於膜層表面形貌複雜且受三維結構因素影響，傳統全域閾值或人工判讀方法難以準確辨識與量化孔洞尺寸、孔隙率及其內部巢狀結構，限制其於材料微結構分析與製程參數優化上的應用。本研究以前期改良型 U-Net 語意分割成果為基礎，進一步聚焦於 PEO 多尺度巢狀孔洞之實例級辨識與量化，提出一套結合端到端 Mask R-CNN、自適應局部閾值、形態學後處理與 FastAPI 後端服務之自動化分析系統。研究流程包括多尺度 SEM 影像資料建置、端到端與雙階段偵測—分割架構比較、外層孔洞實例分割後之 ROI 內 HIH 分析，以及 Web 化量測平台整合。結果顯示，端到端 Original Mask R-CNN 於 mIoU、Dice、Boundary F1 與 Hausdorff Distance 等指標上均優於 YOLO 前置偵測之雙階段流程，並經像素級融合後將整體mIoU 提升至 0.908。系統亦可輸出 Porosity、Hole Count、Total Area、Avg Circularity、HIH Area 與 HIH% 等量化指標。整體結果顯示，本研究可由外層孔洞輪廓進一步延伸至巢狀孔內結構之量化表徵，提供一套具重現性與工程實用性的 PEO 微結構影像分析方案。

1. 簡介

電漿電解氧化（Plasma Electrolytic Oxidation, PEO）為閥金屬表面改質中具代表性的處理技術，可在鋁、鎂與鈦等基材表面形成兼具抗腐蝕、耐磨耗與電絕緣特性之陶瓷化氧化層。然而，PEO 塗層生成過程伴隨放電、熔融、重凝固與局部破裂等複雜機制，最終形成具多孔、跨尺度且邊界模糊之表面拓撲。此類孔洞之孔徑大小、孔隙率、連通性與巢狀分布特徵，與膜層之腐蝕防護能力、生物相容性及界面功能密切相關 [1]–[4]。

現行 PEO 影像量測仍常依賴全域閾值、人工框選或傳統影像分析方法處理孔洞面積與孔隙率；但在面對孔洞黏連、亮暗不均、孔內再生暗區與巢狀拓撲時，常出現過度分割、漏檢與主觀差異等問題，難以支撐高通量且可重現的材料量化分析 [5]–[7]。因此，本研究延續前期以改良型 U-Net 建立之語意分割成果 [8]，進一步將研究重心由孔洞前景擷取推進至實例級外輪廓辨識與孔內深層結構量化，並以端到端 Mask R-CNN 架構為核心，搭配用於孔中有孔（HIH）辨識之自適應局部閾值分析模組與 Web 化部署流程，發展一套可用於 PEO 多尺度巢狀孔洞分析之整合系統。

2. 實驗方法

2.1 整體系統架構

本研究所提出之 PEO 塗層巢狀孔洞量化分析流程如圖 1 所示，整體架構包含資料建置、外層孔洞實例分割、HIH 區域偵測，以及量化分析與系統整合四個模組。

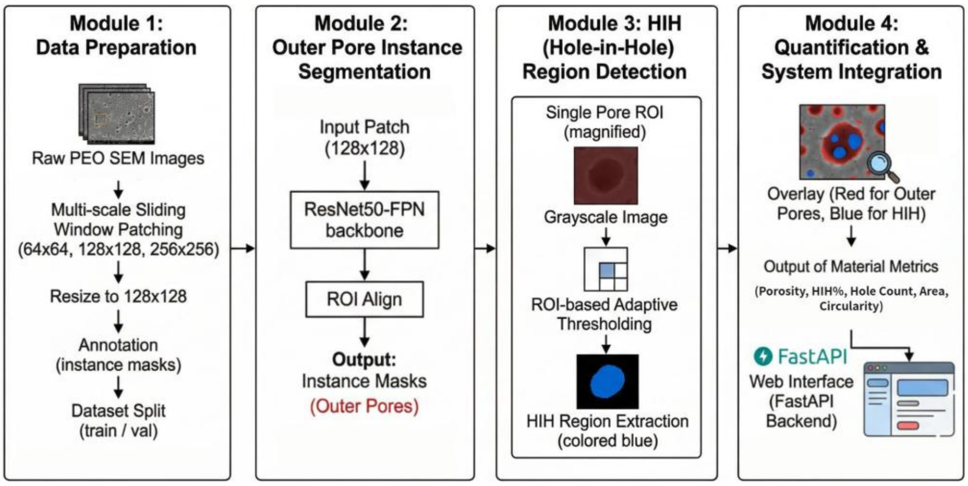

圖 1 本研究 PEO 塗層巢狀孔洞量化分析系統之整體流程圖

系統首先將原始掃描式電子顯微鏡（SEM）影像進行多尺度滑動視窗切割、尺寸統一與實例標註，以建立訓練與驗證資料集；其次，透過端到端 Mask R-CNN 對外層孔洞進行實例分割，輸出像素級孔洞遮罩；接續於單一孔洞 ROI 內執行自適應局部閾值分析，以擷取孔內深層暗區與 HIH 結構；最後，結合幾何量測、孔隙率統計與 FastAPI 後端部署，輸出孔洞與 HIH 相關量化指標並完成 Web 化分析。此一分層式設計可兼顧外層輪廓辨識與內層結構解析，降低全域閾值造成之誤判，並提升巢狀孔洞量化分析之準確性與可解釋性。

2.2 影像資料與實例分割方法

本研究資料來源為 7 張鎂合金 PEO 塗層之掃描式電子顯微鏡（SEM）影像，原始解析度為 1280×840 像素。由於 PEO 表面孔洞具有明顯之跨尺度特性，同一影像中常同時包含微小孔洞、較大孔洞及其相互黏連或巢狀分布之情形，若僅以單一尺度進行分析，容易造成局部細節遺失或整體拓撲資訊不足。因此，本研究採用滑動視窗進行多尺度切塊，分別擷取 64×64、128×128 與 256×256 之影像區塊，並統一縮放至 128×128 作為模型輸入，以兼顧微小孔洞細節與整體結構特徵。另一方面，為降低類別不平衡對模型訓練所造成之影響，本研究進一步依據孔洞覆蓋率進行樣本篩選，捨棄覆蓋率低於 1% 之背景區塊。經上述處理後，最終共建立 8,525 張有效影像區塊，並以固定隨機種子劃分為訓練集 6,820 張與驗證集 1,705 張，以確保實驗設定之一致性與可重現性。

在模型設計上，本研究以 Mask R-CNN 為核心實例分割架構，並採用 ResNet50-FPN-v2 作為主幹網路。該端到端架構可同時建模孔洞間之相對空間關係與局部紋理特徵，特別適合處理 PEO 微孔形貌中常見之黏連邊界、不規則輪廓與巢狀拓撲。相較於僅進行像素前景—背景分類之語意分割方法，實例分割能進一步將相互接觸之孔洞解耦為獨立實體，因而更有利於後續幾何量測與孔內結構分析。本文亦評估以 YOLOv26s 產生候選區域後再進行分割之雙階段方法，惟結果顯示該流程因前置裁切造成上下文資訊不足，易影響邊界重建與整體分割表現。因此，本文後續分析皆以端到端 Mask R-CNN 主線架構作為主要方法。另亦評估多種注意力模組與損失函數設計作為消融比較，以分析不同設計對 PEO 微孔影像之適配性，但本文重點仍聚焦於端到端 Mask R- CNN 主線架構之整體效能表現。

2.3 HIH 分析與量化模組

為進一步識別 PEO 孔洞內部之深層結構，本研究於每一個經實例分割取得之外層孔洞內建立感興趣區域（Region of Interest, ROI），並於該區域中執行自適應局部閾值分析。此設計之核心目的，在於將外層孔洞輪廓辨識與孔內結構解析加以分層處理：前者主要依賴深度學習模型擷取不規則邊界與空間關係，後者則著重於孔洞內部灰階分布變化所反映之深層暗區與巢狀拓撲特徵。

本研究所採用之自適應局部閾值策略，係依據 ROI 內部之局部灰階分布動態調整門檻值，使不同孔洞在亮度、尺度與局部對比度不一致之情況下，仍能保有相對穩定之結構辨識能力。具體而言，系統先以外層孔洞遮罩限制分析範圍，再針對 ROI 內部像素強度分布進行局部統計，以估計適合該孔洞內部的閾值條件，進而萃取潛在之 HIH 區域。此一設計可有效降低整體亮度不均、表面陰影與局部對比變化對偵測結果造成之干擾，並避免全域閾值在低對比區域產生過度分割或漏檢問題。在取得初步 HIH 二值結果後，系統進一步結合形態學開閉運算與小面積雜訊濾除，以去除孤立像素、修補局部破碎區塊，並保留具有空間連續性與幾何合理性之候選結構。經過上述處理後，HIH 遮罩可與對應之外層孔洞遮罩進行關聯分析，以計算單一孔洞內部之 HIH 面積、整體 HIH 面積，以及 HIH 占外層孔洞面積之比例（HIH%）等統計指標。透過這些量化資訊，系統不僅能描述孔洞是否存在，亦可進一步分析其內部是否具有再分化或巢狀化之微結構特徵。

在量化分析模組中，本研究基於像素級遮罩統計及連通元件分析，計算孔洞面積、周長、圓度、平均孔徑與孔隙率等幾何特徵，其中孔隙率定義為孔洞總面積占有效分析區域之比例。相較於僅能輸出外層孔洞面積與總孔隙率之傳統量測方式，本研究所提出之 HIH 分析流程可將量測層級由外輪廓辨識延伸至孔內二級結構解析，提升對 PEO 巢狀孔洞拓撲之表徵能力。

為提升方法之實務應用性，本文另建置以 FastAPI 為基礎之後端服務，整合影像上傳、模型推論、比例尺校準與量測結果視覺化，使整體系統由離線模型延伸為可操作之工程化量測平台。藉由將外層孔洞分割、HIH 結構解析與量化指標輸出整合於同一流程中，本研究不僅提升孔洞分析之自動化程度，也為後續製程參數與微觀結構關聯分析提供更細緻且具可解釋性之量測依據。

3. 結果與討論

前期改良型 U-Net 已建立本研究之語意分割基線，其於驗證集達到 mIoU 0.8880 與 DSC 0.9387，並可結合連通元件分析進行孔洞數量與孔隙率估計 [8]。然而，語意分割方法本質上難以區分相互接觸之孔洞實例，亦不易解析孔洞內部之巢狀結構與再生暗區，因此本研究進一步導入實例分割與 HIH 分析機制，以提升孔洞分離與結構解析精度。如表 1 所示，在 PEO 多孔與巢狀拓撲影像中，端到端實例分割顯著優於雙階段偵測—分割流程。雙階段 YOLOv26s → Mask R-CNN 架構之 mIoU 為 0.7016，而端到端 Mask R-CNN 可達 0.8977，提升 0.1961；在 Dice、Boundary F1 與 Hausdorff Distance 等指標上亦呈現一致性改善，顯示端到端架構在區域完整性與邊界準確性上具明顯優勢。此結果說明，對於 PEO 微孔此類邊界不規則且具巢狀結構之材料影像而言，維持完整影像視野與全域上下文資訊，是提升實例分割效能之關鍵因素。此外，透過像素級融合策略，整體 mIoU 可進一步提升至 0.908，顯示不同模型間之特徵互補有助於提升邊界平滑性並降低局部雜訊影響。

表 1 雙階段與端到端實例分割架構之量化效能比較

評估指標	雙階段架構（YOLOv26s → Mask R-CNN）	端到端架構（Original Mask R-CNN）
架構類型	解耦式（Decoupled）	端到端（End-to-End）
運算流程	YOLOv26s 偵測→裁切→Mask R-CNN 分割	單一 ResNet50-FPN-v2 特徵提取與分割
mIoU	0.7016	0.8977
Dice Coefficient	0.8114	0.9456
Precision	0.7842	0.9258
Recall	0.8728	0.9683
Boundary F1	0.7224	0.9802
Hausdorff Distance (px)	25.55	10.92

在系統實作層面，如圖 2 所示，本研究已完成孔洞與 HIH 分割結果之視覺化展示，並可輸出 Porosity、Hole Count、Total Area、Hole Area、Avg Circularity、Avg Diameter、HIH Area 與 HIH% 等關鍵量測指標。系統並整合影像上傳、比例尺校準、孔洞分割與 HIH 分析流程，使整體方法由模型驗證進一步延伸為具實際量測能力之工程化分析系統。

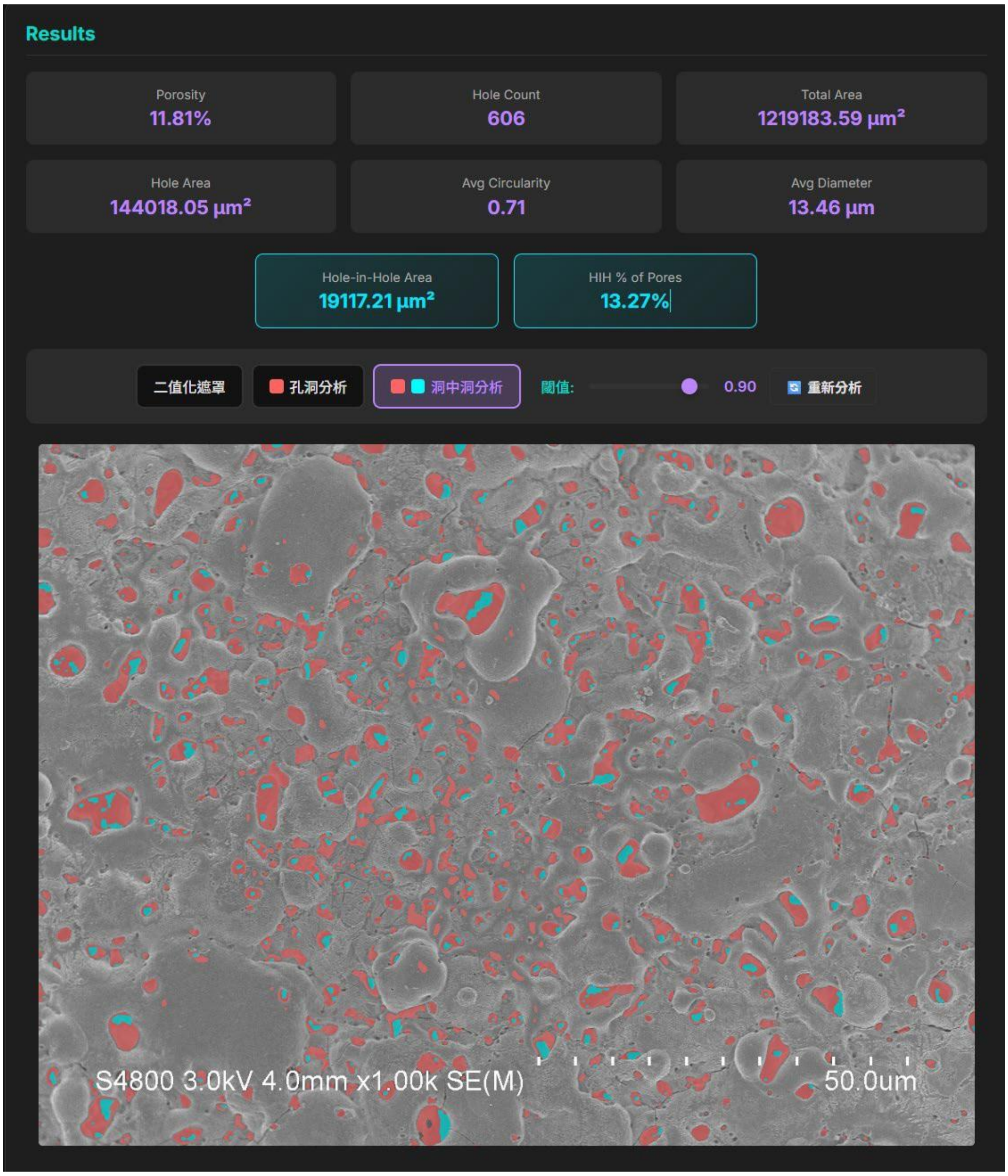

Results

Porosity 11.81%
Hole Count 606
Total Area 1219183.59 μm²
Hole Area 144018.05 μm²
Avg Circularity 0.71
Avg Diameter 13.46 μm
Hole-in-Hole Area 19117.21 μm²
HIH % of Pores 13.27%

閾值: 0.90

圖 2 孔洞與 HIH 分割結果及量化指標視覺化介面

4. 結論

本研究針對 PEO 塗層多尺度巢狀孔洞之量化分析問題，提出一套結合端到端實例分割、自適應局部閾值分析與 Web 化系統整合之方法架構。相較於前期僅能進行前景—背景區分之語意分割模型，本研究進一步實現孔洞實例級辨識，並透過 ROI 局部閾值策略延伸至孔內深層結構（HIH）之量測分析，建立由外層輪廓至內層巢狀結構之分層式解析流程。

實驗結果顯示，端到端 Mask R-CNN 於 mIoU、Dice 及邊界相關指標上均優於雙階段偵測—分割架構，並可透過像素級融合進一步將整體分割表現提升至 mIoU 0.908。此外，本研究完成包含影像上傳、比例尺校準、模型推論與量測輸出之 FastAPI Web 平台，使整體方法由離線模型推進為具工程應用潛力之量測工具。整體而言，本研究顯示深度學習模型可有效嵌入材料分析流程中，提升孔洞量測之效率、一致性與結構解析能力，並為後續 PEO 製程參數分析提供更具解釋性之量化指標。未來可進一步結合 3D 結構重建、多模態影像資訊與製程參數回歸分析，以深化對材料微結構形成機制之理解。

參考文獻

[1] Yerokhin, A.L., Voevodin, A.A., Lyubimov, V.V., et al.: Plasma electrolytic fabrication of oxide-ceramic surface layers for tribotechnical purposes on aluminium alloys. *Surf. Coat. Technol.* 110(3), 140–146 (1998)

[2] Kaseem, M., Fatimah, S., Nashrah, N., Ko, Y.G.: Recent progress in surface modification of metals coated by plasma electrolytic oxidation: Principle, structure, and performance. *Prog. Mater. Sci.* 117, 100735 (2020)

[3] Lugovskoy, A., Zinigrad, M.: Plasma electrolytic oxidation of valve metals. Mater. Sci. - Adv. Topics, 85–102 (2013)

[4] Liang, C.J.: In-situ impedance spectroscopy studies of the plasma electrolytic oxidation coating process. Ph.D. dissertation, The University of Sheffield (2013)

[5] Thompson, G.E.: Porous anodic alumina: Fabrication, characterization and applications. *Thin Solid Films* 297(1–2), 192–201 (1997)

[6] Otsu, N.: A threshold selection method from gray-level histograms. *IEEE Trans. Syst., Man, Cybern.* 9(1), 62–66 (1979)

[7] Koroleva, E.V., Thompson, G.E., Hollrigl, G., et al.: Surface morphological changes of aluminium alloys in alkaline solution: Effect of second-phase material. *Corros. Sci.* 41(8), 1475–1495 (1999)

[8] Hsu, N.-H., Chen, P.-S., Yang, X.-S., Liang, C.-J.: Automated semantic segmentation and quantitative analysis of pore structures in PEO coatings using a modified U-Net framework. In: Proc. IIHMSP (2025)

報告型式：

□英文口頭報告競賽 (□無機材料， □有機材料)
☑海報展示並參加壁報論文競賽(☑無機材料， □有機材料)
□只參加海報展示 (□無機材料， □有機材料)

GO@MOF-177/Matrimid Mixed Matrix Membranes for Enhanced CO_2/N_2 Gas Separation

Ying-Ru Chen[1, †], Hung-Lung Chou[1,2,3,*], Tawqeer Zamrood[1], Chien-Chieh Hu[2] [1]
Graduate Institute of Applied Science and Technology,
National Taiwan University of Science and Technology,Taipei, 10607, Taiwan
[2]Graduate Institute of Applied Science and Technology, Advanced Membrane Materials Research Center,
NationalTaiwan University of Science and Technology, Taipei,10607, Taiwan
[3]Graduate Institute of Energy and Sustainability
Technology, National Taiwan University of Science and Technology,Taipei, 10607, Taiwan
[†]Reporter E-mail: iris0521ru@email.com
*Corresponding E-mail address: HLCHOU@mail.ntust.edu.tw

The NSTC project number: MOST 111-2221-E-011-95-MY3 and MOE

Abstract

This work presents the fabrication of a high-performance mixed matrix membrane (MMM) through the incorporation of graphene oxide-supported MOF-177 (GO@MOF-177) into a Matrimid® polymer matrix using a two-step preparation method. The GO@MOF-177 composite was synthesized via an in-situ growth approach, which improved interfacial compatibility and enabled uniform dispersion of the filler within the polymer matrix. The incorporation of 3 wt% GO@MOF-177 resulted in a significant enhancement in gas separation performance, increasing the CO_2 permeability from 7.3 to 44.5 barrer and improving the CO_2/N_2 selectivity from 28.5 to 59.3. To better understand the gas transport behavior, molecular dynamics (MD) simulations were performed to evaluate gas diffusivity, solubility, permeability, selectivity, and fractional free volume (FFV). The simulation results showed that the FFV increased from 1.72 for pristine Matrimid to 1.99 for the Matrimid/GO@MOF-177 (3 wt%) membrane. This increase in FFV led to a nearly twofold increase in CO_2 diffusivity (from 3.03×10^{-7} to 6.05×10^{-7} cm^2 s^{-1}), while the diffusivity of N_2 increased only slightly from 1.25 to 1.68×10^{-7} cm^2 s^{-1}. In addition, CO_2 exhibited stronger adsorption affinity toward the membrane matrix compared to N_2.The simulated permeability and selectivity were in close agreement with the experimental results, with deviations within 5%, confirming the reliability of the MD simulation approach. Overall, the results demonstrate that GO@MOF-177 is a promising filler for the development of next-generation mixed matrix membranes with improved gas separation performance.

References

[1] M.S. Rostami, M.M. Khodaei, Effect of incorporated hybrid MIL-53 (Al) and MWCNT into PES membrane for CO_2/ CH_4 and CO_2/N_2 separation, Fuel 356 (2024) 129598, https://doi.org/10.1016/j.fuel.2023.129598.

Presentation type：

English oral competition (inorganic materials, organic materials)

Poster competition (inorganic materials, organic materials)

Exhibition only (inorganic materials, organic materials)

Enhanced Gas-Phase Photocatalytic Degradation of Volatile Organic Compounds Using Synthesized Spherical Catalysts in a Fluidized Bed System for Industrial Air Purification

Ming-Wei Chen [1], Chien-Ho Chen [2], and Chao-Wei Huang[1*]
[1]Department of Engineering Science, NCKU
[2]Department of Biotechnology and Bioindustry Sciences, NCKU
*Correspondence: huangcw@gs.ncku.edu.tw

Abstract

In this study, a spherical photocatalyst was synthesized and used to degrade isopropyl alcohol (IPA), which is a common volatile organic compound (VOC), in a fluidized bed system.The spherical catalyst was prepared through a simple synthesis process and then heated to improve its stability and activity. The spherical shape helps increase the surface area and allows better contact with the pollutant.Under UV-visible light, the catalyst can effectively break down IPA in the gas phase. This improves the removal efficiency of VOCs and helps reduce air pollution.The material properties were analyzed by several methods, and the results showed that the synthesized spherical catalyst has good potential for gas-phase photocatalytic degradation. In the future, this system is expected to be widely applied in industrial exhaust gas treatment and large-scale air purification systems, providing an efficient and sustainable solution for environmental pollution control and contributing to the development of green industry.

Presentation type：

☐ English oral competition (☐ inorganic materials, ☐ organic materials)
☑ Poster competition (☑ inorganic materials, ☐ organic materials)
☐ Exhibition only (☐ inorganic materials, ☐ organic materials)

Sustainable and Scalable Aqueous Inorganic Coatings with Low VOC Emissions for Passive Daytime Radiative Cooling

Hsiu-Mei Yao [1], To-Yu Wang[1], Ming-Wei Chen [1], Hsin-Yu Fan [1], Chao-Wei Huang *[1]

[1]*Department of Engineering Science, National Cheng Kung University, Tainan, Taiwan, 701012*

*Corresponding author e-mail: huangcw@gs.ncku.edu.tw

ABSTRACT

Reducing building cooling demand without energy input has become increasingly important for sustainable development. Passive daytime radiative cooling(PDRC)addresses this challenge by combining strong solar reflection with thermal emission through the mid-infrared atmospheric window(8-13 μm)[1]. However, most existing PDRC coatings depend on organic polymer binders and solvent-based fabrication processes, which result in high VOC emissions and compromise mechanical reliability and long-term outdoor performance[2].

To overcome these limitations, we propose an inorganic, water-based radiative cooling coating composed of ball-milled ZrO_2 particles embedded in a Na_2SiO_3 matrix. This system is fabricated through a simple and scalable aqueous process, significantly reducing environmental impact. The coating exhibits a high solar reflectance of 91.39% and a mid-infrared emissivity of 0.89, with a low VOC content of 86 g/L. Under intense solar irradiation(933 W/m²) and humid conditions(65.37%), it achieves a temperature reduction of 5.8°C. In addition, the coating demonstrates strong mechanical durability, hydrophobic behavior, and resistance to contamination, highlighting its potential for practical, low-carbon building applications.

Keywords: Passive radiative cooling coating, Ball-milling method, ZrO_2 particles, Inorganic aqueous coating, Na_2SiO_3 matrix, and Low-VOC content

References:

[1] H. Zhai, D. Fan, Q. Li, Scalable and paint-format-colored coatings for passive radiative cooling, Solar Energy Materials and Solar Cells, 245 (2022) 111853.

[2] W. Huang, Y. Chen, Y. Luo, J. Mandal, W. Li, M. Chen, C.-C. Tsai, Z. Shan, N. Yu, Y. Yang, Scalable Aqueous Processing-Based Passive Daytime Radiative Cooling Coatings, Advanced Functional Materials, 31 (2021) 2010334.

Presentation type：

☐ English oral competition (☐ inorganic materials, ☐ organic materials)
■ Poster competition (■ inorganic materials, ☐ organic materials)
☐ Exhibition only (☐ inorganic materials, ☐ organic materials)

Coherent Transport and Anomalous Thermal Transfer Characteristics in Functional Graphene Phononic Crystals

Chien-Yu Chen[1], I-Ling
Chang[1*] [1] Department of Mechanical Engineering, National Cheng Kung
University, Taiwan
*Correspondence: ilchang@mail.ncku.edu.tw

Abstract

Although graphene has exceptionally high thermal conductivity, practical thermoelectric and thermal-management applications often require structural strategies to reduce and control heat transport. Introducing periodic isosceles triangular nanopores into graphene forms a phononic crystal, where thermal transport may transition from scattering- dominated behavior to wave-interference-related coherent transport as the unit-cell length decreases, resulting in non- monotonic thermal-conductivity trends. This work uses non-equilibrium molecular dynamics (NEMD) to consolidate prior results and evaluate the effects of unit-cell length, pore rotation angle (0°, 60°, 120°, and 180°), free-slab length, system temperature (200K and 300K), and periodic arrangement. Thermal conductivity is calculated using Fourier's law, and phonon-correlation analysis is used to interpret transport mechanisms. The results indicate that coherent transport can be observed in graphene phononic crystals, with low-frequency phonons as the dominant contributors; coherent features are more evident at 200K, increasing free-slab length raises thermal conductivity, and changing periodic arrangement lowers thermal conductivity while preserving the coherent-transport trend.

Keywords: non-equilibrium molecular dynamics, graphene phononic crystal, coherent transport, angle effect, temperature effect

Presentation type：

English oral competition (inorganic materials, organic materials)
☑ Poster competition (☑ inorganic materials, organic materials)
Exhibition only (inorganic materials, organic materials)

具抗菌功能之 CaZnAl-LDHs 作為 PET 觸媒之合成及其酯粒化與物性分析研究

張育慈、賴孝武*
南臺科技大學 化學工程與材料工程系
swlai@stust.edu.tw

摘要

層狀雙氫氧化物（Layered double hydroxides, LDHs）為由二價與三價金屬離子構成之層狀材料，層間含有可交換陰離子與水分子，具備良好的結構可調控性與應用潛力，廣泛應用於吸附、催化及抗菌等領域。

本研究採用共沉澱法合成 CaZnAl-LDHs，並調控金屬莫耳比（4:2:1、3:3:1、2:3:1、2:7:1）以探討其對材料性質之影響。FT-IR 分析結果顯示 O–H、CO_3^{2-} 及金屬–氧鍵（Al–O、Zn–O、Ca–O）等特徵峰，證實 LDHs 結構成功形成。抗菌測試結果顯示，所製備材料對菌種具有抑制效果，具潛在抗菌應用價值。並進一步將 LDHs 導入高分子基材進行酯粒化製程，LDHs 於聚合過程中可參與反應並影響材料形成行為，顯示其具潛在觸媒功能並透過熱重分析（TGA）與差示掃描量熱分析（DSC）評估其熱性質。結果顯示，添加 LDHs 可影響材料之熱穩定性與熱轉換行為，顯示其具材料改質效果。

綜合而言，CaZnAl-LDHs 具備可調控之結構特性與抗菌功能，並可提升高分子材料之性能，展現其於功能性複合材料之應用潛力。

參考文獻

[1] E. L. Crepaldi, P. C. Pavan, and J. B. Valim, “Comparative study of the coprecipitation methods for the preparation of Layered Double Hydroxides,” *Journal of the Brazilian Chemical Society*, vol. 11, no. 1, pp. 64–70, Feb. 2000, doi: 10.1590/s0103-50532000000100012.

[2] K. Xie *et al.*, “Preparation and antibacterial properties of copper phthalate/polyethylene terephthalate composition fiber,” *Alexandria Engineering Journal*, vol. 75, pp. 271–278, Jun. 2023, doi: 10.1016/j.aej.2023.05.083.

[3] S. Dong, Y. Jia, X. Xu, J. Luo, J. Han, and X. Sun, “Crystallization and properties of poly(ethylene terephthalate)/layered double hydroxide nanocomposites,” *Journal of Colloid and Interface Science*, vol. 539, pp. 54–64, Dec. 2018, doi: 10.1016/j.jcis.2018.12.030.

報告型式：

□英文口頭報告競賽 (□無機材料， □有機材料)
☑海報展示並參加壁報論文競賽(☑無機材料， □有機材料)
□只參加海報展示 (□無機材料， □有機材料)

以回收石膏經焙燒與水熱法之長晶製程研究

翁宇賢[1]、賴孝武[1]、黃常寧[2*]
[1] 南臺科技大學 化學工程與材料工程系
[2] 東華大學材料科學與工程學系
cnhuang@gms.ndhu.edu.tw

摘要

本研究以回收石膏為原料，結合焙燒與水熱長晶技術，系統探討焙燒溫度、水熱時間及各類添加劑對二水硫酸鈣晶體生長行為與形貌調控之影響。熱分析結果顯示，回收石膏經適當熱處理後可有效轉化為半水石膏，作為後續水熱反應之反應前驅物。實驗中藉由無機鹼性添加劑與有機羧酸類添加劑調整反應環境，以影響晶體成核與成長行為。

結果顯示，鹼性添加劑可透過提高系統鹼度及提供鈣離子來源，降低過度成核現象並促進既有晶體沿特定方向成長，使晶體於較短時間內形成較完整之柱狀結構；相較之下，溶解速率較低之鈣源添加劑於反應初期仍以細小針狀晶體為主。進一步比較不同有機酸添加劑對晶體形貌之影響，發現適量添加可使晶體由細針狀逐漸轉變為柱狀或塊狀結構，粒徑明顯提升且長寬比降低，而過量添加則可能因抑制晶體生長而生成較多細小等軸晶粒，不利於目標粒徑形成。

結合以上結果，本研究建立了一套水熱長晶及添加劑協同調控之回收石膏晶體成長策略，可有效改善回收石膏晶體形貌，使其接近工業副產石膏之柱狀／塊狀特徵，為回收石膏高值化利用與循環再應用提供可行之技術基礎。

參考文獻

[1] K. He, Y. Wang, X. Zhou, C. Li, and Y. Han, “In situ transmission electron microscopy explores a new nanoscale pathway for direct gypsum formation in aqueous solution,” ACS Applied Nano Materials, vol. 1, no. 10, pp. 5430–5440, 2018.

[2] H. R. Corti and R. Fernandez-Prini, “Thermodynamics of solution of gypsum and anhydrite in water over a wide temperature range,” Canadian Journal of Chemistry, vol. 62, no. 3, pp. 484–488, 1984.

[3] J. D. Qu, J. H. Peng, and B. Z. Li, “Effect of citric acid on the crystal morphology of gypsum and its action mechanism,” Advanced Materials Research, vol. 250, pp. 321–326, 2011.

報告型式：

□英文口頭報告競賽 (□無機材料， □有機材料)
■海報展示並參加壁報論文競賽(■無機材料， □有機材料)
□只參加海報展示 (□無機材料， □有機材料)

微波輔助水熱法製備氧化鎳鈷/硫化鋅異質結構於光催化分解水產氫之應用

張芷芯[1] 潘慧鑫[2] 翁廷華[3] 馬溢恩[4] 劉璟霖[5] 沈柏霖[6] 徐杰綸[7] 張育誠[8]
逢甲大學材料科學與工程學系
D1291400@o365.fcu.edu.tw

NSTC 112-2221-E-035-017-MY3 and NSTC 113-2221-E-035-023-MY3

摘要

近年來，隨著全球能源需求持續攀升與環境永續意識抬頭，開發高效率且穩定的光催化產氫材料已成為新能源研究的重要課題。其中，金屬氧化物半導體因具備優異的化學穩定性、可調控能帶結構以及良好的光催化反應能力，受到廣泛關注，被視為實現潔淨氫能技術的關鍵材料之一。本研究以具快速升溫、反應均勻及節能優勢的微波輔助水熱法，成功合成氧化鎳鈷（$NiCo_2O_4$）奈米結構，並進一步利用相同製程設計與製備氧化鎳鈷/硫化鋅（$NiCo_2O_4/ZnS$）異質結構光催化材料。透過異質接面工程的導入，可有效整合兩種半導體材料的優勢，提升光吸收能力與電荷分離效率，進一步增強光催化產氫表現。在製程優化方面，本研究系統性調控前驅物濃度、反應溫度、反應時間以及不同犧牲試劑等關鍵參數，深入探討各種形成條件對材料表面形貌、晶體結構、界面接觸特性及光催化分解水產氫效率之影響，以建立最佳製備條件與反應機制。材料特性分析則藉由 X 射線繞射儀（XRD）、掃描式電子顯微鏡（SEM）及穿透式電子顯微鏡（TEM）等先進儀器進行全面性鑑定，確認材料之晶相組成、奈米形貌與異質界面結構。研究結果顯示，氧化鎳鈷與硫化鋅複合後所形成之 $NiCo_2O_4/ZnS$ 異質結構，相較於單一氧化鎳鈷奈米材料，能有效促進光生電子與電洞的定向分離與傳輸，顯著抑制電子–電洞復合速率，提升反應活性位點利用率，進而大幅增進整體光催化分解水產氫效能。

參考文獻

[1] Jiafu Qu, Songqi Li, Xiaogang Yang, Cheng Zheng, Yahui Cai, Wei Sun, Jundie Hu, Chang Ming Li. (2022). Hollow porous Co–Ni spinel nanosheet arrays with rich oxygen defects on carbon cloth toward highly efficient and selective CO_2 photofixation. Carbon, *200*, 149-155.

[2] Rania E. Adam, Gallia Pozina, Magnus Willander, Omer Nur. (2018). Synthesis of ZnO nanoparticles by co-precipitation method for solar driven photodegradation of Congo red dye at different pH. Photonics and Nanostructures - Fundamentals and Applications, *32*, 11-18.

[3] Yu-Cheng Chang, Yung-Chang Chiao, Po-Chun Hsu. (2023). Rapid Microwave-Assisted Synthesis of $ZnIn_2S_4$ Nanosheets for Highly Efficient Photocatalytic Hydrogen Production. Nanomaterials, *13*, 1957.

[4] Xin Guo, Linlin Fan, Jiayue Liu, Bo Wen, Youji Li, Zhiliang Jin. (2025). Built-in electric field and oxygen vacancy defects in ZnCdS/Ov- $NiCo_2O_4$ schottky heterojunction to achieve efficient photocatalytic hydrogen evolution. Applied Catalysis B: Environment and Energy, *378*, 125586.

報告型式：

□英文口頭報告競賽 (□無機材料， □有機材料)
■海報展示並參加壁報論文競賽(■無機材料， □有機材料)
□只參加海報展示 (□無機材料， □有機材料)

Achieving Low-Cost, High-Efficiency Blue QLEDs via Atmospheric Processing: Impact of Ambient Conditions on MgZnO Electron Injection and Charge Balance

Zhen-Ming Yang [1], Yen-Tsung Huang [1] , Yong-Sin[2] and Chun-Yuan Huang *
Division of Physics and Optoelectronic Science, Department of Applied Science, National Taitung University, Taitung 950, Taiwan

* Chun-Yuan Huang: laputa@nttu.edu.tw

ABSTRACT

This study investigates the optoelectronic performance discrepancies of All-solution-processed blue quantum dot light-emitting diodes (QLEDs) fabricated under ambient atmospheric versus glovebox (N2) environments. The device architecture consists of ITO/PEDOT:PSS/TFB+TCTA/Blue QD/GACL/MgZnO/Ag. Experimental findings reveal a trade-off between film quality and device efficiency: while samples processed in the glovebox exhibit superior photoluminescence (PL) intensity and longer time-resolved photoluminescence (TRPL) lifetimes, the ambient-processed devices demonstrate significantly higher luminance and external quantum efficiency (EQE). Analysis of electron-only devices (Ag/MgZnO/Ag) confirms that exposure to ambient moisture and oxygen markedly enhances the electron injection capability of the MgZnO layer. We conclude that although atmospheric processing introduces minor non-radiative recombination centers within the QD layer, it effectively optimizes the charge carrier balance by improving electron transport, thereby surpassing the performance of glovebox-fabricated counterparts. This work provides critical insights into the synergy between environmental processing and carrier dynamics for high-efficiency blue QLEDs.

Introduction

The commercialization of blue quantum dot light-emitting diodes (QLEDs) is often hindered by high manufacturing costs associated with vacuum-based or glovebox-controlled processes. Atmospheric processing offers a cost-effective alternative; however, the influence of ambient moisture and oxygen on device physics remains a critical subject of study. This research focuses on how ambient conditions modulate the electronic properties of MgZnO electron transport layers (ETLs) to achieve superior charge balance in blue QLEDs.

(Keywords)： Blue QLEDs, Atmospheric Processing, MgZnO, Charge Balance, Surface Modification.

Presentation type：
☐ English oral competition (☐ inorganic materials, ☐ organic materials)
Poster competition (■ inorganic materials, ☐ organic materials)
☐ Exhibition only (☐ inorganic materials, ☐ organic materials)

可調控的 ZnS 或 CdS 奈米結構中介層作為助催化劑應用於 CuO–ZnO 異質接面以提升光催化活性

藍宇萱、郭晉佑、張育誠
fb20030722@gmail.com

NSTC 112-2221-E-035 -017 -MY3、NSTC 113-2221-E-035 -023 -MY3

摘要

本研究主要聚焦於工業快速發展所衍生的有機污染問題，並探討光催化技術應用於廢水處理之可行性。隨著環境污染日益嚴重，全球研究人員積極投入光催化相關研究，因其具備環保、成本低、操作簡便及穩定性高等優勢，被視為極具潛力的污染控制技術。光催化反應過程中，材料受光激發後可產生電子與電洞，進一步形成氫氧自由基（•OH）與超氧陰離子（•O_2^-）等高活性氧化物種，能有效分解有機污染物，最終轉化為危害較低的二氧化碳與水。本文主要探討在銅網基材上製備 CuO-ZnS-ZnO 與 CuO-CdS-ZnO 異質結構，並比較其光催化性能。製備流程分為三個步驟：首先經加熱氧化形成 CuO 奈米線，其次於奈米線表面沉積 ZnS 或 CdS 奈米結構，最後利用濕式化學法生長 ZnO 奈米線，形成多元異質接面。藉由 FESEM、XRD、FETEM、EDS 及 XPS 等材料分析技術，證實成功製備出結構完整之 CuO-CdS-ZnO 複合材料。ZnO 因具有無毒、高光敏性及良好化學穩定性，被廣泛應用於光催化領域，但其能隙較大且光生載子易復合，限制實際效率，因此常藉由與其他半導體形成異質結構以提升性能。其中，結合窄能隙 CuO 可增強可見光吸收與電荷分離能力，但傳統 ZnO/CuO 系統仍存在氧化還原能力下降的問題，因此再導入 CdS 作為中介層以進一步改善電荷傳輸效率。

在光催化測試中，以 UVC 光源照射羅丹明 B（RhB）溶液評估降解能力，結果顯示當 CdS 前驅物濃度為 5 mM 時，CuO-CdS-ZnO 之光催化效率明顯優於 CuO-ZnS-ZnO。光致發光光譜（PL）分析指出，CuO-CdS-ZnO 具有較佳的電子━電洞分離效果，因此能有效提升反應效率。自由基捕捉實驗進一步證實，氫氧自由基與超氧自由基為降解反應中的主要活性物種。此外，研究亦提出其光催化機制，說明在 CuO-CdS-ZnO 異質結構中，電子與電洞可沿能帶方向快速遷移，降低復合機率，進而提升整體效能。穩定性測試結果顯示，該材料經多次循環使用後仍能維持良好活性，展現優異的耐久性與再利用潛力。

整體而言，本研究證實 CuO-CdS-ZnO 異質結構於高效率且永續性的光催化廢水處理應用上具有相當大的發展潛力。

參考文獻

[1] Y. Wang, Z. Liu, Y. Li, X. Yang, L. Zhao, J. Peng, Boosting photocatalytic performance of ZnO nanowires via building heterojunction with g-C(3)N(4), Molecules 28 (2023).

[2] M. Rani Keshu, J. Yadav, Meenu, S. Chaudhary, U. Shanker, An updated review on synthetic approaches of green nanomaterials and their application for removal of water pollutants: current challenges, assessment and future perspectives, J. Environ. Chem. Eng. 9 (2021) 106763.

[3] A.V. Karim, S. Krishnan, A. Shriwastav, An overview of heterogeneous photocatalysis for the degradation of organic compounds: a special emphasis on photocorrosion and reusability, J. Indian Chem. Soc. 99 (2022) 100480.

[4] S. Dong, J. Feng, M. Fan, Y. Pi, L. Hu, X. Han, M. Liu, J. Sun, J. Sun, Recent developments in heterogeneous photocatalytic water treatment using visible light- responsive photocatalysts: a review, RSC Adv. 5 (2015) 14610–14630.

[5] J. Theerthagiri, S. Salla, R.A. Senthil, P. Nithyadharseni, A. Madankumar, P. Arunachalam, T. Maiyalagan, H.-S. Kim, A review on ZnO nanostructured materials: energy, environmental and biological applications, Nanotechnology 30 (2019) 392001.

[6] A. Rokade, G.K. Rahane, A. ˇ Zivkovi´ c, S.N. Rahane, H.S. Tarkas, K. Hareesh, N.H. de Leeuw, S.D. Sartale, N.Y. Dzade, S.R. Jadkar, S.R. Rondiya, Fabrication of ZnO scaffolded CdS nanostructured photoanodes with enhanced photoelectrochemical water splitting activity under visible light, Langmuir 40 (2024) 6884–6897.

[7] S. Harish, J. Archana, M. Sabarinathan, M. Navaneethan, K.D. Nisha, S. Ponnusamy, C. Muthamizhchelvan, H. Ikeda, D.K. Aswal, Y. Hayakawa, Controlled structural and compositional characteristic of visible light active ZnO/CuO photocatalyst for the degradation of organic pollutant, Appl. Surf. Sci. 418 (2017) 103–112.

報告型式：
□英文口頭報告競賽 (□無機材料， □有機材料)
☑海報展示並參加壁報論文競賽(☑無機材料， □有機材料)
□只參加海報展示 (□無機材料， □有機材料)

錳摻雜普魯士藍結合新型鋅離子膠體電解質可應用於柔性電池中

黃貫綾[1]、鄧名傑[2]
靜宜大學應用化學系
dengmj1020@pu.edu.tw

摘要

柔性多功能儲能裝置因兼具高安全性、高穩定性、機械柔韌性與自供電等特性，隨著穿戴式電子裝置興起，近期被熱門研究與開發並期許能廣泛應用於生活日常中。因此，本研究計畫嘗試透過簡易的自組裝合成法將錳摻雜的普魯士藍(MnHCF)薄膜無電鍍在導電塑膠片(PET-ITO)基材上，作為多功能儲能裝置的正極材料，其開放式立方框架結構、可逆多價氧化還原反應與提供優異的離子傳輸通道，展現出良好的比容量與循環穩定性。透過錳離子的摻雜，可以有效調控晶體空位缺陷濃度與電子結構，提升電導率並穩定離子嵌入/脫嵌過程，進一步延長循環壽命並降低電容量衰退。

在電解質方面，考量到須滿足柔性、安全性與自供電等多功能的需求。本研究計畫將選用聚丙烯醯胺(PaAM)、氯化鋅($ZnCl_2$)和 2-噁唑烷酮(2-Oxazolidone)來打造新式鋅離子膠體電解質(PaZO)，此新式電解質將有助於改善常見水系鋅離子電解液滲漏與枝晶生成等問題，也可提升多功能儲能裝置的機械柔性與安全性。且 PaZO 膠體電解質因其高分子網絡可與鋅深共晶溶劑結合形成特殊三維離子傳輸通道，在彎折或拉伸條件下仍可維持穩定的離子導電性與界面接觸。此外，錳摻雜普魯士藍材料本身具備優異的可逆氧化還原與明顯的變色特性，使該系統同時具備電致變色功能。此裝置同時兼具化學氧化自充電能力，有機會打造出兼具裝置電容量可視化為一體化的柔性多功能儲能裝置。

總結來說，本研究計畫提出利用錳摻雜的普魯士藍(MnHCF)正極材料、新式鋅離子凝膠電解質，搭配鋅箔作為負極，將可開發出兼具高安全性、柔性、可視化變色與化學氧化自充電為一體的多功能儲能裝置，在未來柔性穿戴電子與重複性能源應用提供具潛力，提升實用性與便利性。

參考文獻

(1) Zeng, Y., Liang, J., Zheng, J., Huang, Z., Zhang, X., Zhu, G., ... & Zhang, Y. Z. Recent progress in advanced flexible zinc ion battery design. *Applied Physics Reviews* **2022**, *9*(2).

(2)Liu, J., Shen, Z., & Lu, C. Z. Research progress of Prussian blue and its analogues for cathodes of aqueous zinc ion batteries. *Journal of Materials Chemistry A* **2024**, *12*(5), 2647-2672.

(3) Zhang, X., Hu, J. P., Fu, N., Zhou, W. B., Liu, B., Deng, Q., & Wu, X. W. Comprehensive review on zinc-ion battery anode: challenges and strategies. *InfoMat* **2022**, *4*(7), e12306.

(4) . Li, C.; Xie, X.; Liang, S.; Zhou, J. Issues and Future Perspective on Zinc Metal Anode for Rechargeable Aqueous Zinc-Ion Batteries. *Energy & Environmental Science* **2020**, 13, 175–195.DOI: https://doi.org/10.1002/eem2.12067

(5) Luo, F., Yang, S., Wu, Q., Li, Y., Zhang, J., Zhang, Y., ... & Chen, Y. Hydrogel electrolytes with an electron/ion dual regulation mechanism for highly reversible flexible zinc batteries. *Energy & Environmental Science* **2024**, *17*(22), 8570-8581.DOI: https://doi.org/10.1039/d4ee03067b

(6) Yin, W., Hu, K., Wan, F., Liu, R., & Chen, W. Gel Electrolyte with Excellent Zinc-Ion Conductivity for Achieving Highly Reversible Zinc Anodes. *ACS Sustainable Chemistry & Engineering* **2025**, *13*(35), 14495-14506.DOI: https://doi.org/10.1021/acssuschemeng.5c05126

(7)Zhang, X., & Dutta, J.. X-Fe (X= Mn, Co, Cu) Prussian blue analogue-modified carbon cloth electrodes for capacitive deionization. *ACS Applied Energy Materials*, **2021**, *4*(8), 8275-8284. DOI: https://doi.org/10.1021/acsaem.1c01501

(8) Guo, S. J., Yan, M. Y., Xu, D. M., He, P., Yan, K. J., Zhu, J. X., ... & Cao, F. F. Anti-freezing hydrogel electrolyte with a regulated hydrogen bond network enables high-rate and long cycling zinc batteries. *Energy & Environmental Science* **2025**, *18*(1), 418-429.DOI: https://doi.org/10.1039/d4ee02772h

(9)Zhu, X.; Zhang, H.; Huang, Y.; He, E.; Shen, Y.; Huang, G.; Yuan, S.; Dong, X.; Zhang, Y.; Chen, R.; etal. Recent progress of flexible rechargeable batteries. *Science Bulletin* **2024**, *69* (23), 3730-3755.

(10) Chen, X.; Ma, Y.; Lu, Y.; Zhang, H.; Yang, B.; Liu, Q. A high-performance chemically self-charging aqueous zinc battery using a porous organic polymer cathode. *Chinese Chemical Letters* **2024**, 110666.

報告型式：

□英文口頭報告競賽 (□無機材料， □有機材料)
■海報展示並參加壁報論文競賽(■無機材料， □有機材料)
□只參加海報展示 (□無機材料， □有機材料)

全透明可撓式氨氣氣體感測器開發及特性研究

吳文生 [1] 曾駿逸 [2],蘇平貴 [3]
國立雲林科技大學材料科技研究所 [1] 東吳大學 [2]
jytseng@yuntech.edu.tw

摘要

本研究結合自開裂（self-cracking）丙烯酸脂犧牲層製程與直流磁控濺鍍 DMD 技術，開發出具備高光學穿透率、優異導電特性與良好機械撓曲穩定性的新穎 DMD 網絡透明電極（Dielectric/Metal/Dielectric network transparent electrode； DMD network TE），其中介電層材料與金屬層材料分別為 Al-doped ZnO (AZO)與 Cu。進一步驗證該電極在氣體感測器元件中的應用，故將此透明導電材料藉由金屬光罩(metal mask)製作成指叉電極（interdigital electrode；IDE），並整合混合酸官能基化處理之奈米碳管（CNTs）製備成氣體感測元件。量測實驗針對氨氣(NH_3)進行感測特性分析，開發元件的干擾性影響與感測特性。結合 DMD 網絡透明電極與 CNT 層之感測器，不僅具備透明與可撓性特質，且穩定偵測氨氣特性。

實驗方法

將 4g 水性丙烯酸脂聚合物和 1g 的丙烯酸樹脂混合，以電磁攪拌器 450rpm 攪拌 20 分鐘，超音波機震盪 30 分鐘，形成水性丙烯酸樹脂凝膠。將凝膠滴至 PET 基板上旋塗，轉速為 1000rpm，旋塗 60 秒並烘乾，形成自開裂薄膜。透過直流磁控濺鍍將 AZO/Cu/AZO 濺鍍在薄膜上。用超音波機舉離 30 分鐘，移除丙烯酸樹脂，得到網絡透明電極。進行電性和光學分析。AZO/Cu/AZO IDE 電擊將接腳夾於塑膠基板末端，選用銀膠和乳膠塗在電極末端接腳連接處上，以烘箱溫度 90℃進行熱處裡 60 分鐘後冷卻。取濃硝酸、濃硫酸以 1:3 的比例及奈米碳管 0.1g 於 20ml 藥瓶內，隔水加熱方式在 80℃下攪拌 3 小時。將含有奈米碳管的混酸溶液離心過濾清洗至中性， 以 80℃烘乾，取 5mg 溶於 10ml 的去離水中，超音波震盪 5 分鐘即完成奈米碳管層製備。將奈米碳管溶液以氣動噴漆槍，噴塗至 AZO/Cu/AZO 指叉電擊上，80℃烘烤 10 分鐘，完成氣體感測元件。最後進行氣體干擾性測試、NH_3氣體感測特性。

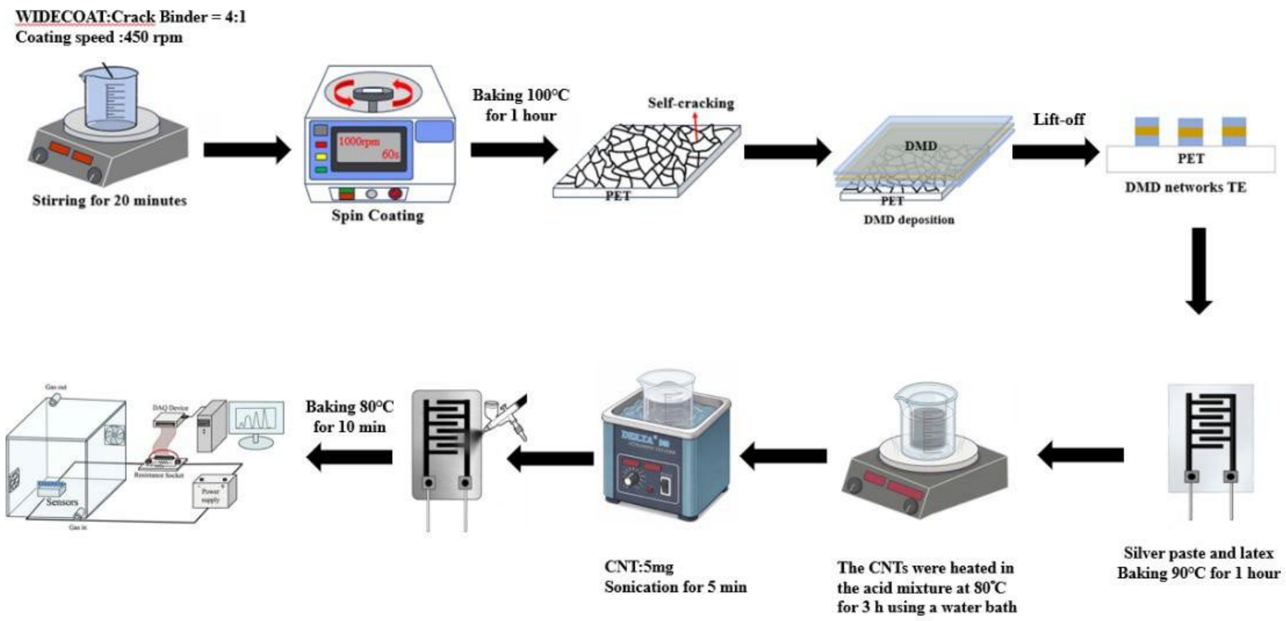

圖 1. NH_3 氣體感測元件製程示意圖

結果與討論

圖 2(a)為 AZO/Cu/AZO DMD network TE 之四點探針電性量測；AZO 厚度固定在 55nm，藉由改變 Cu 金屬層厚度去觀察其導電特性變化，當 Cu 厚度為 30nm 電阻率和片電阻分別為 $1.38\times10^{-3}\ \Omega$-cm 和 98.9Ω/sq，增加至 50nm 時，電阻率下降至 5.18 **x**$10^{-4}\Omega$-cm，片電阻降至 31.2Ω/sq，其導電特性有明顯的改善，展現了 Cu 在特定厚度下 TE 有良好的特性。圖 2(b)為上述 DMD network TE 之光學穿透率全光譜圖，量測的光波長範圍為 400-800nm；在波長 550nm 時的透光率會隨 Cu 厚度增加而逐漸下降，隨著 Cu 金屬層從 30nm 提升至 50nm，穿透度由 91%下降至 87%。圖 2(c)為此 DMD network TE 之品質因子(Figure of merit；FOM)隨著銅金屬厚度變化之關係曲線圖；根據品質因子公式($FOM=T^{10}/R_S$)計算得知銅厚度的增加，品質因子也逐漸增加，在厚度為 50nm 時有最大的品質因子值為 $6.69\times10^{-3}\Omega^{-1}$。

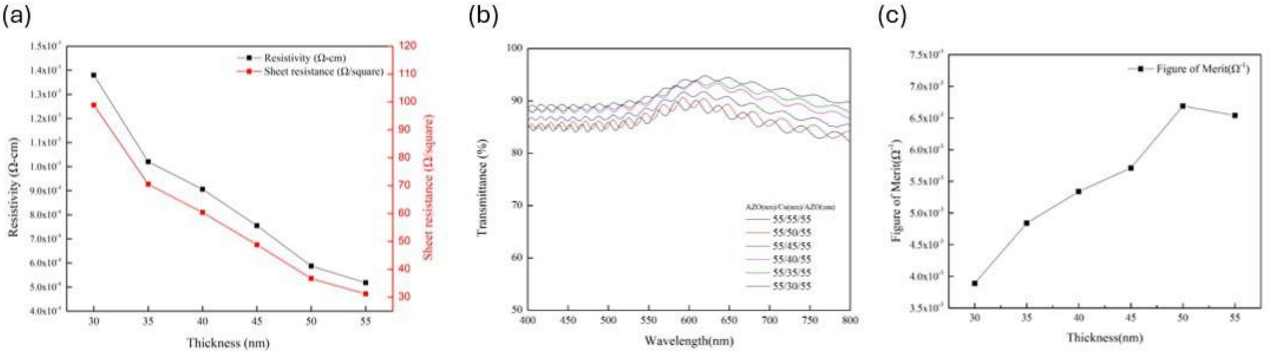

圖 2.(a)為本實驗中不同 Cu 金屬厚度變化之 DMD network 透過四點探針量測所得到的導電特性。

圖 2.(b)為不同 Cu 金屬厚度 DMD network TE 之光穿透光譜圖。光波長為 550nm 下的光穿透度約為 87%。

圖 2.(c)品質因子的變化曲線。利用品質因子公式計算得知，在 DMD 厚度為 AZO(55nm)/Cu(50nm)/AZO(55nm)具有相對小的片電阻及高的穿透度，其品質因子值約為 $6.69\times10^{-3}\Omega^{-1}$。

利用上述最佳化的 DMD network TE (DMD 厚度為 AZO(55nm)/Cu(50nm)/AZO(55nm))結合 CNTs 感測層材料可製備出新穎可撓式全透明氨氣氣體感測元件，該元件基板為軟性 PET，透過金屬光罩將透明電極材料製作成圖形化之指叉電極，最後將 CNTs 漿料噴塗至其上，成功開發出氨氣氣體感測器元件。圖 3 為該感測元件在室溫下通入不同種類氣體的檢測，以進行氣體干擾性測試，加以比較後可發現，在 5 ppm 條件下，NO_2與 NH_3皆呈現較良好的感測反應，且其電阻變化方向相反。由於 NO_2為氧化性氣體，會使感測器電阻上升；而 NH_3 為還原性氣體，則使電阻下降，兩者反應機制不同，沒有明顯的氣體干擾影響。

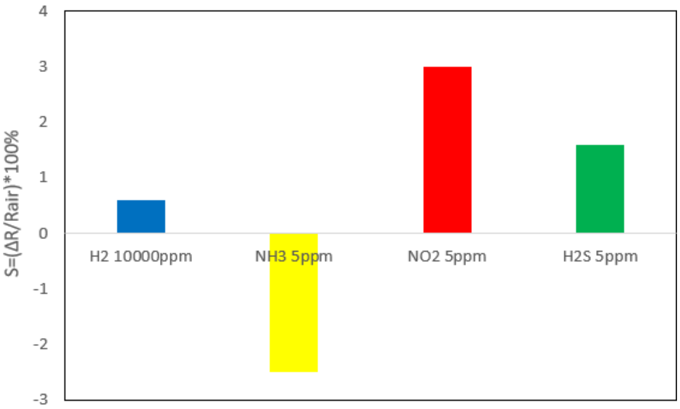

圖 3 氣體感測元件對於不同氣體之干擾性影響

圖 4 實驗結果顯示，在室溫環境下，該氣體感測器對 5~25 ppm 的 NO_2 氣體反應微弱；隨著 NO_2 氣體濃度增加，電阻變化量並未呈現預期的線性趨勢，該元件對於 NO_2 氣體之感測度不理想且不穩定。更進一步作者將量測該元件對 NH_3 氣體之感測特性如以下圖 5(a)、(b)和(c)所示。NH_3 為還原性氣體，材料電阻呈現上升的趨勢，其原因於 CNT 在此感測機制中扮演一個 p 型半導體角色，氧氣會在 CNT 材料表面吸附其傳導帶的電子，形成吸附態的 $O_{2(ads)}^{-}$，產生一個空乏層，當還原性氣體 NH_3 吸附上去後電子會被釋放回材料表面，CNT 的電洞載子變少，空乏層變大，材料電阻進而上升。

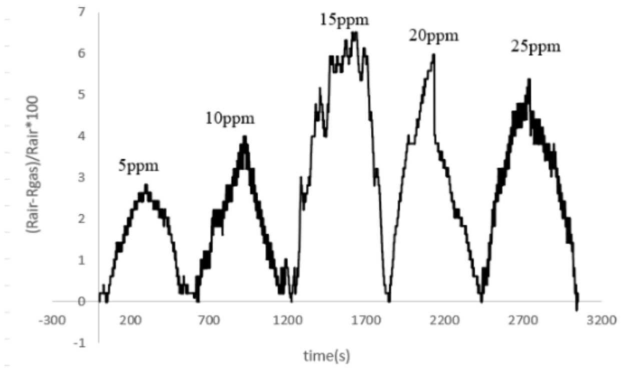

圖 4 AZO/Cu/AZO(55nm/50nm/55nm)DMD 網絡對於 NO_2 氣體 5-25ppm 之感測特性

圖 5(a)為 CNTs 感測層層數效應對於該氣體感測元件之感測靈敏度(S)的影響，量測時 NH_3 氣體濃度固定為 50ppm。實驗結果顯示，感測靈敏度隨感測層層數增加而提升。當感測層數為 7 層時達到最佳感測度表現（S=8%）這歸因於較多層數的 CNTs 提供了更豐富的活性吸附位點；而當層數進一步增加至 9 層時，由於 CNT 過厚導致材料層與層間空乏層變大，導致電子傳遞不易，因此靈敏度下降。在確定最佳感測層層數後，進一步測試元件對不同濃度 NH_3 的動態反應。圖 5(b)與 5(c)為感測層分別是 5 層與 7 層 CNTs 元件分別在 50~600ppm 及 50~250ppm 濃度範圍內之電阻變化曲線的感測特性，；實驗證實，隨 NH_3 濃度增加，感測器的響應值（$\triangle R/R_{air}$）呈現穩定的線性上升趨勢，且 7 層感測層之元件其感測靈敏度遠大於 5 層感測層之元件。再者相較於前述 NO_2 的微弱感測反應，該元件對還原性氣體 NH_3 表現出優異的感測特性和再現性。

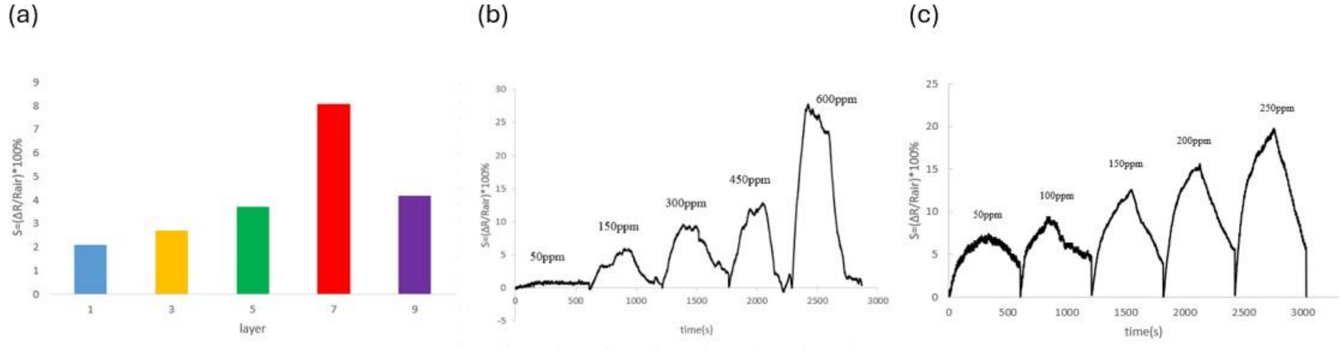

圖 5.(a) 不同奈米碳管層數的影響對 NH_3 氣體感測之 50ppm。
圖 5.(b) 5 層奈米碳管氣體感測元件對 NH_3 氣體之感測特性。
圖 5.(c) 7 層奈米碳管氣體感測元件對 NH_3 氣體之感測特性。

結論

本研究將可撓式 AZO/Cu/AZO DMD 薄膜鍍製在自開裂的丙烯酸樹脂凝膠膜上，接著使用超音波震盪機將基板上的丙烯酸樹脂舉離，形成 AZO/Cu/AZO DMD 網絡透明電極，此 DMD 厚度為 AZO(55nm)/Cu(50nm)/AZO(55nm)，其品質因子為 $6.69\mathrm{x}10^{-3}\Omega^{-1}$，片電阻為 31.2Ω/sq，電阻率為 $5.18\mathrm{x}10^{-4}\Omega$-cm，光波長 550nm 下的穿透度為 87%在室溫氣體感測測試中，該氣體感測元件對氧化性氣體 NO_2 與還原性氣體 NH_3 表現出截然不同的感測行為。實驗結果顯示，該元件對 NO_2 的反應較為微弱且缺乏線性趨勢，而對於 NH_3 氣體則有好的感測特性。透過噴塗官能基化奈米碳管（CNTs）作為感測層，該氣體感測元件對 NH_3 氣體展現出良好的感測靈敏度與線性反應。在 50 ppm 濃度下，噴塗 7 層 CNTs 之元件其響應值最佳（S=8%）；而在 50ppm 至 250ppm 的濃度區間內，感測訊號隨濃度增加呈現穩定的線性增長，證實此 DMD 網絡透明電極結合 CNTs 感測層之架構所開發之室溫型、透明且可撓式氨氣氣體感測器具有極佳的應用潛力。

参考文獻

[1] G. Haacke, New figure of merit for transparent conductors, J. Appl. Phys, 47, 4086(1976) .

[2] Ha, Bonhee, and Sungjin Jo. "Hybrid Ag Nanowire Transparent Conductive Electrodes with Randomly Oriented and Grid-Patterned Ag Nanowire Networks." *Scientific Reports*, vol. 7, no. 1, p. 11614, (2017).

[3] Yu, Shihui, et al. "Enhanced Adhesion of Ag Nanowire Based Transparent Conducting Electrodes for Application in Flexible Electrochromic Devices." *Optical Materials*, vol. 120, p. 111414, (2021).

[4] Hwang, Yooji, et al. "Ag-Fiber/Graphene Hybrid Electrodes for Highly Flexible and Transparent Optoelectronic Devices." *Scientific Reports*, vol. 10, no. 1, p. 5117, (2020).

[5] Wei, Wei, Wei Li, and Lili Wang. "High-Selective Sensitive NH_3 Gas Sensor: A Density Functional Theory Study." Sensors and Actuators B: Chemical, vol. 263, pp. 502–507, (2018).

[6] Ma, Jiangwei, et al. "Multi-Walled Carbon Nanotubes/Polyaniline on the Ethylenediamine Modified Polyethylene Terephthalate Fibers for a Flexible Room Temperature Ammonia Gas Sensor with High Responses." *Sensors and Actuators B: Chemical*, vol. 334, p. 129677, (2021).

[7] M. M. Gomaa, M. H. Sayed, V. L. Patil, M. Boshta, and P. S. Patil, "Gas sensing performance of sprayed NiO thin films toward NO_2 gas," *J. Alloys Compd.*, vol. 885, p. 160908, (2021).

[8] C. T. Lee, Fabrication of flexible gas sensors by layer-by-layer self-assembly technique, Master's thesis, Chinese Culture University(2009).

[9] X. H. Liu, "Preparation and NH3 Gas-Sensing Properties of Double-Shelled Hollow ZnTiO3 Microrods," M.S. thesis, Dept. Appl. Chem., Chinese Culture University, (2021).

[10] 盧宛渝, "利用一鍋化法製備板狀二氧化鈰奈米片並探討其 在室溫下對氨氣感測特性," 碩士, 化學系應用化學碩士班, 中國文化大學,(2022).

報告型式：

□英文口頭報告競賽 (□無機材料， □有機材料)
☑海報展示並參加壁報論文競賽(☑無機材料， □有機材料)
□只参加海報展示 (□無機材料， □有機材料)

AZO/Cu/AZO DMD 透明電極應用在 5G/6G WiFi 可撓式透明天線元件之研究

陳彥佑[1*]曾駿逸[2*]王政一[3*]
[1] 國立雲林科技大學材料科技研究所
E−mail: *jytseng@yuntech.edu.tw

摘要

本研究透過直流磁控濺鍍法，在高真空的環境下進行操作，製作出新穎 AZO/Cu/AZO (dielectric/metal/dielectric)透明電極(transparent electrode, TE)材料，作為透明天線(optical transparent antenna,OTA)之基礎材料[1]，應用於 2.4 GHz 之透明天線元件中。實驗中使用具元件幾何形狀之金屬光罩(hard mask)，AZO/Cu/AZO 薄膜沉積於 PET 可撓式基板上，製作透明天線元件。透過 電壓駐波比（VSWR）量測，評估所製作透明天線於 2.4 GHz 操作頻段中訊號源至負載之傳輸效率，結果顯示此銅基 DMD 透明電極(Cu-based DMD TE)具備良好的射頻匹配特性與應用於透明天線元件之可行性。

實驗方法

如圖 1(a)及圖 1(b)所示，首先對 PET 基板進行熱處理，然後先在 PET 基板上覆蓋圖案化金屬光罩，接著沉積 AZO/Cu/AZO 形成 DMD 圖案化天線元件，接著蓋上第二道光罩，鍍上 Ti/Cu 當作測量電極(electrode pad)。將上述透明天線對損耗頻率量測、結構、光學、電性進行分析。

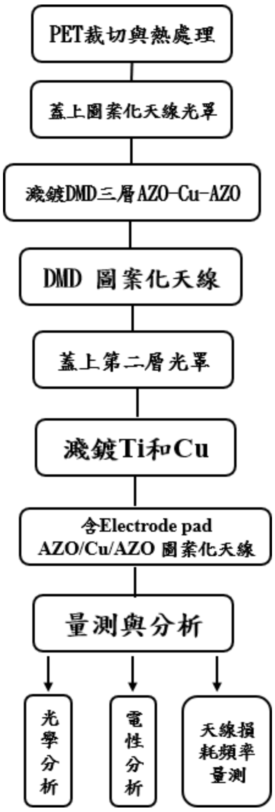

圖 1(a).為 DMD TE 天線製程流程圖

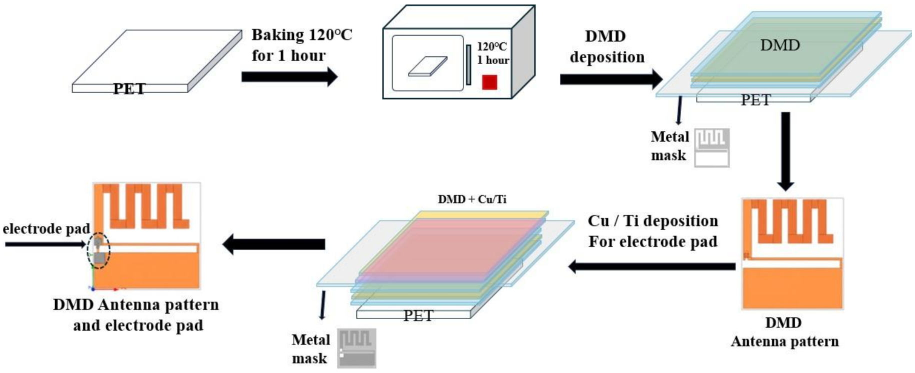

圖 1(b).為 DMD TE 天線製程示意圖

結果與討論

圖 2a 為 AZO/Cu/AZO DMD TE 之四點探針導電特性分析，將 AZO 厚度固定在 45nm，改變 Cu 厚度 12nm 至 14nm。在 12nm 時電阻率及片電阻分別為 8.52x10-5 Ω-cm 和 8.35 Ω/sq，當增加至 14nm 時電阻率及片電阻分別來到 7.51x10-5 Ω-cm 和 7.22 Ω/sq。上述結果顯示導電特性的變化主要是受到中間金屬層的影響，中間金屬層在 DMD 結構中扮演著關鍵角色，其厚度調控對於透明電極之性能具有顯著影響，隨著金屬厚度的增加，其導電特性逐漸增加。

圖 2(b)為上述 DMD TE 之光學穿透率全光譜圖，量測的光波長為 400-800nm，在波長 550nm 時的透光率會隨 Cu 厚度增加而逐漸下降，隨著 Cu 金屬層從 12nm 提升至 14nm，穿透度由 74%下降至 68.8%。

圖 2(c)為 DMD TE 之品質因子(Figure of merit;FOM) [2]分析，利用品質因子公式(FOM=T10/RS)計算得知，隨著銅厚度的增加，品子因子也逐漸增加，在厚度為 12nm 時有最大的品質因子值為 5.89x10-3Ω-1。表 1 為 DMD TE 天線透光、導電特性與品質因子之總整理表，比較改變不同金屬厚度(12、13、14nm)狀態下的光電特性。

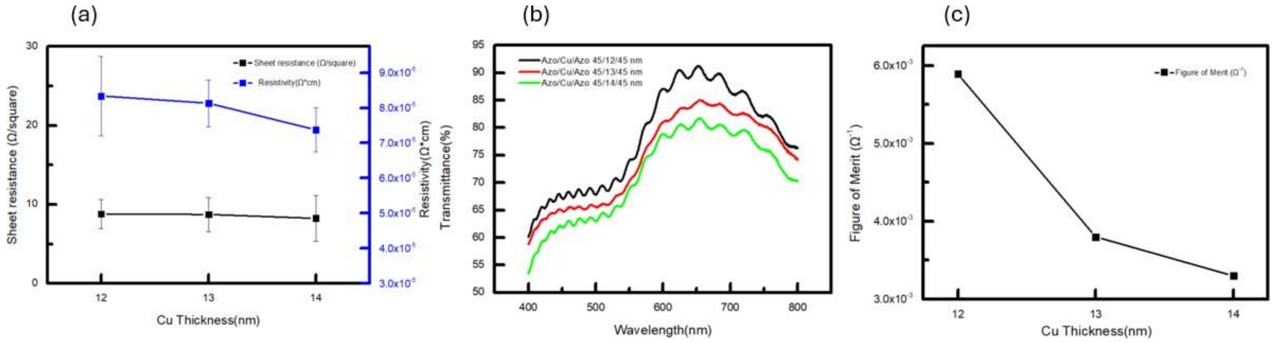

圖 2.(a)為本實驗中不同 Cu 金屬厚度變化之 DMD TE 透過四點探針量測所得到的導電特性。

圖 2.(b)為不同 Cu 金屬厚度 DMD TE 之光譜圖。Cu 厚度 12nm，光波長為 550nm 下的光穿透度約為 74%。圖 2.(c)為品質因子的變化。利用品質因子公式計算得知，在 DMD 厚度為 AZO(45nm)/Cu(12nm)/AZO(45nm)具有相對良好的片電阻及穿透度，其品質因子值為 $5.89\text{x}10^{-3}\Omega^{-1}$。

表 1.為 DMD TE 天線光學及電性特性

Thickness(nm) AZO/Cu/AZO	Sheet resistance (Ω/square)	Resistivity (Ω*cm)	Transmittance (%)(550nm)	(FOM,(Ω^{-1}))
45/14/45(天線)	**7.22**	**7.51x10^{-5}**	**68.8**	**3.3x10^{-3}**
45/13/45(天線)	**7.78**	**8.01x10^{-5}**	**70.3**	**3.8x10^{-3}**
45/12/45(天線)	**8.35**	**8.52x10^{-5}**	**74**	**5.89x10^{-3}**

圖 3(a) 為 DMD(AZO/Cu/AZO)所製作之透明天線元件之圖像，是透過天線元件理論模擬所優化之元件幾何形狀，尺寸大小由右上角開端開始大約為 1.2mm，圖 3(b)為透明天線在新穎低維度材料與元件實驗室(NLDMD LAB)之 logo 下的照片，可以看到該元件呈現良好透明度，可看見下方字體與 logo，圖 3(c)為電壓駐波（Voltage Standing Wave Ratio;VSWR）[**3**] 之量測為評估天線匹配程度之參數。本實驗於 2.20 GHz 時量測之 VSWR 為 1.39，而於 7.12 GHz 時為 1.80，顯示天線在 2.20 GHz 具有較佳之阻抗匹配特性，電磁波能量損失較小。

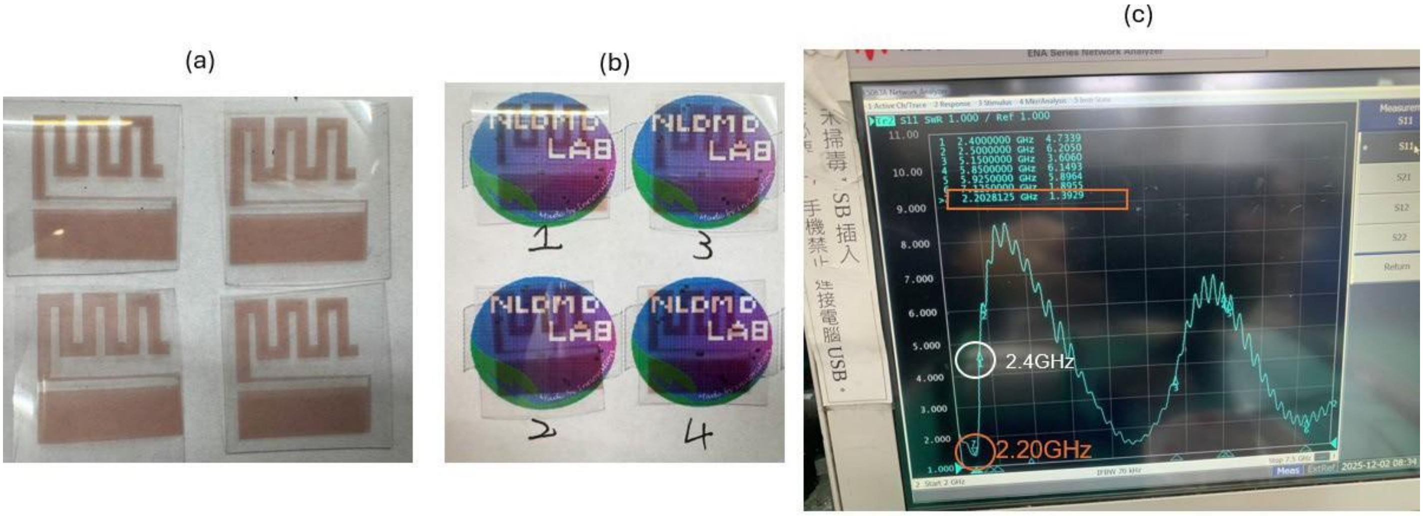

圖 3.為 DMD TE 天線成品及天線模態測試

結論

本研究將 AZO/Cu/AZO DMD 薄膜濺鍍在可撓式 PET 基板上，成功製作出軟性 5G/6G WiFi 形成 AZO/Cu/AZO 透明天線元件，其最佳的 DMD 厚度為 AZO(45nm)/Cu(12nm)/AZO(45nm)，其品質因子為 5.89x10^{-3}Ω^{-1}，片電阻為 8.35Ω/sq，電阻率為 8.52x10^{-5}Ω-cm，光波長 550nm 下的穿透度為 74%。VSWR 電壓駐波比天線模態測試下，本天線之主要共振頻率位於 2.20 GHz，與目標之 2.4 GHz 仍存在些微偏移，但後續可透過調整天線結構進行優化。本研究工作成果展現了此 DMD 透明天線元件具有極大的潛力、創新性與商業化的價值[4]。

參考文獻

[1] B. Dominguez, F. Silva, A. Baghel, D. Albuquerque, and P. Pinho, "Optically Transparent Antennas for 5G and Beyond: A Review," Sensors, vol. 24, no. 4, p. 1150, Feb. 2024.

[2] G. Haacke, New figure of merit for transparent conductors, J. Appl. Phys, 47, 4086(1976)

[3] Analog Devices, *Voltage Standing Wave Ratio Definition and Formula*

[4] K. Ellmer, Past achievements and future challenges in the development of optically transparent electrodes, Nat. Photon., 6, 809–817 (2012)

[5] X. Xing et al., "Ag-Functionalized macro-/mesoporous AZO synthesized by solution combustion for VOCs gas sensing application," RSC advances, vol. 6, no. 103, pp. 101304-101312, 2016.

[6]C. Guillen and J. Herrero, "TCO/metal/TCO structures for energy and flexible electronics," *Thin Solid Films,* vol. 520, no. 1, pp. 1-17, 2011.

[7] H. Najafi-Ashtiani, B. Akhavan, F. Jing, and M. M. Bilek, "Transparent conductive dielectric− metal− dielectric structures for electrochromic applications fabricated by high-power impulse magnetron sputtering," *ACS applied materials & interfaces,* vol. 11, no. 16, pp. 14871-14881, 2019.

[8] Hong, S., Kim, Y., & Jung, C. W. (2016). Transparent UWB antenna with IZTO/Ag/IZTO multilayer electrode film. International Journal of Antennas and Propagation, 2016, 6751790.

[9] M. E. Zamudio, M. Behzadirad, C. Christodoulou, and T. Busani, "Optimization of AZO films for integrating optically transparent antennas with photovoltaics," Applied Physics Letters, vol. 110, no. 23, p. 234101, Jun. 2017.

[10] Morimoto, Y., Shiu, S., Huang, I. W., Fest, E., Ye, G., & Zhu, J. (2023). Optically transparent antenna for smart glasses. *IEEE Open Journal of Antennas and Propagation*, *4*, 159-167.

報告型式：

□英文口頭報告競賽 (□無機材料， □有機材料)
☑海報展示並參加壁報論文競賽(☑無機材料， □有機材料)
□只參加海報展示 (□無機材料， □有機材料)

WO_3/Cu/WO_3 DMD 網絡透明電極之光電特性與機械性質研究

鄞瑞彥 1[#]林晉良 2[#]曾駿逸 3[*]
國立雲林科技大學材料科技研究所
E−mail:* jytseng@yuntech.edu.tw

摘要

本研究工作透過直流磁控濺鍍製程，於高真空的環境下成功開發出新穎 DMD 網絡透明電極(DMD network transparent electrode； DMD network TE)於軟性 PET 基板上。實驗將 DMD(WO_3/Cu/WO_3)三層薄膜濺鍍於已自開裂(self-cracking)形成網絡裂紋圖形之丙烯酸樹脂模板(template)上，再經由超音波震盪移除丙烯酸樹脂模板以形成 WO_3/Cu/WO_3 網絡透明電極，此新穎複合式透明電極不僅大幅提升其光學透光性並在彎曲疲勞測試後仍保有良好導電特性。本實驗所開發之 WO_3/Cu/WO_3 DMD network TE 展現出優異的光電與可撓曲機械性能，亦具備高度應用潛力與商業價值。

實驗方法

將 6 g 水性丙烯酸樹脂(WIDECOAT CT-407)與 1 gCrack Binder 812 裂紋膠於室溫下混合，使用電磁加熱攪拌器以 450 rpm 攪拌 20 分鐘，隨後以超音波震盪 30 分鐘以促進顆粒均勻分散，形成穩定的水性溶膠。所得溶膠滴於 PET 基板上，經旋轉塗佈（600 rpm，60 秒）後，置於 100 °C 烘箱中乾燥，即可形成自開裂網絡裂紋之丙烯酸樹脂模板。使用高真空濺鍍法將 WO_3/Cu/WO_3 薄膜濺鍍在自開裂的凝膠模板上，最後利用超音波震盪將試片上的丙烯酸樹脂凝膠模板舉離(lift-off)，形成 WO_3/Cu/WO_3 網絡透明電極。最後再進行光學、電性和機械可撓曲性質之量測與分析。

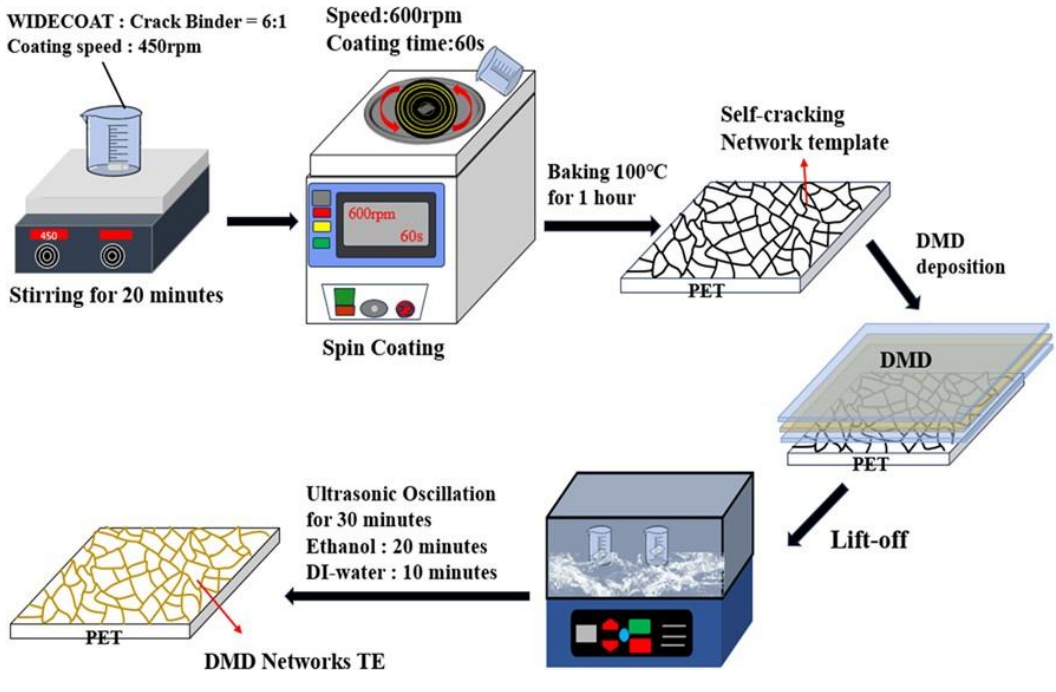

圖 1 為自開裂 DMD 網絡透明電極製備流程示意圖

結果與討論

圖 2(a)和(b)為旋轉塗鍍(spin coating)兩層丙烯酸樹脂(即在 600rpm 旋塗轉速下塗佈 60 秒，進行塗佈兩次)，確保塗膜均勻性與可重現性，塗佈後樣品經 100 °C 乾燥處理 1 小時，形成具有自開裂裂紋結構之丙烯酸樹脂模板，此模板中的網絡線寬範圍約為 25-45µm，網絡覆蓋率約為 24.2%。

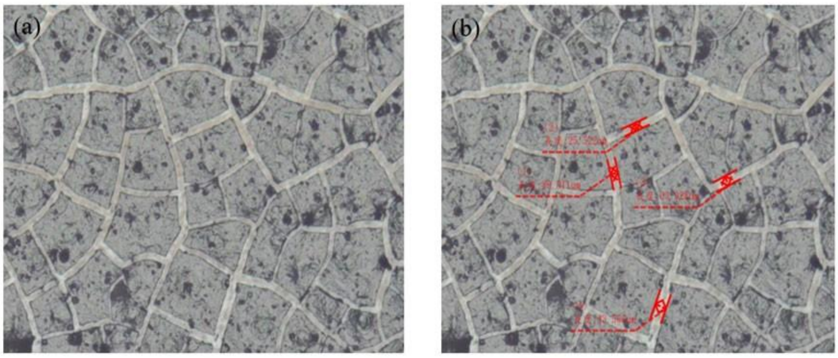

圖 2(a)和(b)為兩層丙烯酸樹脂薄膜在 600rpm 旋塗轉速下塗佈 60 秒後自開裂裂紋網絡之 OM 影像

圖 3(a–d)分別為不同銅(Cu)薄膜厚度(分別為 50、60、70、75nm)條件下所得 DMD Network TE on PET 的光學顯微鏡影像，可用以觀察 DMD 網絡分布情形及其連續性，作為評估導電通道形成與結構均勻性的依據，這裡可以發現電極表面並無太大差異非常均勻。其 DMD 網絡線寬約為 35 µm，DMD 網絡覆蓋率約為 24.2%。

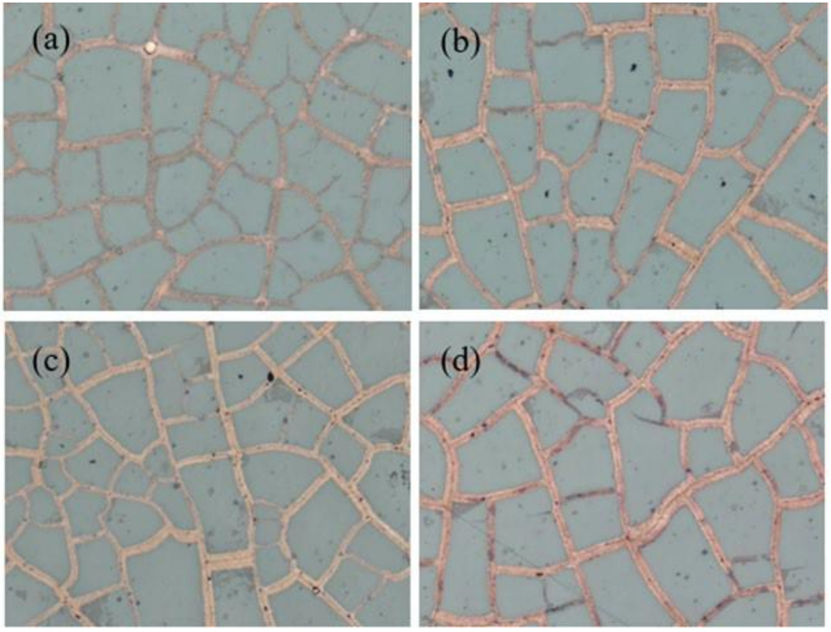

圖 3 (a–d)分別為 WO_3 10nm / Cu(50nm~75nm)/ WO_3 10nm 之 OM 圖

圖 4(a)為在 WO_3 介電層厚度固定為 10 nm 條件下，調變中間 Cu 金屬層厚度所得之具網絡結構 DMD 透明電極的導電特性結果。可觀察到，隨著 Cu 厚度的增加，DMD network TE on PET 的電阻率與片電阻皆呈現明顯下降趨勢。其中，當 Cu 厚度為 50nm 時，片電阻高達 88.0 Ω/sq，電阻率約為 $6.16\times10^{-4}\Omega\cdot cm$；而當 Cu 厚度提升至 75 nm 時，片電阻降至 23.2 Ω/sq，電阻率也明顯下降至 $2.01\times10^{-4}\Omega\cdot cm$。圖 4(b)為 $WO_3/Cu/WO_3$ DMD network TE 中改變 Cu 金屬層厚度所測得之透光光譜圖。由圖中可觀察到，隨著 Cu 厚度的增加，透光率逐漸下降。當 Cu 厚度為 50 nm 時，在可見光範圍（400–800 nm）內的平均透光率最高，其波長在 550nm 時光的穿透度約為 88%；而當厚度增至 75 nm 時，透光率明顯降低，其波長在 550nm 時光的穿透度約為 83%。圖 4(c)為 DMD Network TE 之品質因子(FoM)分析，根據 Haacke 公式 $FoM = T^{10}/R_s$ 計算得知，FoM 隨 Cu 厚度的增加而提升，在 70 nm 有最高值 $7.11\times10^{-3}\Omega^{-1}$。

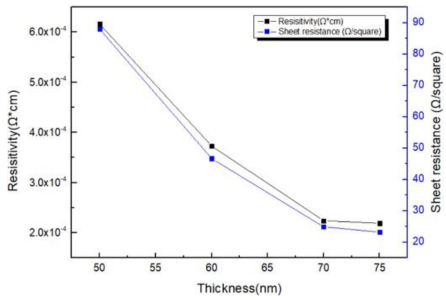

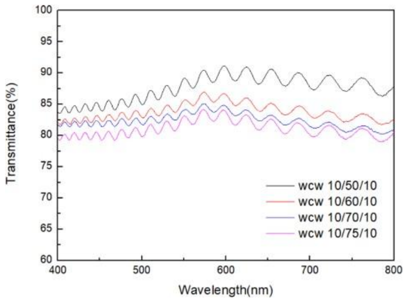

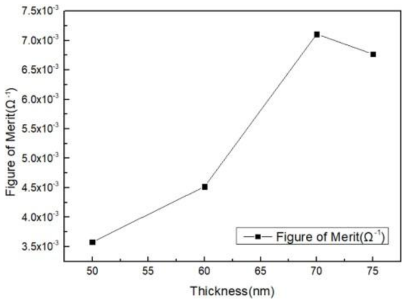

圖 4(a) WO_3 10nm / Cu(50nm~75nm)/ WO_3 10nm DMD networks 四點探針之電性分析

圖 4(b) WO3 10nm / Cu(50nm~75nm)/ WO3 10nm DMD networks 之光譜圖

圖 4(c) WO_3 10nm / Cu(50nm~75nm)/ WO_3 10nm DMD networks 品質因子(FoM)分析

圖 5(a)顯示 WO_3/Cu/WO_3（10/70/10 nm） DMD network TE 在不同曲率半徑（10 mm、7.5 mm、5 mm）下，進行五次外部彎曲測試(outer bending test)後的電阻變化率($\Delta R/R_0=R-R_0/R_0$)，其中 R_0 為彎曲前的初始片電阻 24.9 Ω/sq，R 為彎曲後量測之片電阻值。由結果可發現，即使曲率半徑由 10 mm 縮小至 5 mm，電阻變化率經過外部彎曲測試後並無顯著差異。圖 5(b)顯示 WO_3/Cu/WO_3（10/70/10 nm） DMD network TE 在 10 mm 彎曲曲率半徑條件下，進行外部彎曲疲勞測試(outer bending fatigue test)的電阻變化趨勢。初始片電阻為 24.9 Ω/sq，當疲勞彎曲次數從 0 次增加至 2000 次時，電阻變化率從 0%上升至 37.8%，對應片電阻為 35.7 Ω/sq 變化幅度尚屬穩定； 而於疲勞彎曲 5000 次時變化率增加至 65.5%，對應片電阻為 41.2 Ω/sq 顯示電阻略有上升。當疲勞彎曲循環達到 20000 次時，電阻變化率上升至 497.2%，對應片電阻為 148.7 Ω/sq，雖有明顯上升，但導電性仍保有一定水平。

圖 5(a)不同彎曲曲率半徑下軟性 WO_3/Cu/WO_3 DMD network TE 之外彎曲測試圖

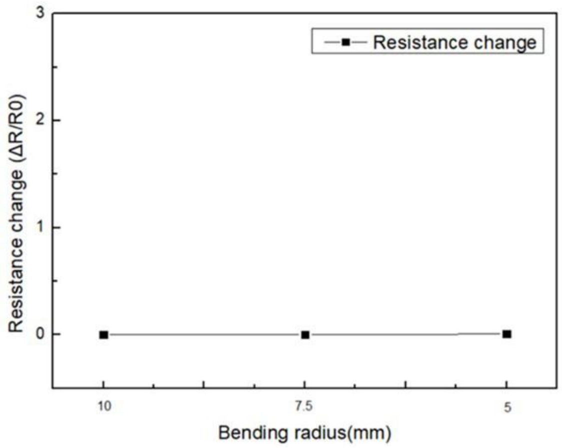

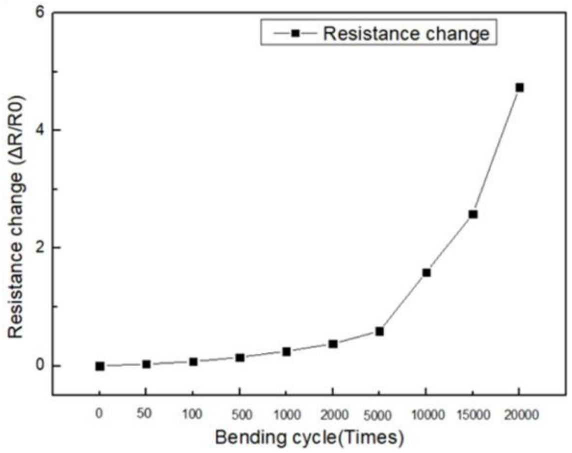

5(b) WO_3/Cu/WO_3 DMD network TE 在 10mm 曲率半徑下之疲勞彎曲測試結果

結論

本研究將 WO_3/Cu/WO_3 DMD 薄膜沉積於具有自開裂裂紋網絡的丙烯酸樹脂模板上，經超音波震盪舉離丙烯酸樹脂模板後成功開發出新穎軟性複合式 DMD Network TE on PET。量測結果顯示，當 DMD network TE 其 DMD 薄膜厚度分別為 10/70/10 nm 時有最好的光電性質，該電極電阻率與片電阻分別為 2.24×10^{-4} Ω·cm 與 24.9 Ω/sq，且於 550 nm 光波長下透光率達 84.1%，品質因子提升至 7.11×10^{-3} Ω^{-1}，其在彎曲曲率半徑 10 mm、經 20,000 次彎曲疲勞測試後依然保有穩定的導電性，其電阻變化率為 497.2%，證實此 DMD Networks TE 的潛力與創新性，具有高度的發展前景。

參考文獻

[1] Li, Y., Chen, Y., Qiu, M. et al. Preparation of Aluminum Nanomesh Thin Films from an Anodic Aluminum Oxide Template as Transparent Conductive Electrodes. Sci Rep 6, 20114 (2016).
[2] Yunfei Han, Xiaolian Chen, Junfeng Wei, Guoqi Ji, Chen Wang, Wenchao Zhao, Junqi Lai, Wusong Zha, Zerui Li, Lingpeng Yan, Huiming Gu, Qun Luo, Qi Chen, Liwei Chen, Jianhui Hou, Wenming Su, and Chang-Qi Ma*,Efficiency above 12% for 1 cm2 flexible organic solar cells with Ag/Cu grid transparent conducting electrode, Advanced science, November 20, 2019, Volume6, Issue22
[3] Ashutosh K. Singh, R.K. Govind, S. Kiruthika, M.G. Sreenivasan, Giridhar U. Kulkarni, Hybrid transparent conducting glasses made of metal nanomesh coated with metal oxide overlayer,Materials Chemistry and Physics,Volume 239,2020,121997,ISSN 0254-0584, https://doi.org/10.1016/j.matchemphys.2019.121997
[4] Zue Chin Chang, The Effect of Aging of ZnO, AZO, and GZO Films on the Microstructure and Photoelectric Property, World Academy of Science, Engineering and Technology International Journal of Chemical and Molecular Engineering, 9, 2015,p 737-742.
[5] Matthias, B., & Wood, E. A. (1951). Low Temperature Polymorphic Transfor mation in WO3. Physical Review, 84(6), 1255.
[6] Gholami, M., Tajabadi, F., Taghavinia, N. et al. Chemically-stable flexible transparent electrode: gold-electrodeposited on embedded silver nanowires. Sci Rep 13, 17511 (2023). https://doi.org/10.1038/s41598-023-44674-7
[7] Balian, H.G. and N.W. Eddy, Figure-of-merit (FOM), an improved criterion over the normalized chi-squared test for assessing goodness-of-fit of gamma-ray spectral peaks. Nuclear Instruments and Methods, 1977. 145(2): p.389-395.
[8] Haacke, G., New figure of merit for transparent conductors. Journal of Applied physics, 1976. 47(9): p. 4086-4089.
[9] Basic Electronics Tutorials, Electronics Tutorial about Sensors and Transducers ,2013. http://www.electroni
[10] 卓世明，電子感測器介紹, Introduction of Electronic Senor。

報告型式：

□英文口頭報告競賽 (□無機材料， □有機材料)
☑海報展示並參加壁報論文競賽(☑無機材料， □有機材料)
□只參加海報展示 (□無機材料， □有機材料)

奈米複合材料 BiSbTe-W 熱電薄膜在玻璃基板上的特性研究

蘇郁翔 [1] 陳文照 [2] 曾駿逸 [3*]
國立雲林科技大學材料科技研究所
E−mail: jytseng@yuntech.edu.tw

摘要

本研究藉由磁控濺鍍製程於高真空環境製備 BiSbTe/W 奈米複合熱電薄膜。首先製備出特定厚度比例關係之 A/B/A/B••••(A 為 BiSbTe sublayer、B 為 W metal sublayer)二維多層薄膜，A sublayer 厚度為 40nm、B sublayer 厚度為 0nm~6nm。進一步藉由高真空的環境($6*10^{-7}$ torr)，在 150~200℃下做長時間的後退火處理，透過低溫長時間熱處理使得週期性多層薄膜(BiSbTe)中產生零維的奈米結構(0 dimensional nano-structures)包含W 奈米晶粒、W-based nanocomponds 與奈米空孔結構，期望經由奈米結構所形成的界面(interfaces)能在較不影響帶電載子傳輸情況下，能有效抑制聲子(phonons)傳輸，進而降低其熱傳導係數。另外此薄膜材料中透過金屬鎢（W）與 BiSbTe 界面產生低能量載子過濾效應(low-energy carrier filtering effect)，希望提升其熱電功率因子(TE power factor)。本研究工作中，透過改變鎢金屬層厚度探討其對微觀結構與導電特性之影響。根據 TEM 分析顯示，此薄膜由多晶BiSbTe、W-based 化合物奈米結構、W 奈米晶粒及奈米孔洞所組成。

實驗方法

首先，將玻璃基板裁切成 1.5 cm × 1.5 cm 的尺寸，並進行基板清洗程序，以去除基板表面的雜質與油汙。隨後，分別確認 W 薄膜與 BiSbTe 薄膜鍍率後，利用濺鍍製程先製備具週期性厚度的 BiSbTe/W/BiSbTe/…./W/BiSbTe/Glass substrate 多層薄膜，此為初鍍(as-deposited)膜，鍍膜完成後進行高真空（6×10^{-7} Torr）低溫(150~200°C)長時間(6~15 小時)熱處理，期望形成具有零維奈米結構的 BiSbTe 薄膜材料。最後，對所得薄膜進行結構與性質分析，包括結構影像分析、四點探針電性量測、霍爾效應量測（Hall effect measurement）西貝克係數量測（Seebeck coefficient measurement）以及 X 光繞射分析（XRD），以系統性探討薄膜之晶體結構、載子傳輸行為與熱電特性。實驗流程如圖一所示。

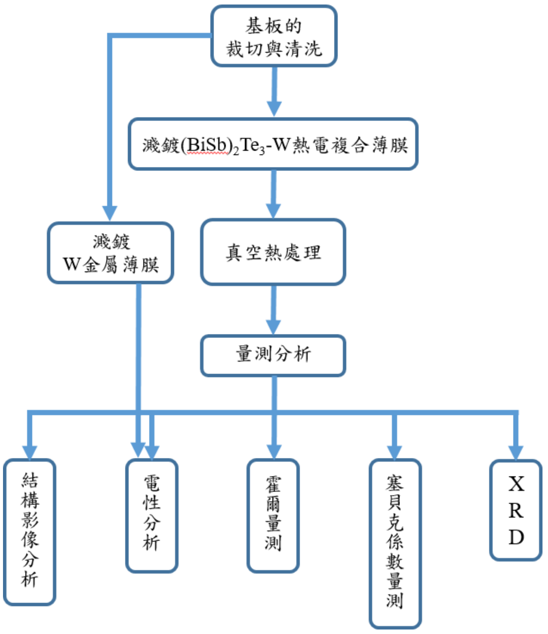

圖 1.為 BiSbTe/W 奈米熱電複合薄膜實驗製備與量測流程示意圖

結果與討論

圖 2(a)與(b)分別為 BiSbTe 與 W 之能帶圖，能帶示意圖可知 BiSbTe 之電子親和力約為 4.5 eV，能隙約為 0.2 eV，使費米能階接近價帶頂部，為典型 p-type 半導體。當兩材料接觸後達到熱平衡時費米能階對齊，於界面產生輕微能帶彎曲，並形成對低能載子的能量過濾障壁（energy filtering barrier）如圖 2(c)所示。此能障會阻擋低能載子，僅使較高能載子容易跨越界面傳輸，因此有助於提升西貝克係數量測（Seebeck coefficient measurement）進而改善熱電功率因子(TE power factor)。

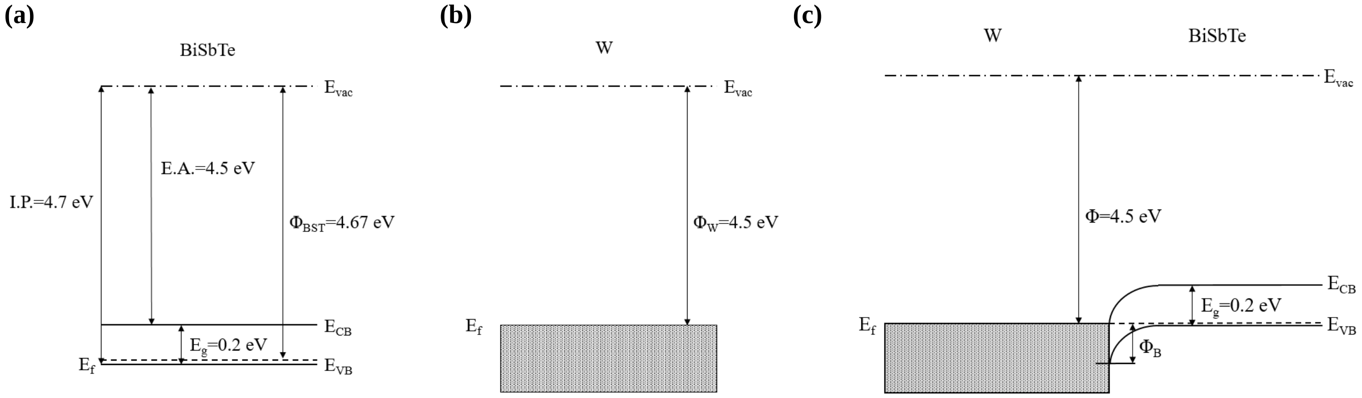

圖 2(a)BiSbTe 能帶圖，(b)金屬 W 的能帶圖，(c)BiSbTe/W 界面所形成的能帶示意圖。

圖 3(a)與(b)為試片高真空長時間低溫熱處裡前、後結構示意圖。退火前試片為具有週期性變化之多層薄膜如圖 3(a)所示。在高真空中經長時間(6~15 小時)低溫(150~200°C)熱處理後，由於 BST 層中元素 Bi、Sb、Te 向 W 層的擴散速率較快，而 W 向 BiSbTe 層的擴散速率相對緩慢，使其 BiSbTe/W 界面處產生 Kirkendall effect，進而在界面附近形成奈米尺度空孔（nano-voids），擴散過程同時可能使 W 與 BST 發生局部反應，並且使原本連續的 W 層轉變為零維奈米結構並部分生成 W-based nanoconponds(WTe_2)。這樣的結構因著增加的許多界面與表面不僅增加界面的聲子散射(phonon scattering)，期望有助於降低晶格熱導率，同時在不影響帶電載子傳輸性能下，對熱電特性提升具有正面的影響。

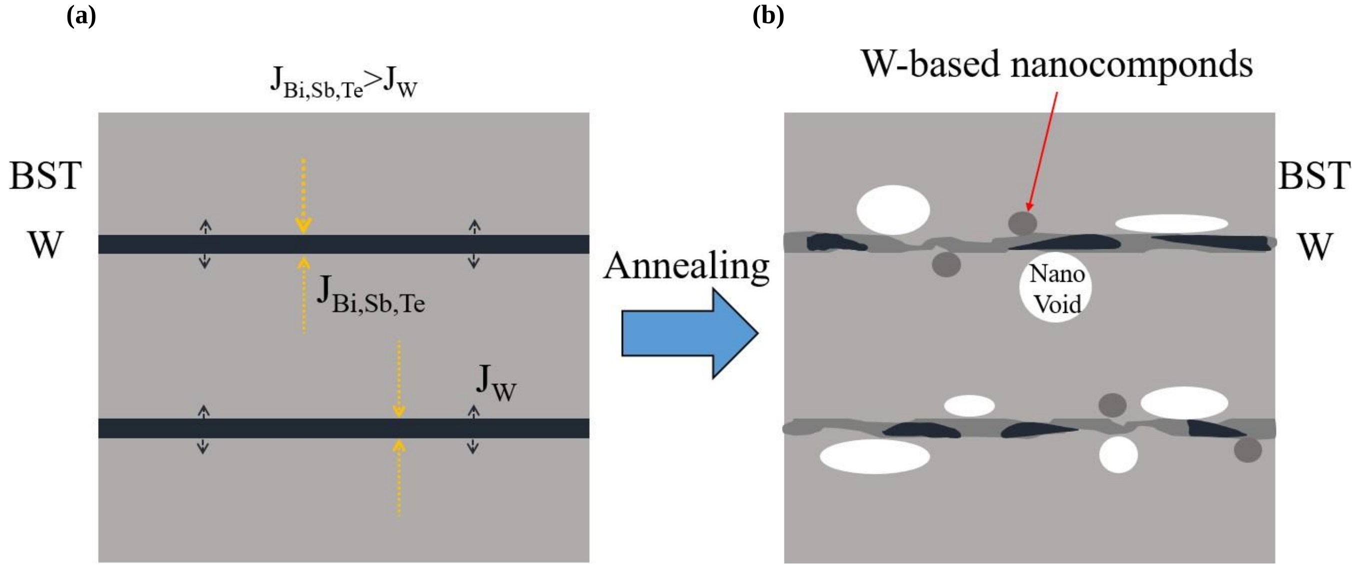

圖 3.(a)為初鍍 BiSbTe/W/BiSbTe/W…多層薄膜結構示意圖，(b)為熱處理後具零維奈米結構 BiSbTe 薄膜材料

圖 4(a)為初鍍膜 BiSbTe/W/BiSbTe/W/..多層膜 TEM 影像，圖 4(b)與(c)為熱處理後零維奈米結構 BiSbTe 薄

膜材料之 TEM 影像。圖 4(a)影像中可見明顯 BiSbTe/W 層狀結構，BiSbTe 層與 W 層之間有清楚連續的界面，BiSbTe 每層厚度約為 40 nm，W 層厚度約為 4.8 nm。圖 4(b)高倍率 TEM 影像中觀察到 BiSbTe 與 WTe_2之清晰晶格條紋同時顯示原本的層狀結構轉變為相對不規則、不清楚的界面形貌，顯示材料內部各個元素產生交互擴散重新分佈變化與局部反應，且因著大量質量傳輸不平衡使得材料界面附近形成奈米孔洞（nano-voids）。此外，量測分析得到 BiSbTe 晶格間距約為 0.320 nm（對應為(015)）、0.492 nm（對應為(006)）以及 0.2185 nm（對應為(110)），而 W 零維奈米結構則為非晶狀態。

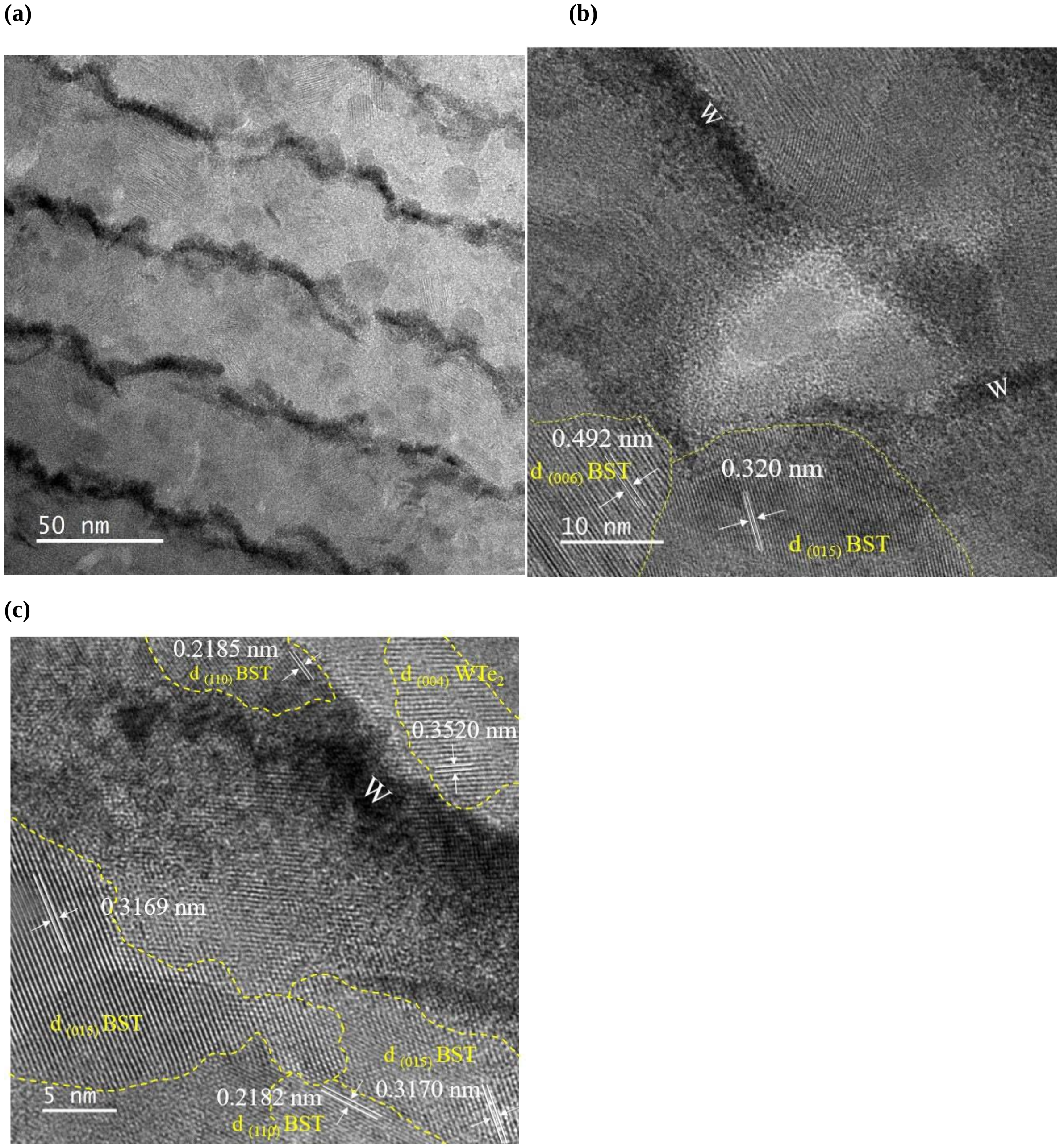

圖 4(a)初鍍膜 BiSbTe/W/BiSbTe/W/..多層膜結構 TEM 影像，(b)與(c)熱處理後具零維奈米結構 BiSbTe 薄膜材料之高倍率 TEM 影像

圖 5 為具零維奈米結構 BiSbTe 薄膜材料之四點探針導電特性分析，將 BiSbTe 每層厚度固定在 40 nm，藉

由改變 W 層厚度(0 nm~ 6 nm)去觀察其電性變化。尚未加入 W 層之 BiSbTe 薄膜(厚度約 600 nm)其電阻率和片電阻分別為 29.7 x10^{-3} Ω-cm 和 495 Ω/sq，當 W 層增加至 1.2 nm 時，電阻率大幅下降至 9.91 x10^{-3} Ω-cm，片電阻降至 160 Ω/sq。隨著 W 厚度再增加（>2.4 nm），電阻下降趨於平緩，在厚度 6 nm 時最佳電阻率和片電阻分別為 6.15 x10^{-3} Ω-cm 和 90 Ω/sq。

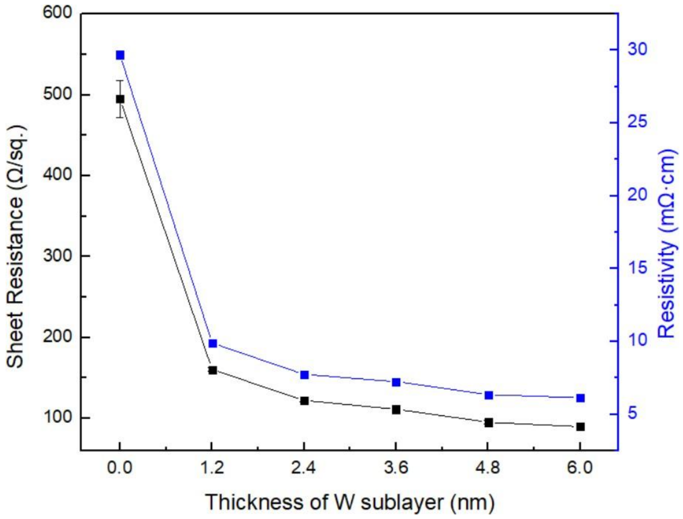

圖 5 具零維奈米結構 BiSbTe 薄膜材料之四點探針導電特性分析。

結論

本研究透過磁控濺鍍製備 BiSbTe/W 奈米複合熱電薄膜，成功開發出具零維奈米結構 BiSbTe 薄膜材料，期望透過鎢(W)的加入，在真空中低溫長時間熱處理後所形成的零維奈米結構與 BiSbTe 界面能提升聲子散射能力。能帶分析顯示，BiSbTe/W 界面形成低能量載子過濾效應，有助過濾低能載子，提高其西貝克係數。TEM 影像分析結果證明退火後因材料擴散係數不同產生 Kirkendall effect，使其界面處有奈米孔洞形成，此結構能增加聲子散射，同時維持導電通道。電性量測顯示，隨 W 厚度增加，電阻率顯著下降，最佳電阻率和片電阻達到 6.15 x10^{-3} Ω-cm 和 90 Ω/sq。整體而言，透過界面工程與奈米結構調控，可在電性與熱傳導間取得平衡，顯示本材料具有應用於熱電元件之潛力。

參考文獻

[1] Dong-Kyun Ko, Yijin Kang, and Christopher B. Murray, Enhanced Thermopower via Carrier Energy Filtering in Solution-Processable Pt-Sb_2Te_3 Nanocomposites. Nano Lett. 2011, 11, 2841–2844

[2] Guoxiang Wang, Fanzheng Meng, Yingqi Chen, Andriy Lotnyk, and Xiang Shen, Boosting Thermoelectric Performance of Bi_2Te_3 Material by Microstructure Engineering. Adv. Sci. 2024, 11, 2308056

[3] S. Aria Hosseini, Giuseppe Romano, and P. Alex Greaney. Mitigating the Effect of Nanoscale Porosity on Thermoelectric Power Factor of Si. ACS Applied Energy Materials 2021 4 (2), 1915-1923

[4] J. P. Heremans et al. Enhancement of thermoelectric efficiency in PbTe by distortion of the electronic density of states, Science, 2008.

[5] X. ZIANNI and D. Narducci, Synergy between defects, charge neutrality and energy filtering in hyper-doped nanocrystalline materials for high thermoelectric efficiency. Nanoscale, 2019

[6] S. Aria Hosseini, Giuseppe Romano, and P. Alex Greaney Mitigating the Effect of Nanoscale Porosity on Thermoelectric Power Factor of Si. ACS Appl. Energy Mater. 2021, 4, 1915−1923

[7] G. J. Snyder and E. S. Toberer, Complex thermoelectric materials. Nature Materials, 2008.

報告型式：

□英文口頭報告競賽 (□無機材料， □有機材料)
☑海報展示並參加壁報論文競賽(☑無機材料， □有機材料)
□只參加海報展示 (□無機材料， □有機材料)

鎂離子多功能整合裝置用之柔性 PPy/PB 複合電極

1.張庭浚 2.鄧名傑
靜宜大學
e-mail dengmj1020@pu.edu.tw

摘要

目前常見的儲能技術中，鋰離子電池雖具備高能量密度的優勢，但其易燃性等安全隱患、高製造成本及資源稀缺等問題限制了其在穿戴式電子裝置與新興應用領域的發展。為了解決上述挑戰，我們選擇開發新式低成本高安全性的鎂離子膠體電解質作為柔性儲能裝置的電解質。這是因為水系鎂離子電解質兼具安全、環境友善、不易產生晶枝以及低成本的等特性，有望成為未來儲能技術的重要方向。為驗證所設計的新型鎂離子膠體電解質其相關電化學儲能性能，本研究將採用普魯士藍 (PB)結合導電高分子材料聚吡咯(PPy)複合材料薄膜作為正極、鋅箔為負極並搭配新型鎂離子膠體電解質組成柔性多功能儲能裝置來進行儲能測試。由於普魯士藍電極具備穩定的開放框架結構、高電導率及優異的氧化還原與電致變色特性，有助於提升儲能裝置的穩定性及實用性。我們將進一步在普魯士藍(PB)的基礎架構上加入聚吡咯(PPy)並搭配新型鎂離子膠體電解質來賦予此儲能裝置有更強的儲能與空氣氧化自充電等性能，讓裝置兼備柔性、安全性、高效儲能、快速空氣自充電等多功能，適合應用於各種穿戴式裝置。此外，普魯士藍及聚吡咯均有具有電致變色功能，會因儲能裝置剩餘電量變化呈現不同顏色，有望實現電量可視化、儲能與自充電為一體的多功能整合式儲能裝置，為穿戴式電子產品開發增添便利性。

參考文獻

(1) Yang, P.; Liang, X.; Wang, Y.; Pan, J.; Tong, Q.; Wang, Q.; Guan, L. Study on a deep eutectic solvent of magnesium chloride hexahydrate and urea as a high-performance electrolyte for supercapacitors. *Journal of Energy Storage* **2025**, *112*, 115558. DOI: https://doi.org/10.1016/j.est.2025.115558.

(2) Zhu, J., Wang, Y., Sun, Z., Fu, J., Zhu, J., Li, R., & Chang, G. (2025). Polypyrrole- modified prussian blue for enhanced conductivity and cycling stability in sodium-ion batteries. Colloids and Surfaces A: Physicochemical and Engineering Aspects, 137038. DOI:https://www.sciencedirect.com/science/article/abs/pii/S0927775725009410

(3) Zhu, X.; Zhang, H.; Huang, Y.; He, E.; Shen, Y.; Huang, G.; Yuan, S.; Dong, X.; Zhang, Y.; Chen, R.; et al. Recent progress of flexible rechargeable batteries. *Science Bulletin* 2024, *69* (23), 3730-3755. DOI: https://doi.org/10.1016/j.scib.2024.09.032.

(4) Ballavenuto, J. M. A.; Tongtip, N.; Fischer, N. L. S.; Bardus, M. Wearable devices, ischemic heart disease and cardiovascular outcomes: A systematic review and meta- analysis. *Maturitas* **2025**, *193*, 108186. DOI: https://doi.org/10.1016/j.maturitas.2024.108186.

(5) Khalid, A.; Tahir, S.; Khalid, A. R.; Hanif, M. A.; Abbas, Q.; Zahid, M. Breaking new grounds: metal salts based-deep eutectic solvents and their applications- a comprehensive review. *Green Chemistry* **2024**, *26* (5), 2421-2453, 10.1039/D3GC04112C. DOI: http://dx.doi.org/10.1039/D3GC04112C.

(6) Bezgin Carbas, B. Fluorene based electrochromic conjugated polymers: A review. *Polymer* **2022**, *254*, 125040. DOI: https://doi.org/10.1016/j.polymer.2022.125040.

(7) Banasz, R.; Wałęsa-Chorab, M. Polymeric complexes of transition metal ions as electrochromic materials: Synthesis

and properties. *Coordination Chemistry Reviews* **2019**, *389*, 1-18. DOI: https://doi.org/10.1016/j.ccr.2019.03.009.

(8) Cai, G.; Wang, J.; Lee, P. S. Next-Generation Multifunctional Electrochromic Devices. *Accounts of Chemical Research* **2016**, *49* (8), 1469-1476. DOI: https://doi.org/10.1021/acs.accounts.6b00183.

(9) Kraft, A. Too blue to be good? A critical overview on the electrochromic properties and applications of Prussian blue. *Solar Energy Materials and Solar Cells* **2024**, *278*, 113195. DOI: https://doi.org/10.1016/j.solmat.2024.113195.

(10)Ding, Y.; Sun, H.; Li, Z.; Jia, C.; Ding, X.; Li, C.; Wang, J.-G.; Li, Z. Galvanic-driven deposition of large-area Prussian blue films for flexible battery-type electrochromic devices. *Journal of Materials Chemistry A* **2023**, *11* (6), 2868-2875, 10.1039/D2TA08023K. DOI: https://doi.org/10.1039/D2TA08023K.

報告型式：

□英文口頭報告競賽 (□無機材料， □有機材料)
□海報展示並參加壁報論文競賽(□無機材料， □有機材料)
□只參加海報展示 (□無機材料， □有機材料)

Improving lithium-ion battery performance and safety by using lithium polyphosphate-coated silicon dioxide particles

Jui-Huan Shen (沈睿煥), Sheng-Hsun Tseng (曾晟勛), Chih-Hao Tsao (曹志豪) and Chien-Hsiang Chang (張鑑祥)*
Department of Chemical Engineering, National Cheng Kung University, Tainan 701, Taiwan
*Correspondence: changch@mail.ncku.edu.tw

NSTC 113-2923-E-006-002

Abstract

With the increasing demand for high-energy-density batteries, safety and ion transport efficiency of lithium metal batteries during cycling have become critical technical bottlenecks. Developing high-performance composite modified separators has thus emerged as a core strategy to address the challenges. Silicon dioxide (SiO_2) particles, with their excellent mechanical strength and chemical stability, effectively compensate for the thermal stability deficiencies of traditional polyolefin separators. In addition, further integration with polymers possessing charge-regulation functions can more effectively optimize ion transport behavior at the electrolyte and electrode interfaces.

To simultaneously enhance ion-transport kinetics and thermal safety, lithium polyphosphate (LPP) was coated onto SiO_2 particles to prepare a multifunctional SiO_2@LPP composite for separator application. To confirm the core-shell architecture, transmission electron microscopy clearly showed an LPP coating layer approximately 22 nm thick surrounding the SiO_2 core, increasing the total particle diameter from 92.8 nm to 137 nm. Raman spectrum analysis suggested that the strong partial negative charges on the LPP surface competed with solvent molecules in the electrolyte for lithium ions. This weakened the EC-Li^+ coordination intensity, facilitating the desolvation of lithium ions and accelerating their migration and diffusion rates. In terms of electrochemical performance, probably by leveraging LPP's partial negative charge to accelerate ion-transport kinetics, the SiO_2@LPP separator maintained 61.0 mAh/g at 15C, significantly outperforming both the pure SiO_2-coated and uncoated groups. In variable current stripping and plating tests, the composite separator maintained stable and symmetrical voltage curves under varying current densities from 0.255 to 5.103 mA/cm^2. This indicated that the lithium-rich layer induced by LPP effectively supported rapid reaction kinetics and suppressed instabilities that may occur under high current densities. Thermal shrinkage test showed that both the SiO_2@LPP and pure SiO_2 coatings significantly enhanced the thermal stability of the separator, effectively reducing the risk of thermal shrinkage at high temperatures. This work established a universal design strategy for charge-regulating interfaces that simultaneously optimized high-power performance and thermal safety, providing a broad framework for developing next-generation multifunctional separators.

Presentation type：

☐ English oral competition (☐ inorganic materials, ☐ organic materials)
■ Poster competition (■ inorganic materials, ☐ organic materials)
☐ Exhibition only (☐ inorganic materials, ☐ organic materials)

二維二硫化鉬/三維氧化鎵異質結構的晶體結構與光電特性研究

林奕私 [1]、張博彥 [2]、林士弘 [1]、李昭德 [3]、蕭銘華 [3]、Phu-Qui Nguyen[4]、歐信良 [5*]
[1] 國立雲林科技大學電子工程系
[2] 國立雲林科技大學材料科技研究所
[3] 財團法人國家實驗研究院國家儀器科技研究中心
[4] 大葉大學電機工程學系
[5] 大葉大學半導體學士學位學程
*E-mail: slo@mail.dyu.edu.tw

NSTC 114-2622-E-212-002

摘要

本研究使用客製化坩堝製備 MoS_2 薄膜，並探索氣相成長條件下成長不同參數之 MoS_2 薄膜，之後再以「MoS_2 轉移至 Ga_2O_3 薄膜」之方式進行製備，實現異質結構，並展現 Ga_2O_3/MoS_2 異質結構的寬頻光響應特性，期望可帶來更佳的界面連結性與製程整合潛力，再進行二維 MoS_2/三維 Ga_2O_3 異質結構的晶體結構與光電特性研究[1- 3]。

在本研究中，我們結合了管式爐化學氣相沉積（CVD）與射頻磁控濺鍍，以及化學轉移法三種技術，在 c 面藍寶石基板上製備了二維 MoS_2/三維 Ga_2O_3 異質結構。首先，利用 CVD 製程在基板上成長 MoS_2 單層薄膜。我們特別設計了一種氧化鋁坩堝，使基板的放置方式可由傳統的水平放置改為垂直放置。在最佳化的成長條件下，MoS_2 單層薄膜可在整個基板表面達到近乎 100%的均勻覆蓋率。隨後透過磁控濺鍍技術沉積 Ga_2O_3 薄膜，我們調變濺鍍溫度（100、300 與 500℃）及 Ga_2O_3 薄膜厚度（10 與 20 nm），再將 MoS_2 以化學轉移法轉移至 Ga_2O_3 薄膜上(圖一、圖二)。

在材料特性分析方面，我們使用光學顯微鏡（OM）觀察薄膜的表面形貌；透過拉曼光譜（Raman）與光致發光光譜（PL）分析其光學性質；此外，根據上述各項表徵結果，我們進一步探討了在不同製程條件下沉積的 Ga_2O_3 薄膜對 MoS_2 單層造成的影響，及研究各參數對薄膜成長之影響及量測光電特性。

藉由光學顯微鏡、多光子激發掃描顯微鏡、穿透式電子顯微鏡的量測結果可知，本研究所提出的新穎製程能在藍寶石基板上成功成長出大面積高品質且高均勻性的單層 MoS_2 薄膜與 MoS_2/Ga_2O_3 雙層異質結構。多光子觀察結果顯示，成功將 MoS_2 單層轉移至氧化鎵基板上，且覆蓋率及高，形成連續且完整的大面積單層薄膜。TEM 影像可觀察到 MoS_2 的三角形結構之影像，截面影像也顯示出轉移後的 MoS_2 成功貼附在 Ga_2O_3 薄膜上。

本研究成功結合化學氣相沉積（CVD）與射頻磁控濺鍍（RF magnetron sputtering）兩種技術，在 c 面藍寶石基板上製備出二維 MoS_2/三維 Ga_2O_3 凡德瓦爾異質結構薄膜。透過 CVD 成長的 MoS_2 單層具備良好的均勻性與高品質晶體結構，而後續轉移至濺鍍後的 Ga_2O_3 薄膜並與其形成穩定的異質界面。藉由光學顯微鏡（OM）、拉曼光譜（Raman）及光致發光光譜（PL）等分析結果可確認 MoS_2 的特徵峰明顯且保持完整，顯示在適當濺鍍條件下，Ga_2O_3 的沉積對 MoS_2 層的結構影響有限。

二維 MoS_2/三維 Ga_2O_3 凡德瓦爾異質結構薄膜兼具 MoS_2 的高光吸收特性與 Ga_2O_3 的寬能隙特性，顯示其在實現寬頻光偵測器（broadband photodetector）製作技術方面具有潛在應用價值。雖然本研究尚未進行元件製作，但初步的光電特性量測結果已顯示此結構具備良好的光學響應特性，為未來發展高性能光電元件奠定基礎。

關鍵字：二硫化鉬單原子層、氧化鎵薄膜 、化學氣相沉積、磁控濺鍍 、凡德瓦爾異質結構

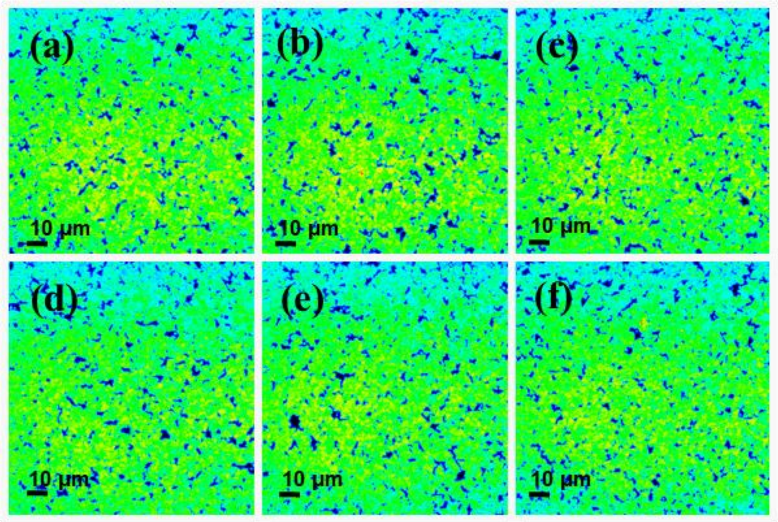

圖一：單層MoS$_2$薄膜轉移至氧化鎵基板上之多光子激發掃描顯微鏡影像。

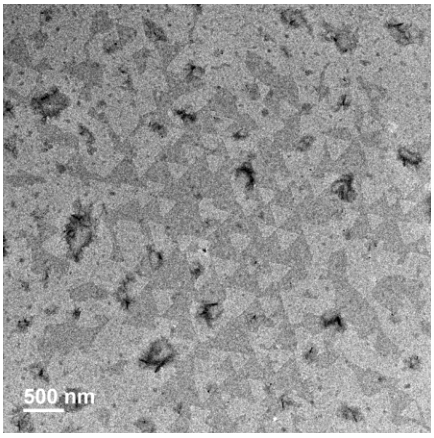

圖二：單層MoS$_2$薄膜轉移至氧化鎵基板上之TEM表面影像。

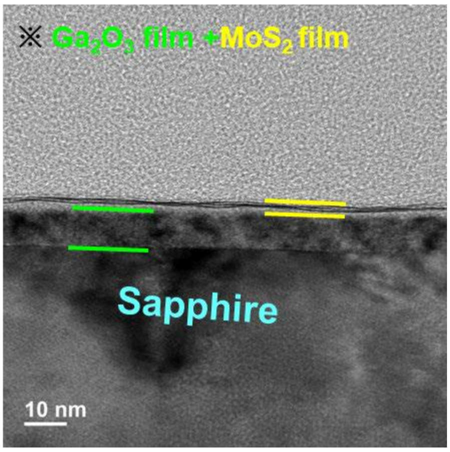

圖三：單層MoS$_2$薄膜轉移至氧化鎵基板上之TEM截面影像。

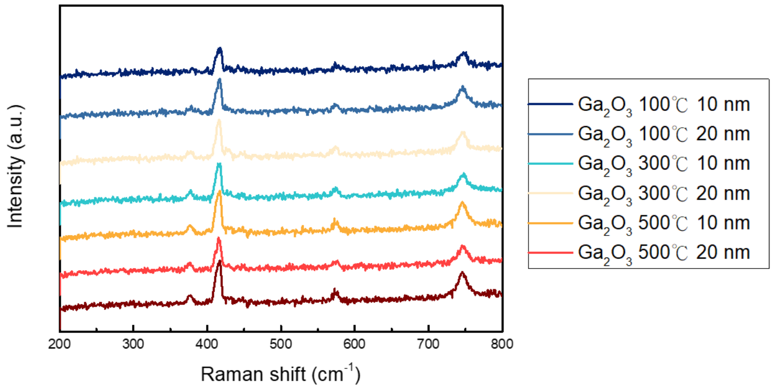

圖四：單層MoS$_2$薄膜轉移至氧化鎵基板上Raman分析。

參考文獻

1. Xiao-Meng Jiang et al., “Electron Transfer Mechanism and Nonlinear Optical Properties of Ga_2O_3/MoS_2 Nanoheterostructures: Implications for Optoelectronic Devices,’’ ACS Appl. Nano Mater. 7, 10068–10078 (2024).
2. Riya Wadhwa et al., “Fast response and high-performance UV-C to NIR broadband photodetector based on MoS_2/a-Ga_2O_3 heterostructures and impact of band-alignment and charge carrier dynamics,” Applied Surface Science, Volume 632, 157597 (2023).
3. Jie Su et al., “Triple Modulation of MoS_2/β-Ga_2O_3 van der Waals Heterojunction on the Response Performance of β-Ga_2O_3 Deep Ultraviolet Photodetector,” ACS Photonics, 12, 2, 847−854(2025).

報告型式：

□英文口頭報告競賽　　　　　(□無機材料，　□有機材料)
■海報展示並參加壁報論文競賽(■無機材料，　□有機材料)
□只參加海報展示　　　　　　(□無機材料，　□有機材料)

利用新穎製程技術成長高均勻性二硫化鉑單原子層二維薄膜

江彥熹[1]、張博彥[1]、戴程洊[2]、黃重凱[2]、馮志龍[1]、蕭銘華[3]、歐信良[4*]
[1]國立雲林科技大學材料科技研究所 [2]大葉大學醫學工程學系 [3]財團法人國家實驗研究院國家儀器科技研究中心
[4]大葉大學半導體學士學位學程
slo@mail.dyu.edu.tw

NSTC114-2622-E-212-002

摘要

目前利用高溫爐管結合化學氣相沉積（Chemical Vapor Deposition, CVD）技術為成長過渡金屬二硫化物二維材料的主要方法，然而傳統製程多採用基板水平擺放方式，且成長面朝下覆蓋於前驅物上方，此方式容易導致氣流分佈不均，使得薄膜均勻性與覆蓋率受到限制。為改善上述問題，本研究設計並製作一種特製金屬載台，將基板以垂直 90°方式固定於載台上，藉由改變氣流動態與前驅物傳輸行為，提升成長環境之穩定性與均勻性， 成功利用 CVD 製備單層二硫化鉑 PtS_2(二硫化鉑)二維薄膜。

在材料特性分析方面，本研究透過光學顯微鏡（Optical Microscopy, OM）觀察薄膜表面形貌與覆蓋情形，並利用拉曼光譜（Raman Spectroscopy） 分析其晶格振動特性與層數資訊， 進一步搭配光致發光光譜（Photoluminescence, PL）探討其能隙與光學性質。此外，採用多光子激發掃描顯微鏡（Multiphoton Excitation Microscopy, MPEM）進行高解析光學影像分析，以提升對材料光學響應之理解；同時利用穿透式電子顯微鏡（Transmission Electron Microscopy, TEM）觀察其晶體結構與晶格排列，確認薄膜之結晶品質與單層特性。

實驗結果顯示，透過特製金屬載台所建立之垂直成長機制，可有效提升單層 PtS_2 薄膜之均勻性與覆蓋率，並改善傳統水平擺放所造成的成長不均問題，顯示此方法在高品質二維材料製備上具有良好潛力與應用價值。

關鍵詞：二硫化鉑、化學氣相沉積、 單層二維材料、特製金屬載台、垂直成長機制

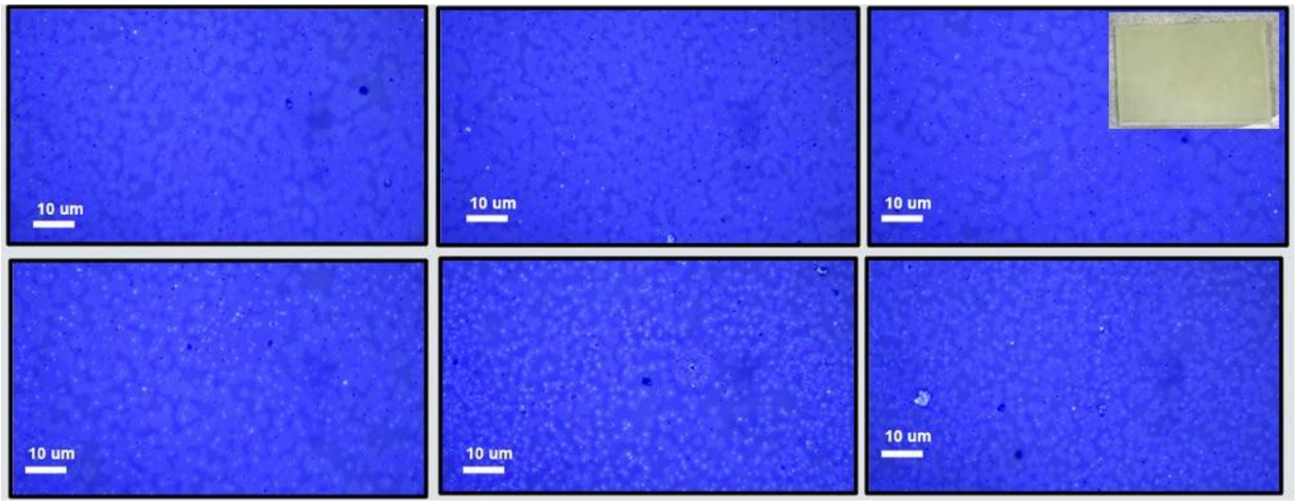

圖一、單層 PtS$_2$ 光學顯微鏡影像圖

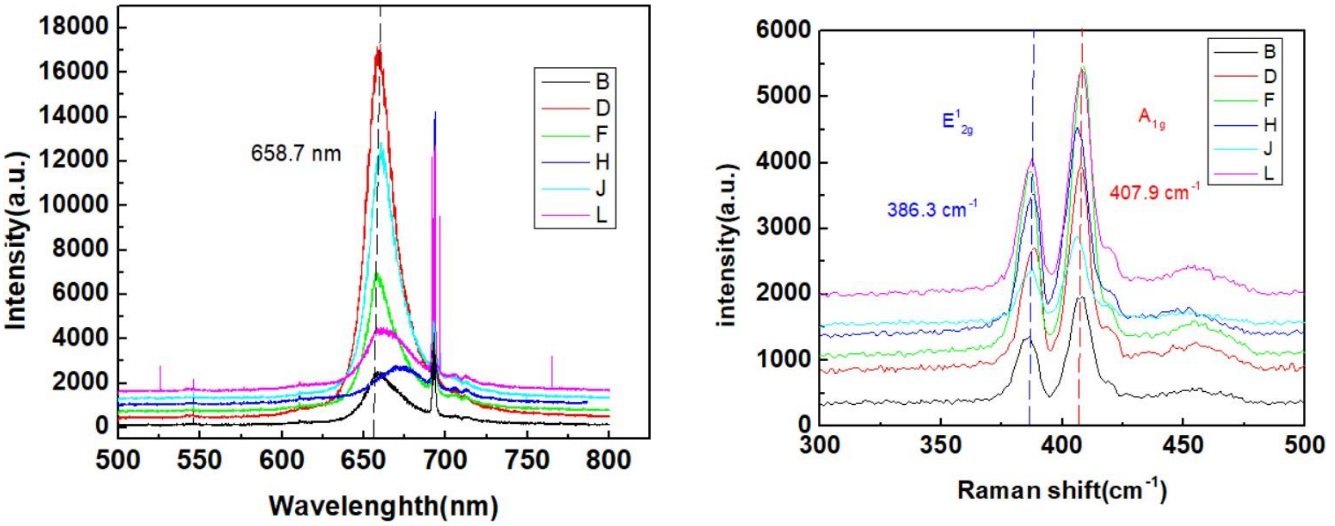

圖二、左圖為 PtS$_2$ 光致發光光譜分析六個位置特徵峰 658.7 nm 能隙為 1.88eV，右圖為 PtS$_2$ 拉曼光譜六個位置特徵峰 386.3 cm^{-1}~407.9 cm^{-1} 兩峰相距 21.6 cm^{-1} 確定為單層。

報告型式：

□英文口頭報告競賽 (□無機材料， □有機材料)
✓海報展示並參加壁報論文競賽(✓無機材料， □有機材料)
□只參加海報展示 (□無機材料， □有機材料)

上轉換奈米複合材料於近紅外光誘導之應用

易盈萍 [1] 王宗棡 [1] 鍾宜璋 [12]
[1] 國立高雄大學 化學工程及材料工程學系
[2] 國立高雄大學 健康及仿生科技研究中心
E-mail: ycchung@nuk.edu.tw

摘要

光動力治療 (photodynamic therapy, PDT) 可藉由光敏劑 (photosensitizer, PS) 在光照下產生活性氧 (reactive oxygen species, ROS)，已廣泛應用於癌症與皮膚疾病相關研究。然而，傳統 PDT 多仰賴可見光活化，受限於組織穿透深度不足，因而限制其於深層組織治療之應用[1]。為克服此限制，上轉換奈米粒子 (upconversion nanoparticles, UCNPs) 可將近紅外光 (near-infrared, NIR) 轉換為較高能量之可見光發射，提供於 NIR 激發下間接活化光敏劑之可行策略，如圖 1 所示。

本研究以熱分解法成功合成核殼結構 $LiYF_4:Yb^{3+}/Tm^{3+}@LiYF_4:Yb^{3+}$ 上轉換奈米粒子，並結合光敏劑以建立可於近紅外光下產生 ROS 之奈米複合系統[2]，如圖 2 所示。穿透式電子顯微鏡 (TEM) 分析顯示，所製備 UCNPs 呈四方晶系形貌，長軸約為 216 nm，如圖 3 所示。X 光繞射 (XRD) 結果與 JCPDS No. 17-0874 比對後，確認其為四方晶相；選區電子繞射 (SAED) 則進一步證實其具有多晶特性。螢光光譜分析顯示，其發射波段涵蓋 440–500 nm、620–720 nm 及 750–850 nm，如圖 4 所示。相較於常見之 $NaYF_4$ 主體材料，$LiYF_4$ 具有較低晶格對稱性與較明顯之晶格扭曲，有助於提升部分禁阻躍遷機率與能量轉移效率，因此更有利於作為 FRET 耦合平台。螢光量測結果亦顯示，UCNPs 於 450–500 nm 區域之發射峰與光敏劑吸收帶具有良好重疊，證明其具備進行螢光共振能量轉移 (Fluorescence resonance energy transfer, FRET) 之潛力。

由於 UCNPs 與光敏劑多屬疏水性材料，難以直接應用於水相生物環境中，因此本研究進一步引入磷脂質體作為包覆材料，以提升其水分散性與生物相容性。磷脂質為細胞膜之主要組成成分，作為載體可望改善奈米複合材料於生醫環境中的穩定性與應用可行性[3]。於成功建構上轉換奈米複合脂質體後，本研究進一步以 2’,7’-dichlorodihydrofluorescein diacetate ($DCFH_2$-DA) 作為活性氧偵測探針，並於近紅外光照射下評估其 ROS 產生能力。$DCFH_2$-DA 經去乙醯化後可形成非螢光性 $DCFH_2$，隨後被 ROS 氧化生成具螢光訊號之 DCF，因此可藉由螢光強度變化半定量比較不同系統之相對 ROS 生成能力[4]。

綜合上述結果，本研究成功建立一套以 $LiYF_4$ 為主體之 UCNP-光敏劑-磷脂質奈米複合系統，證實其兼具近紅外光激發、能量轉移可行性與 ROS 生成潛力。此成果顯示該系統於提升 PDT 深層組織治療應用方面具有發展潛力，未來可望進一步應用於新型生醫治療平台之開發。

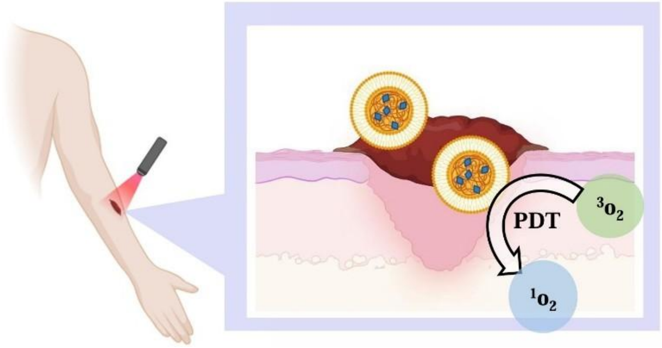

圖 5 上轉換奈米複合材料於近紅外光下之光動力療法

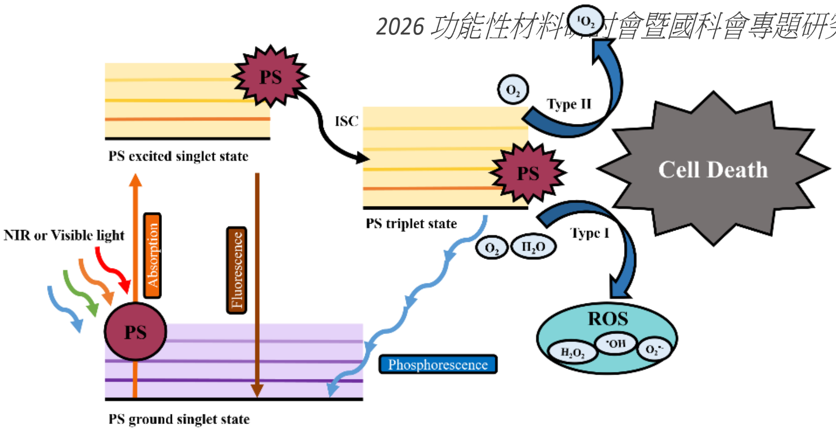

圖 6 活性氧機制 (PS：Photosensitizer, 光敏劑；ISC：Intersystem Crossing, 係間躍遷)

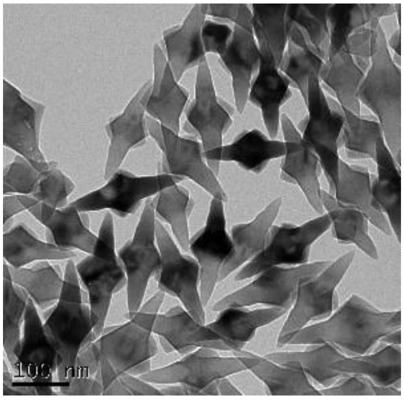

圖 7 UCNP 之 TEM 分析圖

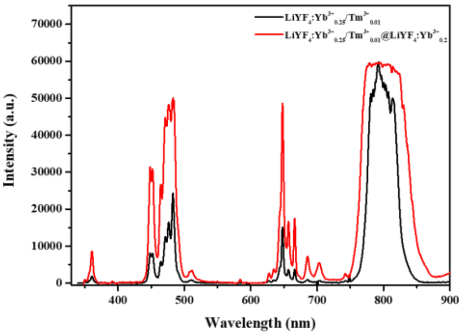

圖 8 UCNP 之螢光光譜圖

參考文獻

[1] M. Wang, G. Abbineni, A. Clevenger, C. Mao, and S. Xu, "Upconversion nanoparticles: synthesis, surface modification and biological applications," *Nanomedicine,* vol. 7, no. 6, pp. 710-29, Dec 2011, doi: 10.1016/j.nano.2011.02.013.

[2] B. Ling, Y. Wang, H. Dong, H. Chen, and L. Wang, "Enzyme-triggered aggregation of upconversion nanoparticles for targeted photodynamic therapy via NIR irradiation," *Nanoscale Advances,* vol. 7, no. 10, pp. 3068-3076, 2025, doi: 10.1039/d4na01050g.

[3] L. Huang, X. Zhao, Q. Zhao, F. Zhou, and M. Zhao, "Recent Progress, Application, and Quality Evaluation of Plant-Based Double Emulsions in Low-Fat Foods," *Food and Bioprocess Technology,* vol. 18, no. 2, pp. 1160-1180, 2024, doi: 10.1007/s11947-024-03567-x.

[4] X. Zhu *et al.*, "Upconversion nanoparticle-mediated photodynamic therapy induces THP-1 macrophage apoptosis via ROS bursts and activation of the mitochondrial caspase pathway," *Int J Nanomedicine,* vol. 10, pp. 3719-36, 2015, doi: 10.2147/IJN.S82162.

報告型式：

□英文口頭報告競賽 (□無機材料， □有機材料)
■海報展示並參加壁報論文競賽(■無機材料， □有機材料)
□只參加海報展示 (□無機材料， □有機材料)

元素摻雜高熵合金奈米催化劑之製備與電化學產氫動力學分析

李欣頤 [1]、胡晨曦 [2]、邱聖貴 [1*]
[1] 國立臺南大學材料科學系 700301 台南市中西區樹林街二段 33 號
[2] 逢甲大學材料科學與工程學系 407102 臺中市西屯區文華路 100 號
*E-mail: shengkuei@mail.nutn.edu.tw

NSTC114-2221-E-024 -016 -

摘要

氫能是乾淨、高效且多用途的未來能源，其中水電解作為單純無汙染的產氫方式，更是受到眾多關注[1-3]。本研究為合成硫化高熵金屬甘油酸鹽催化劑材料，目的在於提升析氫反應的效率，在實驗中利用溶劑熱合成法將摻雜釩(V)的鈷鉬鐵錳鎳(CoMoFeMnNi)多金屬甘油酸鹽材料生長於石墨氈的基材上，並藉由二次溶劑熱合成進行硫化改質，針對硫化過程之反應溫度、持溫時間、硫添加量三個製程參數進行探討，並透過掃描式電子顯微鏡(SEM)、穿透式電子顯微鏡(TEM)等表徵技術對催化劑結構進行分析，利用三極電化學系統分析其催化動力學特性，輔以氣相層析儀量測並計算實際產氫速率，綜合評估其在析氫反應的催化性能表現。實驗結果顯示催化性能與高溫及長持溫時間成正相關趨勢，得出最佳參數為反應溫度 160℃、反應時間 12 小時、硫添加量 5 毫升的條件下，最低過電位達 302mV 並擁有 69.41mV•dec-1 之低塔弗斜率值，表明所合成出之硫化高熵金屬甘油酸鹽催化劑材料展現出優異催化性能。本研究透過材料設計及性能優化，對高熵催化劑材料的潛力及後續改質可能性進行初步的探究，期望提升這類材料之性能，以實現更經濟高效之氫氣生產，為氫能發展與推廣提供新的思路。

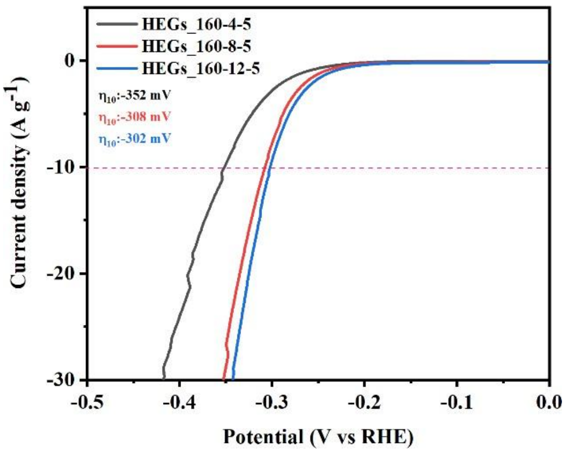

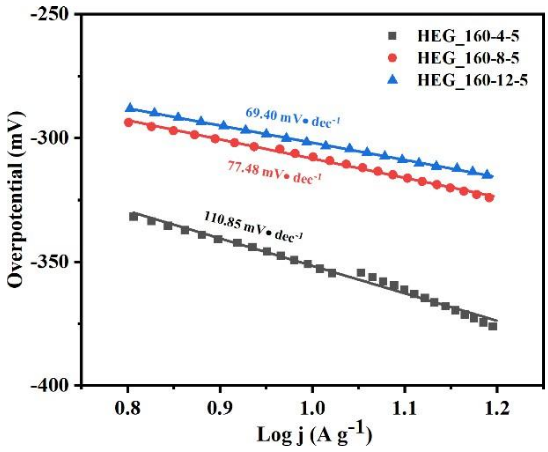

參考文獻

[1] B. Ranjith, L. Gnanasekaran, P. C. Karthika, J. R. Rajabathar, H. A. Al-Lohedan, W. K. Kim, V. R. M. Reddy, M. Kapoor, S. Singh, M. Lavanya, and G. Devendrapandi, “Enhancing the activity of transition metal-based sulfides via synergistic effects for electrochemical overall water splitting,” *International Journal of Hydrogen Energy*, vol. 112, pp. 255–265, 2025, doi: 10.1016/j.ijhydene.2025.01.349.

[2] Y. Liu, Y. Wu, X. Chen, Y. Ying, J. Wen, H. Wang, L. Chen, Y. Qu, M. Li, J. Wu, and Z. Fu, “Metal sulfide-based electrocatalysts for water splitting: From rational design to advanced applications,” *Fuel*, vol. 404, Art. no. 136208, 2026, doi: 10.1016/j.fuel.2025.136208.

[3] D. L. T. Nguyen, V. V. Tran, C. C. Nguyen, and T. M. Nguyen, “Transition metal sulfides/selenides as cathode electrocatalysts for enhanced hydrogen evolution: Nanostructure engineering strategies and recent progress,” *International Journal of Hydrogen Energy*, vol. 229, Art. no. 154736, 2026, doi: 10.1016/j.ijhydene.2026.154736.

報告型式：

□英文口頭報告競賽 (□無機材料， □有機材料)
☑海報展示並參加壁報論文競賽(☑無機材料， □有機材料)
□只參加海報展示 (□無機材料， □有機材料)

LLM 大模型驅動之可攜式光譜現場材料分析智慧平台評估

呂居樺
台灣中油股份有限公司 綠能科技研究所 品保驗證組
295914@cpc.com.tw

摘要

在石化產業與高階材料製造的品保檢驗中，傳統材料分析高度依賴實驗室儀器，不僅耗時且難以滿足生產線即時監控或工安意外現場的快速鑑識需求。為突破此實務瓶頸，本研究旨在開發一套整合大型語言模型（LLM）與可攜式光譜技術的端到端智慧檢驗平台。

本研究建構了一套自動化 AI 工具鏈，形成完整的研究與檢驗閉環：利用 Perplexity 進行即時且附帶引用的文獻調查；透過 Gemini 執行深度文獻分析與研究規劃；使用 NotebookLM 跨來源整合光譜數據並自動生成可視化報告；最後以 Notion 作為專案管理與知識庫平台。在檢驗硬體端，本研究結合可攜式拉曼光譜（提供高選擇性分子指紋，適用於定性鑑別）與近紅外光譜（NIR，適用於多參數定量分析），發揮雙光譜互補優勢。針對無法移動之特殊樣品或高風險場域，實測結果顯示，結合機器學習與 LLM 輔助光譜解讀（如最新的 IR-Agent 多任務推理技術），系統能在 60 秒內完成複雜材料的就地（in-situ）鑑定。其中，拉曼光譜對混合物的定性辨識準確率達 93%以上，而 NIR 的定量預測 R^2 亦可達 0.98 以上。

本平台最大的創新在於「持續進化」機制：每次現場分析的專案經驗與光譜數據皆會記錄於 Notion 知識庫，並回饋至 AI 模型進行再訓練。此流程不僅大幅降低了現場人員解讀光譜的專業門檻，更讓檢驗系統隨著專案經驗累積而愈發精準，實現從被動送驗到主動即時監控的智慧轉型。

參考文獻

[1] J. Goldie, "NotebookLM + Gemini 3 + Perplexity AI Workflow," Julian Goldie SEO. [Online]. Available: https://juliangoldie.com/notebooklm-gemini-3-perplexity-ai/

[2] Analytik Ltd., "Whitepaper: Comparison of portable spectroscopy techniques (FTIR, NIR and Raman)," 2015. [Online]. Available: http://www.analytik.co.uk/wp-content/uploads/2015/12/whitepaper-comparison-of-portable-spectroscopy-techniques-ftir-nir-and-raman.pdf

[3] Exanodia, "Customized Solutions for AI-Assisted Inspection." [Online]. Available: https://www.exanodia.com/en/customized-solutions-for-ai-assisted-inspection/

[4] Koehler Instrument Company, Inc., "How AI is used to improve petroleum laboratory testing and instrumentation," Petro Online. [Online]. Available: https://www.petro-online.com/article/analytical-instrumentation/11/koehler-instrument-company-inc/how-ai-is-used-to-improve-petroleum-laboratory-testing-and-instrumentation/3743

報告型式：

□英文口頭報告競賽 (□無機材料， □有機材料)
□海報展示並參加壁報論文競賽(□無機材料， □有機材料)
■只參加海報展示 (□無機材料， ■有機材料)

降解聚乳酸廢棄物之微生物材料應用

謝式弘*、張育誠、李信毅、吳柏龍、李筱萍
台灣中油煉製研究所生物科技事業中心
296791@cpc.com.tw

摘要

聚乳酸(PLA)為發展最成功的生質塑膠，全球市場高達 10 億美金(2020 年)。其原料為農作物或農業廢棄物經發酵後產出的乳酸。製程中不使用任何石化原料且廢棄的 PLA 可利用堆肥分解，不殘留於自然環境中。因此，相較於石化塑料，PLA 具有極高的減碳及減塑效益。但工業堆肥並不適用於台灣地區，除土地資源不易取得外，實務上而言，PLA 廢棄物無法與其他塑膠完全分開，且常與其他塑膠混煉生產。台灣消費後的 PLA 僅能以焚化處理(固體再生燃料)，不能有效回收利用，因而無法形成循環經濟產業鏈。本研究針對台灣消費後 PLA 廢棄物回收難題，開發專一性之生物解聚方法。自中油場域篩選特有之 CPCBT01 菌株(*A. clausii*)，並成功以非堆肥的發酵方式解聚 PLA。CPCBT01 菌株具有高度專一性，僅針對 PLA 成份降解，而不解聚其他台灣常見的廢塑膠，如 PET、PP、PS、PE、PVC 等，可由混合塑料廢棄物中，精準碎解回收 PLA，而不影響其他塑膠回收。經菌株碎解後的 PLA，可再解聚為乳酸單體，回收作為聚乳酸的原料，實現聚乳酸永續循環經濟之目標。

參考文獻

1. M. Hussaina, S. M. Khana, M. Shafiq and N. Abbas(2024) *Giant*, 18, 100261.
2. Y.C. Li, S. W. Song, Q. Z.Liu, Y.J. Weng and Y.L. Zhang(2024) *ACS Omega* 9, 13509−13521.

報告型式：

□英文口頭報告競賽 (□無機材料， □有機材料)
□海報展示並參加壁報論文競賽(□無機材料， □有機材料)
■只參加海報展示 (□無機材料， ■有機材料)

雙環戊二烯於高附加價值光固化材料之開發及其光電應用研究

徐偉智、陳維彥、蔡志勇、李欣隆、黃麟強、高瑞富、黃銘郁、林建琛
台灣中油股份有限公司煉製研究所
246719@cpc.com.tw

摘要

近年國際地緣政治風險持續升高，中東局勢動盪及伊朗相關衝突導致原油供應不穩與價格劇烈波動，進一步影響石化原料取得與整體成本控制。在此情勢下，煉製與石化工廠之穩定操作更顯關鍵，如何有效降低非計畫性停機、提升設備可靠度並確保製程連續性，已成為營運管理與製程研發的重要課題。同時，中國大陸石化產業持續擴張，憑藉規模經濟與成本優勢對區域市場形成強大競爭壓力，促使國內業者必須加速技術升級，並朝高效率與高附加價值產品發展，以維持長期競爭優勢。

紫外光固化（Ultra Violet Curing）技術係利用光照射誘發聚合反應，使分子於短時間內產生交聯結構而達到快速硬化，具有反應速率快、能耗低及製程簡化等優點，相較於傳統熱固化技術更具環保與經濟效益，已成為高性能材料發展的重要方向之一。

本研究以雙環戊二烯（DCPD）為前驅物，透過其特有之雙環剛性結構與高反應活性，進行末端官能基修飾並導入光敏基團，開發具紫外光可硬化特性之樹脂材料。藉由分子結構設計與配方調控，使材料兼具良好交聯能力、熱穩定性與應用適應性。該材料除具備應用於光電元件封裝等高階領域之潛力外，亦可有效提升煉油副產物之利用價值，進一步推動石化產業朝高值化與差異化發展。

報告型式：

□英文口頭報告競賽　　　　(□無機材料，　□有機材料)
□海報展示並參加壁報論文競賽(□無機材料，　□有機材料)
■只參加海報展示　　　　　(□無機材料，　■有機材料)

彈性調控微粒技術及其低應力封裝材料

顏巨倫[1]、林建琛[1]
[1] 台灣中油公司煉製研究所
078816@cpc.com.tw

摘要

高分子微粒子由於其粒子的形狀和粒徑大小可輕易變化，粒子的表面性質更可藉由各種不同的改質方法而有多種機能化的應用。例如，調控其折射率、電氣特性、分散性、流動性、彈性、反射性等，使高分子粒子早已成為基礎材料而應用於塗料、塑膠加工、OA 產品及化妝品中。近年來隨著 IoT、行動裝置、甚至穿戴裝置的應用市場越加的廣泛、產品種類也更加多元化，在攜帶式或是穿戴式應用產品中因為使用情境需求、而需要高韌性、低應力的封裝結構及封裝材料特性，如圖一所示。

現有的封裝材料雖有高接著強度、高信賴性的特性，但是在薄型化構裝時則面臨到低應力的挑戰、因此有研究運用彈性微粒來增加封裝材料的韌性、降低整體封裝材料的應力以符合應用需求。然而這樣重要的關鍵機能材料卻完全掌握在歐洲和日本製造商手中，國內廠商除中油公司外、其餘只能生產供應非交聯的高分子塑膠微粒、只能應用到中低階、較低成本的產品上。國內高階光電組件上游原料則有供貨不穩定、品質競爭力不足的隱憂。

有鑑於此，本研究建置高分子塑膠微粒合成製備平台，如圖二所示，進行高分子塑膠微粒彈性調控技術開發，建立不同粒徑範圍下、彈性調控技術開發，深化高值化塑膠微粒合成製備技術、增加彈性微粒的應用廣度，並導入光電元件封裝材料進行應用驗證。

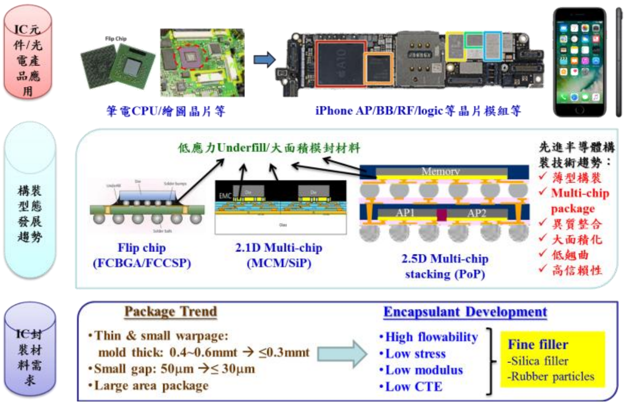

圖一、構裝發展趨勢與需求

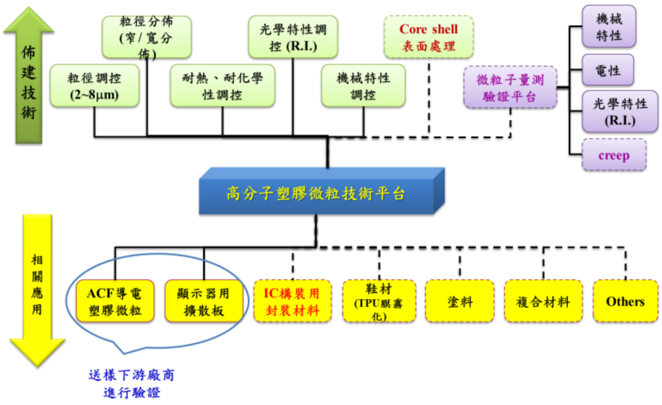

圖二、高分子塑膠微粒技術平台及其應用

參考文獻

[1] Yan, J.L.; Ho, Chyi-Liuh.; Wang, Yih-Ping. et al.; 石油季刊 第 55 卷第 4 期 中華民國 108 年 12 月

報告型式：

□英文口頭報告競賽 (□無機材料， □有機材料)
□海報展示並參加壁報論文競賽(□無機材料， □有機材料)
■只參加海報展示 (□無機材料， ■有機材料)

回收 PET 脫色之化學循環法

陳冠瑜 [1],顏巨倫,林建琛
台灣中油股份有限公司煉製研究所嘉義市西區民生南路 217 號
E-mail:079707@cpc.com.tw

摘要

為了推動塑料的多元化再利用，本研究旨在將回收且具有雜色的聚對苯二甲酸乙二醇酯（PET）塑膠瓶片加入苯甲醚解聚成 BHET 單體[1]，並進一步改質為環氧樹脂乳化劑[2]。傳統的 PET 乙二醇醇解通常需要在 190℃以上的高溫下進行，而加入苯甲醚作為助溶劑後，反應溫度可顯著降低至約 150℃-153℃，同時保持極高的轉化率[3]-[5]。除此之外，藉由苯甲醚能與 PET 的芳香環產生分子間作用力，使催化劑更容易接觸到酯鍵部位，進而加速反應速率[3]- [5]。基於上述實驗結果，苯甲醚克服了傳統 PET 醇解「高能耗」與「反應慢」的缺點，作為實現低溫高效化學回收的關鍵輔助試劑，其研究結果為塑料回收再利用提供了新的方向。

參考文獻

[1]劉春秀,廢聚對苯二甲酸乙二酯酯化解聚及其產物應用研究進展,石油化工技術與經濟,2023,39(2)

[2]Lin,C.T;Yu,C.H,r-PET 化學回收再製技術平台展望,工業材料雜誌,2023,437

[3] Le,N.H;Van,T.T Ngoc;Shong,B;Cho,J,Low-Temperature Glycolysis of Polyethylene Terephthalate, ACS Sustainable Chem. Eng,2022, 10(51),17261-17273.

[4] Qu, C., Han, X., & Wang, H. (2025). Synergistic Catalysis Driven by Solvent Effect: Efficient Glycolysis of Polyethylene Terephthalate (PET) by the Zn(OAc)2/DBU-DMSO System. ACS Sustainable Chemistry & Engineering, 13(31), 12496–12508.

[5] Luna, E., Olazabal, I., & Roosen, M. (2024). Towards a Better Understanding of the Cosolvent Effect on the Low-Temperature Glycolysis of Polyethylene Terephthalate (PET). Chemical Engineering Journal, 482(15), 148861.

報告型式：

□英文口頭報告競賽 (□無機材料， □有機材料)
□海報展示並參加壁報論文競賽(□無機材料， □有機材料)
■只參加海報展示 (□無機材料， ■有機材料)

應用於智慧鞋墊之 PVA/H_3PO_4 微結構離子導電材料特性分析

謝幃勝 [1], 黃榮堂 [2], 邱瓏峻 [3]
國立臺北科技大學
113408088@ntut.org.tw

摘要

本研究旨在開發一種兼具高柔韌性與離子導電性之介電材料，並藉由於聚乙烯醇(Polyvinyl Alcohol, PVA)與磷酸(H_3PO_4)混合之離子導電介電層表面導入微結構，提升壓力感測器之靈敏度與整體感測性能，以改善傳統平滑介電層在靈敏度與導電度方面之不足。研究中採用不同號數砂紙(#240、#1200、#10000)作為翻模模具，透過簡易翻模製程於PVA/ H_3PO_4 薄膜表面形成隨機微結構，並搭配 PCap04 電容數位轉換晶片進行即時電容訊號量測與分析。實驗結果顯示，導入表面微結構確實可有效改善介電層之壓力感測表現；然而，感測性能並非隨表面粗糙度增加而呈線性提升，而是存在一最佳化之微結構尺度，可在靈敏度、訊號變化與穩定性之間取得較佳平衡。研究結果證實，利用低成本且製程簡便之砂紙翻模方法，即可有效調控 PVA/ H_3PO_4 介電材料之微結構特性與感測特性。此技術未來在可撓式壓力感測器、智慧鞋墊及步態分析監測等應用領域。

關鍵字： 聚乙烯醇 (PVA)、磷酸 (H_3PO_4)、壓力感測器、智慧鞋墊、砂紙翻模。

報告型式：

□英文口頭報告競賽 (□無機材料， □有機材料)
□海報展示並參加壁報論文競賽(□無機材料， □有機材料)
☑只參加海報展示 (□無機材料， ☑有機材料)

天然型 N-乙醯葡萄糖胺抗黑色素生成及抗黑色素體吞噬之功能性研究

張育誠，謝式弘，李信毅，吳柏龍，李筱萍
台灣中油股份有限公司煉製研究所生物科技事業中心
078638@cpc.com.tw

摘要

N-乙醯葡萄糖胺(N-Acetylglucosamine，簡稱 NAG)是幾丁質分解之後的單體，NAG 除了存在於甲殼類、昆蟲、軟體動物及真菌細胞壁中的幾丁質外，更是人體中廣泛存在的胺基糖(Aminosugar)，可以進一步合成胺基葡聚醣、醣蛋白和蛋白多醣，這些聚合物是構成身體組織與血管的原料，並在消化道和呼吸道形成保護性屏障，同時具有調節物質進出人體的功能。本公司專利技術生物轉化法為利用微生物將廢棄蝦蟹殼中幾丁質分解轉化為天然型 NAG，為了開發 NAG 的應用性，本研究分別以小鼠黑色素瘤細胞和人類角質細胞為模型，觀察 NAG 是否具有抗黑色素生成或抗黑色素體吞噬之功效，結果發現，NAG 在濃度 5%可抑制 23.5%小鼠黑色素瘤細胞內黑色素生成；而 NAG 在濃度 0.5%、2%及 8%時細胞內螢光微珠評分為 2.84、1.04、1.06 beads/cell，顯示 NAG 濃縮液具有抑制人類角質細胞吞噬黑色素體功效。綜合上述結果，本研究發現 NAG 具有抑制黑色素細胞生成黑色素以及抑制角質細胞吞噬黑色素體之功效，代表未來 NAG 極具潛力應用於美白相關化粧品。

報告型式：

□英文口頭報告競賽 (□無機材料， □有機材料)
□海報展示並參加壁報論文競賽(□無機材料， □有機材料)
■只參加海報展示 (□無機材料， ■有機材料)

丙烯酸酯類兩親性梳狀無規共聚物在環氧樹脂中微結構增韌效果之研究

林佑穎 [1]、曾國鎰 [1]、鄭力誠 [1]
國立高雄科技大學化學工程與材料工程系
lcjheng@nkust.edu.tw

摘要

環氧樹脂是應用最廣泛的樹脂材料之一，但其高度交聯的網絡結構，使其性質硬脆，必須額外添加增韌劑進行改質，以滿足應用需求。近十年來，兩性共聚物(Amphiphilic copolymers)被視為環氧樹脂中新型的增韌劑。本研究比較無甲基（PEGMA-ODA）與含甲基（PEGMMA-SMA）兩親性梳狀無規共聚物於不同組成比例下之自組裝行為，並進一步探討其對環氧樹脂微結構調控與增韌效果之影響。將 5wt%增韌劑分別摻入熱固型環氧樹脂之雙酚 A 二縮水甘油醚(Bisphenol-A diglycidyl ether， DGEBA)和甲基四氫酞酐(Methyltetrahydrophthalic anhyolricle，MTHPA)中，進行固化反應。並利用高解析度掃描式電子顯微鏡(SEM)觀察破斷面處表面形貌，分析其增韌機制。由組成及製備條件可將環氧基質中的奈米微胞結構區分為囊泡狀微胞(Vesicles micelles)、蠕蟲狀微胞(Wormlike micelles)和球狀微胞(Sphere micelles)等。此外，我們採用了衝擊測試、平面應變斷裂韌性測試和拉伸測試來比較改質後環氧樹脂之機械性能。

參考文獻

(1) Hattori, G.; Takenaka, M.; Sawamoto, M.; Terashima, T. Nanostructured Materials via the Pendant Self-Assembly of Amphiphilic Crystalline Random Copolymers. J Am Chem Soc 2018, 140 (27), 8376-8379. DOI: 10.1021/jacs.8b03838 From NLM PubMed-not-MEDLINE.

(2) Kishi, H.; Kunimitsu, Y.; Nakashima, Y.; Imade, J.; Oshita, S.; Morishita, Y.; Asada, M. Relationship between the mechanical properties of epoxy/PMMA-b-PnBA-b-PMMA block copolymer blends and their three-dimensional nanostructures. Express Polymer Letters 2017, 11 (10), 765-777. DOI: 10.3144/expresspolymlett.2017.74.

(3) Jheng, L. C.; Chang, T. Y.; Fan, C. T.; Hsieh, T. H.; Hsieh, F. M.; Huang, W. J. Toughening of epoxy thermosets by self-assembled nanostructures of amphiphilic comb-like random copolymers. RSC Adv 2023, 13 (47), 33484-33494. DOI: 10.1039/d3ra06349f From NLM PubMed-not-MEDLINE.

(4) Ikami, T.; Kimura, Y.; Takenaka, M.; Ouchi, M.; Terashima, T. Design guide of amphiphilic crystalline random copolymers for sub-10 nm microphase separation. *Polymer Chemistry* ***2021, 12 (4), 501-510. DOI: 10.1039/d0py01618g.***

報告型式：

□英文口頭報告競賽 (□無機材料， □有機材料)
□海報展示並參加壁報論文競賽(□無機材料， □有機材料)
✓只參加海報展示 (□無機材料， ✓有機材料)

咖啡渣不同處理方式應用於水泥砂漿之性能與剪黏工藝適應性研究

林佩萱[1] 張家瑞 [2]
[1]國立宜蘭大學永續建築與規劃研究所
通訊作者：林佩萱
jill90121660@gmail.com

一、摘要

隨著建築材料對環境永續與資源再利用之重視，尋求可替代傳統材料之再生資源成為重要研究方向。水泥砂漿雖為常用建材，但其製程具高碳排放，且在施工過程中易出現乾燥過快及收縮裂縫等問題，影響其使用性能。咖啡渣為日常生活中大量產生之有機廢棄物，相關研究指出其具有多孔性與保水特性，若能應用於水泥基材料中，除可降低廢棄物負擔，亦可能改善材料之施工性與性能表現。

本研究將咖啡渣分為兩種處理方式，包括經水洗並烘乾至恆重之未處理咖啡渣，以及經焚燒處理後之咖啡渣灰， 並分別以不同比例（0%、0.5%、1%、3%、5%、10%）添加於水泥砂漿中進行試驗。實驗項目包含抗壓強度、吸水率、乾縮率及裂縫觀察，並透過剪黏試體實作，評估其可塑性、雕刻性與黏結性之差異。此外，透過匠師實際操作與訪談，分析材料於傳統工藝應用之可行性。

試驗結果顯示，在低添加比例（約 0.75%至 1%）下，未處理咖啡渣可提升砂漿之保水能力與施工操作性，並降低乾縮與裂縫產生，於剪黏工藝操作中表現較為穩定；相關研究亦指出，當添加比例增加時，材料孔隙率上升，將導致抗壓強度下降之趨勢。焚燒處理咖啡渣於低比例添加時可提升材料強度，顯示其具有改善結構性質之潛力，但其保水性與可塑性較差，在細部造型及黏附表現上不如未處理材料。

匠師訪談結果顯示，材料是否具備穩定性能、施工便利性及合理成本，為影響新材料導入之主要因素。對於咖啡渣砂漿之應用，若能兼顧操作性與材料穩定性，仍具有實務發展空間。

綜合本研究結果，咖啡渣作為水泥砂漿添加材料具一定應用潛力，其中未處理咖啡渣較適用於需高可塑性之剪黏工藝，而焚燒咖啡渣則較適用於強度需求較高之材料系統。本研究結果可作為再生材料應用於建築材料與傳統工藝之參考依據。

二、簡介

隨著永續發展與資源再利用議題日益受到重視，建築材料逐漸朝向低碳與再生材料方向發展。水泥砂漿為常用建材之一，然而其製程伴隨高碳排放，且於施工過程中易產生乾燥過快及收縮裂縫等問題，影響材料之使用性能。因此，如何在兼顧材料性能的前提下導入再生資源，成為近年重要研究課題。

咖啡渣為日常生活中大量產生之有機廢棄物，相關研究指出其具有多孔結構與良好保水特性，具備應用於水泥基材料之潛力。另一方面，傳統建築中的剪黏工藝對材料之可塑性與黏著性要求較高，但目前相關研究多集中於材料力學性質，較少探討其於實際工藝操作之適用性。

基於上述背景，本研究探討不同處理方式之咖啡渣應用於水泥砂漿之性能差異，並進一步評估其於剪黏工藝中的應用可行性，以期提供再生材料結合傳統工藝之參考依據。

三、研究方法

本研究將咖啡渣分為兩種處理方式進行比較：

未處理咖啡渣（SCG-N）

經清洗後烘乾至恆重，保留其原有多孔結構與有機成分。

焚燒處理咖啡渣（SCG-A）

經高溫焚燒後轉化為灰質材料，降低有機含量並提升結構穩定性。

試驗中將咖啡渣以不同比例（0%、0.5%、1%、3%、5%、10%）添加於水泥砂漿中，並保持其他配比條件一致，以比較不同變因之影響。

材料性質試驗項目包括：
抗壓強度試驗
吸水率試驗
乾縮行為觀察
裂縫生成情形分析

此外，透過剪黏試體製作，評估材料於實際工藝操作中之可塑性、雕刻性與黏結性，並結合匠師實際操作與半結構式訪談，分析材料於實務應用之適用性。

四、結果與討論

試驗結果顯示，咖啡渣之添加對水泥砂漿性能具有顯著影響，且不同處理方式呈現不同趨勢。在未處理咖啡渣組中，低添加比例（約 0.75%至 1%）可提升砂漿之保水能力與施工操作性，並有效降低乾縮與裂縫產生，使材料於剪黏操作中具有較佳之可塑性與穩定性。然而，當添加比例提高時，材料孔隙率增加，導致抗壓強度下降，此趨勢亦與既有研究結果相符。

焚燒處理咖啡渣則於低比例添加時呈現較佳之抗壓強度表現，顯示其對材料結構具有強化效果，相關研究亦指出焚燒或熱處理後之咖啡渣可提升材料之力學性能。但其保水性與可塑性相對不足，在細部造型與黏附操作上表現較不理想。

整體而言，兩種處理方式呈現不同材料特性：未處理咖啡渣有利於施工操作與工藝應用，而焚燒咖啡渣則較適合提升材料強度。

匠師訪談結果亦顯示，材料是否具備良好操作性、穩定性與合理成本，為影響其應用之關鍵因素。多數匠師對新材料持開放態度，但前提為其不影響施工品質與工藝表現。

五、結論

本研究結果顯示，咖啡渣作為水泥砂漿添加材料具備應用潛力，其性能表現受處理方式與添加比例影響顯著。在低比例添加條件下，未處理咖啡渣較適用於剪黏工藝等需高度可塑性之應用，而焚燒咖啡渣則較適用於強度需求較高之材料系統。

本研究透過材料試驗與工藝實作之整合分析，提供再生材料應用於建築材料與傳統工藝之初步依據，未來可進一步擴展至其他材料系統與應用場域。

參考文獻

Shahid, M., et al. (2024). Application of spent coffee grounds in cementitious materials.
Şenol, A. F. (2025). Performance of geopolymer mortar incorporating spent coffee grounds.

報告型式：

□英文口頭報告競賽 (□無機材料， □有機材料)
□海報展示並參加壁報論文競賽(□無機材料， □有機材料)
✓只參加海報展示 (□無機材料， ✓有機材料)

2026 功能性材料研討會暨國科會專題研究計畫成果發表會

二甲酸單體比例調控之原位磷酸摻雜聚苯並咪唑共聚膜之結構與性能研究

許恩碩、賴孝武*
南臺科技大學 化學工程與材料工程系
E-mail: swlai@stust.edu.tw

摘要

隨著氫能技術的快速發展，高純度氫氣的需求日益提升，特別是在電化學氫氣純化 (Electrochemical Hydrogen Separation, EHS)系統中，質子交換膜 (Proton Exchange Membrane, PEM)的性能直接影響整體系統效率與穩定性。高溫操作環境下，傳統全氟磺酸膜受限於水的依賴性與熱穩定性不足，難以滿足中高溫應用需求。因此本研究以高熱穩定性與機械強度的聚苯並咪唑 (Polybenzimidazole, PBI) 為主要過間苯苯二甲酸 (IPA)與對苯二甲酸 (TPA) 單體聚合，合成不比例的 meta/para-PBI膜材，並探討單體比例對膜材結構、磷酸摻雜量、質子導電性與機械性質的影響。本研究以聚磷酸 (PPA)為反應溶劑，進行高溫縮合聚合反應製備 PBI膜材。過間傅立葉轉換紅外光譜 (FTIR)與固態 ^{13}C SS-NMR分析，確認苯並咪唑環結構已成功形成。熱重分析 (TGA)指出所有膜材於 200°C 以下皆具良好熱穩定性。磷酸摻雜量分析顯示，各樣品的OA/PBI 值介於 7.03–8.75 mol H_3PO_4/mol PBI r.u.，現非線性性化化勢，，中中 m/p 7:1樣品具有最高磷酸負載量。質子導電測試發非導電度隨溫度升高而增加，在 180°C條件下，m/p 7:1 膜材展非最佳質子傳導能力。顯示出適度引入 para結構，讓分子鏈規整性與自由體積之苯取得平衡，有利於形成穩定的氫鍵傳輸網絡並提升高溫質子導電性能。機械性質分析顯示，純 meta- PBI具有最高抗拉強度，而 m/p 7:1樣品則在強度與延展性之苯達到較佳協調，整體機械性能表非最為均衡。整體分析顯示，m/p 7:1為最佳單體比例，在高溫下兼具優異質子導電性與機械穩定性，並可作為高溫型 PBI 膜材料設計的重要數據。

關鍵字:聚苯並咪唑、高溫質子交換膜、meta/para-PBI

參考文獻

Y. Luan, Y. Xiong, G. He, C. Liu, and S. J. S. S. o. C. A. o. E. Li, "Research progress of hydrogen separation membrane," vol. 24, no. 3, p. 140, 2022.

L. A. Murdock and B. C. J. A. A. E. M. Benicewicz, "Teaching an old dog new tricks: synthesis, processing, and application of polybenzimidazole (PBI) membranes," vol. 7, no. 1, pp. 239-249, 2023

L. K. Seng, M. S. Masdar, and L. K. J. M. Shyuan, "Ionic liquid in phosphoric acid-doped polybenzimidazole (PA-PBI) as electrolyte membranes for PEM fuel cells: A review," vol. 11, no. 10, p. 728, 2021

報告型式：

□英文口頭報告競賽 (□無機材料， □有機材料)
□海報展示並參加壁報論文競賽(□無機材料， □有機材料)
■只參加海報展示 (□無機材料， ■有機材料)

透明光學級液態酸酐光電半導體高值化應用研究

張行*，林政凱，顏巨倫，林建琛
台灣中油股份有限公司煉製研究所，E-mail:078051@cpc.com.tw

摘要

近年來，高性能 LED 透明封裝材料以矽氧烷樹脂(silicone)為主要封裝材料系統，矽氧烷樹脂材料雖然在本質特性上具有優異的高溫安定性及 UV 安定性，然而矽氧烷樹脂材料主要缺點是環境中的水氣很容易進入膠材內部，對LED晶片、導線及電極等造成破壞，另外矽氧烷樹脂材料本身缺少極性的官能基團，無法提供較好的接著性，必須藉由添加接著性促進劑以達到較好的接著，這也成為高性能 LED 開發的一大材料技術障礙。反觀矽氧烷樹脂材料阻氣性以及接著性不足之處，正是環氧樹脂的特性優點，因此開發出兼俱矽氧烷光熱安定性和環氧樹脂機械與阻氣性的矽氧烷改質環氧樹脂混成封裝材料技術值得加以重視。然而在實際 LED 封裝應用和信賴性測試結果表現卻又呈現出用矽氧烷改質環氧樹脂混成封裝材料之 LED 元件出光信賴性並不如預期，且往往和矽氧烷改質環氧樹脂混成封裝材料本身的光熱安定性表現大相逕庭，這些都說明如果僅是量測評估封裝原材料、硬化塊材的光學和機械特性是遠遠不夠的，必須要進行完整的 LED 封裝元件效能和信賴性驗證，才能確保相關材料開發結果的完整性和產業化可行性。

本研究主要是分別將提純後之光學級液態酸酐、高耐熱與耐水解液態酸酐或是配方液態酸酐進行高功率 LED 透明封裝材料高值化應用驗證，實驗結果顯示台灣 N 公司純化酸酐之 LED 元件封裝良率 100%、MSL Level III 衰減 12.9%、85°C/85% R.H.1000 小時衰減 0.0%、TCT -40°C~120°C/300Cycles 衰減 3.2%，其整體表現已和日本酸酐LED 元件相同，均可達到信賴性要求，同時也發現純化酸酐與日本 N 公司酸酐都無法通過 130°C/1000 小時信賴性測試。另外也發現過量添加抗氧化劑(抗氧化劑=2.4 phr)會加劇 LED 元件耐熱性劣化，此外台灣 N 公司純化酸酐與日本 N 公司 MHHPA 共混酸酐(當量比=1/4)製備 LED 元件封裝良率 100%、TCT -40°C~120°C/300Cycles 衰減0.0%，130°C/1000 小時衰減 18.8%，耐熱性可獲得大幅提昇，最後純化酸酐與日本 N 公司共混製備 SMD-LED，在高溫信賴性配方改善和信賴性驗證方面，抗氧化劑=1.2phr、共混酸酐當量比=1/1，LED 元件封裝良率 100%、MSL Level III 衰減 2.9%、130°C/1000 小時衰減 14.7%，高溫耐熱性已達信賴性要求。

参考文獻

Lin, Chih-Hao; Chen, Kai-Chi; Huang, Shu-Chen; Li, Hsun-Tien, “The study of thermal cycling performance of enacpasulant material in SMD LEDs application”, ICEP-IAAC 2015 - 2015 International Conference on Electronic Packaging and iMAPS All Asia Conference, p 642-645, 2015.

Hsu, Chia-Wen; Ma, Chen-Chi M.; Tan, Chung-Sung; Li, Hsun-Tien; Huang, Shu-Chen; Lee, Tzong-Ming; Tai, Hsin, “Effect of thermal aging on the optical, dynamic mechanical, and morphological properties of phenylmethylsiloxane-modified epoxy for use as an LED encapsulant”, Materials Chemistry and Physics, Vol.134(2-3):789-796,2012.

報告型式：

□英文口頭報告競賽 (□無機材料， □有機材料)
□海報展示並參加壁報論文競賽(□無機材料， □有機材料)
■只參加海報展示 (□無機材料， ■有機材料)

Extending Taguchi-Based Materials Process Design Using Bayesian Optimization

Yu-Xian,Weng,Wen-Yu Lin, Hung-Mao Lin[1] and Ching-Feng Mao[2]
Department of Chemical and Materials Engineering, Southern Taiwan University of Science and Technology
*Correspondence: cfmao@stust.edu.tw

NSTC 114-2637-E-218-002-

Abstract

The Taguchi method is a widely used approach in materials process design for improving process robustness by maximizing the signal-to-noise (S/N) ratio. Using orthogonal arrays, Taguchi Design of Experiments (DOE) enables efficient screening of multiple process parameters with a limited number of experiments. However, the resulting analysis is restricted to the discrete design points defined by the orthogonal array and does not inherently support predictive modeling or sequential exploration of the continuous design space. In this work, we extend the Taguchi-based materials process design framework by integrating Bayesian Optimization (BO) with Gaussian Process (GP) surrogate modeling.

Using a simple quadratic test function that represents the true signal-to-noise (S/N) ratio of a simulated materials process, three process variables were normalized to standardized levels (−1, 0, 1) and incorporated into an L9 orthogonal array to generate the initial experimental dataset. The test function includes a cross term (x1·x2) and a deliberately shifted global maximum away from the symmetric center, reflecting realistic scenarios where the true optimum does not coincide with the midpoint of the variable ranges. While the initial Taguchi DOE provides efficient coverage of the design space and an interpretable starting point for analysis, the discrete L9 design points are generally insufficient to locate or approach the true optimum S/N ratio when the optimum lies between the predefined factor levels.

A Gaussian Process (GP) surrogate model was first constructed using the Taguchi DOE results, and Bayesian Optimization (BO) was then employed to sequentially propose new experimental conditions. At each iteration, the expected improvement acquisition function balances exploration and exploitation, enabling progressive refinement of the surrogate model and guiding the search toward the true optimum. A visual demonstration in the x1–x2 plane illustrates how BO sequentially moves from the discrete Taguchi design points toward the global optimum of the true S/N ratio. These results highlight the potential of integrating classical DOE with modern machine learning–driven optimization to extend Taguchi-based materials process design beyond discrete experimental settings.

This integrated framework offers several advantages over traditional Taguchi DOE alone. First, it preserves the interpretability and low experimental cost associated with orthogonal arrays. Second, by incorporating predictive surrogate modeling, it enables exploration of regions between discrete DOE points, thereby improving the search for optimal process conditions. Finally, the framework provides a foundation for future extensions, including multi-objective optimization, Pareto front exploration, and multi-fidelity modeling using existing laboratory datasets. Overall, the proposed methodology illustrates a practical pathway for bridging classical DOE practices with modern machine learning and active learning techniques, providing an efficient and data-driven strategy for materials process optimization.

Keywords: Bayesian Optimization, Taguchi Method, Materials Process Optimization

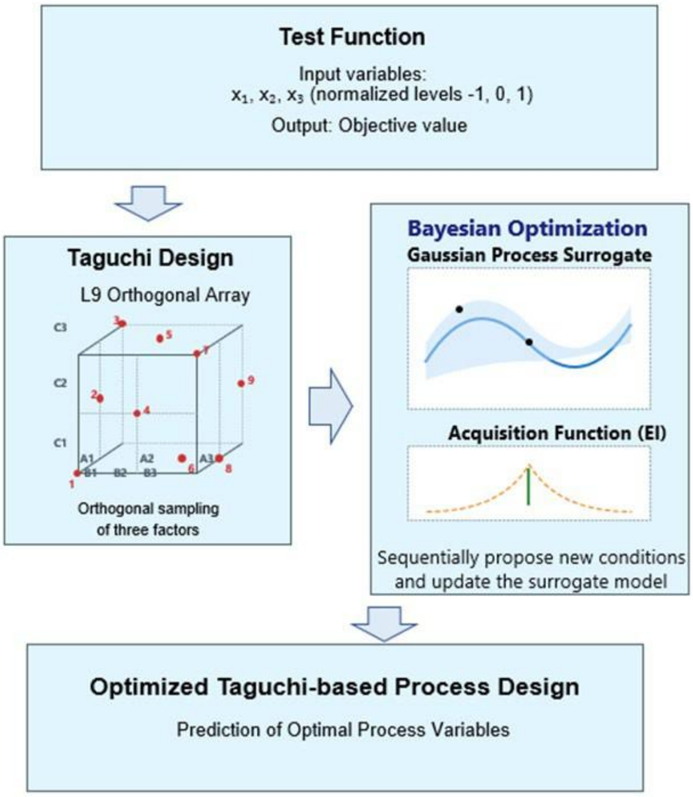

Figure 5. Schematic workflow extending the traditional Taguchi method to modern Machine Learning and Bayesian Optimization

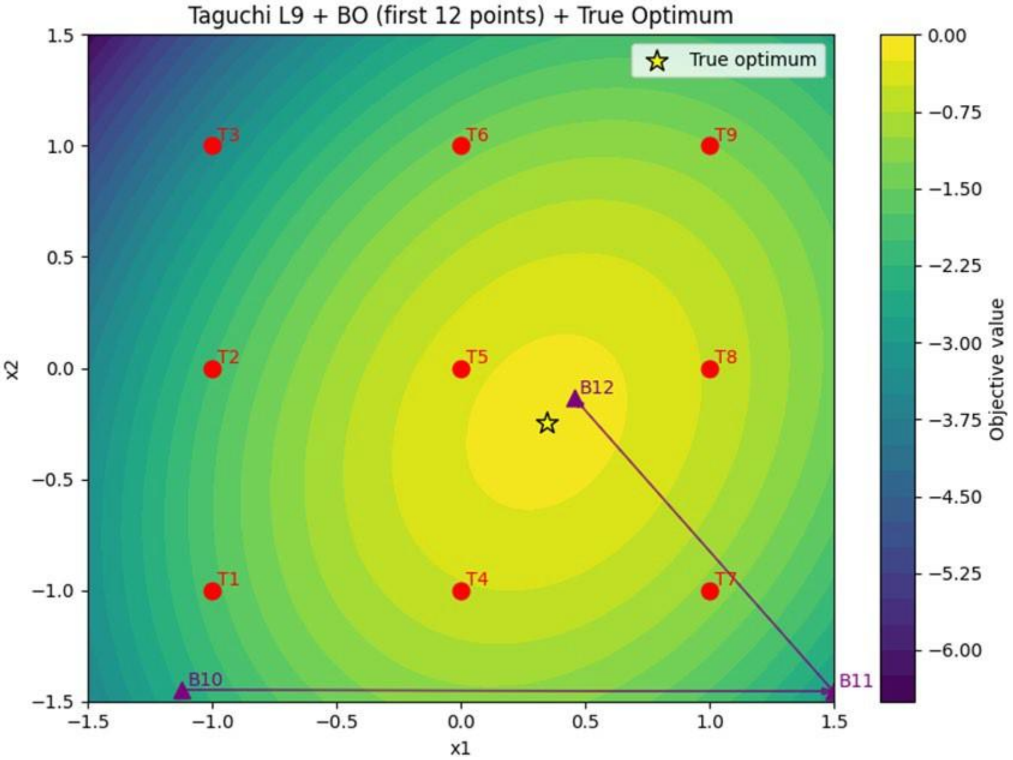

Figure 6. Heat map of the objective function on the x1-x2 plane with x3 fixed. (The star denotes the global maximum. Red circles represent the experimental points from the Taguchi L9 orthogonal array, and purple triangles indicate the sampling points suggested by Bayesian optimization.)

References

[1] Prabhu S, Kumar PA, Selwinston A, Taduvai P, Bairi S, Batra R. Enhancing experimental efficiency in materials design: a comparative study of Taguchi and machine learning methods. arXiv preprint arXiv:2506.03910; 2025.
[2] Rodic D, Sekulic M, Savkovic B, et al. Gaussian process modeling of EDM performance using a Taguchi design. Eng. 2026;7(1):14. doi:10.3390/eng7010014.
[3] Zubair SWH, Arafat SM, Khan SA, et al. Coupling Taguchi experimental designs with deep adaptive learning enhanced AI process models. Sci Rep. 2024;14:3428. doi:10.1038/s41598-024-73669-1.

Presentation type：

☐ English oral competition (☐ inorganic materials, ☐ organic materials)
☐ Poster competition (☐ inorganic materials, ☐ organic materials)
■ Exhibition only (■ inorganic materials, ☐ organic materials)

鈉離子電池正極材料合成與改質對電化學性能影響研究

林秀芬*、吳逸祥、洪祥恩、黃筠珊、何茂庭、吳尉鳴、李柏萱
國立虎尾科技大學材料科學與工程系材料科學與綠色能源工程所
tiffany1030@nfu.edu.tw

國科會計畫: NSTC 114-2637-E-150-015

摘要

本研究利用噴霧造粒法合成具有 O3 型層狀結構之 $NaNi_{0.33}Fe_{0.33}Mn_{0.33}O_2$ 鈉離子電池正極材料，並以離子摻雜與調整燒結溫度及燒結時間等製程條件，以提升材料之電化學性能並抑制 Mn^{3+}所造成的 Jahn–Teller 結構相變。實驗中將未改質樣品與 Mg 摻雜樣品分別於 850 °C 燒結 16 小時與 20 小時，以及於 900 °C 燒結 16 小時進行熱處理，樣品依製程條件命名為 NFMSD-850-1S、NFMSD-850-3S、NFMSD-900-1S、NFMSD-2Mg-850-1S、NFMSD-2Mg-850-3S 與 NFMSD-2Mg-900-1S，比較不同製程條件對材料結構與電化學行為之影響。

XRD 結果顯示，所有樣品皆為 R-3m 空間群之 O3 型層狀結構，表示 Mg 元素摻雜或燒結條件改變，都不會破壞原有晶體結構，樣品均具有良好的結晶性。以 SEM 觀察，各樣品的一次粒子形貌皆為不規則板狀顆粒，代表改變製程條件不會影響材料表面形貌。電化學循環測試，在未改質樣品中，以 NFMSD-850-3S 最佳，其容量保持率可達66%；而在 Mg 摻雜樣品中，NFMSD-2Mg-850-3S，其容量保持率為 65%。

dQ/dV 分析 NFMSD-850-3S 與 NFMSD-2Mg-850-3S 具有最小的氧化還原峰電位差（0.04 V），代表材料具有較低的極化與穩定的電化學反應。CV 結果指出，NFMSD-850-3S 與 NFMSD-2Mg-850-3S 中 Mn^{4+}/Mn^{3+}的比例較低，其中 NFMSD-2Mg-850-3S 的 Mn^{4+}/Mn^{3+}還原峰幾乎消失，代表 Mg 摻雜可有效抑制 Mn^{3+}所引發的 Jahn–Teller 結構畸變，提升材料之循環穩定性。此外，EIS 測試結果顯示 NFMSD-850-3S 與 NFMSD-2Mg-850-3S 具有最小的電荷轉移阻抗，較佳的離子傳輸能力。

參考文獻

[1] D. Zhou, W. Hang, X. Lv, F. Zhao, A novel P2/O3 biphase $Na_{0.67}Fe_{0.425}Mn_{0.425}Mg_{0.15}O_2$ as cathode for high-performance sodium-ion batteries, J. Power Sources, 2019, 421, 147-155.
[2] J. Yu, Y. Liu, S. Han, Q. Tan, L. Liu, J. Li, Unveiling Sodium Ion Pollution in Spray-Dried Precursors and Its Implications for the Green Upcycling of Spent Lithium-Ion Batteries, Environ. Sci. Technol., 2021, 55, 14897-14905.
[3] J. Tian, L. A. Zhu, H. Miao, X. Li, Y. Liu, Effect of the position of Mg replacing Ni on O3-$NaNi_{1/3}Fe_{1/3}Mn_{1/3}O_2$ on the structural stability of cathode materials, Solid State Ionics.¸ 2024, 417, 116718.

報告型式：

□英文口頭報告競賽 (□無機材料， □有機材料)
□海報展示並參加壁報論文競賽(□無機材料， □有機材料)
☑只參加海報展示 (☑無機材料， □有機材料)

O3 型鈉離子電池正極材料製程優化與電化學性能研究

林秀芬*、余立捷、洪祥恩、黃筠珊、柯昱汎、王靖雅、游舜承、吳亞澄
國立虎尾科技大學材料科學與工程系材料科學與綠色能源工程所
tiffany1030@nfu.edu.tw

國科會計畫:NSTCNSTC 114-2637-E-150-015

摘要

隨著鋰離子電池原料成本逐漸提高以及鋰資源供應受到限制，鈉離子電池因其鈉資源豐富、成本低廉及安全性高等優勢，逐漸成為儲能系統的重要技術。然而，鈉離子半徑較鋰離子大，使其在材料中的嵌入與擴散較為緩慢，易使結構不穩定與循環壽命下降。因此，本研究將優化合成條件以提升材料性能。

本研究以噴霧造粒法合成層狀結構之 $NaNi_{1/3}Mn_{1/3}Fe_{1/3}O_2$ 正極材料，並系統性研究球磨次數與燒結溫度對 O3 型層狀鈉離子電池正極材料之晶體結構、微觀形貌與電化學性能的影響。結果顯示，不論經過球磨處理或不同燒結溫度條件，所合成之材料皆維持屬於 R-3m 空間群的 O3 型層狀結構，且具有良好的結晶性與穩定的晶體結構。SEM 觀察材料形貌，發現球磨與燒結溫度會顯著影響材料之一次粒徑大小與晶粒間的緻密程度。

在球磨處理方面，適當球磨可有效降低二次粒子尺寸，使材料顆粒更加細化並增加反應界面，有助於縮短鈉離子擴散距離，因此在倍率性能測試具有較好的放電容量。然而，過度球磨會在顆粒內部累積機械應力，使二次粒子結構變得鬆散且不穩定，使材料在充放電循環過程中產生結構劣化，降低循環穩定性與容量保持率。

在燒結溫度方面，結果發現當溫度提高 900 ℃ 有助於一次粒子的成長與晶粒間的緻密化，使顆粒間形成更強的結合力。較高的燒結溫度可改善材料結晶品質並降低結構缺陷，在充放電過程中能有效減少顆粒破裂與分散現象，提升材料的初始放電容量與循環壽命。電化學測試結果亦顯示，在較高燒結溫度條件下合成之材料具有較好的倍率性能與循環穩定性。

參考文獻

[1] X. Li, X. Shen, J. Zhao, Y. Yang, Q. Zhang, F. Ding, M. Han, C. Xu, C. Yang, H. Liu, Y. S. Hu, 2021, ”O3-$NaFe_{(1/3-x)}Ni_{1/3}Mn_{1/3}Al_xO_2$ Cathodes with Improved Air Stability for Na-Ion Batteries” ,ACS Appl. Mater. Interfaces, 13,28.
[2] J. Liu, W. Qin, Z. Yang, Q. Liu, Y. Liu, 2023, “Enhanced structural and cycling stability of O3-type $NaNi_{1/3}Mn_{1/3}Fe_{1/3}O_2$ cathode by Al replacement of Mn studied in half cell/full sodium-ion batteries” ,J. Alloys Compd, 933, 167714.
[3] K. N. Jung, J. Y. Choi, H. S. Shin, H. T. Huu, W. B. Im, J. W. Lee, 2020, “Mg-doped $Na[Ni_{1/3}Fe_{1/3}Mn_{1/3}]O_2$ with enhanced cycle stability as a cathode material for sodium-ion batteries” ,Solid State Sci, 106, 106334.

報告型式：

□英文口頭報告競賽 (□無機材料， □有機材料)
□海報展示並參加壁報論文競賽(□無機材料， □有機材料)
☑只參加海報展示 (☑無機材料， □有機材料)

Phase-Dependent Phototoxicity of MoS_2 Nanosheets in Zebrafish Embryos: Interplay Between Crystal Structure and Oxidative Stress Regulation

Yu-Ren Chiou [1*], Yu-Tai Chiou[2], Tsung-Rong Kuo[3]
[1]College of Biomedical Engineering, Taipei Medical University, Taiwan*

[2]College of Biomedical Engineering, Taipei Medical University, Taiwan

[3]Graduate Institute of Nanomedicine and Medical Engineering, Taipei Medical University, Taiwan

trkuo@tmu.edu.tw[3]

Abstract

Introduction

Two-dimensional transition metal dichalcogenides (TMDs) have attracted considerable interest in biomedical and environmental fields due to their tunable physical properties and biocompatibility. Among these, molybdenum disulfide (MoS_2) exhibits polymorphic phases—namely, the metallic 1T and semiconducting 2H phases—which significantly affect their physicochemical behavior and biological interactions. In particular, the photothermal conversion properties of these materials under near-infrared (NIR) irradiation raise both therapeutic potential and safety concerns, yet their phase-dependent biological effects remain inadequately characterized in vivo.

Experimental Methods

In this study, 1T- and 2H-phase MoS_2 nanosheets (NSs) were synthesized using a solvothermal method followed by controlled thermal conversion. Structural and optical characteristics were verified using SEM, TEM, XRD, Raman spectroscopy, XPS, and UV–vis spectroscopy. The photothermal capacity of each phase was evaluated through absorption profiling and literature-referenced NIR activity. Zebrafish embryos were exposed to MoS_2 NSs at concentrations ranging from 0.01 to 0.08 mg/mL under both dark and simulated solar light conditions. Mortality rates were recorded to assess phase- and light-dependent toxicity profiles.

Results and Discussion

Material characterization confirmed successful synthesis of phase-pure MoS_2 nanostructures with distinct morphologies and optical signatures. The 1T phase exhibited a broad, featureless absorbance in the NIR region, correlating with its known photothermal behavior. In contrast, 2H-MoS_2 displayed discrete excitonic peaks indicative of its semiconducting nature. Zebrafish toxicity assays revealed a concentration-dependent decline in survival rates, more pronounced under light exposure. Embryos exposed to 1T-MoS_2 exhibited greater phototoxicity due to NIR-induced heating effects, whereas 2H-MoS_2 demonstrated higher baseline toxicity in the absence of light, suggesting oxidative stress-mediated effects. The lethal concentration 50 (LC_{50}) values further supported the distinct toxicity mechanisms: 1T-MoS_2 showed enhanced cytotoxicity under illumination, while 2H-MoS_2 posed risks even under dark conditions.

Conclusion

This study highlights the critical role of crystalline phase and environmental light exposure in modulating the biological impact of MoS_2 nanomaterials. The 1T phase, due to its photothermal responsiveness, poses significant risk under irradiated conditions, while the semiconducting 2H phase exhibits inherent cytotoxicity independent of photoactivation. These findings provide essential insights for the design of phase-selective 2D materials and underscore the need to assess nanomaterial safety under realistic environmental parameters.

References

1. Voiry, D., et al. Phase Engineering of Transition Metal Dichalcogenides. Chem. Soc. Rev. 2015, 44, 2702–2712.
2. Mutalik, C., et al. Phase-Dependent 1T/2H-MoS_2 Nanosheets for Effective Photothermal Killing of Bacteria. ACS Sustain. Chem. Eng. 2022, 10, 8949–8957.
3. Wang, Z., et al. Biological and Environmental Interactions of Emerging Two-Dimensional Nanomaterials. Chem. Soc. Rev. 2016, 45, 1750–1780.
4. Feng, W., et al. PEGylated MoS_2 Nanoflakes for Near-Infrared Photothermal Cancer Therapy. Sci. Rep. 2015, 5, 17422.
5. Zhou, Z., et al. Metallic 1T Phase Enabling MoS_2 Nanodots as an Efficient Agent for Photothermal Therapy. Small 2020, 16, 2004173.

Presentation type：

☐ English oral competition (☐ inorganic materials, ☐ organic materials)
☐ Poster competition (☐ inorganic materials, ☐ organic materials)
❐ Exhibition only (☑ inorganic materials, ☐ organic materials)

藉由非化學計量比鋅氟非晶界面強化二氧化碳電催化還原生成一氧化碳之性能

黃筱嵐
陽明交通大學生物醫學工程學系
huangalice043@gmail.com

摘要

研究背景

隨著全球氣候變遷問題日益嚴峻，減少溫室氣體排放並發展可持續的碳循環利用技術，已成為國際間的重要共識。二氧化碳不僅是全球暖化的主要驅動因素，也是工業製程中最常見的排放副產品之一。如何將 CO_2 從「環境負擔」轉化為「可再生資源」，不僅有助於減緩氣候變遷，亦能為能源與化工產業開啟全新的經濟模式。

在眾多碳轉化途徑中，二氧化碳電催化還原反應（CO_2RR）因能在常溫常壓條件下進行，並可直接利用太陽能、風能等可再生能源驅動，將 CO_2 高效轉化為具高附加價值的化學品或燃料，因而受到廣泛關注。這項技術的核心價值在於建立一條兼顧環境效益與經濟可行性的低碳製程路徑，並具備廣泛的產業應用潛力。例如，在高度依賴石化資源的醫用塑膠產業中，若能利用 CO_2 作為碳源合成聚合物前驅物，不僅能降低對化石燃料的依賴，還能顯著減少產品的碳足跡，提升產業永續競爭力。這一方向與聯合國永續發展目標（SDGs）高度契合， 特別呼應 SDG 7「可負擔且潔淨能源」、SDG 9「工業、創新及基礎設施」、SDG 12「負責任的消費與生產」，並直接推動 SDG 13「氣候行動」的落實。

若能透過催化技術，將捕獲的 CO_2 高效轉化為一氧化碳、乙烯等基礎化學品，並將成本降至接近傳統石化製程，將有機會徹底改變碳資源的供應模式，形成新型綠色產業鏈。本研究團隊專注於開發能以水與太陽能為驅動條件，實現 CO_2 高選擇性還原的電催化技術，並可針對不同碳排放源進行靈活應用。然而，雖然鋅基催化劑因資源豐富、成本低廉且在 CO_2RR 中表現優異而備受關注，傳統的鋅氧化物（ZnO）在反應選擇性與穩定性上仍存在明顯瓶頸。

為突破這一限制，我們提出以氟化鋅（ZnF_2）作為新一代催化劑設計策略。氟元素憑藉其高電負度與促水解特性，能有效調控催化劑界面的電子結構，優化反應路徑，進而提升 CO_2RR 的活性、選擇性與長期穩定性。與 ZnO 相比，ZnF_2 在界面反應中具備更佳的電子傳輸與結構穩定性，並填補了目前 CO_2RR 研究在「氟化鋅材料應用」上的空白。透過本研究的開發成果，不僅能為學術界提供全新的催化材料選擇，也能為醫用塑膠及其他高碳排放產業提供低碳、再生的碳源，推動綠色能源技術與碳資源化策略的深度融合，最終在減碳、產業創新與永續發展三個面向產生長遠且深刻的影響。

研究目的

本研究旨在開發並驗證氟化鋅奈米凝膠（nanoZnF_2）於二氧化碳電催化還原反應（CO_2RR）中的應用潛力，並建立其性能優勢與反應機理。首先，將專注於材料的設計與合成，確保 nanoZnF_2 具備高分散性與穩定結構，同時透過物理化學表徵深入解析其表面特性與活性中心分佈，以確認其在催化反應中的結構優勢。接著，進行反應效能的系統性驗證，包含與傳統鋅氧化物（ZnO）的性能比較，並結合電化學測試與光譜分析， 探討氟引入對電子結構調控與中間體吸附行為的影響，進一步釐清催化劑結構與 CO_2RR 選擇性之間的內在關聯，並解析反應路徑的調控機制。最後，針對實際應用的可行性，本研究將評估 nanoZnF_2 在高電流密度與長時間操作條件下的穩定性，並測試其在流通池反應器中提升 CO 選擇率的能力，以模擬工業化條件並探討工程放大潛力。

透過這一連串研究，本計畫不僅致力於催化劑材料創新的突破，更著重於從基礎機理到應用實證的完整鏈結， 期望推動二氧化碳資源化技術走向產業化，協助醫療與工業製程邁向低碳轉型，並實質響應聯合國永續發展目標中 SDG7「可負擔且潔淨能源」、SDG 9「工業、創新及基礎設施」、SDG 12「負責任的消費與生產」以及SDG 13「氣候行動」，為全球淨零碳排放願景提供可行的技術解決方案。

討論與貢獻

1. 減碳價值

本電化學系統之陰極將發生 CO2RR 與電解水產氫(hydrogen evolution reaction, HER),其中,

CO2RR 淨反應如下所示:

$$CO2 + 2e^- + 2H^+ \longrightarrow CO + H2O \qquad (1)$$

依照(1)式,可以推論出此系統中,每平方公分之陰極於每小時消耗的 CO2 應滿足下列等式:

$$M_{CO_2} = \frac{\int_0^{3600} I_{CO}(t)dt \times \text{一庫倫之電子量}}{\text{一次反應電子轉移數量} \times 6.02 \times 10^{23}} \times CO_2\text{分子量} \qquad (2)$$

其中, M_{CO_2} 為每平方公分之陰極於每小時消耗的 CO_2; I_{CO} (t)為 CO2RR 反應中,CO 之分電流;一庫倫之電子量約為 6.24 $\times 10^{18}$;一次反應電子轉移數量為 2; CO_2分子量為 44。另外,CO2RR 持續進行時,電力將產生碳排放,則該排放量應為:

$$\overline{M_{CO_2}} = \frac{\int_0^{3600} I_{CO}(t) \times V(t)dt}{\text{一度電之能量}} \times \text{電力排碳係數} \qquad (3)$$

其中,M_{CO_2}為每平方公分電極於每小時的碳排放量;I(t)為系統電流;V(t)為系統電壓;一度電之能量為 3.6 $\times 10^6$焦耳;太陽能板之電力排碳係數為 35gCO2/度電。因此,若依據 ISO 14607:2018 之標準,本電化學系統作為合成氣產品的製造階段,其碳排放量應為:

產品製造階段之碳排放(每小時、每平方公分) = $\overline{M_{CO_2}} - M_{CO_2}$ (4)

近年來，二氧化碳電催化還原反應（CO_2RR）因能在常溫常壓下將 CO_2 轉化為高附加價值化學品與燃料，並結合再生能源達成低碳製程，而受到廣泛關注。本研究聚焦於開發高效、低成本且具負碳效益的催化系統，並評估其在工業化應用上的可行性與減碳潛力。

以性能最佳的陰極材料為例，將其數據帶入（2）（3）式後，並經由（4）式計算，得碳排放約 **-64.2 mg·CO_2**，相較於傳統合成氣製造階段減少 **175.9 mg·CO_2**。若系統進一步推向工業化，陰極面積與應用時數將呈倍數成長，整體負碳效益可望呈指數提升，展現極高的**減碳價值**。

在技術創新方面，本研究**首次將氟化鋅（ZnF_2）應用於 CO_2RR**，填補了該領域的研究空白，並驗證其作為低成本且高效能催化劑的可行性，有助於推進兼具經濟性與環境友善的碳轉化技術，呼應 **SDG 9「產業、創新及基礎設施」**。

在性能表現方面，所開發的**氟化鋅奈米凝膠（nanoZnF_2）**於 -1.05 V vs. RHE 下可實現 **82%** 的一氧化碳法拉第效率，在流通池條件下 CO 選擇率高達 **95%**，並能在 100 mA/cm² 的高電流密度下穩定運作超過 8 小時。此結果顯示其兼具高效率與耐久性，具備工業化應用的潛力，並呼應 **SDG 7「可負擔且潔淨能源」**。

在催化機制方面，本研究揭示**氟原子導入可有效調控催化劑的界面電子結構、優化反應中間體吸附，並抑制析氫反應（HER）**，進而提出全新的催化劑設計策略，推動綠色製程與材料創新，再度呼應 **SDG 9** 的技術創新要求。

在產業應用層面，本研究可為醫用塑膠製程提供低碳且可再生的碳源，減少對石化原料的依賴，促進碳資源循環，呼應 **SDG 12「負責任的消費與生產」**。該技術具備改變傳統化工製程的潛力，能同時兼顧能源效率、資源再生與負碳效益，對永續發展與綠色經濟具有深遠影響。

綜合而言，結合再生能源與 CO_2RR 技術，不僅能提升部分工業製程的能源轉換效率與環境效益，更可有效減少碳排放，支撐 **2050 年淨零排放**的全球願景，並對 SDG 13「氣候行動」做出積極貢獻。憑藉廣泛的應用前景，本研究成果可望吸引產業界投入合作，推動低碳轉型、降低化石燃料依賴，並以太陽能驅動廢物再利用，提升廢棄資源的回收與利用效率，進一步落實負碳技術與綠色經濟模式。

參考文獻

[1] Thimont, Yohann, et al.*Solar Energy Materials and Solar Cells* 107 (2012): 136–141.
[2] Guo, Ying, et al.Journal of Materials Chemistry 22.29 (2012): 14587–14593.
[3] O'Toole, Nicholas J., and Victor A. Streltsov.Structural Science 57.2 (2001): 128–135.
[4] Nguyen, Dang Le Tri, et al.Catalysis Communications 114 (2018): 109–113.
[5] Rosen, Jonathan, et al.Acs Catalysis 5.7 (2015): 4293–4299.
[6] Lin, Song, et al.Science 349.6253 (2015): 1208–1213.
[7] Hu, Xin-Ming, et al.ACS Catalysis 8.7 (2018): 6255–6264.
[8] Zhang, Yin-Jia, et al.Acs Catalysis 4.10 (2014): 3742–3748.
[9] Luo, Wen, et al.Applied Catalysis B: Environmental 273 (2020): 119060.
[10] Ma, Jiangping, et al. Nano Energy 121 (2024): 109258.
[11] Jeon, Hyo Sang, et al. Journal of the American Chemical Society 140.30 (2018): 9383–9386.
[12] Hu, Chenghong, et al. Advanced Science 11.4 (2024): 2306095.
[13] Ma, Wenchao, et al. Nature Catalysis 3.6 (2020): 478–487.
[14] Chen, Yiqun, et al.Nano Research 15.9 (2022): 7896–7902.
[15] Andrade, Joseph D.Surface and Interfacial Aspects of Biomedical Polymers: Volume 1 (1985): 105–195.
[16] Biesinger, Mark C.Surface and Interface Analysis 49.13 (2017): 1325–1334.
[17] Hsieh, P-T., et al.Applied Physics A 90 (2008): 317–321.
[18] Zheng, Weiran.ACS Energy Letters 8.4 (2023): 1952–1958.
[19] Heenan, Alexander R., et al.ACS Energy Letters 7.7 (2022): 2357–2361.
[20] 劉致中 經濟部產業技術司新聞 (2024). 連結
[21] 國家發展委員會 "臺灣 2050 淨零排放路徑及策略總說明." (2022): 1–83.
[22] Grand View Research, Inc. (2024): GVR-1-68038-823-7. URL

報告型式：

□英文口頭報告競賽 (□無機材料， □有機材料)
□海報展示並參加壁報論文競賽(□無機材料， □有機材料)
☑只參加海報展示 (☑無機材料， □有機材料)

Photothermal Behavior of Phase-Tuned MoS_2 Nanosheets and Their Redox-Dependent Toxicity in Zebrafish Embryos

Yu-Tai, Chiou[1*], Yu-Ren, Chiou[2], Tsung-Rong Kuo[3]
[1]College of Biomedical Engineering, Taipei Medical University, Taiwan[*]
[2]College of Biomedical Engineering, Taipei Medical University, Taiwan
[3]Graduate Institute of Nanomedicine and Medical Engineering, Taipei Medical University, Taiwan
trkuo@tmu.edu.tw

Abstract

Introduction.

The biological behavior of two-dimensional (2D) nanomaterials is intricately tied to their crystal structure. Among them, molybdenum disulfide (MoS_2) exhibits distinct properties in its 1T (metallic) and 2H (semiconducting) phases, making it a promising candidate for biomedical applications and environmental interaction studies. The photothermal conversion efficiency of MoS_2, particularly in the near-infrared (NIR) region, further enhances its potential for light-activated therapeutic applications. However, phase-dependent toxicity mechanisms in living organisms, especially under varying light conditions, remain underexplored.

Experimental Methods.

In this study, 1T- and 2H-phase MoS_2 nanosheets (NSs) were synthesized via solvothermal and combustion methods, respectively. Structural and optical properties were characterized using SEM, TEM, XRD, Raman spectroscopy, XPS, and UV–vis spectroscopy. Photothermal performance was assessed under simulated solar irradiation using temperature mapping and NIR absorption analysis. Zebrafish embryos were exposed to increasing concentrations of both phases (0.01–0.08 mg/mL) under light and dark conditions to evaluate photothermal-induced toxicity and mortality.

Results and Discussion.

The 1T-MoS_2 NSs exhibited broader NIR absorbance and superior photothermal conversion compared to the 2H counterpart, consistent with their metallic electronic structure. Under light exposure, the 1T phase induced significant lethality in zebrafish embryos, attributed to its strong NIR-triggered thermal effects. In contrast, 2H-MoS_2 displayed a higher baseline toxicity in the dark, likely due to oxidative interactions independent of photothermal activation. Survival rates declined in a concentration- and light-dependent manner, with marked differences between the two polymorphs, revealing distinct phase-governed toxicity mechanisms.

Conclusion.

These findings demonstrate that the photothermal behavior and biological toxicity of MoS_2 are intricately governed by crystal phase and environmental light exposure. The 1T phase exhibits light-induced photothermal cytotoxicity, while the 2H phase displays phase-inherent toxicity even without illumination. This study underscores the importance of phase-engineering and light-responsive behavior in the safe design of 2D materials for biomedical and environmental applications.

References

1. Voiry, D., et al. Phase Engineering of Transition Metal Dichalcogenides. Chem. Soc. Rev. 2015, 44, 2702–2712.

2. Mutalik, C., et al. Phase-Dependent 1T/2H-MoS_2 Nanosheets for Effective Photothermal Killing of Bacteria. ACS Sustain. Chem. Eng. 2022, 10, 8949–8957.

3. Wang, Z., et al. Biological and Environmental Interactions of Emerging Two-Dimensional Nanomaterials. Chem. Soc. Rev. 2016, 45, 1750–1780.

4. Zhou, Z., et al. Metallic 1T Phase Enabling MoS_2 Nanodots as an Efficient Agent for Photothermal Therapy. Small 2020, 16, 2004173.

5. Feng, W., et al. PEGylated MoS_2 Nanoflakes for Near-Infrared Photothermal Cancer Therapy. Sci. Rep. 2015, 5, 17422.

Presentation type：

☐ English oral competition (☐ inorganic materials, ☐ organic materials)
☐ Poster competition (☐ inorganic materials, ☐ organic materials)
❐ Exhibition only (☑ inorganic materials, ☐ organic materials)

應用薄層氟基人工介面於鋅金屬負極以實現高穩定性與長循環壽命

彭郁晴 [1]、劉大中 [1]
國立陽明交通大學生物醫學工程學系
tcliu@nycu.edu.tw

摘要

本研究為解決水系鋅離子電池（AZIBs）中鋅陽極的枝晶生長與析氫副反應等挑戰，受全氟聚醚（PFPE）反應啟發，開發出一種原位（In-situ）生成氟化鋅（ZnF_2）陽極保護層策略。透過控制電化學反應時間（30、60、200 秒），在鋅箔表面成功構建出具微米級球狀特徵的穩定界面層。XRD、SEM 與 EDS 分析證實，隨反應時間增加，ZnF_2 的特徵繞射峰愈顯著且氟元素含量也隨之提升。電化學測試表明，該保護層能有效降低界面腐蝕電流密度（i_{corr}），並將電荷轉移電阻（R_{ct}）由 507.6 Ω 大幅降至 112.8 Ω；結合離子遷移數與成核過電位的同步改善，證實 ZnF_2 構建了快速離子傳輸通道並誘導鋅離子均勻沉積。在對稱電池測試中，改質後的鋅陽極在 5 mA cm^{-2}、1 mAh cm^{-2} 條件下展現出卓越的穩定性，循環壽命突破 4800 小時，且在 20 mA cm^{-2} 極端電流密度下仍可穩定循環。為了模擬實際應用之高利用率狀況，本研究在 60% 高放電深度（DoD）下實現了 1344 小時 的長循環壽命。綜上所述，本研究提出的原位 ZnF_2 保護策略顯著提升了鋅電池的耐久性與界面強度。

簡介

隨著人口高齡化，醫療監測需求增加，帶動穿戴式裝置及電池產業發展。鋰離子電池因高能量密度成為主流，但其高成本與易燃性限制了大規模應用[1]。鋅因地殼豐富、-0.763 V 氧化還原電位及 819 mAh g^{-1} 理論容量而受矚目，惟鋅離子電池在實際應用中面臨鋅負極腐蝕、析氫及枝晶等問題，限制了其循環壽命[2]。

為了解決上述所提到鋅離子電池之問題，目前已發展出各種解決方法，如鋅陽極保護層[3]、調整電解質[4]等，而形成人工固態電解質介面膜層不僅可以調節表面微環境，還具備物理保護的功能。在 Jin Han 等人研究中[5]，提到透過熱分解方式在鋅陽極上異位形成氟化鋅，氟化鋅能允許鋅離子通過間隙，提供離子與鋅陽極擴散通道。在氟化鋅層作用下增強鋅離子電池的庫倫效率，同時抑制鋅枝晶生成，從而增強陽極的電化學性能。帶氟化鋅的鋅陽極在 0.5 mAh cm^{-2} 的面容量下具 700 小時之循環壽命，而 Zn-ZnF_2/MnO_2 全電池在 3000 次循環後實現 89 % 的容量保持。

本研究受 Shiwei Tao 等人利用全氟聚醚(PFPE)鋅箔反應，原位生成氟化鋅(ZnF_2)技術之啟發 [6]，進一步將此修飾策略應用於鋅離子電池負極保護層，製備 ZnF_2 如圖一所示。

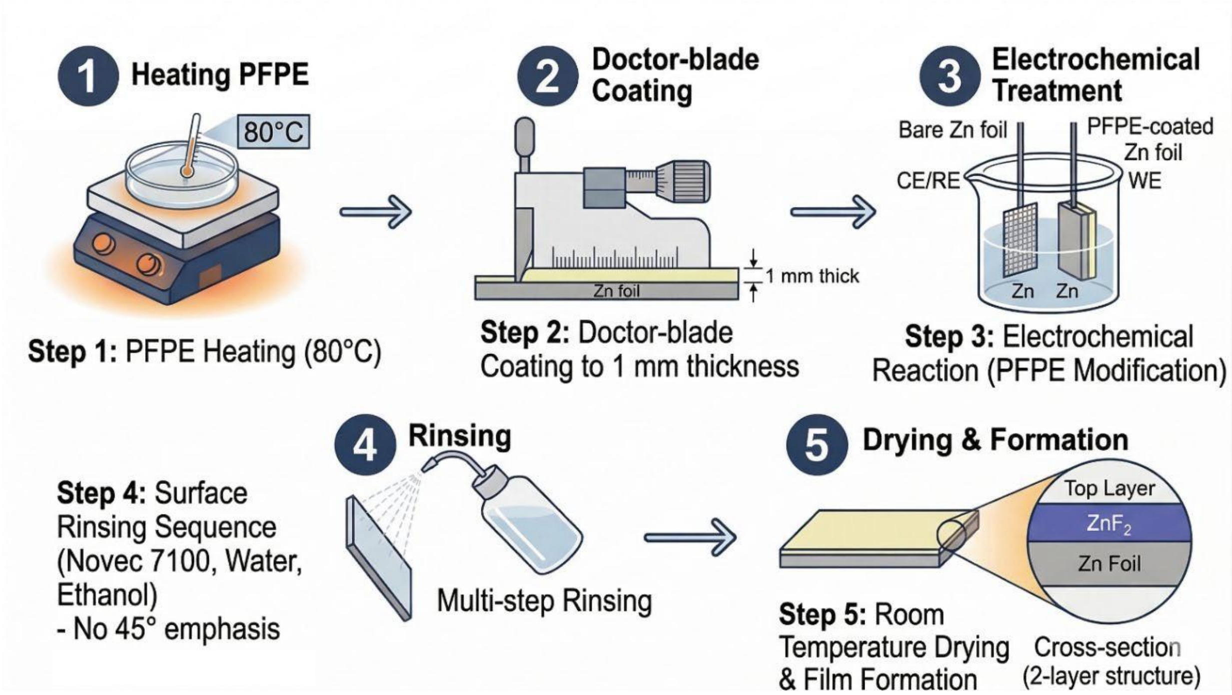

圖一、製備氟化鋅實驗示意圖

結果與討論

首先以 XRD 進行特徵繞射分析，原位生成 ZnF_2 是於相同測試電流密度 -0.1 mA cm^{-2} 下，分別比較作用時間 30、60、200 秒差異，並觀察 ZnF_2 繞射特徵圖譜變化，綜合結果顯示，在 -0.1 mA cm^{-2}，200 秒條件下得到最清晰的兩個氟化鋅特徵峰。接下來採用掃描式電子顯微鏡(SEM)觀察形貌，經氟化處理後則生成微米級球狀聚集體，符合氟化物常見的顆粒化特徵。配合能量色散 X 射線光譜(EDS)分析，改質樣品表面可明顯檢出氟離子與鋅離子之訊號，證實氟元素已成功導入並與鋅共存於表層，且秒數越長氟離子比例越高。

為評估電極之電化學性能，本研究首先透過塔菲爾(Tafel)極化曲線進行分析。結果顯示，具 ZnF_2 保護層的三組樣品其腐蝕電流密度(i_{corr})皆低原始鋅箔，證實原位生成的保護層能有效抑制電解液對鋅陽極的腐蝕，進而提升電池之循環壽命。電化學阻抗譜(EIS)測試結果顯示，修飾後的電極在 Nyquist 圖中高頻區的半徑顯著減小。經等效電路擬合，電荷轉移電阻(R_{ct})從原始鋅箔的 507.6 Ω 降低至最低 112.8 Ω，結合離子遷移數(Transference number) 分析發現，含有 ZnF_2 保護層的樣品遷移數其離子遷移數均優原始鋅箔，尤其以改質時間 30 秒的離子遷移數表現最為優異，此趨勢與 Nyquist 圖擬合後之 R_{ct} 趨勢高度吻合，說明該保護層提升離子傳輸速度。此外，ZnF_2 對於鋅沉積過程的引導作用也反映在成核過電位的降低上，成核過電位的數值由純鋅的 85 mV 顯著下降至 30 mV， 反映出 ZnF_2 能促進鋅沉積過程，降低鋅枝晶的生成。上述結果共同證實，原位形成的 ZnF_2 保護層不僅大幅降低了電荷轉移動力學能壘，更有效加速了界面處的離子傳輸，在電池循環後能有更均勻的鋅沉積。

為進一步評估電極之倍率性能與長期循環穩定性，本研究將鋅箔與經原位 ZnF_2 改質之鋅箔組裝成 CR2032 鈕扣鋅對稱電池，倍率性能以 0.5、1、2、5 及 10 mA cm^{-2} ，電容量都是 1 mAh cm^{-2} 來進行壓力測試，再回到 0.5 mA cm^{-2} 觀察電池之可逆性。結果顯示，純鋅箔在電流密度增加到 1 mA cm^{-2} 時，電位曲線就出現劇烈波動。相比之下，具 ZnF_2 保護層的電池在各電流密度下均有穩定表現，即使從高電流密度切換回低電流密度，也能恢復平穩得初始狀態，證實該保護層具有優異的倍率耐受性及可逆性。長期循環穩定性測試中，原始鋅箔對稱電池在 5 mA cm^{-2}、1 mAh cm^{-2} 的條件下僅維持了 1000 小時；相較之下，具備 ZnF_2 保護層的電池展現出卓越的耐久度，目前已穩定存活 4800 小時，其中，改質時間 200 秒的樣品具最小的過電位波動(Overpotential fluctuation)，接下來僅會以 200 秒樣品去測試不同電流密度。即使在更嚴苛的條件下，該保護層仍表現出極高的界面強度，在 10 mA cm^{-2} 下可存活 1800 小時，甚至在 20 mA cm^{-2} 運行 1600 小時仍能保持平穩的電位平台。多數文獻常採用厚度 100 µm 鋅箔進行測試，導致循環過程中的能量輸出極低，難以反映實際應用情況。考慮到低放電深度(Depth of Discharge, DoD)測試可能掩蓋電極介面失效並高估循環壽命，本研究金一步測試在相同電流密度(5 mA cm^{-2})，不同 DoD 對電池性能的影響。實驗結果顯示，在 20 % DoD 已運行 1440 小時，而在極具挑戰的 40% DoD 與 60% DoD 條件下，分別達到了 736 小時與 1344 小時循環壽命。上述數據驗證原位生成 ZnF_2 保護層能顯著抑制鋅枝晶生長與副反應，大幅提升鋅電池的循環壽命。

結論

本研究成功開發出一種高效、無毒且製成簡易的原位 ZnF_2 陽極保護層，有效克服鋅陽極枝晶生長及副反應問題。透過實驗證實，該保護層不僅顯著降低了電荷轉移阻抗並建構出快速離子傳輸通道，更能有效降低成核過電位，誘導鋅離子在電極表面均勻沉積。在對稱電池循環測試中，改質後鋅陽極在 5 mA cm^{-2}、1 mAh cm^{-2} 循環壽命突破 4800 小時；即使在極端電流密度條件也能穩定循環超過 700 小時。在高 DoD 方面，亦展現出卓越的循環穩定性，在極具挑戰的 60% DoD 下仍可持續 1344 小時，已經超越目前多數陽極保護層相關論文。綜合上述， 本研究所提出的原位 ZnF_2 陽極保護層不僅大幅提升鋅電池的耐久性，更為高能量、長壽命的水性鋅電池提供具商業化的潛力。

參考文獻

［1］ Alkhedher, M., Al Tahhan, A. B., Yousaf, J., Ghazal, M., Shahbazian-Yassar, R., & Ramadan, M. (2024). Electrochemical and thermal modeling of lithium-ion batteries: A review of coupled approaches for improved thermal performance and safety. *Journal of Energy Storage,* 86 (Part A),111172.doi:10.1016/j.est.2024.111172.

［2］ Yang, Y., Liu, C., Lv, Z., Yang, H., Zhang, Y., Ye, M., Chen, L., Zhao, J., & Li, C. C. (2021). Synergistic manipulation of Zn^{2+} ion flux and desolvation effect enabled by anodic growth of a 3D ZnF_2 matrix for long-lifespan and dendrite-free Zn metal anodes. *Advanced Materials, 33*(11), 2007388. doi:10.1002/adma.202007388.

［3］ Liao, D., Kou, Y., Du, T., Li, K., Li, Z., & Wang, Y. (2025). Natural volcanic mud with de-solvation function as a protective layer for dendrite-free Zn anode. *Chemical Engineering Journal, 519,* 165144. doi:10.1016/j.cej.2025.165144.

［4］ Cao, P., Zhou, X., Wei, A., Meng, Q., Ye, H., Liu, W., Tang, J., & Yang, J. (2021). Fast-charging and ultrahigh-capacity zinc metal anode for high-performance aqueous zinc-ion batteries. *Advanced Functional Materials, 31*(20), 2100398. doi:10.1002/adfm.202100398.

［5］ Han, J., Euchner, H., Kuenzel, M., Hosseini, S. M., Groß, A., Varzi, A., & Passerini, S. (2021). A thin and uniform fluoride-based artificial interphase for the zinc metal anode enabling reversible Zn/MnO_2 batteries. *ACS Energy Letters, 6*(9), 3063–3071. doi:10.1021/acsenergylett.1c01249.

［6］ Tao, S., Zhang, C., Zhang, J., Jiao, Y., Li, M., Lin, W., Ran, L., Clement, B., Lyu, M., Gentle, I., Wang, L., & Knibbe, R. (2022). A hydrophobic and fluorophilic coating layer for stable and reversible aqueous zinc metal anodes. *Chemical Engineering Journal, 446*(Part 1),136607.doi:10.1016/j.cej.2022.136607.

報告型式：

□英文口頭報告競賽 (□無機材料， □有機材料)
□海報展示並參加壁報論文競賽(□無機材料， □有機材料)
■只參加海報展示 (■無機材料， □有機材料)

不同燒結溫度對(La, Nb)共摻雜 TiO_2 陶瓷微結構與介電性質之影響

彭嘉禾、*尤孝雯
國立臺南大學材料科學系
hwyu@mail.nutn.edu.tw

摘要

本研究以固態反應法製備不同燒結溫度的(La, Nb)共摻雜 TiO_2 陶瓷，探討樣品微結構與介電性質。研究結果顯示，1500°C 燒結的樣品，具最高的電阻率與最低的介電常數，而 1450°C 燒結的樣品介電特性最佳（1kHz 時，$\varepsilon_r' = 10483$ 與 $\tan\delta = 0.168$）。優良的介電性質可歸因於材料的內部阻擋層電容 IBLC，電子釘扎缺陷偶極 EPDD 與晶界雜相造成的隔離結構。

關鍵字：TiO_2、共摻雜、EPDD、IBLC、晶界雜相

1.前言

巨電容率（colossal permittivity, CP）材料因具高介電常數，對高能量密度電容、濾波與微型化元件皆具應用價值。近年研究顯示，施體與受體共摻雜可在 TiO_2 中形成電子釘扎缺陷偶極(EPDD)以提升 ε_r'、抑制載子長距離躍遷以降低損失正切 $\tan\delta$，且在相當大的頻率與溫度範圍內皆可保持良好的介電特性[1]。目前被廣泛接受 CP 現象之成因，即材料內部形成 IBLC 結構，使半導體晶粒與高阻抗晶界共同貢獻極大的等效電容[2，3]。共摻雜 La 與 Nb 的 TiO_2 陶瓷，由於 La^{3+}的離子半徑明顯大於 Ti^{4+}，容易在晶界造成第二相析出[4-6]。析出的第二相可阻擋電子於晶粒間遷移，將其運動局域化，維持低損耗[7]。此外，由於燒結溫度會改變樣品氧空缺濃度，而氧空缺會影響 Ti^{3+}形成以及晶界電荷遷徙。所以本實驗製作變化燒結溫度的 $(La_{0.5}Nb_{0.5})_{0.01}Ti_{0.99}O_2$ 巨介電陶瓷，希望能以晶界隔離結構與缺陷偶極設計，共同提升介電常數、降低損耗與提高頻率穩定性，並觀察燒結溫度對介電性質的影響。

2.實驗方法

我們利用固態反應法製備$(La_{0.5}Nb_{0.5})_{0.01}Ti_{0.99}O_2$ 陶瓷。依化學劑量法秤重、濕式球磨後的粉末，蒸發水分再使用瑪瑙研缽研磨，接著以 1200°C 煆燒 8 小時，再以 1300°C 煆燒 8 小時。煆燒完的粉末添加 5wt%聚乙烯醇(PVA)凝膠研磨混合，經油壓機 620 MPa 壓錠成形，放入高溫爐分別以 1400°C、1450°C 與 1500°C 燒結 3 小時。取出之樣品直徑為 9 mm，厚度為 1 mm。使用 SEM 觀察樣品的表面形貌，並使用影像處理軟體 Image J 計算平均晶粒尺寸。部分樣品研磨成粉，使用 XRD 粉末繞射分析晶體結構。樣品表面先使用細砂紙拋光，再塗上銀膠當作電極。利用阻抗分析儀(HP4192)測量頻率範圍為 10 -10^6 Hz 的樣品阻抗 $Z = Z' + jZ''$數值，複數介電常數 $\varepsilon_r = \varepsilon_r' - j\varepsilon_r''$可由 Z'與 Z''計算出來，損失正切 $\tan\delta$ 則為 ε_r''與 ε_r'的比值。

3. 結果與討論

圖一的 SEM 照片顯示不同樣品的表面形貌。平均晶粒尺寸隨燒結溫度增加而增大。我們將樣品做 EDS 元素分析，結果顯示一些 La 含量豐富的雜相在晶界析出。樣品的 XRD 繞射圖僅呈現 Rutile TiO_2 四方晶系的特徵峰， 沒有顯現 EDS 檢測到的雜相，推論是因為較低的摻雜濃度造成雜相含量較少，因此 XRD 圖形無法清楚呈現。圖二(a)顯示樣品的 ε_r'對頻率關係曲線。在量測頻率範圍內，1450°C 燒結的樣品具有最高的 ε_r'數值，所有樣品的$\varepsilon\varepsilon_{rr}'$ 皆具良好的頻率穩定性。圖二(b)顯示樣品的 $\tan\delta$ 對頻率關係曲線。所有樣品的 $\tan\delta$ 皆隨頻率增加而減少，在 10^3 Hz 附近 $\tan\delta$ 降低至約 0.1，然後隨頻率增加，出現一與晶粒內部極化鬆弛有關的局部峰值。表一列出在 1 kHz 時，不同摻雜比例樣品的 ε_r'與 $\tan\delta$ 值。圖三為樣品複數阻抗圖譜，圖形皆呈現一個由晶界極化貢獻的半圓，我們以 ZView 軟體擬合數據，擬合所使用的等效電路顯示於圖形上方。右上角插圖為高頻區的放大圖，晶粒電阻 R_g 可由圖形與 Z'軸的截距得出。 我們將擬合結果同列於表一，可看出 $R_{gb} \gg R_g$，符合 IBLC 假說。塊材電阻 $R_{bulk} = R_{gb} + R_g$，1500°C 燒結的樣品具有最大的 R_{bulk}。由於離子可在排列較為鬆散的晶界中遷徙，促進電傳導，當晶粒在 1500°C 高溫燒結中成長，造成晶界減少，塊材電阻就會增加。

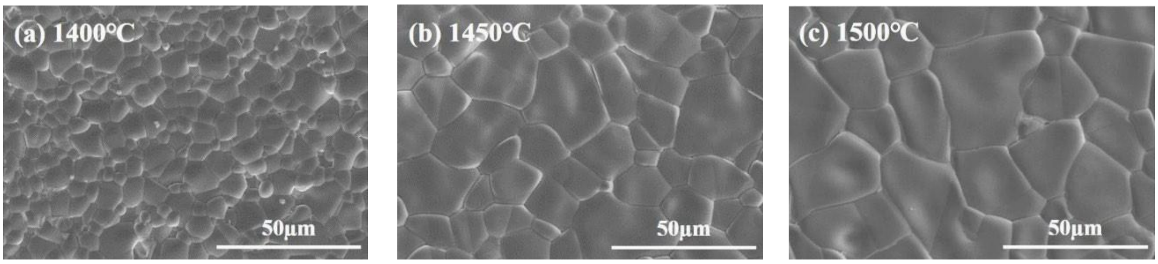

圖一 在(a) 1400°C、(b) 1450°C 和(c) 1500°C 燒結的樣品，SEM 表面形貌。

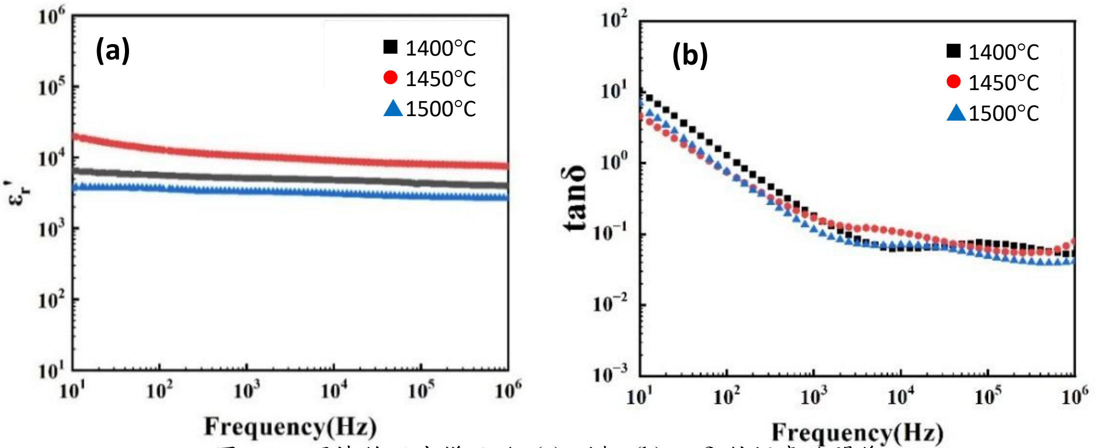

圖二 不同燒結溫度樣品的 (a) ε_r'與 (b) tanδ 對頻率的關係。

4. 結論

本研究製備不同燒結溫度的$(La_{0.5}Nb_{0.5})_{0.01}Ti_{0.99}O_2$ 陶瓷樣品，隨燒結溫度升高，樣品晶粒成長，電阻增大。樣品的複數阻抗圖的擬合結果符合 IBLC 假說。EDS 元素分析顯示在晶界有一些 La 含量豐富的雜相析出。樣品的ε_r'具良好的頻率穩定性，1450°C 燒結的樣品具有最佳的介電性質，在 1 kHz 下 ε_r'為 10483，tanδ 為 0.168。這樣的介電特性，遠優於 1kHz 時 ε_r'值僅為數百的純 TiO_2 [8]。我們將介電性質的大幅提升，歸因於 La 與 Nb 共摻雜所形成的電子釘扎缺陷偶極以及晶界雜相造成的隔離結構。

表一

燒結溫度	**ε_r'**	**tanδ**	R_{gb}(Ω·cm)	Rg(Ω·cm)	R_{bulk}(Ω·cm)
1400°C	5097	0.181	3.1E6	3.6	3.1E6
1450°C	10483	0.168	2.4E6	1.9	2.4E6
1500°C	3278	0.116	7.3E6	6.6	7.3E6

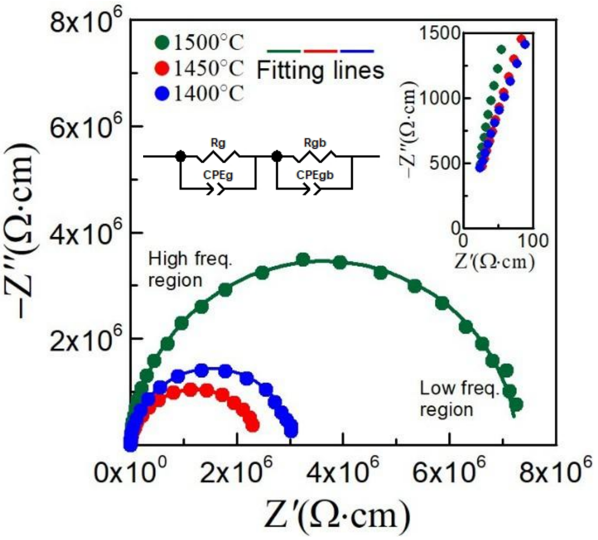

圖三 不同燒結溫度樣品的複數阻抗譜，符號代表實驗數據，實線代表擬合結果。插圖為高頻區域放大圖。

誌謝

感謝張閎斌（XRD 量測與圖譜分析）與林宸安（XRD 量測）之協助。本研究獲國家科學及技術委員會（NSTC 112-2635-M-024-001）及國立臺南大學（AB114-102）經費補助。

參考文獻

[1] W. Hu, Y. Liu, R.L. Withers, T.J. Frankcombe, L. Nor´en, A. Snashall, M. Kitchin, P. Smith, B. Gong, H. Chen, J. Schiemer, F. Brink and J. Wong-Leung, Electron-pinned defect-dipoles for high-performance colossal permittivity materials, *Nat. Mater*. 12, 821–826(2013).

[2] Derek C. Sinclair, Timothy B. Adams, Finlay D. Morrison and Anthony R. West, $CaCu_3Ti_4O_{12}$: One-step internal barrier layer capacitor, *Appl. Phys. Lett.*, 80, 2153-2155 (2002).

[3] Wang, Y., Jie, W., Yang, C., Wei, X., and Hao, J. Colossal Permittivity Materials as Superior Dielectrics for Diverse Applications, *Adv. Funct. Mater.*, *29*(27), 1808118(2019).

[4] Baochun Guo, Peng Liu, Xiulei Cui, Yuechan Song, Colossal permittivity and dielectric relaxations in $(La_{0.5}Nb_{0.5})_xTi_{1-x}O_2$ ceramics, *J. Alloys Compd.*, 768, 368-376(2018).

[5] X.W. Wang, Y.P. Zheng, B.K. Liang, G. Zhang, Y.C. Shi, B. H. Zhang, L.L. Xue1, S.Y. Shang, J. Shang, S.Q. Yin and Y.C. Hu, Preparation and properties of La and Nb co-doped TiO_2 colossal dielectric ceramic materials, *J. Mater. Sci.: Mater. Electron.*, 31, 16044-16052(2020).

[6] Muhsen, K.N.D.K., Osman, R.A.M. and Idris, M.S., Microstructural characteristics and dielectric properties of (Nb, La) co-doped TiO_2 ceramics sintered at different temperatures. *Appl. Phys. A* 128, 726(2022).

[7] Lingxia Li, Te Lu, Ning Zhang, Jiangteng Li and Zhaoyang Cai, The effect of segregation structure on the colossal permittivity properties of $(La_{0.5}Nb_{0.5})_xTi_{1-x}O_2$ ceramics, *J. Mater. Chem. C*, 6(9), 2283-2294(2018).

[8] J. Fan, G. He, Z. Cao, Y. Cao, Z. Long, H. Zhanggui, Thermal stable and ultralow dielectric loss in $(Gd_{0.5}Ta_{0.5})_xTi_{1-x}O_2$ giant permittivity ceramics by defect engineering, J. Mater. 9 (2023) 157–165.

報告型式：

□英文口頭報告競賽 (□無機材料， □有機材料)
□海報展示並參加壁報論文競賽(□無機材料， □有機材料)
☑只參加海報展示 (☑無機材料， □有機材料)

Comparison of product yield under two operating modes in SCT-RT unit using spent RFCC catalyst

Jing Lai (賴倞), Hsiang-Yao Sun (孫祥耀), Che-Yuan Chang(張哲源) and Hsien-Chang Yang * **(楊憲昌)**
Refining & Manufacturing Research Institute, CPC Corporation, Taiwan
*Correspondence: 078751@cpc.com.tw

Abstract

In a petroleum refinery, resid fluid catalytic cracking (RFCC) is one of the chief conversion processes, producing gasoline and C3, C4 streams from heavy feedstocks. Therefore, it is important to evaluate the performance of RFCC catalysts. Accurate laboratory evaluations of the catalyst, the short contact time resid test (SCT-RT) is a small-scale fluidized bed unit in which the catalytic performance of fluid cracking catalysts was used to measure. Realistic simulation of commercial operation is achieved by the unique reactor and unit design [1]. There are two operating models in SCT-RT unit, adiabatic and constant temperature model, of which the adiabatic model simulates the adiabatic behavior of a commercial riser.

In this study, in order to understand the performance of the two operating model, we use spent RFCC catalysts (equilibrium catalyst, ECAT) form CPC refinery in SCT-RT unit. The oil time-on-stream is only one second and provides performance measurements at fixed cat-to-oil weight ratio (CTO = 6 w/w) and vapor contact times. Liquid product yields, gasoline (C5~221℃), LCO (221~343℃) and bottoms (343℃+) were calculated using GC (Agilent 8890) Simulated Distillation based on ASTM D 2887. Mass balances were within 97% to 103% range. The properties of catalyst were also investigated by BET, XRF.

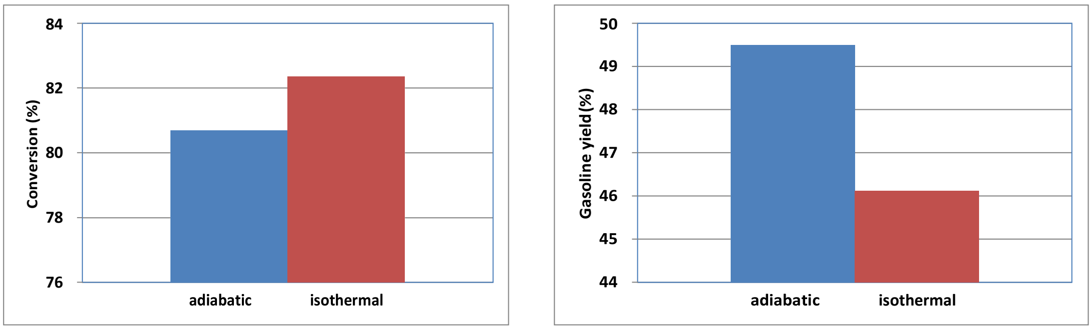

Conversion and gasoline yields with differential operating modes.

References

[1] P. Imhof, M. Baas, J.A. Gonzalez, Fluid catalytic cracking catalyst evaluation: the short contact time resid test, Catal. Rev. 46 (2) (2004) 151–161

Presentation type：

☐ English oral competition (☐ inorganic materials, ☐ organic materials)
☐ Poster competition (☐ inorganic materials, ☐ organic materials)
◆ Exhibition only (■ inorganic materials, ☐ organic materials)

2026 功能性材料研討會暨國科會專題研究計畫成果發表會 – 南臺化材 Date : 2026/5/29

碘化銅薄膜成長及光電特性參數分析

陳柏安 [1] 王麒兆 [2] 林得裕 [3] 石豫臺 [4]
[123] 電子工程學系,國立彰化師範大學,彰化市師大路二號
[4] 物理系,國立彰化師範大學,彰化市進德路一號
dylin@cc.ncue.edu.tw(林得裕)

NSTC-114-2221-E018-013

摘要(Abstract)

本研究以低成本之氣相碘化法成功製備高品質 CuI 薄膜，並且與 N 型的 Silicon 基板結合形成異質結構二極體。結構分析結果顯示，所成長之 CuI 薄膜為γ相，展現出優異的結晶品質，且其元素組成比例接近理論值 1：1，顯示該製程能穩定製備高品質之 CuI 薄膜。光學與電性量測指出，CuI 之能隙約為 3eV，並確認其為 p 型半導體，使其在光電元件應用上具備潛在價值。在元件特性方面，由 CuI 與 p 型矽基板所構成之異質接面二極體呈現明顯的整流行為，且在 AM1.5 模擬太陽光照射下，即使於零偏壓條件下亦可產生光電流，顯示其具備自供電光響應能力。進一步的光響應分析顯示，該異質結構在無外加偏壓下仍維持良好響應，其截止頻率可達 700 Hz，反映出元件具備一定的響應速度與應用潛力。整體而言，本研究證實 CuI 薄膜可透過簡易製程獲得良好結晶品質，並成功與 n 型矽基板形成穩定之異質接面二極體，實驗結果亦驗證其具備良好的接面特性與應用可行性。

一、簡介

矽基半導體技術長期為光電元件的發展核心，然而矽屬於間接能隙材料，在光電轉換效率與光響應速度上存在一定限制。近年來，透明導電氧化物與寬能隙半導體材料逐漸受到關注，其中碘化亞銅（CuI）因其具備高透明度、良好電洞傳輸能力以及低成本製程優勢，成為具潛力之 p 型半導體材料。CuI 具有約 3.0 eV 的寬能隙與優異的電洞遷移率，可應用於透明電子元件、太陽能電池及光偵測器等領域。透過與矽基板形成異質結構，不僅可提升光生載子的分離效率，也可拓展元件應用範圍。

二、實驗方法

本研究採用氣相碘化法製備 CuI 薄膜[1]，首先於 n 型矽基板上沉積銅（Cu）薄膜，接著置於含碘氣氛之密閉環境中進行反應，使 Cu 薄膜轉化為 CuI 薄膜。薄膜製備完成後，利用掃描式電子顯微鏡（SEM）觀察其表面形貌，並透過能量散射光譜（EDS）分析元素組成比例；再以 X 光繞射（XRD）分析其晶體結構。在元件製作方面，將 p-CuI 與 n-Si 組成異質結構二極體，並進行電流-電壓（I–V）量測分析其整流與光伏特性。此外，透過阻抗分析獲得尼奎斯特圖並建立等效電路模型。進一步進行持續性光電導（PC）量測與變頻光響應分析，以評估元件之動態響應能力，並透過橫向光電壓量測探討其位置感測特性。

三、結果與討論

3.1 材料結構與晶體特性分析

(1) SEM 表面形貌分析

圖 1 為 CuI 薄膜正面的 SEM 薄膜影像，可以看見薄膜有結晶在基板上，晶粒連續均勻大小一致無不連續或大顆粒產生，表示成長的薄膜品質良好。

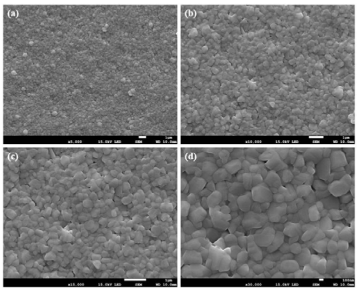

圖 1 :p-CuI / n-Silicon 薄膜 SEM 影像，
(a)5K，(b)10K，(c)15K，(d)30K

(2) EDS 樣品組成分析

圖 2 為 EDS mapping，原子比分別為 Cu 53.61 %、I 為 46.39 %，其比例非常接近理論值 1：1 的化學計量比，展示元素均勻分佈在薄膜上。

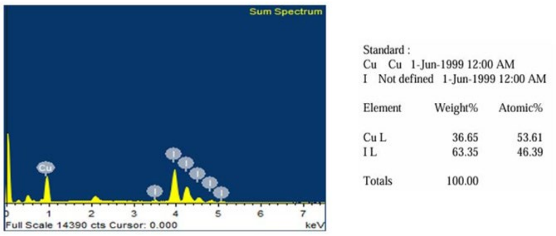

Standard :
Cu Cu 1-Jun-1999 12:00 AM
I Not defined 1-Jun-1999 12:00 AM

Element	Weight%	Atomic%
Cu L	36.65	53.61
I L	63.35	46.39
Totals	100.00	

圖 2 :p-CuI / n-Silicon 薄膜 EDS 元素比例分析

(3) Raman 散射光譜分析

圖 3 為拉曼光譜圖，可以看到生長出的 CuI 在拉曼 123cm^{-1} 處觀察到的顯著峰值，是 CuI 的典型特徵峰。它對應於晶格中 Cu-I 鍵結的 TO (Transverse Optical, 橫向光學) 振動模式。[2]

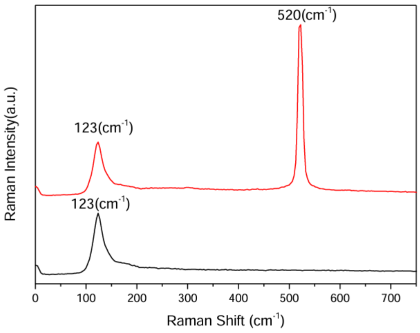

圖 3 : CuI 拉曼光譜圖

(4)XRD 晶體結構分析

圖 4 為生長於玻璃基板與矽基板上的 CuI 薄膜 XRD 數據，結果顯示 CuI 已製備為結晶性良好的薄膜，而後我們分別將數據與 CuI 的三種不同相的 JCPDS 標準數據進行比對，比對後可確認本論文生長出的 CuI 為γ相，且並無雜相或是混合相的峰存在。[3]

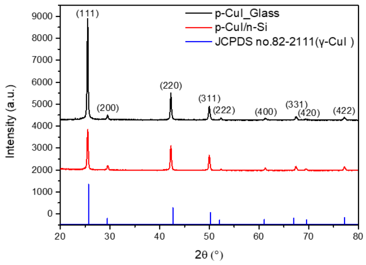

圖 4 : p-CuI / n-Silicon 薄膜 XRD 圖

(5) X 射線光電子能譜儀分析

圖 5 為 CuI 的 XPS 全為高純度的碘化亞銅(CuI)。此外，譜圖中除了作為能量校正參考的 C 1s 碳峰外，並未偵測到其他明顯的雜質信號，反映出樣品具有優異的化學純淨度。譜圖，從譜圖特徵來看，位於 620 eV 附近的 I 3d 強烈雙峰與 930 eV 附近的 Cu 2p 峰位高度吻合，結合兩者顯著的峰值強度，足以判定該材料

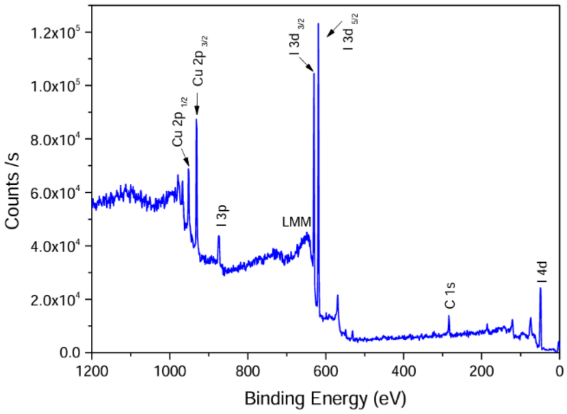

圖 5 : CuI XPS 全譜圖

3.2 材料光學電性分析

(1) 電流-電壓特性曲線分析

本元件展示了典型的二極體整流特性，在黑暗環境下（黑線）具有極低的漏電流與清晰的開啟電壓，證明 p 型 CuI 與 n 型矽基板之間形成了良好的異質接面與內建電場。在光照條件下（紅線），元件於反向偏壓區域表現出顯著的光生電流增益，證實光激發載子能在界面處被有效分離與收集；此結果不僅驗證了 CuI 作為電洞傳輸層的潛力，更說明該結構在自供電光偵測器與高性能太陽能電池應用中的高度可行性。

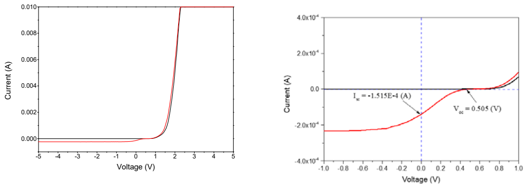

圖 6 (a) : n-Silicon/p-CuI 照光、不照光 I-V 特性 (b) n-Silicon/p-CuI I-V 特性曲線之 I_{sc} 和 V_{oc} 位置。

(2) 吸收光譜分析

圖 7 呈現的分別是 p-CuI 的穿透和吸收光譜，透過穿透、吸收譜確認本論文生長的 CuI 能隙為 3.0eV。[4]

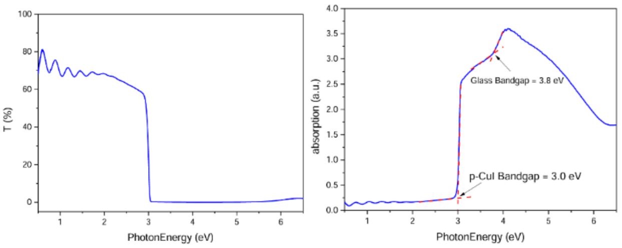

圖 7: (a) p-CuI/Glass 穿透光譜(b) p-CuI/Glass 吸收光譜

(3) 光致發光(Photoluminescence, PL)分析

透過 PL 數據可以發現在 409 nm 處有非常明顯的特徵峰，此峰為 CuI 發出的光，並利用 1240/409nm 公式計算出 CuI 的能隙位於 3.03eV，此結果與上方的穿透、吸收數據得到的數據非常相近，因此可確定本論文生長出的 CuI 能隙為 3.03eV，屬於寬能隙的半導體。[5]

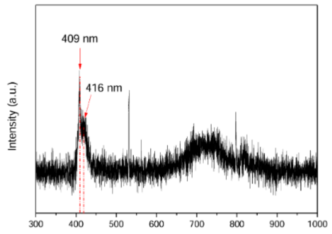

圖 8 : CuI PL 光致發光量測數據

3.3 異質結構二極體特性分析

(1)電流-電壓特性曲線分析

n-Silicon/p-CuI 為異質結構二極體，照光/不照光的 I-V 曲線，也同樣具有良好的二極體整流特性。

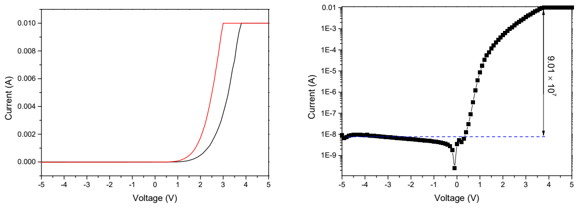

圖 9 : n-Silicon/p-CuI 異質結構二極體，(a)照光/不照光 I-V 曲線，(b)照光/不照光電流以對數尺度表示

(2) 太陽能電池參數分析

表一量化了元件在標準光照環境下的光電轉換能力，其開路電壓（Voc）達到 0.505 V，短路電流（Isc）為-1.515 E-4 A，並在最大功率點（Pmax）穩定輸出約 12.75 W 的電能；數據顯示該異質接面已成功建立有效的光伏效應機制，可將入射光能直接轉化為電能。整體光電轉換效率為 1.904%，薄膜在極小受光面積下表現出了電壓穩定性與電流響應，充分驗證了其作為高效、低成本透明電洞傳輸層在矽基光伏元件中的應用價值。

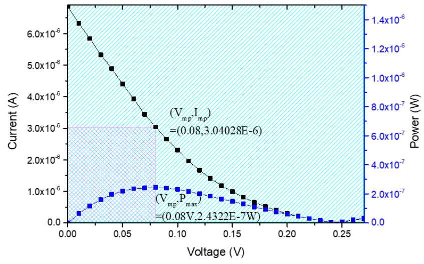

圖 10：n-Silicon/p-CuI 電流對功率做雙 Y 圖

表一：n-Silicon/p-CuI 太陽能電池參數量測結果。

	p-CuI / n-Silicon
V_{mp} (V)	0.17
I_{mp} (A)	7.5026×10^{-5}
P_{max} (W)	1.2753×10^{-5}
V_{oc} (V)	0.505
I_{sc} (A)	-1.515E-4
Sample Area (cm^2)	0.00669536
Light Power（mW/cm^2）	100
Fill Factor（%）	21.96
Efficiency η（%）	1.904

(3) 持續性光電導分析

透過持續性光電導的量測，可量測 n-Silicon / p-CuI 異質結構對雷射光的響應速度，此實驗是量測當樣品照射到雷射光時產生的光電流，當光電流到飽和時，即為上升時間(Rise Time)，當下降至起始暗電流值則為下降時間(Fall Time)。使用 808nm 的雷射光進行持續性光電導分析的量測，由於 n-Silicon / p-CuI 異質結構在偏壓為零時，有出電的現象，因此樣品皆在不施加外部偏壓的情況下進行量測。光響應結果顯示該異質結構二極體展現良好快速響應特性。

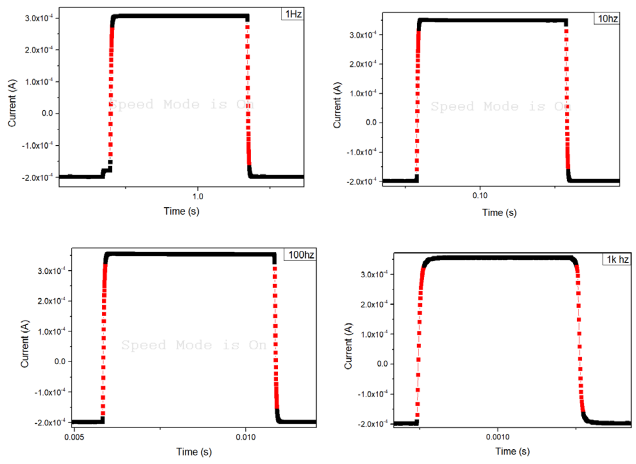

圖 11：n-Silicon / p-CuI /分別在 1 Hz、10 Hz、100 Hz 及 1 kHz 的量測圖 。

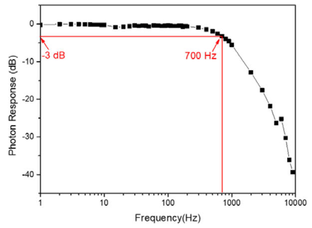

圖 12：n-Silicon / p-CuI 變頻 PC。

表二：n-Silicon / p-CuI 上升時間與下降時間數據。

Frequency（Hz）	**Rise Time（s）**	**Fall Time（s）**
1Hz	6.52 ms	6.0 ms
10Hz	0.62 ms	0.62 ms
100Hz	80 µs	66 µs
1KHz	20 µs	20 µs

(4) 變光功率光響應分析

圖 13 為 n-Silicon / p-CuI 異質結構的變光功率響應實驗數據，實驗時分別會使用三個 ND Filter，分別是：無衰減、衰減 10 倍以及衰減 100 倍。

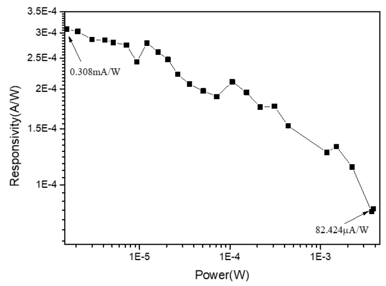

圖 13：n-Silicon / p-CuI 變光功率響應數據

四、結論

本研究成功以氣相碘化法製備出高品質之 CuI 薄膜，驗證該製程具備低成本以及操作簡便等優勢。材料分析結果顯示，我們生長的 CuI 薄膜具有良好的結晶性與均勻的晶粒分布，元素組成比例接近理論化學計量比 1：1，顯示薄膜具備良好之化學純度與組成穩定性。XRD 分析進一步確認薄膜為 γ 相，且未觀察到明顯雜相生成，顯示本研究之製程能有效控制材料之晶體結構。光學與電性量測結果顯示，CuI 薄膜之能隙約為 3.0 eV，屬於寬能隙 p 型半導體材料，具備應用於光電元件之潛力。在元件應用方面，所製備之 CuI/Si 異質結構二極體展現出良好之整流特性與穩定之電性行為；於 AM1.5 模擬太陽光照射下，元件於零偏壓條件即可產生明顯光電流。此外，持續性光電導與變頻量測結果顯示，在不同頻率條件下仍然可以維持穩定、快速之光響應，其響應時間可達微秒等級，顯示其於高速光偵測應用上具備發展潛力。 綜合上述結果，本研究不僅證實氣相碘化法可有效製備高品質 CuI 薄膜，亦成功將其應用於矽基異質結構光電元件，並展現良好之界面特性與光電響應能力。未來可透過製程參數優化與界面工程進一步提升效能，以拓展其在光偵測器與太陽能轉換元件等領域之應用價值。

參考文獻

[1] L. Hu et al., “In-situ fabrication of AgI–BiOI nanoflake arrays film photoelectrode for efficient wastewater treatment, electricity production and enhanced recovery of copper in photocatalytic fuel cell,” Catalysis Today, vol. 355, pp. 379-390, 2020.

[2] L. Zhang et al., “A facile room-temperature iodination route to in situ fabrication of patterned copper–iodide/silicon quasi-bulk heterojunction thin films for photovoltaic application,” Dalton Transactions, vol. 44, no. 12, pp. 5848-5853, 2015.

[3] Morais Faustino, B.M., Gomes, D., Faria, J. et al. “CuI p-type thin films for highly transparent thermoelectric p-n modules,” Sci Rep 8, 6867 (2018).

[4] S. Koyasu and M. Miyauchi, “Recent research trends in point defects in copper iodide semiconductors,” Journal of Electronic Materials, vol. 49, no. 2, pp. 907–909, 2019.

[5] Guochen Lin ., et al, “Luminescence Properties and Mechanisms of CuI Thin Films Fabricated by Vapor Iodization of Copper Films”, Materials (Basel), pp：6-7, 2016.

報告型式：

□英文口頭報告競賽 (□無機材料， □有機材料)
□海報展示並參加壁報論文競賽(□無機材料， □有機材料)
☑只參加海報展示 (☑無機材料， □有機材料)

具有摻雜的硫化鎵晶體成長與其光電特性研究

[1] 陳國豪 [2] 徐啟仁 [3] 張程傑 [4] 林得裕 [5] 石豫臺 [6] 黃勝斌
[134] 電子工程學系,國立彰化師範大學,彰化市師大路二號
[25] 物理系,國立彰化師範大學,彰化市進德路一號
[6] 電子工程學系,建國科技大學,彰化縣彰化市介壽北路一號

NSTC-114-2221-E018-013

摘要(Abstract)

本研究主要探討硫化鎵（GaS）晶體成長與摻雜不同元素在電性與光電特性上的表現，研究採用 CVT（Chemical Vapor Transport）生長出晶體，在完成 GaS 晶體生長後，我們會進行以下的實驗，使用 SEM(**Scanning Electron Microscope**)量測表面形貌，證實了材料確實為層狀結構；使用 EDS (Energy Dispersive Spectrometer)量測樣品組成證實了材料經 CVT 成長正確；使用 X 光繞射分析(XRD)量測晶格常數；使用電流-電壓特性曲線量測系統（I-V Curve Measurement），量測樣品在照光與不照光的環境下電阻變化證實樣品摻雜後光響應提升；最後透過紫外/近紅外光分光光譜儀（Ultraviolet/Visible Spectrophotometer）V570 量測樣品對不同波長光的穿透率(T%)變化，證實摻雜後 GaS 能隙上升。

一、簡介

GaS 是一種 III-VI 族化合物半導體材料，屬於層狀硫族化合物。 GaS 晶體具有層狀結構、寬能隙和優異的光電性能。在室溫下，GaS 呈現六方層狀結構，晶格常數約為 a≈3.58 Å 和 c≈15.5 Å[1]。其基本單層結構由四個原子層組成：S-Ga-Ga-S，層間相互作用主要由范德瓦力[2]主導。

在眾多二維材料中，GaS（硫化鎵）因具備約 2.4~2.6 eV 的可見光能隙、良好的化學穩定性及適合異質接面的能帶結構，展現出優異的光電應用潛力[3]。其可透過多種製程方法製備薄膜，並與矽或其他材料整合，以提升光載子分離效率與元件效能。因此，GaS 為材料特性、製程彈性與應用潛力皆優異的重要候選材料，值得進一步研究於光電與能源元件之研究。

硫化鎵作為一種新興的層狀半導體材料[4]，在光電、奈米電子與感測領域具有廣泛應用潛力。隨著二維材料技術成熟，其應用有望逐步從實驗室走向產業化。

因純 GaS 在實際應用上仍存在一些限制，例如：載子濃度不足、導電率較低、能帶結構固定、光電轉換效率有限等因素，故需要透過摻雜不同元素來調整材料的光學與電學特性。因此，本研究透過適當的摻雜元素來探討改變載子濃度（carrier concentration）、改變導電型態（n-type → p-type）、調整能帶結構（band structure）、提升光電響應，探討不同摻雜元素對 GaS 的影響。

二、實驗方法

本研究以化學氣相傳輸法（CVT）[5]生長 GaS 晶體，實驗中，我們使用了高純度的鎵粉、硫粉作為主要材料以及碘作為傳輸劑，接著將生長材料和傳輸劑放入石英管中密封，然後放入溫度範圍為 850°C至 750°C 的高溫爐中進行生長，經過一週的材料汽化並反應最後結晶，成長出多層狀的 GaS 塊材樣品，接續，將上述樣品進行 SEM 觀察表面、EDS 量測樣品組成、XRD 量測晶格常數、使用 I–V 量測分析 GaS 與摻雜不同元素之照光、不照光樣本結構整流、穿透光譜儀量測能隙。

三、結果與討論

3.1 材料結構與晶體特性分析

(1) SEM 表面形貌分析

圖一為 SEM 50K 影像[6]，在圖一(a)(c)50K 影像中可觀察到表面大部分無明顯起伏，且圖一(b)50K 影像中可清晰觀察到階梯狀邊緣與薄片層狀結構層疊。此反應了 GaS 材料是一種典型的二維層狀半導體材料，層與層之間由較弱的凡德瓦力結合。材料結構有利於電化學儲能、催化或二維電子元件的基礎材料。

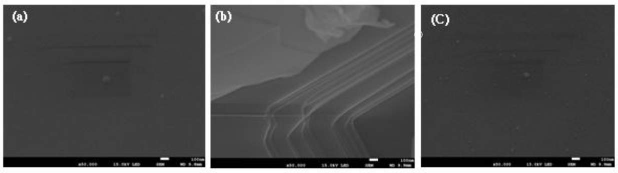

圖一：SEM50K 影像，(a)GaS(b) GaS:Zn(c) GaS:Nb

(2) 能量散射 X 射線譜（Energy-Dispersive X-ray Spectroscopy，EDS）

圖二中顯示 Ga 與 Zn 的複合峰在約 1.0–1.2 keV，對應其 L 層電子躍遷。S 峰在約 2.3 keV，對應其 K 層電子躍遷。原子量分別為 Ga 約 69.72、Zn 約 65.38，S 約 32.06，Ga：Zn 非常接近理論值 1：1 的化學計量比。Zn 的原子半徑約為 134 pm，Ga 的原子半徑約為 135 pm。因為尺寸極為接近，Ga 進入 ZnS 晶格時產生的應變較小，結構穩定。以上說明我們所製備的晶

體具有良好的化學準確度。

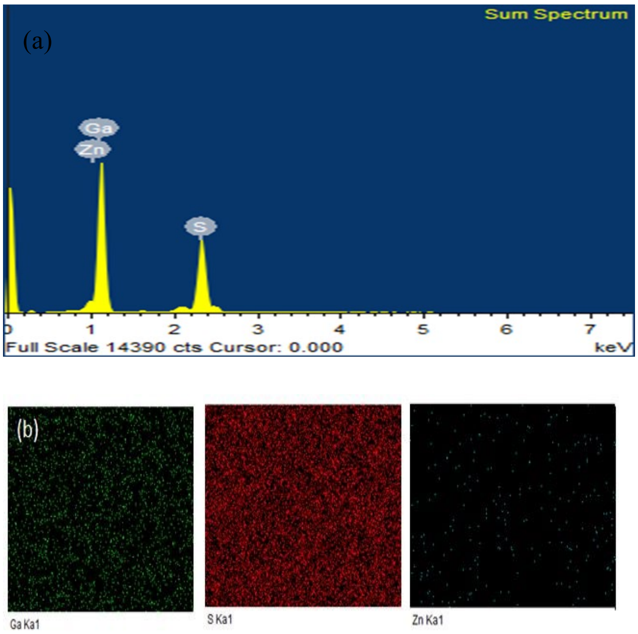

圖二：GaS:Zn 0.5% (a) EDS 元素比例分析(b) EDS 元素映射圖 Ga (鎵)(綠色圖)、S(硫) (紅色圖)、Zn(鋅) (黑色圖)

圖二(b)中顯示 Ga 在樣品表面均勻分佈;顯示 S 同樣呈現高密度且均勻的分佈；Zn 圖則是僅有極少數雜訊點分佈。表示 Ga 與 S 佔比高且均勻，證明此材料為均相 GaS 化合物，Zn 圖則顯示確實有摻雜進 0.5%Zn。Ga 與 Zn 的分佈區域與 S 的空缺區域完全吻合，證實 Zn 原子確實取代了 GaS 晶格中的 S 位置。

(4) XRD 晶體結構分析

圖三中 GaS PDF 線代表標準對照卡（JCPDS），用來確認樣本是否為 GaS 相。GaS:Zn 0.5%可見其強度顯著增加，顯示晶體品質或取向性改變。GaS:Nb 0.5%依據布拉格定律計算晶格常數：

$d=\frac{\lambda}{2\sin\theta}$，$d_{002}$=7.81 Å；$d_{103}$=2.59 Å

c＝4×3.83≈ 15.62 Å，a ≈ 3.45 Å，

圖三中出現 (103) 與 (106) 峰值代表該樣本並非完全的單晶，而是具有隨機取向的多晶性質成分，樣本確認為六方結構 GaS。GaS:Zn 0.5%的峰值強度遠高於純 GaS，表示鋅的加入顯著提升了樣本的結晶度。所有實驗峰位與粉紅色的 GaS PDF 標準卡完全重合，證明摻雜 Nb 或 Zn 並未破壞 GaS 的基本層狀結構[6]。

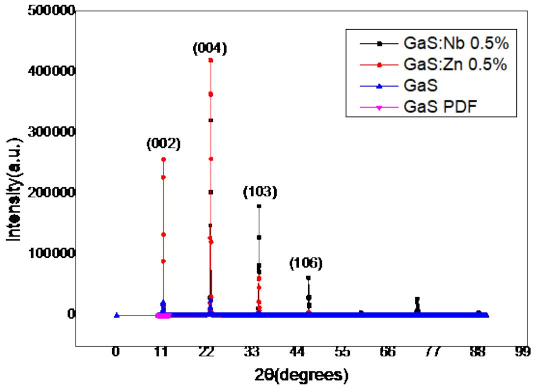

圖三：GaS:Zn 0.5% & GaS:Nb 0.5% XRD 和各面相 JCPDS 標準數據

3.2 材料光學電性分析

(1) 電流-電壓特性曲線分析

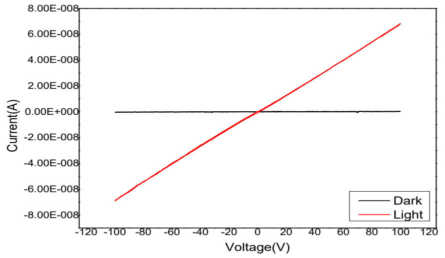

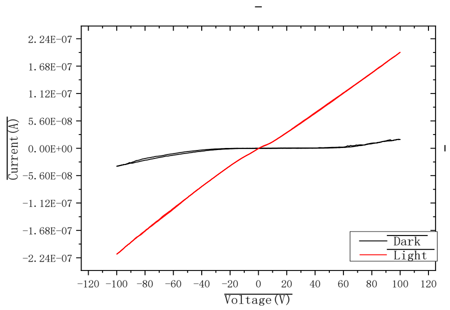

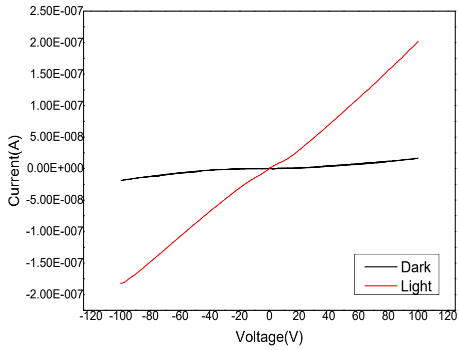

圖四: 照光、不照光 I-V 量測(-100 V~100 V),

(a)GaS(b)GaS:Zn 0.5%(c)GaS:Nb 0.5%

圖四中黑線表不照光時，紅線表照光，不照光十 3 種材料皆幾乎是水平線，表示材料的本質載子濃度極低，暗電流非常微小，說明 GaS 在黑暗中具有高阻抗特性。

照光時，電流隨電壓的增加而顯著線性增加。顯示材料產生了相對大量的光生載子因此電阻大幅下降，呈現典型的歐姆接觸特性之線性 I-V 關係。

圖四：(b)GaS:Zn 0.5%(c) GaS:Nb 0.5% 顯示樣本材料照光下電流大幅提升，電阻下降，代表 GaS 元件摻雜後照光產生電流大幅提升。對稱性方面，曲線在正負偏壓下的反應是一致的，再次確認了元件結構的對稱性與載子在兩端的傳輸效率相同。

表一：**偏壓在 100 伏時照光與不照光的電流值,照光方式採用 AM 1.5 太陽能模擬光**

樣品	**照光**	**不照光**	**電流值相減**
GaS	68.30 nA	0.258 nA	68.042 nA
GaS:Zn 0.5%	196 nA	17.9 nA	178.1 nA
GaS:Nb 0.5%	202 nA	16.6 nA	185 .4 nA

從表一中之數據可見 GaS 各樣本材料的電學表現，GaS:Zn 0.5%或 GaS:Nb 0.5%顯著改變樣本材料的光電特性，摻雜不同元素對光電流與暗電流具顯著影響[7]，導電性大幅提升，與純 GaS 相比，摻雜 0.5%的 Zn 或 Nb 後，光電流（Photo-current）從 68.30 nA提升至 202 nA，增長了約 3 倍。

I-V 曲線特性與電極接觸分析如下：光敏特性優異方面，照光後曲線斜率顯著變大，證實 GaS 樣本對 AM1.5 模擬光源具有高度敏感性，適合開發為光偵測器。摻雜後材料本質方面低暗電流斜率與高光電流斜率的對比，反應樣本材料摻雜後具備更高的光電流淨值（ΔI），**GaS：** 68.3 nA–0.258 nA約68.042 nA，**GaS:Zn 0.5%**：196 nA-17.9 nA 約 178.1 nA ，**GaS:Nb 0.5%**：202 nA-16.6 nA 約 185 .4 nA 顯示摻雜不同元素能有效產生更多的非平衡載流子，增強光電導效應。由上述結論推得摻雜後作為光電開關材料之特性會更為理想。

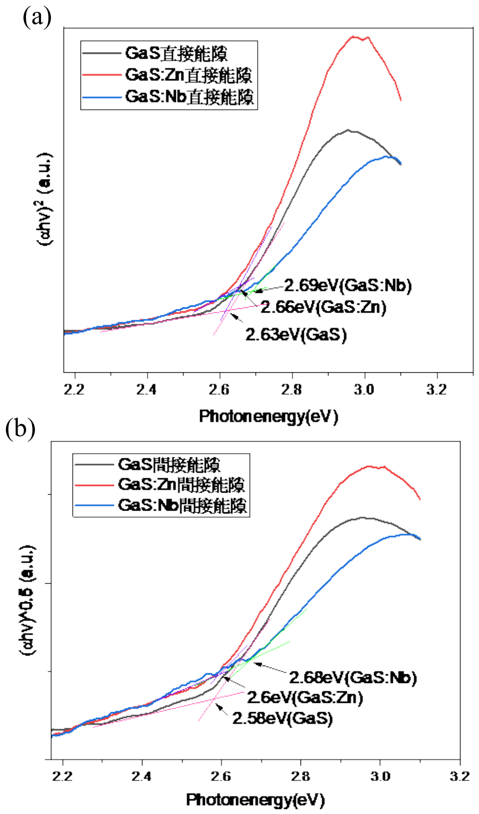

(2) 穿透光譜分析

圖五: GaS、GaS:Zn 0.5%、GaS:Nb 0.5%的(a)室溫直接能隙光譜 (b)室溫間接能隙光譜

由穿透率光譜分析並依據能隙理論 $\alpha hv=A(hv-Eg)^{n-}$ 可得圖四，由圖五(a)可知 GaS 直接能隙約 2.63 eV 而 GaS:Nb 0.5%和 GaS:Zn 0.5%的直接能隙則是分別為 2.66 eV 和 2.69 eV，這是因為摻雜後電子結構改變使能帶改變。且由 GaS:Nb 0.5%的直接能隙為 2.69 eV 比 GaS:Zn 0.5%的直接能隙 2.66 eV 大，可知摻雜 Nb 對 GaS 的影響更大，這是因為 GaS 組成導帶底與價帶頂

Sample	直接能隙	間接能隙
GaS	2.63 eV	2.58 eV
GaS:Zn 0.5%	2.66 eV	2.6 eV
GaS:Nb 0.5%	2.69 eV	2.68 eV

的分別是 Ga 的 4s、4p 軌域與 S 的 3p 軌域，而 Zn 會與導帶底與價帶頂產生反應的軌域是 4s^2，Nb 則是 4d^4，Zn 的軌域已填滿因此對 GaS 能隙影響較小，Nb 則是軌域仍有空位，因此對能隙的影響更大。

圖五(b) 可知 GaS 間接能隙約 2.58 eV 而 GaS:Nb 0.5%和 GaS:Zn 0.5%的間接能隙則是分別為 2.60 eV 和 2.68 eV，這是因為摻雜後電子結構改變使能帶改變。且由 GaS:Nb 0.5%的間接能隙為 2.68 eV 變化比 GaS:Zn 0.5%的直接能隙 2.6 eV 大，可知摻雜 Nb 對 GaS 的影響更大，這與直接能隙原因一樣是因為軌域導致。且由 GaS:Zn 0.5%的間接能隙為 2.68 eV 幾乎等同於直接能隙，這表明摻雜 Zn 的情況下間接能隙幾乎消失，更驗證了上述摻雜 Zn 對能帶影響極大。

表二 GaS、GaS:Zn 0.5%、GaS:Nb 0.5%的室溫能隙值表

四、結論：

本研究之電性與光電量測結果指出，摻雜樣品皆展現顯著的光電導效應，且相較於未摻雜 GaS，其光電流提升約達三倍，其中以 GaS:Nb 0.5%表現最佳，顯示摻雜可有效提升載子濃度並改善導電行為，同時維持低暗電流特性，對高靈敏度光偵測具有關鍵意義。此外，光學分析結果證實摻雜可調控材料能隙與光吸收特性，進一步提升其應用彈性。

綜合而言，本研究證實透過適當元素摻雜可有效調控 GaS 之能帶結構與光電特性，並顯著提升其光電轉換效能，突顯其於光偵測器與二維光電元件應用之潛力。本成果對於層狀半導體材料之功能設計與實際應用提供具體且重要之參考依據[8]。

本研究成功以化學氣相傳輸法（CVT）成長高品質層狀硫化鎵（GaS）晶體，並系統性探討鋅（Zn）與鈮（Nb）摻雜對其結構與光電特性之影響。結構分析結果顯示，摻雜元素在不破壞 GaS 六方層狀晶體結構的前提下，有效提升材料之結晶性與成分均勻性，顯示本製程具備穩定且可控制之優勢。

References

[1] Hahn, F. (1955). *Crystal structure of gallium sulfide (GaS).*Zeitschrift für anorganische und allgemeine Chemie, 278, 346.

[2] Sharma, M., & Ahluwalia, P. K. (2020, June). The electronic, optical, and transport properties of two-dimensional GaS-doped group II and IVa devices are highly tunable. *Physica E：Low-dimensional systemss and Nanostructures*, 120, 114040.

[3] Cui, Q. X., Wang, L., & Ji, X. H. (2025, July). Synthesis, Characterization, and Self-Powered Ultraviolet Light Detection Properties of GaS. *Physica E：Low-dimensional systemss and Nanostructures*, 172, 116281.

[4] AlMutairi, A., Xhameni, A., Guo, X., Chircă, I., Nicolosi, V., Hofmann, S., & Lombardo, A. (2024). Controlled fabrication of native ultra-thin amorphous gallium oxide from 2D gallium sulfide for emerging electronic applications

[5] Attolinia, G., Negria, M., Besagnia, T., Peczc, B., & Corac, I. (2020, July). CVT and PVT growth and characterization of GaS crystals. *Materials Science & Engineering B*, 261, 114623.

[6] Goldstein, J. I., Newbury, D. E., Michael, J. R., Ritchie, N. W. M., Scott, J. H. J., & Joy, D. C., (2018, Dec. 1). Scanning Electron Microscopy and X-ray Microanalysis. Fourth Edition, *Microscopy and Microscopic Analysis*, *Springer*,*24*(6), 768. https://doi.org/10.1017/S1431927618015271

[7] Zhong, W. H., Liu, Y. Q., Yang, X. H., Wang, C., Wei, X., Li, Y. Z., Liu, W. Z., & Xu, H. Y. (2021, Dec.). Suspended few-layer GaS photodetector with sensitive fast response. *Materials & Design*, 212, 110233.

[8] Zappia, M. I., Bianca, G., Bellani, S., Curreli, N., Sofer, Z., Serri, M., Najafi, L., Piccinni, M., Oropesa-Nuñez, R., Marvan, P., Pellegrini, V., Kriegel, I., Prato, M., Cupolillo, A., & Bonaccorso, F. (2021, May. 26). Two-Dimensional Gallium Sulfide Nanoflakes for UV-Selective Photoelectrochemical-type Photodetectors. *The Journal of Physical Chemistry C: Energy Conversion and Storage*, *125*(22), 11857-11866.

報告型式：

□英文口頭報告競賽 (□無機材料， □有機材料)
□海報展示並參加壁報論文競賽(□無機材料， □有機材料)
☑只參加海報展示 (☑無機材料， □有機材料)

透過石墨烯層間共價相互作用增強 Sc-N-C 單原子催化劑之ORR 性能

1 葉弘舜、1*陳信安
2 國立臺北科技大學材料科學與工程學研究所
hachen@ntut.edu.tw
NCTC-114-2122-M-027-001

隨著全球對綠色能源轉換技術的重視，開發高效能且低成本的氧還原反應(ORR)催化劑已成為燃料電池與金屬空氣電池領域的核心課題。單原子催化劑(SACs)因具備極高的原子利用率與可調控的活性中心，展現出取代傳統貴金屬鉑(Pt)的潛力。然而，現有研究多集中於單層碳基底模型，忽視了實驗製備中常見的多層石墨烯結構及其層間相互作用。本研究利用第一性原理計算(DFT)，系統性地探討了石墨烯層間共價相互作用對 Sc-N-C 單原子催化劑 ORR 性能的影響。

研究重點在於層間 C-C 共價鍵的形成對催化活性的誘導效應，這與單純的凡德瓦力作用力顯著不同。計算結果顯示，這種層間共價鍵會對 ScN_4 活性位點產生強烈的結構拉扯，進而引發明顯的晶格扭曲(Lattice distortion)。根據我們定義的幾何畸變描述符，在適度的層間相互作用下，Sc 原子與周圍氮原子的配位環境得到優化，使得系統能有效地打破尺度關係(Scaling relations)的限制，從而大幅降低了 ORR 反應路徑中的過電位，展現出優於單層 Sc-N-C 模型的催化潛力 。

在熱力學穩定性方面，本研究透過結合能(Binding energy)的計算證實，引入層間共價相互作用能顯著提升Sc 單原子的穩定性，降低其在反應過程中發生團聚的風險。此外，我們詳細分析了 ORR 的反應路徑，發現層間相互作用改變了含氧中間體(如 OOH*、O*、OH*)在 Sc 位點上的吸附能。特別是在最關鍵的決速步驟 OH* 脫附過程中，雙層共價模型的 Sc 位點展現出適中的吸附強度，避免了單層模型中因吸附過強而導致催化劑中毒的問題，進而提升了整體的反應速率。

為了深入揭示其微觀電子機制，本研究進行了電子結構分析。透過 Bader charge analysis，我們觀察到層間共價作用促使電荷在石墨烯層間與活性中心之間重新分布，顯著改變了 Sc 原子的氧化態與電負性環境。Density of state (DOS)則進一步顯示，結構扭曲導致 Sc 的 3d 軌域發生分裂與分化，特別是軌域中心的上移加強了其與氧 2p 軌域的雜化程度。最後，利用 Crystal Orbital Hamilton Population (COHP)分析，我們成功量化了 Sc-O 鍵的成鍵與反鍵貢獻。結果證實，雙層共價模型增加了反鍵能帶的填充，弱化了共價鍵結強度，這正是 Sc-N-C 催化劑能達成高效能中間體脫附與優異 ORR 活性的物理根源。本研究的發現為早期過渡金屬單原子催化劑的載體工程提供了全新的理論視角 。

關鍵詞：二維材料、共價鍵、石墨烯、氧還原反應、單原子催化劑、第一性原理計算

參考文獻

1. HAO, Menchengzhen; ZHANG, Jiamei; LIU, Enzuo. Interlayer Covalent Interaction of Graphene Enhancing the Formation of C_2 Products in CO_2 Reduction Reaction Electrocatalyzed by Cu Single Atom Catalysts. *Surface Science*, 2026, 122964.
2. MENG, Depeng, et al. Enhanced ORR and OER bifunctional performance of Co-NC single atom catalyst by interlayer covalent interaction of graphene. *Applied Surface Science*, 2025, 695: 162879.

報告型式：

□英文口頭報告競賽 (□無機材料， □有機材料)
□海報展示並參加壁報論文競賽(□無機材料， □有機材料)
■只參加海報展示 (■無機材料， □有機材料)

以第一原理計算 Ta_3B_4 作為載體之單原子摻雜於氮還原反應之研究

[1] 簡瑞恩、[1*]陳信安
國立台北科技大學材料科學與工程學研究所
hachen@ntut.edu.tw

NSTC-114-2122-M-027-001

隨著全球能源需求增加與氣候變遷壓力升高，開發低碳能源載體已成為當務之急。氨(NH_3)因具備高能量密度與零碳排放特性，被視為具潛力的綠色能源載體。然而，傳統哈伯法(Haber–Bosch process)具有高能耗與高碳排放的缺點，難以符合永續發展需求。電化學氮氣還原反應(eNRR)提供了較溫和的替代途徑，但受氫氣析出反應(HER)競爭影響，導致產氨速率與法拉第效率偏低。[1]

為提升氮氣還原反應(NRR)催化劑的效能，本研究著重於透過原子摻雜調控結構材料之電子結構[2,3]，並結合密度泛函理論(density functional theory, DFT)進行系統性篩選。具體而言，本研究比較 3d(Ti–Zn)、4d(Zr–Rh)及 5d(Hf–Pt)過渡金屬摻雜於 Ta_3B_4 載體之催化性能，並進一步將篩選出的潛在優異金屬完全取代 Ta 原子，以探討其對催化表現之影響。

在上述設計與篩選的基礎上，為了進一步驗證與解析材料之催化行為，本研究採用 Vienna Ab initio Simulation Package(VASP)進行系列第一原理計算。首先透過結合能與吸附能分析，確定最穩定之幾何結構，並評估其熱力學穩定性與結合強度；對於篩選出的高效催化劑，進一步以 Ab initio Molecular Dynamics(AIMD)模擬驗證其熱穩定性。此外，結合 bader charge、Crystal Orbital Hamilton Population (COHP)與 d-band center 等方法，從電子結構角度闡明摻雜原子與載體間之交互作用及其電催化反應機制。

關鍵詞: 密度泛函理論、第一原理計算、氮氣還原反應、原子摻雜、過渡金屬硼化物

參考文獻

[1] Deng J, Iñiguez J, Liu C Electrocatalytic Nitrogen Reduction at Low Temperature,Joule, 2018; 2, 846-856

[2] SHUKLA, Aarti. Tailoring Hydrogen Evolution Reaction with single-atom catalysts on Ti2B MBenes: Insights from computational screening. *International Journal of Hydrogen Energy*, 2024, 77: 479-485.

[3] ZHAO, Ziming, et al. Phosphorus doped carbon nitride with rich nitrogen vacancy to enhance the electrocatalytic activity for nitrogen reduction reaction. *Chemical Engineering Journal*, 2022, 430: 132682.

報告型式：

□英文口頭報告競賽 (□無機材料， □有機材料)
□海報展示並參加壁報論文競賽(□無機材料， □有機材料)
■只參加海報展示 (■無機材料， □有機材料)

NaBH$_4$ 輔助超聲空化條件下之聲化學還原快速製備具可控缺陷之黑色 TiO$_{2-x}$ 及其光催化應用

龍泓升、賴孝武*
南臺科技大學 化學工程與材料工程系
E-mail: swlai@stust.edu.tw

摘要

本研究採用硼氫化鈉 (NaBH$_4$) 結合超聲處理技術製備表面缺陷氧化鈦。NaBH$_4$ 具有強還原性分解產生氫，能夠在超聲空化效應下有效誘導 TiO$_2$ 晶格內部形成氧空缺與 Ti^{3+} 缺陷中心，進而改變其能帶結構與表面化學性質。超聲輔助處理不僅提升還原劑與加速氧化鈦的接觸效率，同時伴隨局部高溫高壓效應，有助於加速缺陷生成過程。所得缺陷氧化鈦表現出顏色加深、可見光吸收增強以及電荷分離效率改善等特徵，顯示此方法能有效提升 TiO$_2$ 在光催化與能源轉換領域的應用潛力。結果顯示，以 Tauc plot 估算能隙，最佳樣品 B10–US60 之能隙為 Eg = 2.89 eV；並以 Urbach energy 評估吸收尾端之能態無序程度，其 Eu = 137 meV，顯示材料內部具有較顯著之局部能態分佈與缺陷相關吸收行為。

在可見光光催化降解（甲基藍，MB）測試中，最佳樣品（B10–US60）之降解率可達 68%；相較於對照組（僅超聲處理 US540 之空白樣品，降解率最高 40%），顯示適度缺陷引入有助於拓展可見光響應並提升反應效能。綜合而言，本研究結果證實超音波結合還原之缺陷工程可有效調控 TiO$_2$ 之光學吸收特性，並在可見光條件下展現之光催化表現，提供後續缺陷程度最佳化與材料設計之參考依據。綜合而言，NaBH$_4$ 超聲處理更有利於促進缺陷生成，但高劑量與長時間條件下需注意副產物生成及殘留問題。

關鍵詞：黑色二氧化鈦（B–TiO$_2$）、聲化學還原、硼氫化鈉（NaBH$_4$）、氧空缺、光催化

參考文獻

[1] Fang, W.; Xing, M.; Zhang, J. Modifications on reduced titanium dioxide photocatalysts: A review. J. Photochem. Photobiol. C Photochem. Rev. 2017, 32, 21–39.

[2] Kang, Q.; Cao, J.; Zhang, Y.; Liu, L.; Xu, H.; Ye, J. Reduced TiO2 nanotube arrays for photoelectrochemical water splitting. J. Mater. Chem. A 2013, 1, 5766–5774.

[3] Xing, M.; Fang, W.; Nasir, M.; Ma, Y.; Zhang, J.; Anpo, M. Self-doped Ti3+-enhanced TiO2 nanoparticles with a high-performance photocatalysis. J. Catal. 2013, 297, 236–243

[4] Fan, C.; Chen, C.; Wang, J.; Fu, X.; Ren, Z.; Qian, G.; Wang, Z. Black hydroxylated titanium dioxide prepared via ultrasonication with enhanced photocatalytic activity. Sci. Rep. 2015, 5, 11712.

[5] Chen, X.; Liu, L.; Yu, P.Y.; Mao, S.S. Increasing solar absorption for photocatalysis with black hydrogenated titanium dioxide nanocrystals. Science 2011, 331, 746–750.

[6] Liu, N.; Zhou, X.; Nguyen, N.T.; Peters, K.; Zoller, F.; Hwang, I.; Schneider, C.; Miehlich, M.E.; Freitag, D.; Meyer, K.; et al. Black magic in gray titania: Noble-metal-free photocatalytic H2 evolution from hydrogenated anatase. ChemSusChem 2017, 10, 62–67.

[7] Tan, H.; Zhao, Z.; Niu, M.; Mao, C.; Cao, D.; Cheng, D.; Feng, P.; Sun, Z. A facile and versatile method for preparation of colored TiO2 with enhanced solar-driven photocatalytic activity. Nanoscale 2014, 6, 10216–10223.

報告型式：

□英文口頭報告競賽 (□無機材料， □有機材料)
□海報展示並參加壁報論文競賽(□無機材料， □有機材料)
■只參加海報展示 (■無機材料， □有機材料)

應用於離岸風電結構之 S355ML 功能性金屬材料：基於 AGSD 系統之智能缺陷檢測與海洋腐蝕風險評估

洪孟傑[1]、劉何昇[2]、洪唯峻[3]、李秉睿[4]、陳志文、楊萬騏*
龍華科技大學
xylitol21@gmail.com

摘要

離岸風電結構件之銲接品質直接關係到整體結構的安全性與服役壽命。本研究針對 S355ML 高強度低合金細晶粒鋼，探討其在高鹽、高濕、高負載海洋環境下之服役可靠性。S355ML 雖具備優異的 TMCP 微觀組織與低溫韌性，但在服役期間，任何因銲接熱循環產生的微小缺陷（如裂縫、氣孔、咬邊）皆會破壞材料的功能完整性，成為化學腐蝕與應力集中的發生處，對結構完整性與維護成本構成潛在威脅。

為解決傳統檢測效率低且缺乏定量化評估之瓶頸，本研究開發一套創新的「異常導向語意檢測系統（AGSD）」。該系統整合無監督卷積自動編碼器與深度語意分割技術，針對 S355ML 銲道特性進行高效率自動化監測。實驗結果顯示，系統於異常檢知階段達成 100% 的檢出率，並在語意分割中精準辨識各類瑕疵，平均IoU 達 75.90%。此外，本研究建立基於幾何特徵的量化評估機制，將缺陷之面積與形狀特徵連結至材料的腐蝕劣化指標。AGSD 流程不僅提升了功能性金屬材料的智慧監測水準，更為離岸風電製程和後續檢修的數位化與品質可視化奠定堅實基礎。

簡介

S355ML 鋼材係依據歐洲標準 EN 10025-4 生產之熱機軋製細晶粒高強度低合金（HSLA）結構鋼。其微觀組織主要由細晶肥粒鐵與變韌鐵組成，並可能含有少量波來鐵(Pearlite)；透過細晶強化、析出強化與固溶強化等多重機制，使其在具備高降伏強度（≥355 MPa）的同時，仍能於低溫環境（-50°C）下符合規範要求之夏比衝擊韌性，因此成為離岸風電水下基礎（如單樁、套筒式平台）之關鍵功能性金屬材料。

然而，在離岸風場嚴苛的海洋服役環境下，S355ML 結構件長期暴露於高鹽霧與高濕度之中。銲接過程中因熱循環導致的熱影響區（HAZ）組織粗化，以及表面產生的微觀銲道缺陷（如裂縫、氣孔、咬邊），極易成為氯離子（Cl^-）富集點並形成局部電化學腐蝕或差異曝氣電池。這些缺陷不僅是腐蝕的起始源，亦會造成嚴重的應力集中現象，進而加速疲勞裂紋萌生，嚴重威脅結構的完整性與服役壽命。

實驗方法

本研究選用工業級離岸風電用 S355ML 鋼板，係依據 EN 10025-4 標準製造之熱機軋製細晶粒高強度低合金鋼。其化學成分包含 C: 0.12%、Mn: 1.32%、Si: 0.25%，碳當量約為 0.35%，係依 IIW 標準公式估算（實際數值依完整合金元素組成計算），試件厚度為 10 mm。銲接接頭設計採單 V 型坡口，坡口角度為 60°，根部間隙為 3 mm，並設置約 1–2 mm 鈍邊以確保熔透穩定性，並配置同材質金屬襯板。銲接製程採用氣體保護金屬電弧銲（GMAW），填充金屬為符合低溫韌性要求之低合金鋼實心銲線，其機械性質為降伏強度 550 MPa、抗拉強度 610 MPa 及伸長率 28%，保護氣體採 80% Ar + 20% CO_2 混合氣。為建立多樣化缺陷樣本庫，本研究透過系統性調整銲接參數（如熱輸入、電流與銲速），並輔以人為模擬方式，製造出包含正常銲道與裂縫、氣孔及咬邊等典型缺陷之試件，尺寸為 200 mm × 100 mm。

影像資料採用高解析度工業相機搭配恆定光源系統進行銲道表面掃描，以確保影像品質之穩定性與一致性。於預處理階段，首先利用語意分割技術擷取銲道區域（ROI），以排除背景干擾；並透過資料增強方法（包含對比度調整、隨機翻轉與高斯雜訊注入）提升模型對不同光照與環境條件之泛化能力。

在檢測方法上，本研究提出異常導向語意檢測流程，採雙階段深度學習架構。第一階段為無監督異常檢知， 採用卷積自動編碼器僅以正常銲道影像進行訓練，並於推論時透過重建殘差定位潛在異常區域；第二階段則針對異常區域導入以 ResNet50 為骨幹網路並結合金字塔池化模組之語意分割模型，進行像素級缺陷分類，以辨識裂縫、氣孔與咬邊等缺陷類型。

最後，針對語意分割結果之缺陷遮罩進行幾何特徵擷取，包含缺陷投影面積、最大長度、長寬比及分形維度等指標，並建立其與電化學腐蝕行為之經驗關聯模型，以評估材料劣化程度。依據量化結果，將銲接品質分級為 OK、ACC 與 NG，作為結構健康監測與服役壽命評估之依據。

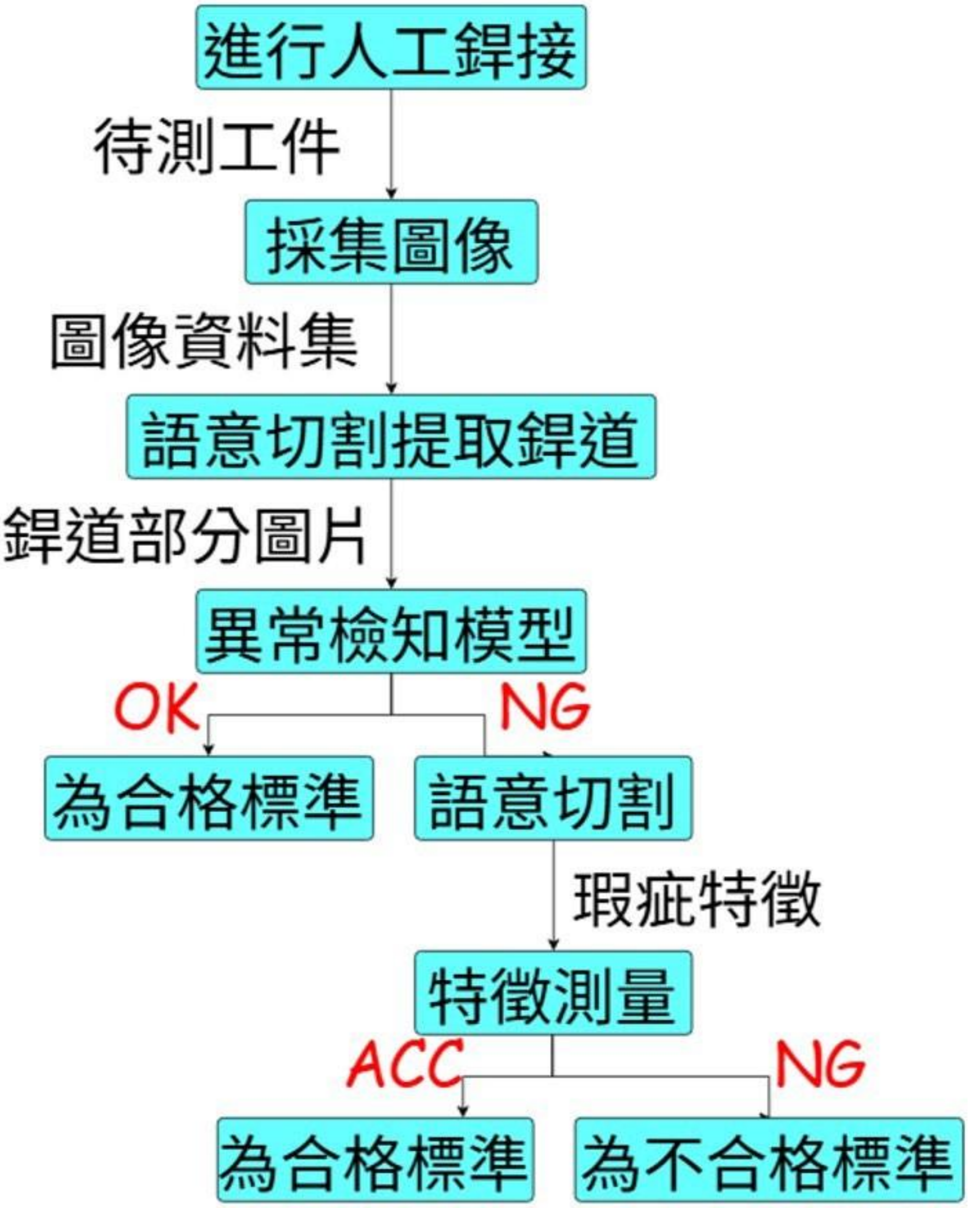

圖 1.實驗流程示意圖

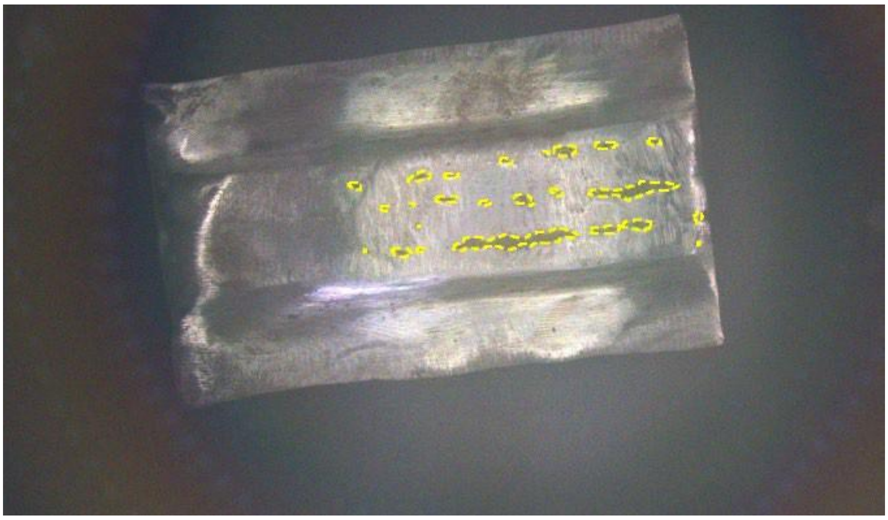

圖 2.瑕疵檢測圖

結論

首先，在檢測效能方面，所提出之 AGSD 流程於 Phase I 異常檢知階段，透過多尺度特徵融合機制，於本研究測試資料集中達成近 100% 之異常檢出率（F1-score）；於 Phase II 語意分割階段，針對裂縫、氣孔及咬邊等典型銲接缺陷之平均交並比達 75.90%，顯示該方法具備良好之缺陷辨識能力與定位精度，並展現高度穩定性與客觀性。

其次，在材料劣化分析方面，本研究透過系統化特徵擷取方法，成功將銲道微觀缺陷之幾何特徵（如投影面積、長寬比與分形維度）進行量化。相關特徵可作為後續材料腐蝕行為與疲勞劣化之潛在關聯分析依據，為 S355ML 材料於海洋環境下之服役狀態評估提供具體之數據基礎。

在產業應用層面，AGSD 系統採用無監督結合有監督之分層架構，有效降低對大量標記資料之依賴，提升模型於實際產線導入之可行性與彈性。該技術不僅有助於提升離岸風電製造過程之品質控管能力，亦於結構健康監測（Structural Health Monitoring, SHM）及數位孿生（Digital Twin）應用中展現潛在發展價值。

未來研究將進一步結合現地暴露試驗與長期監測數據，持續優化缺陷特徵與材料劣化行為之關聯模型，以提升預防性維護與結構安全預警之準確性。

參考文獻

[1]. Liu, T., Zheng, P., & Bao, J. (2023). Deep learning-based welding image recognition: A comprehensive review. *Journal of Manufacturing Systems*.

[2]. Jiao, W., Wang, Q., Cheng, Y., & Zhang, Y.(2020). End-to-end prediction of weld penetration: A deep learning and transfer learning based method. *Journal of Manufacturing Processes*.

[3]. Wang, Q., Jiao, W., Wang, P., & Zhang, Y. (2020). A tutorial on deep learning-based data analytics in manufacturing through a welding case study. *Journal of Manufacturing Processes*.

[4]. Wang, Q., Jiao, W., & Zhang, Y. (2020). Deep learning-empowered digital twin for visualized weld joint growth monitoring and penetration control. *Journal of Manufacturing Systems*, 57

報告型式：

□英文口頭報告競賽 (□無機材料， □有機材料)
□海報展示並參加壁報論文競賽(□無機材料， □有機材料)
■只參加海報展示 ■無機材料， □有機材料)

Tuning the Photocatalytic Performance of NiO Films through Ce Doping via Liquid Phase Deposition

Chih-Feng-Yen , Yan-Yun Mou* , Kuan-Cheng Peng and Wei-Run Cheng
Department of Microelectronics Engineering, National Kaohsiung University of Science and Technology, Kaohsiung, Taiwan (R.O.C.)
*C112198109@nkust.edu.tw

Abstract

Ce-doped NiO films were fabricated using the liquid phase deposition (LPD) method to investigate the effect of Ce doping ratio on photocatalytic performance. Films with Ce concentrations ranging from 1 to 20 mol% were prepared, and characterization by energy-dispersive X-ray spectroscopy (EDS), confirmed that tungsten doping significantly changes the surface structure and morphology of the composite film. The photocatalytic activity was evaluated by the degradation of methylene blue under visible light irradiation for 8 hours. The results indicated that the Ce doping ratio significantly influenced the photocatalytic activity. The 5 mol% Ce-doped NiO film exhibited the highest degradation efficiency of 88%, followed by the 3 mol% (85.3%) and 1 mol% (83%) samples. As the doping ratio increased further, the degradation efficiency decreased to 78%, 75.2%, 73%, and 70.3% for Ce concentrations of 7 mol%, 10 mol%, 12 mol%, and 20 mol%, respectively. These results demonstrate that excessive Ce doping reduces photocatalytic activity, whereas an appropriate doping ratio enhances photocatalytic performance by improving charge separation and suppressing electron–hole recombination.

Keywords: Ce-doped NiO thin films, Liquid phase deposition, Photocatalysis, Methylene blue degradation, Visible-light photocatalysis.

Experimental Method

Ce-doped NiO films were prepared on silicon substrates using liquid phase deposition (LPD). Prior to deposition, the silicon substrates were ultrasonically washed sequentially with acetone, isopropanol (IPA), and deionized water to remove surface contaminants. Then, the substrates were immersed in buffered oxide etchant (BOE) to etch away the native oxide layer. Finally, the substrates were immersed in nitric acid (HNO_3) to generate hydroxyl radicals (·OH) on the surface, resulting in better hydrophilicity and easier film adhesion during deposition. The substrates were then immersed in deionized water and dried using a nitrogen gun. For the preparation of the precursors, 0.5 M nickel nitrate hexahydrate ($Ni(NO_3)_2·6H_2O$), 1 to 20 mol% cerium nitrate hexahydrate ($Ce(NO_3)_3·6H_2O$), and 1 M urea (NH_2CONH_2) were dissolved in deionized water. The mixed precursor solution was stirred magnetically at room temperature for 24 hours to obtain a homogeneous reaction solution. After cleaning, the silicon substrate was immersed in a precursor solution and deposited using liquid phase deposition (LPD) at 90 °C for 5 hours. Following deposition, to convert the precursor layer into a Ce-doped NiO film, the prepared sample was annealed in air at 400 °C for 1 hour, promoting the formation of a stable oxide film. The surface morphology and microstructure of the film were characterized using field emission scanning electron microscopy (FE-SEM). Elemental composition and doping distribution were analyzed using energy-dispersive X-ray spectroscopy (EDS) connected to the SEM system. These analyses confirmed the successful incorporation of Ce into the NiO film and investigated the effect of Ce concentration on the film morphology. Photocatalytic activity was evaluated by degrading methylene blue under visible light irradiation for 8 hours.

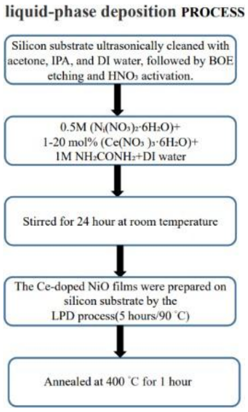

Fig.1 Flow chart of liquid-phase deposition method for Ce-doped NiO thin films.

Results and Discussion

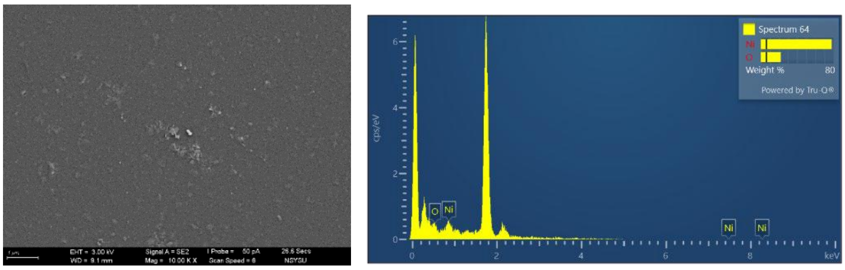

(a) pure NiO

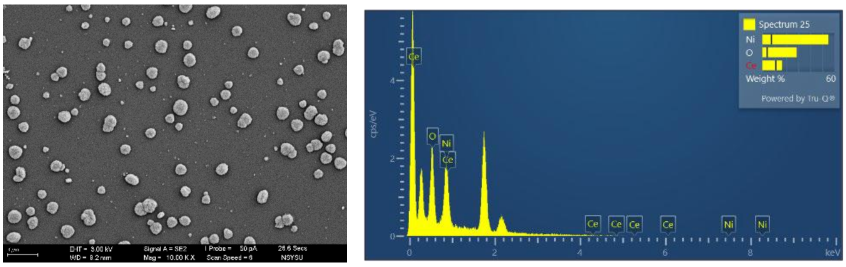

(b) 1 mol% Ce-doped NiO

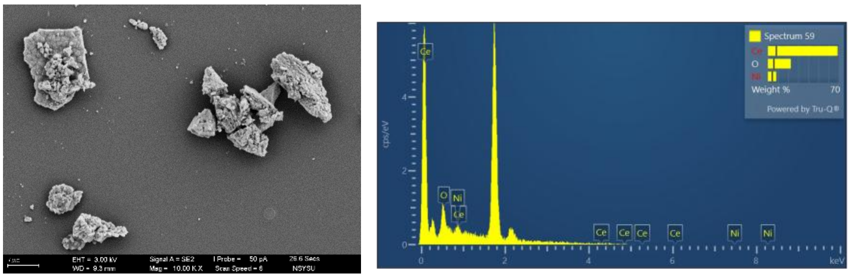

(c) 3 mol% Ce-doped NiO

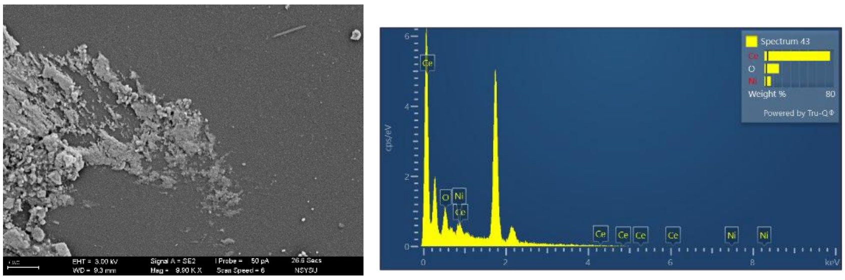

(d) 5 mol% Ce-doped NiO

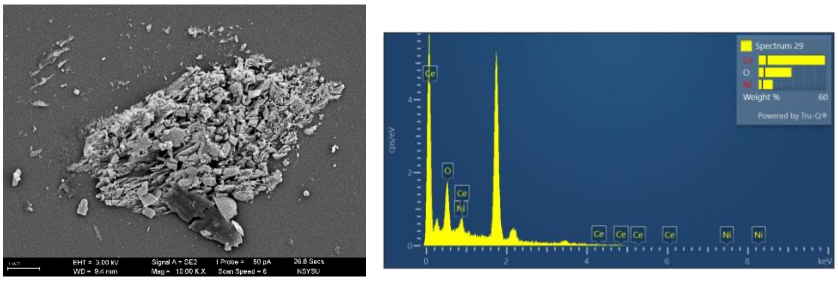

(e) 7 mol% Ce-doped NiO

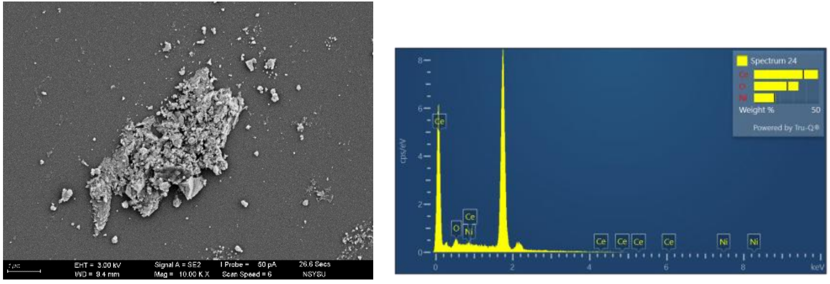

(f) 10 mol% Ce-doped NiO

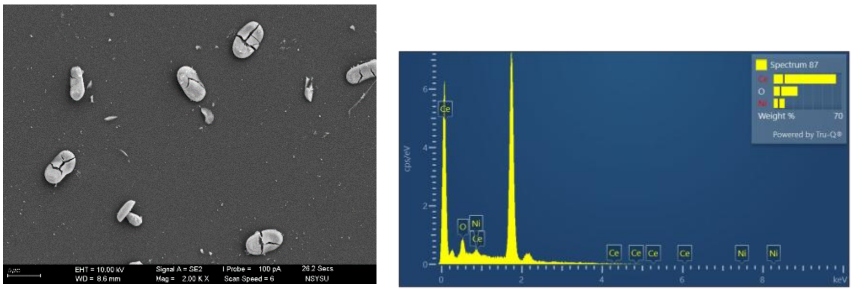

(g) 12 mol% Ce-doped NiO

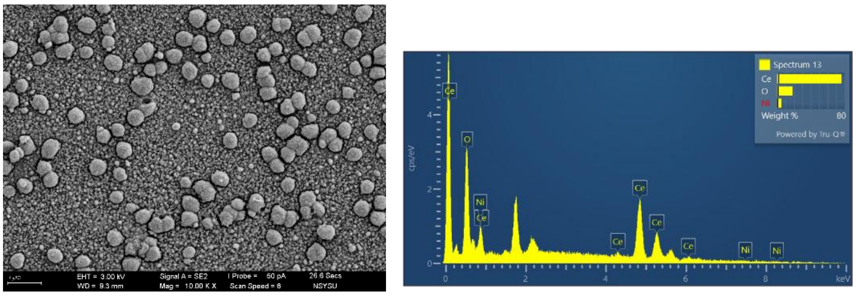

(h) 20 mol% Ce-doped NiO

Fig.2 FE-SEM observation of growth behaviors in pure NiO, Ce doped NiO thin films. At various concentration ratios, and characterization by energy-dispersive X-ray spectroscopy (EDS), confirmed that tungsten doping significantly changes the surface structure and morphology of the composite film. (a) pure NiO (b) 1 mol% Ce-doped NiO, (c) 3 mol% Ce-doped NiO, (d) 5 mol% Ce-doped NiO, (e) 7 mol% Ce-doped NiO, (f) 10 mol% Ce-doped NiO, (g) 12 mol% Ce-doped NiO and (h) 20 mol% Ce-doped NiO, The enhanced photocatalytic activity can be caused by the increased specific surface area and the reduced recombination of photogenerated charge carriers, due to the synergistic effect between the Ce-doped NiO thin films.

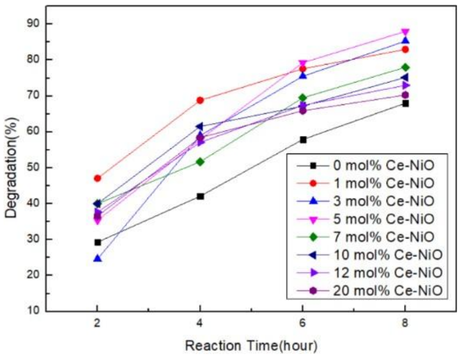

Fig.3 The 1-20 mol% Ce-doped NiO thin films and pure NiO (0 mol% Ce-NiO) of Concentration changes of degraded methylene blue.

Conclusion

The results indicate that excessive addition of Cerium (Ce) does not enhance photocatalytic efficiency. Instead, Ce-doped NiO films with specific concentration ratios exhibit optimal performance. Notably, the film containing 5 mol% Ce demonstrated the highest visible light photocatalytic efficiency, achieving a degradation rate of 88%. Therefore, the MB dyes in wastewater may be effectively degraded by the Ce doped NiO photocatalyst. This underscores the significance of controlling dopant concentration to maximize photocatalytic activity, which is very useful for environmental remediation.

References

[1] Y. Lv, C. Pan, X. Ma, R. Zong, X. Bai, Y. Zhu, "Production of visible activity and UV performance enhancement of ZnO photocatalyst via vacuum deoxidation." Applied Catalysis B: Environmental, 137-138(2013), 26-32

[2] A. Houas, H. Lachheb, M. Ksibi, E. Elaloui, C. Guillard, J.-M. Herrmann, "Photocatalytic degradation pathway of methylene blue in water." Applied 64 Catalysis B: Environmental, 31(2)(2001), 145-157

[3] Thakur, S., Kumar, R., Dhiman, N. K., & Kumar, A. (2024). Enhanced photocatalytic performance of Ce-doped NiO nanoparticles synthesized by coprecipitation method. Hybrid Advances, 6, 100225.

[4] Chen, W.-T. (2021). Silver and cerium-doped iron manganese oxyhydroxide film for seawater splitting [Master's thesis, National Sun Yat-sen University

[5] Vidales-Hurtado, M. A., & Mendoza-Galván, A. (2008). Optical and structural characterization of nickel oxide-based thin films obtained by chemical bath deposition. Materials Chemistry and Physics, 107(1), 33–38.

[6] Yu, J.; Cao, Q.; Li, Y.; Long, X.; Yang, S.; Clark, J. K.; Nakabayashi, M.; Shibata, N.; Delaunay, J.-J., Defect-Rich NiCeOx Electrocatalyst with Ultrahigh Stability and Low Overpotential for Water Oxidation. ACS Catal. 2019, 9, 1605-1611.

Presentation type：

☐ English oral competition (☐ inorganic materials, ☐ organic materials)

■ Poster competition (■ inorganic materials, ☐ organic materials)

☐ Exhibition only (☐ inorganic materials, ☐ organic materials)

基於 FTIR 穿透率與勞倫茲振子模型之藍寶石光學常數反演研究

鄒立瑜
中原大學電子工程學系
陳至信
g11276614@cycu.ed

摘要

本研究以藍寶石基板之傅立葉轉換紅外光譜（FTIR）穿透率為基礎，針對 180–300 cm-1 波數區間建立一套可供研究與報告使用的光學常數反演流程。方法上，先由原始穿透率光譜擷取目標頻段，再以 勞倫茲振子模型複介電函數結合法向入射平行平板 coherent slab transmission 模型，透過最小平方擬合求得最佳介電參數，最後由複折射率 $N=n+ik=\sqrt{}\varepsilon\varepsilon$ 反推出折射率 n 與消光係數 k。本研究同時將反演結果與 refractiveindex.info 公開資料庫所得的數據[1]進行比較，並討論兩者在趨勢與數值上的差異。結果顯示，模型可重現 FTIR 穿透率的主要變化趨勢，但反演所得 n、k 與資料庫仍存在系統性偏差，顯示厚度設定、各向異性、基線誤差與振子數目皆可能影響反演結果。本文整理反演過程、關鍵公式、擬合指標與差異來源，可作為後續模型優化之基礎。

Abstract

This study investigates the inversion of sapphire optical constants in the 180-300 cm-1 spectral range from measured FTIR transmittance. A Lorentz-oscillator dielectric function was combined with a normal-incidence coherent slab transmission model, and the unknown parameters were extracted by least-squares fitting. The complex refractive index was then obtained from $N=n+ik=\sqrt{}\varepsilon\overline{\varepsilon}$, allowing the estimation of n and k. The inverted results were further compared with refractiveindex.info literature data.[1] The results show that the proposed model reproduces the main trend of the measured transmittance, while systematic deviations remain between the inverted optical constants and the reference data. These differences are likely related to thickness assumptions, anisotropy, baseline uncertainty, and the limited number of oscillators. The present paper summarizes the inversion procedure, key equations, fitting metrics, and physical interpretation, and is intended as a concise conference-style report for advisor discussion.

關鍵詞： FTIR、藍寶石、勞倫茲振子模型、光學常數、複介電函數。

研究背景

在遠紅外與太赫茲頻段的材料分析中，FTIR可直接提供樣品的穿透率光譜；然而，光學元件設計與材料性質討論真正需要的物理量，通常是折射率n與消光係數k，而非僅有穿透率曲線。為將光譜轉換成具有材料意義的參數，必須建立合理的前向模型，再由量測結果反推出材料常數。

由於n與k本質上來自同一複介電函數，若直接將兩者視為互相獨立的曲線進行擬合，常會得到數學上貼合但物理上不一致的結果。因此，本研究採用具Kramers–Kronig一致性的勞侖茲振子模型模型，將介電響應、Fresnel界面效應與平板多重反射同時納入分析。此類方法已廣泛應用於光譜反演與THz-TDS/紅外材料參數擷取[2]–[5]。

本研究之目標有三點：其一，建立藍寶石在180–300 cm-1範圍內的FTIR反演流程；其二，比較反演所得n、k與web data文獻資料；其三，整理擬合假設、公式與限制，以作為後續增加振子數與優化模型的依據。

研究方法

2.1 反演流程

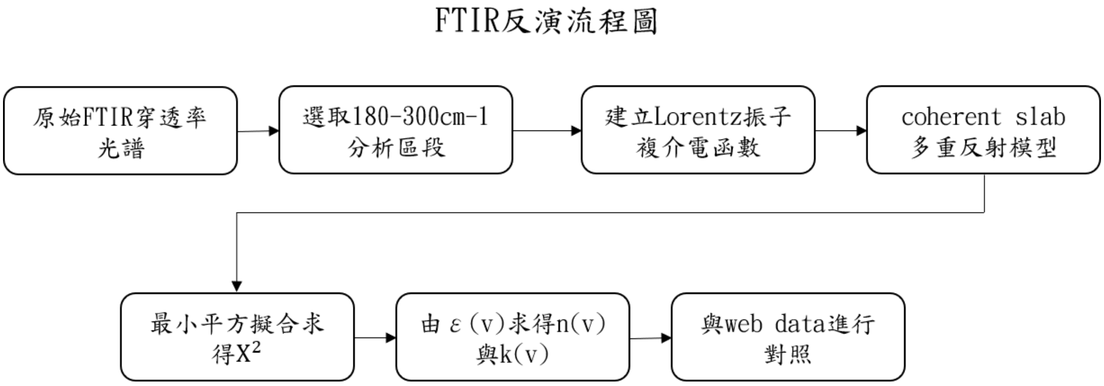

圖 1.FTIR反演流程圖

研究結果

3.1 FTIR 原始穿透率與擬合

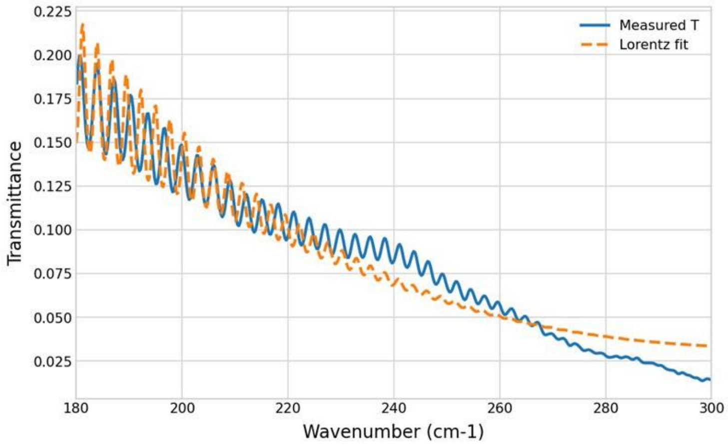

圖 2.180–300 cm-1 區間 FTIR 原始穿透率與 Lorentz-slab 擬合

以單一 勞侖茲振子模型配合固定厚度 432 μm 的 coherent slab 模型擬合後，目標區段可重現主要的包絡線與振盪趨勢。依先前計算，該組擬合對應之最小平方指標約為 $\chi^2=0.09590$，RMSE=0.01388。這說明模型已能描述量測曲線的主要物理行為，但仍存在局部區段偏差。

3.2 反演之 n、k 與 web data 比較

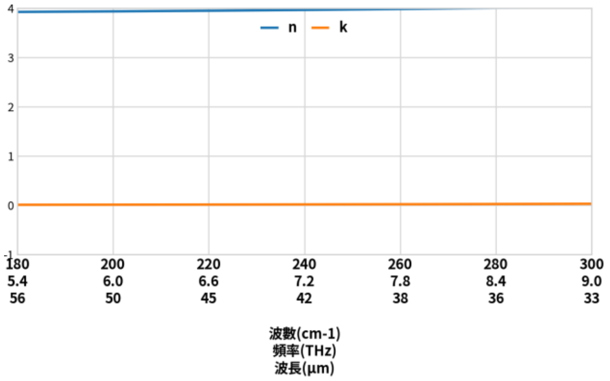

FTIR反演計算結果

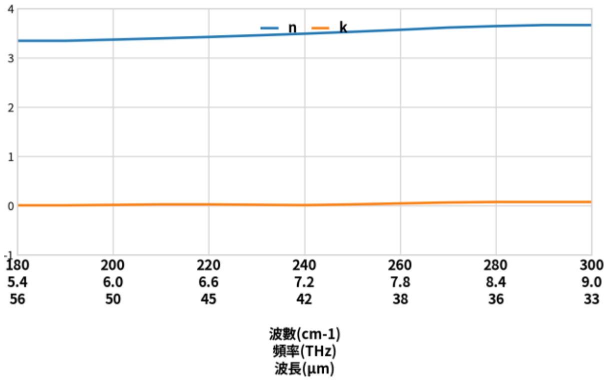

web data文獻對照數據

圖 3.上：FTIR 反演計算結果；下：web data 文獻對照數據

討論與結論

造成 FTIR 反演結果與 web data 差異的可能原因包括：第一，藍寶石為各向異性晶體，而本研究為簡化處理，將其視為有效各向同性介質；第二，厚度固定為 432 μm，若實際厚度存在偏差，將直接影響相位延遲與反演出的 n、k；第三，單一 勞侖茲振子模型對於 180–300 cm-1 之完整響應可能仍過於簡化；將光譜依斜率變化分為三段並引入包絡線約束，可進一步改善擬合品質，說明光譜的區域特徵確實值得在模型中被單獨考慮。第四，原始 FTIR 光譜可能受基線漂移、參考光譜選取與儀器函數影響。

從研究意義來看，本方法最大的價值不在於一次即得到最終真值，而在於建立一個可重複、可檢驗、可逐步優化的反演框架。透過該框架，可以持續增加振子數、導入分段包絡線權重、放寬厚度條件，並視需要納入各向異性模型，以逐步提升擬合品質與材料參數可信度。

參考文獻

[1] M. R. Querry. Optical constants, Contractor Report CRDC-CR-85034(1985)

[2] A. B. Kuzmenko, “Kramers-Kronig constrained variational analysis of optical spectra,” Review of Scientific Instruments, vol. 76, no. 8, Art. no. 083108, 2005, doi: 10.1063/1.1979470.

[3] L. Duvillaret, F. Garet, and J.-L. Coutaz, “Highly precise determination of optical constants and sample

thickness in terahertz time-domain spectroscopy," Applied Optics, vol. 38, no. 2, pp. 409–415, 1999.

[4] T. D. Dorney, R. G. Baraniuk, and D. M. Mittleman, "Material parameter estimation with terahertz Time-domain spectroscopy," Journal of the Optical Society of America A, vol. 18, no. 7, pp. 1562–1571, 2001.

[5] G. Cataldo, J. A. Beall, H.-M. Cho, B. McAndrew, M. D. Niemack, and E. J. Wollack, "Infrared dielectric properties of low-stress silicon nitride," Optics Letters, vol. 37, no. 20, pp. 4200–4202, 2012, doi: 10.1364/OL.37.004200.

[6] S. Schöche et al., "Anisotropic optical constants of sapphire from infrared to vacuum-ultraviolet spectral regions," Journal of Applied Physics, vol. 113, Art. no. 013502, 2013.

報告型式：
□英文口頭報告競賽 (□無機材料， □有機材料)
□海報展示並參加壁報論文競賽(□無機材料， □有機材料)
■只參加海報展示 (■無機材料， □有機材料)

低碳可撓式乾法電極開發與高功率儲能電池性能驗證

曾豐順[1*]、李彥良[1]、黃群傑[1]、李乃維[1]、鄧禮濤[1]、王月利[2]、呂俊麟[2]
[1] 工業技術研究院 綠能與環境研究所
[2] 佑順發機械股份有限公司
fengshuntseng@itri.org.tw

摘要

隨著全球對減碳與環境議題的重視，再生能源快速發展，但其間歇性與不穩定性使儲能系統成為關鍵技術。現行電化學儲能包含鋰離子電池、鈉離子電池與液流電池等，已廣泛應用。另一方面，超級電容器具備高功率密度與長循環壽命，但能量密度不足，限制其應用範圍。為解決能量與功率之間的落差，鋰離子電容器（LIC） 作為混合型儲能元件應運而生。LIC 結合電池的法拉第反應與電雙層電容的電荷吸附機制，在維持高功率輸出的同時提升能量密度，並兼具快速充放電與長壽命優勢，已成為高功率儲能應用的重要發展方向。

本計畫整合超級電容器、鋰離子電容（LIC）與鈉離子電池技術，結合客戶第二代可撓式乾法電極設備，開發具高活物承載率、厚度可調與可撓曲特性之乾法膜電極，以取代高碳排之傳統濕式塗佈製程。技術核心包括透過物理混摻、機械壓延與乾燥製程，建立相容乾電極製程之 LIC 活性材料與結構設計，以及鈉離子電池電極配方與製程技術，並驗證其製程適應性與儲能穩定性。同時，結合國內廠商開發之軟式乾電極成型設備，建立完整電芯製作與測試平台，最終將試量產乾電極導入軟包儲能電芯進行性能驗證，推動低碳、高效率儲能技術之實際應用與商業化發展。

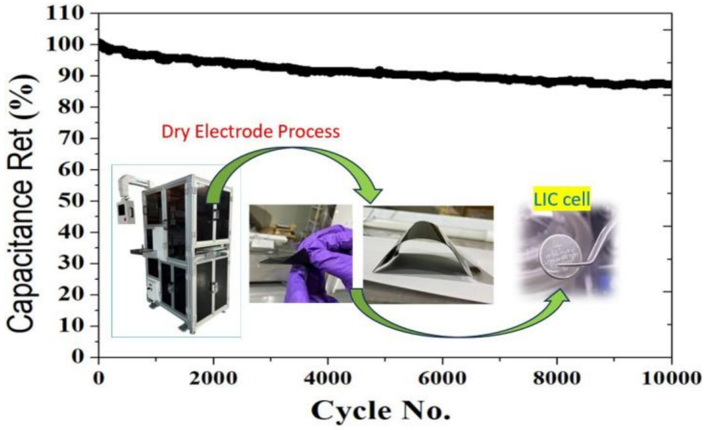

參考文獻

1. [1] Y. Qiao, Y. Jia, G. Ren,G. Long, K. Wang, Z. Luo, Y. Chen, Crystal-defect enriched graphite sieve for lithium-ion capacitors, Chemical Engineering Journal, Vol. 532, 15 March 2026.

報告型式：

□英文口頭報告競賽 (□無機材料， □有機材料)
☑海報展示並參加壁報論文競賽(☑無機材料， □有機材料)
□只參加海報展示 (□無機材料， □有機材料)

2026 功能性材料研討會暨國科會專題研究計畫成果發表會 – 南臺化材　Date ： 2026/5/29

定域化表面電漿共振感測滯留式概念探針加工探討

林峻立、賴孝武、吳勁葦*
南臺科技大學 化學工程與材料工程系
e-mail: wucw@stust.edu.tw

摘要

靜脈留置針 (IC) 主要應用於多次或連續注射，但重症監護患者在臨床病理檢驗中仍須多次採集血液檢體，可能造成發炎、醫源性貧血甚至靜脈塌陷，若在 IC 中加入即時血液監測功能，即可解決前述臨床重複採樣之困境。

本研究使用反射式光纖探針及光感測系統並以金屬奈米粒子的定域化表面電漿共振效應為原理進行生化檢測[2]，過去使用的光纖加工方法是將塗層及包層環狀去除，此法會造成光纖機械強度大幅下降，若要以 IC 作為載體進行侵入式檢測，光纖須有一定的機械強度。本研究開發雷射局部去塗層技術，旨在維持感測精度及靈敏度同時提高光纖的機械強度。

本研究中使用 CO_2 雷射切割機對光纖進行加工，將光纖單側的塗層及包層執行局部去除，並以化學自組裝的方式將金奈米粒子及氧化石墨烯修飾於裸露的核心 (core) 提昇檢測靈敏度[1]。實驗結果顯示，以雷射局部去塗層法加工之光纖在機械強度上較原先環狀去除法有顯著提昇，得以驗證此系統在進行侵入式檢測上具備可行性。除機械強度的驗證外，本研究初步於多濃度蔗糖水溶液中測試，數據證實在蔗糖水溶液折射率介於 1.333 至 1.373 時有良好的決定係數 ($R^2 > 0.99$)。

現階段實驗已驗證此系統於檢測應用的可行性，未來將對光纖探針的機械強度及不同生化樣品的感測效能持續優化。此外，由於實際應用須長時間置於生物體內，生物相容性亦是研究中須解決的問題。

參考文獻

Chen, C.H.; Chiang, C.Y.; Wu, C.W.; Wang, C.T.; Chau, L.K. Integrated Graphene Oxide with Noble Metal Nanoparticles to Develop High-Sensitivity Fiber Optic Particle Plasmon Resonance (FOPPR) Biosensor for Biomolecules Determination. MDPI AG. Nanomaterials. 2021, 11, 3, 635

Satija, J., Punjabi, N.S., Sai, V.V.R. *et al.* Optimal Design for U-bent Fiber-optic LSPR Sensor Probes. *Plasmonics* 9, 251–260 (2014). https://doi.org/10.1007/s11468-013-9618-7

報告型式：

□英文口頭報告競賽　(□無機材料，　□有機材料)
□海報展示並參加壁報論文競賽(□無機材料，　□有機材料)
□只參加海報展示　(□無機材料，　□有機材料)

不同 NiMg 莫耳比對 NiMg-LDH 作為超級電容器電極材料性能的影響

蔡明樺[1] 李颺[2] 傅湧竣[3] 鄒華軒[4] 劉政軒[5] 黃興正[6] 楊育承[7] 張育誠 8
逢甲大學材料科學與工程學系
D1291283@o365.fcu.edu.tw

NSTC 112-2221-E-035-017-MY3 and NSTC 113-2221-E-035-023-MY3

摘要

為突破層狀雙氫氧化物（Layered Double Hydroxides, LDHs）在實際儲能應用中導電性不足、活性位點易堆疊及離子傳輸效率受限等關鍵瓶頸，本研究採用簡便且具高效率的一步水熱法，直接於三維多孔發泡鎳基材上原位成長具分層級玫瑰球狀結構（Hierarchical Rose-Ball-Like Structure）的鎳鎂層狀雙氫氧化物（NiMg LDHs）無黏結劑電極。此設計不僅可避免傳統黏結劑造成的界面阻抗問題，更能有效提升電子傳導路徑與材料附著穩定性，展現優異的電化學應用潛力。為全面優化材料結構與儲能性能，本研究系統性探討鎳鎂莫耳比例、水熱反應溫度及反應時間三大關鍵製程參數。首先，在固定水熱溫度 120 ℃與反應時間 12 小時條件下，調控五組 Ni:Mg 莫耳比（1:1、3:2、2:3、4:1、1:4），分析雙金屬組成對晶相形成與電荷儲存行為之影響。其次，在固定反應時間與不同金屬比例條件下，比較 100 ℃、120 ℃與 140 ℃等不同水熱溫度對材料成核、生長速率及形貌演化之影響。最後，在最佳溫度與金屬比例基礎上，進一步調整水熱時間為 6、9 與 12 小時，以深入解析奈米結構形成機制及其對電化學動力學之影響。微觀結構分析（SEM/XRD）結果顯示，經最佳化製程後，可成功誘導超薄二維奈米片透過自組裝機制形成高度開放的三維玫瑰球狀架構。此特殊分層級結構具備豐富孔隙通道與大量暴露活性位點，可有效提升電解液滲透效率、增加比表面積，並大幅縮短離子擴散距離與電子傳輸路徑。電化學測試結果進一步證實，受惠於 Ni 與 Mg 雙金屬間的協同氧化還原反應，以及獨特三維花球狀形貌所帶來的快速傳輸優勢，該電極於 1 $A\cdot g^{-1}$電流密度下預期可展現 1000–2000 $F\cdot g^{-1}$之高比電容，同時具備低電荷轉移阻抗與優異倍率性能長時間。

參考文獻

[1] Xuejin Li, Dongfeng Du, Yu Zhang, Wei Xing, Qingzhong Xue, Zifeng Yan. (2017). Layered double hydroxides toward high-performance supercapacitors. Journal of Materials Chemistry A, 30(5), 15460-15485.

[2] Dongmei Zhai, Jie Wen, Qianyao Ding, Yanyan Feng, Wen Yang. (2023). Hierarchical design of NiCo-LDH NFs@Co(OH)$_2$ nanosheets supercapacitor electrode material with boosted electrochemical performance. International Journal of Hydrogen Energy, 48(27), 10108-10117.

[3] P.S. Dighe, R.S. Redekar, N.L. Tarwal, P.B. Sarawade. (2024). Design and development of the high-performance aqueous asymmetric supercapacitor based on the hydrothermally grown binder-less Ni-Co LDH nanosheets. Journal of Energy Storage, 88, 111467.

報告型式：

□英文口頭報告競賽 (□無機材料， □有機材料)
■海報展示並參加壁報論文競賽(■無機材料， □有機材料)
□只參加海報展示 (□無機材料， □有機材料)

Optimization of Annealing Temperature and Atmosphere for Chemical Bath Deposited SnO_2 Gate Dielectric in MOS Devices

Chih-Feng Yen, Yu-Min Chien*, Hung-Jiuan Tsai, Bo-Cheng Wei, Guan-Han Su[1]Affiliation
National Kaohsiung University of Science and Technology
*c112198132@nkust.edu.tw

Abstract

Tin oxide (SnO_2) is a promising material for gate oxide applications. In this study, SnO_2 thin films were synthesized on silicon substrates using chemical bath deposition. A two-stage annealing process was employed to optimize electrical properties: initially evaluating 180°C, 300°C, and 400°C in ambient air, followed by comparing air versus pure oxygen at 300°C and 400°C. At +5V bias, ambient samples (180°C, 300°C, 400°C) exhibited leakage current densities of 1.86×10^{-6}, 2.05×10^{-4}, and 1.32×10^{-4} A/cm^2, with interface state densities (D_{it}) of 1.58×10^{11}, 6.19×10^{11}, and 1.52×10^{12} eV^{-1}cm^{-2}, respectively. Under pure oxygen, 300°C and 400°C samples showed suppressed leakage of 4.97×10^{-6} and 9.19×10^{-6} A/cm^2, with improved D_{it} of 2.18×10^{10} and 2.56×10^{11} eV^{-1}cm^{-2}. These results confirm that oxygen-rich annealing repairs interface defects and enhances the reliability of Metal-Oxide-Semiconductor capacitors.

Experimental Method

In the initial preparation phase, a precursor solution is synthesized by mixing 0.25g of Urea with 0.15g of Tin(II) chloride dihydrate in 250 μL of Hydrochloric acid. To ensure a complete chemical reaction and a homogeneous mixture, the solution is subjected to continuous magnetic stirring at room temperature for 24 hours.The process then moves to film deposition. Prior to growth, the silicon wafer undergoes a standard cleaning protocol to eliminate surface contaminants. Using the Liquid Phase Deposition technique, the cleaned substrate is immersed in the precursor solution maintained at 75°C, allowing the SnO_2 thin film to grow on the surface. Following deposition, the samples are placed in a furnace for an annealing treatment at 400°C for one hour, a critical step for improving the crystallinity and structural integrity of the films.The final stage involves device formation and analysis. Metal electrodes are deposited on both the front and back sides of the wafer via evaporation, followed by a thermal process to ensure proper Ohmic contact. For characterization, Scanning Electron Microscopy is employed to observe the surface morphology and microstructure. Finally, the electrical properties of the fabricated devices are evaluated through I-V (Current-Voltage) and C-V (Capacitance-Voltage) measurements to assess their performance.

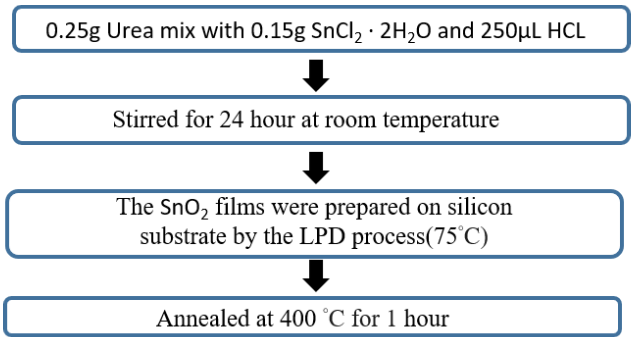

Figure 1.Experimental flowchart for the preparation of SnO_2 thin films via the Liquid Phase Deposition process.

Results and Discussion

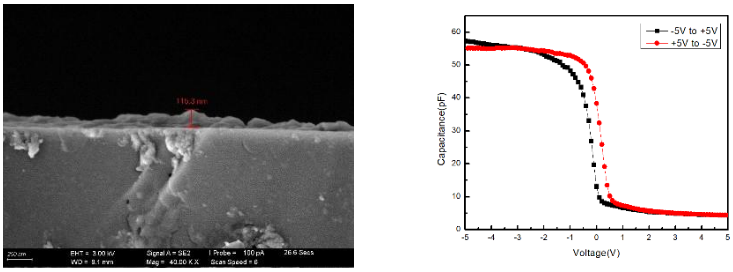

(a) SnO_2 for Air 180°C

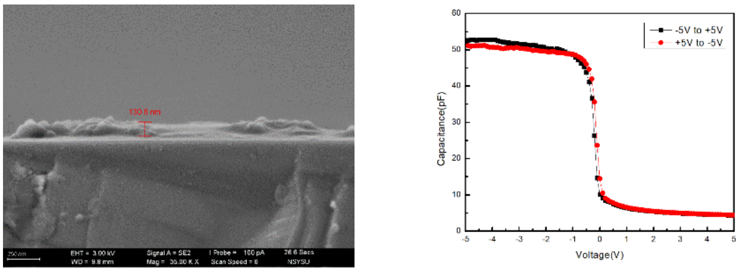

(b) SnO_2 for Air 300°C

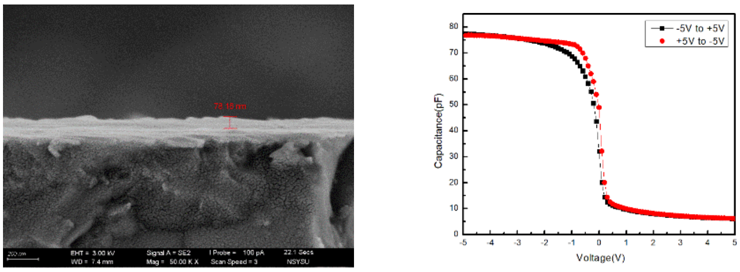

(c) SnO_2 for O_2 300°C

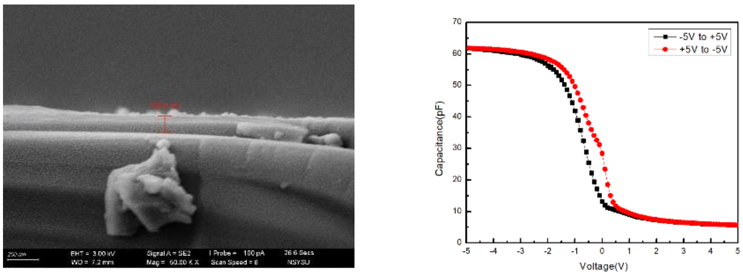

(d) SnO_2 for Air 400°C

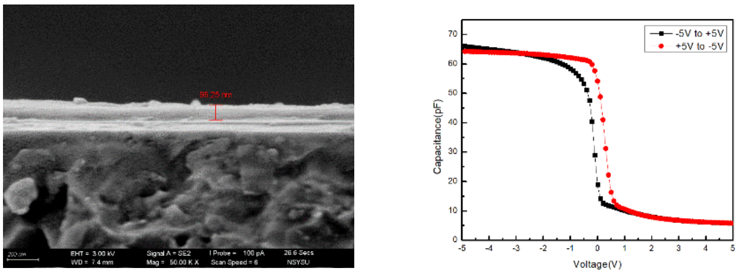

(e) SnO_2 for O_2 400°C

Figure 2.The left column shows the FE-SEM observation results of SnO_2 films growth behavior. The right column is the CV characteristics curve. (a) SnO_2 for Air 180°C, (b) SnO_2 for Air 300°C, (c) SnO_2 for O_2 300°C, (d) SnO_2 for Air 400°C and (e) SnO_2 for O_2 400°C.

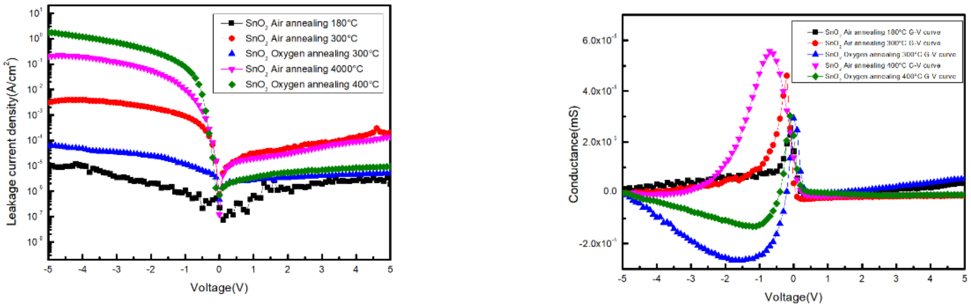

Figure 3. Electrical characteristics of SnO_2 thin films under various annealing conditions (Air 180°C, Air 300°C, O_2 300°C, Air 400°C, O_2 400°C): (a) IV characteristic curve and (b) GV characteristic curve.

Table 1. Device parameters of SnO_2 under different annealing conditions.

	Air annealing 180℃	Air annealing 300℃	Oxygen annealing 300℃	Air annealing 400℃	Oxygen annealing 400℃
C_{FB} (pF)	27.8	26.01	32.7	28.55	30.08
C_{OX} (pF)	55.1	51.2	76.8	61.9	64.2
V_{FB} (V)	0.17	-0.11	0.08	-0.03	0.31
ΔV_{FB} (V)	0.38	0.08	0.09	0. 55	0. 41
Thickness (nm)	115.3	130.8	78.16	109.4	98.25
EOT (nm)	53.59	51.01	30.48	42.67	38.31
D_{it} ($cm^{-2}eV^{-1}$)	1.58×10^{11}	6.19×10^{11}	2.56×10^{11}	7.97×10^{11}	2.89×10^{11}
N_{OM} ($* \ 10^{10}\ cm^{-2}$)	18.5	3.62	6.11	30.0	23.3
Q_{eff} ($* \ 10^{11}\ C/cm^{-2}$)	-4.77	-3.16	-6.03	-4.26	-6.35
Leakage current density (A/cm^2) @ 5V	1.89×10^{-6}	2.05×10^{-4}	4.97×10^{-6}	1.32×10^{-4}	9.19×10^{-6}

Conclusion

While low-temperature annealing yields low leakage current, it suffers from electrical instability; conversely, high-temperature annealing improves stability but increases leakage and induces film degradation. Our findings demonstrate that optimal thermal energy combined with sufficient oxygen supply is key to enhancing film quality. Specifically, 300°C oxygen annealing emerged as the ideal parameter, effectively reducing leakage current density and film thickness (EOT) while maintaining superior electrical stability and high capacitance.

References

[1] Hlali, S., Fargi, A., & Hizem, N. (2017). High temperature and voltage dependent electrical and dielectric properties of TiN/Al_2O_3/p-Si MIS structure. Journal of Alloys and Compounds, 713, 194-203.

[2] St. John, N. (2023, November 1). MOSFET structure and operation for analog IC design. All AboutCircuits.
[3] Khallaf, H., Chen, C.-T., Chang, L.-B., Lupan, O., Dutta, A., Heinrich, H., Haque, F., del Barco, E., & Chow, L. (2012). Chemical bath deposition of SnO_2 and Cd_2SnO_4 thin films. Applied Surface Science, 258(16), 6069–6074.
[4] J. Robertson, "Band structures and band offsets of high K dielectrics on Si," Applied Surface Science, vol. 190, no. 1-4, pp. 2-10, May 2002.
[5]Source: Adapted from S. M. Sze, Physics of Semiconductor Devices.
[6]Barnaby, H. J. (2006). Total-ionizing-dose effects in modern CMOS technologies. IEEE Transactions on Nuclear Science, 53(6), 3103-3121.

Presentation type：

☐ English oral competition (☐ inorganic materials, ☐ organic materials)
☐ Poster competition (☐ inorganic materials, ☐ organic materials)
■ Exhibition only (■ inorganic materials, ☐ organic materials)

呼吸感測材料元件製程

徐呈和
高雄科技大學
e-mail:e97325461577@gmail.com

摘要

本研究旨在探討多閘極氮化物/氧化物異質結構元件之製作與其在氣體感測及人體呼吸監測之應用。隨著智慧醫療與穿戴式裝置的發展，如何以低成本且高靈敏度之方式即時監測人體生理訊號，已成為重要研究方向。本研究利用濺鍍製程於矽基板上製作多層半導體薄膜，設計三種不同結構之感測元件，並進行電性與氣體感測特性分析。

在元件製作方面，於矽基板上沉積 n 型氮化鋁作為緩衝層，再分別沉積 p 型氮化銦與 p 型氧化銦形成異質接面。為提升元件控制能力，設計多閘極結構，並以二氧化矽作為絕緣層，搭配鋁電極形成源極與汲極。所有薄膜皆於室溫條件下進行濺鍍製程，以確保製程簡單且具可重現性。

在量測方法方面，本研究除了進行基本電性量測外，亦導入霍爾量測分析材料之載子濃度、遷移率與導電型態， 以深入探討薄膜材料之電性特性。並進一步量測 D-S、D-G1、D-G2 及 D-G3 之電阻、電容、電感及電流-電壓特性，分析多閘極控制下之載子傳輸行為。此外，透過建立濕度與氧氣氣氛環境，觀察元件在不同氣體條件下之電性變化。

由於氮化物與金屬氧化物半導體具備良好氣體吸附特性，當環境濕度或氧氣濃度變化時，將影響材料表面電荷分佈與載子傳輸機制，進而改變元件導電特性。實驗亦將元件應用於胸腔呼吸感測，透過人體呼吸過程中濕度與氣體變化，量測其即時電訊號響應。結果顯示元件對呼吸週期具有穩定且明顯之響應能力，可有效區分吸氣與呼氣過程。

比較不同材料結構之元件表現可知，氧化銦結構在氣體感測靈敏度上較佳，而氮化銦結構則具有較穩定之電性表現。透過多閘極設計與異質結構整合，可有效提升元件整體性能。本研究開發多閘極異質結構感測元件，並透過霍爾量測與電性分析驗證其材料特性，進一步證明其於氣體感測與呼吸監測之應用潛力。

報告型式：

英文口頭報告競賽　(□無機材料，　□有機材料)

海報展示並參加壁報論文競賽(□無機材料，　□有機材料)

☑只參加海報展示(☑無機材料，　□有機材料)

鈦金屬陽極氧化之顏色機制與電壓及電解質影響探討

[1] 王正全、[2] 王蕙、[2] 方家齊
[1] 工業技術研究院、[2] 國立彰化女子高級中學
chengchuan@itri.org.tw

摘要

本研究系統性探討了鈦金屬在陽極氧化過程中，表面二氧化鈦(TiO2)薄膜的生成機制及其光學顏色規律。研究主要探討施加電壓(10V 到 80V)與電解質化學性質(酸性與鹼性環境)對氧化膜微觀結構與色彩表現的交互影響。實驗過程採用定電壓法進行陽極氧化電解，並透過電流之衰減，以確認膜層生長的動力學特徵。研究結果顯示，氧化膜厚度與施加電壓呈現極佳的線性相關，其生長速率推估約為 1.3~1.6nm/V，這證實了透過電壓調控能精準控制薄膜在 15nm 至 125nm 之間。隨著膜厚增加，反射光譜產生的相長干涉位移(Constructive Interference Shift)，使鈦金屬表面呈現出黃、紫、藍、綠等干涉色。此外，本研究導入 CIELAB(L*a*b*)色彩空間對鈦陽極薄膜進行定量評估，結果顯示，電解質的酸鹼特性對色彩飽和度(chroma)具備顯著影響：在鹼性溶液中生成的氧化膜，其色度座標分布範圍較廣，呈現出較高的色彩純度與明亮度；相較之下，酸性環境下的成色則偏向灰暗，此差異推測與不同電解質對氧化膜緻密性及表面粗糙度的修飾作用有關。

實驗結果

透過顏色波長推算厚度 $tt = \frac{\lambda\lambda_{cccccccccc}}{44nn}$，並繪製操電壓與厚度關係。

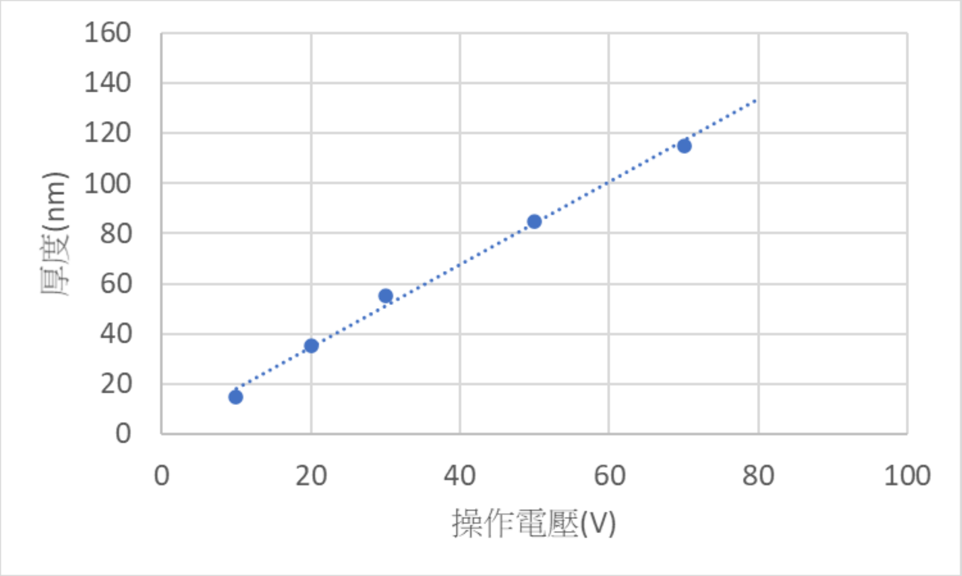

圖 1. 鈦氧化層厚度與電壓關係

參考文獻

1. 賴耿陽(1990)，金屬鈦理論與應用，復漢出版社。
2. 王正全、顏佳瑩、呂春福，金屬陽極氧化處理技術與半導體設備零件應用，工業材料雜誌，464 期，65-73 (2025)。
3. 鈦工房有限公司網頁，https://www.titan-innovation.com/en/

報告型式：

□英文口頭報告競賽 (□無機材料， □有機材料)
□海報展示並參加壁報論文競賽(□無機材料， □有機材料)
■只參加海報展示 (■無機材料， □有機材料)

黑色二氧化鈦複合石墨烯量子點與氮摻雜石墨烯量子點之合成及其光催化性能研究

戴瑞君、賴孝武*
南臺科技大學 化學工程與材料工程系
swlai@stust.edu.tw

摘要

本研究採用缺陷工程策略製備黑色二氧化鈦（Black TiO_2），並進一步引入石墨烯量子點（GQD）與氮摻雜石墨烯量子點（NGQD）進行複合修飾，探討其結構特性與光催化性能之影響。

FTIR 分析結果顯示量子點已成功負載於 TiO_2 表面；XRD 分析指出各樣品皆維持銳鈦礦相結構，且未觀察到其他雜相生成。XPS 分析進一步證實黑色 TiO_2 中存在氧空缺與 Ti^{3+} 物種，顯示缺陷成功導入；於 NGQD 複合材料中亦可辨識多種氮鍵結型態，顯示氮元素參與界面電子結構調控。UV-Vis 與 Tauc plot 分析結果顯示黑色TiO_2出現吸收邊紅移與能隙縮小現象，而經量子點修飾後，其可見光吸收能力進一步提升。

光催化實驗以亞甲基藍（MB）為目標污染物，結果顯示缺陷濃度對降解效率具有顯著影響。其中 B24 樣品於 120 分鐘之降解率達 27.94%；相較之下，缺陷程度較高之 B27 與 B30，其降解率分別為 16.38% 與 9.82%， 呈現下降趨勢。此結果顯示適度缺陷有助於促進光生載子分離，而過高缺陷濃度則可能增加電子電洞復合機率， 進而降低整體光催化效率。

綜合而言，缺陷工程與量子點修飾可有效調控 TiO_2 之電子結構與表面特性，進而提升其可見光響應與光催化表現。本研究提供可見光活性光催化材料之設計策略，對環境淨化應用具有參考價值。

關鍵字：黑色二氧化鈦、石墨烯量子點、氮摻雜、缺陷工程、光催化

參考文獻

[1] Shafaee, M., et al. (2018). "TiO_2 nanoparticles and TiO_2@ graphene quantum dots nancomposites as effective visible/solar light photocatalysts." Journal of Photochemistry and Photobiology A: Chemistry 357: 90-102.

[2] Kalluri, A., et al. (2018). "Graphene Quantum Dots: Synthesis and Applications." Methods Enzymol 609: 335-354.

[3] Li, B., et al. (2021). "Review of performance improvement strategies for doped graphene quantum dots for fluorescence-based sensing." Synthetic Metals 276.

報告型式：

□英文口頭報告競賽 (□無機材料， □有機材料)
☑海報展示並參加壁報論文競賽(☑無機材料， □有機材料)
□只參加海報展示 (□無機材料， □有機材料)

週期性偏壓對「金屬-絕緣層-金屬」複合材料的電阻影響

陳穗斌
國立嘉義大學電子物理學系
spchen@mail.ncyu.edu.tw

摘要

我們所研究的「金屬-絕緣層-金屬」(M_1-I_2-M_3)複合材料的基本結構如圖一，對應的 potential profile 如圖二。使用的相關參數如下，左邊金屬位能：U_{M1}=0 eV，右邊金屬位能：U_{M3}=0 eV，中間絕緣體的厚度：d=8Å，中間絕緣體的位能障：U=4 eV，電子入射能量：E=2.5 eV。

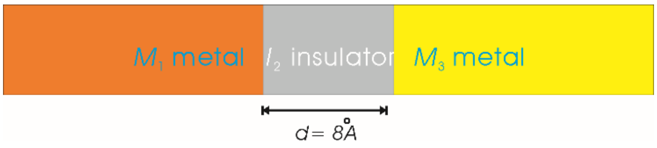

圖一結構示意圖

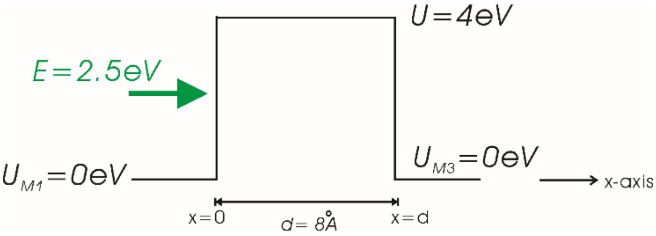

圖二 potential profile 的簡圖

我們要探討的是：在「金屬-絕緣層-金屬」(M_1-I_2-M_3)複合材料中，在絕緣層 I_2 外加具週期性的偏壓(圖三)，對於穿隧電阻的影響。

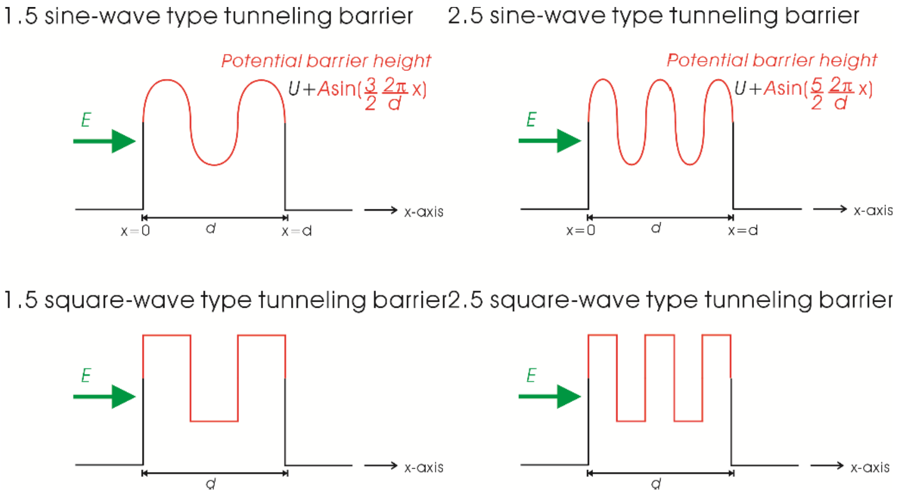

3.5 sine-wave type tunneling barrier　4.5 sine-wave type tunneling barrier

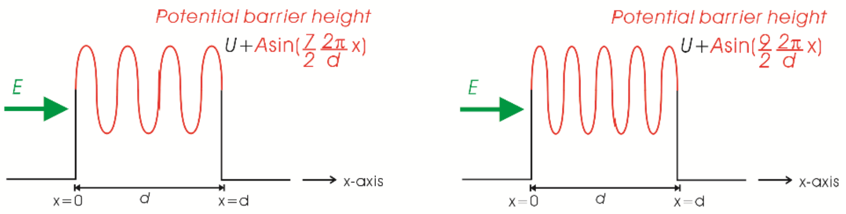

3.5 square-wave type tunneling barrier　4.5 square-wave type tunneling barrier

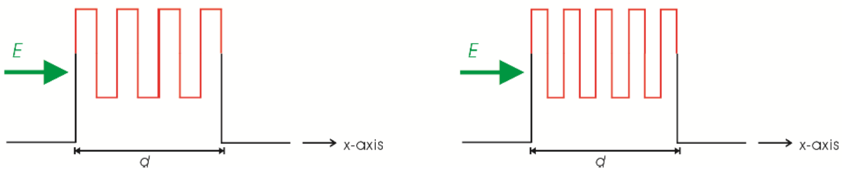

5.5 sine-wave type tunneling barrier　6.5 sine-wave type tunneling barrier

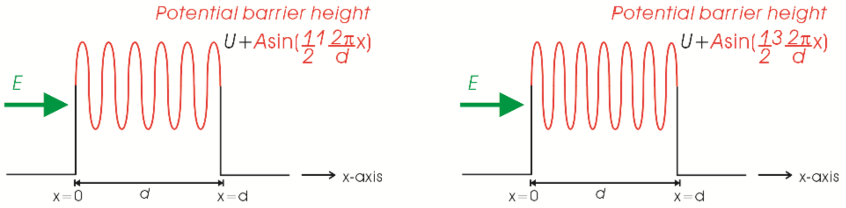

5.5 square-wave type tunneling barrier　6.5 square-wave type tunneling barrier

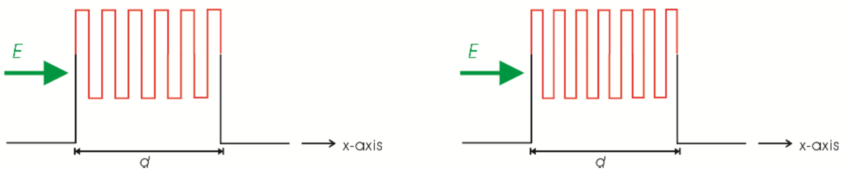

圖三 施加週期性偏壓的絕緣層 potential profile 簡圖

我們採用研究的理論方法為 Transfer Matrix Method，求解的方式是：把絕緣層 I_2 區域中的位能障(potential barrier)切割成許 n 段可以計算的階梯位能障(step potential barrier)的相加。然後，利用 MatLab 將其運算撰寫為程式，得到對應的數值結果。我們發現可以利用有無施加週期變化的偏壓，來改變電阻。在電子能量是 3.7 eV 時， 改變 10%；在電子能量是 4.5eV，改變達 100%。此外，若加入界面的影響，在電子未散射下，不會有明顯的改變。

參考文獻

1. M. Julliere, Phys. Lett. 54 (1975) 225.
2. S. Yuasa, T. Nagahama, Y. Suzuki, Science 297 (2002) 234.
3. S. Zhang, P.M. Levy, Phys. Rev. Lett. 81 (1998) 5660.
4. S.-P. Chen, C.-R. Chang, IEEE Trans. Magn. 45 (2009) 2410.

5. S.-P. Chen, J. Appl. Phys. 107 (2010) 09C716.
6. S.-P. Chen, Thin Solid Films 519 (2011) 8215.
7. J.C. Slonczewski, Phys. Rev. B 39 (1989) 6995.
8. J. Q. You, L. Zhang, and P. K. Ghosh, Phys. Rev. B 52 (1995) 17243.
9. J. D. Burton and Evgeny Y. Tsymbal, Physical Review B 93 (2016) 024419.
10. Xiaohong Zheng, Shili Yang, Zhifan Zheng, Chun-Sheng Liu, Weiyang Wang, and Lei Zhang, Appl. Phys. Lett. 125 (2024) 223503.
11. Yingmei Zhu, Shiqi Liu; Qirui Cui, Jiawei Jiang; Hongxin Yang, Tiejun Zhou, Bo Liu, Appl. Phys. Lett. 127 (2025) 082401.

報告型式：

□英文口頭報告競賽 (□無機材料， □有機材料)
□海報展示並參加壁報論文競賽(□無機材料， □有機材料)
■只參加海報展示 (■無機材料， □有機材料)

sol-gel 合成矽磷酸鈣

謝家翔、莭志倫、陳孟賢、黃子芸、賴孝武*

南臺科技大學 化學工程與材料工程系

e-mail swlai@stust.edu.tw

摘要

本研究利用 sol-gel 法製備聚乙二醇（Polyethylene Glycol, PEG）改質之 $Ca_5(PO_4)_2SiO_4$（CPS）生醫陶瓷，探討 PEG 添加量與燒結溫度對材料結晶性、微結構及化學組成之影響。實驗中以 TEOS、 P_2O_5 與 $Ca(NO_3)_2 4H_2O$ 作為前驅物，加入不同含量 PEG400 後調整 pH 值至 10–10.5，經 aging、乾燥後分別於 450°C、500°C 與 600°C 燒結。XRD 分析結果顯示，450°C 時材料仍具有部分非晶特性，但添加 5%PEG 後於 $2\theta \approx 26\text{–}32^\circ$ 出現較明顯繞射峰，顯示適量 PEG 有助於晶體生成與結晶性提升；隨燒結溫度提升至 600°C，繞射峰逐漸尖銳化，顯示材料結晶度提高且晶相趨於穩定。SEM 結果顯示，隨燒結溫度提升，材料表面逐漸緻密化並形成較完整微結構。EDX 分析證實材料中 Ca、P、Si 元素均勻分布，而 XPS 分析則確認材料中存在 phosphate 結構之 P–O 鍵結。

綜合結果顯示，PEG 改質可有效改善 CPS 生醫陶瓷之結晶行為與微結構穩定性，其中以 5% PEG 具有較佳改質效果；此外，提高燒結溫度亦有助於材料晶相形成與結晶性提升。此研究結果顯示 PEG 改質 CPS 生醫陶瓷具潛力應用於骨修復與組織工程材料。

關鍵字：Sol-gel、$Ca_5(PO_4)_2SiO_4$、PEG、XRD、生醫陶瓷

參考文獻

(1)Polyethylene Glycol (PEG) Modified Porous Ca5(PO4)2SiO4 Bioceramics: Structural, Morphologic and Bioactivity Analysis 2020, 10(6), 538

報告型式：

□英文口頭報告競賽 (□無機材料， □有機材料)

□海報展示並參加壁報論文競賽(□無機材料， □有機材料)

☑ 只參加海報展示 (☑ 無機材料， □有機材料)

碘化銀薄膜成長及光電特性參數分析

張程傑 ^{1}、王麒兆 ^{2}、林得裕 ^{3,*}、石豫臺 ^{4}
^{123} 電子工程學系,國立彰化師範大學,彰化市師大路二號
^{4} 物理系,國立彰化師範大學,彰化市進德路一號
dylin@cc.ncue.edu.tw(林得裕)

NSTC-114-2221-E-018-013

摘要(Abstract)

本研究以低成本之氣相碘化法成功製備高品質 AgI 薄膜，並與 P 型 Silicon 基板形成 n-AgI/p-Si 異質結構二極體。結構分析結果顯示，所成長之 AgI 薄膜為 β 相六方晶系，具有良好結晶性，且元素比例接近理論值 1：1，證明此製程可有效成長品質穩定之 AgI 薄膜。光學與電性分析結果顯示，AgI 之能隙約為 2.8 eV，並確認其為 N 型半導體，具有作為光電材料之潛力。在元件特性方面，n-AgI/p-Si 異質結構二極體具有良好的整流特性，且於 AM1.5 模擬太陽光照射下，在 0 V 條件下即可產生光電流，顯示元件具有自供電光響應能力。進一步之光電量測顯示，n-AgI/p-Si 異質結構在無外加偏壓下仍具有良好的光響應表現，其轉角頻率可達 1 kHz，顯示元件具備一定之響應速度與應用潛力。整體實驗結果而言，本研究證實 AgI 薄膜不僅可透過簡易製程獲得良好薄膜品質，我們成長了 AgI 薄膜晶體，並成功與 P 型半導體 Silicon 基板形成異質結構二極體，透過實驗證明異質結構二極體擁有良好的異質接面。

一、簡介

台灣的半導體產業長期以矽基積體電路製程為核心，相關技術的持續精進也是維持競爭力的重要基礎。然而，矽屬於間接能隙材料，輻射復合效率偏低，使其在發光與部分光電功能元件的應用上受到先天限制。為突破此瓶頸，近年來二維材料（2D materials, 2DMs）因其層狀結構以凡得瓦力（van der Waals force）作用堆疊，且表面缺乏懸空鍵結，能有效降低表面復合與暗電流等問題，而逐漸成為與矽互補的關鍵材料。藉由將具有不同能隙與載子傳輸特性的二維材料彈性整合至矽或其他基板上，可在維持製程成本優勢的同時，實現高性能且涵蓋紅外至可見光的寬頻光感測元件（photodetectors, PDs）。因此，二維材料與矽的異質整合提供了一條兼顧成本、製程相容性與光電性能的可行路徑，也促使寬頻、高速與低功耗光感測元件成為近年重要的研究方向。

近年來，AgI 薄膜及其異質結構在光催化應用（如廢水處理與污染物分解）上展現出良好潛力，並被視為可在太陽光條件下驅動產氫與 CO_2 還原的候選材料。雖然 AgX（X＝Cl、Br、I）材料在光催化領域備受關注，但其在光照下常出現光分解現象，導致效能衰退且不利於回收，因此如何透過材料改質提升其穩定性，成為重要研究方向。[1]AgI 具有合適的能帶結構，其能隙約為 2.8 eV，且導帶電位相對較負，當其與其他材料形成異質界面時，有助於促進光生載子的分離效率並提升反應活性。AgI 不僅具備合適的能隙、良好的能帶結構與異質整合潛力[2]，亦可透過多樣化製程進行薄膜成長，例如氣相碘化法[3],[4]、熱蒸法、反應性濺鍍法、旋塗法、噴塗法及噴墨印刷等。[5]因此，AgI 為兼具材料特性、製程彈性與應用潛力的重要候選材料，值得進一步探討其薄膜製備、結構特性及在光電與能源元件上的應用表現。

二、實驗方法

本研究以氣相碘化法製備 AgI 薄膜，先利用熱蒸鍍在玻璃基板與 p-type Si 基板上沉積 Ag 薄膜，再將樣品置於含碘的密閉容器中於室溫反應，使 Ag 薄膜轉化為 AgI 薄膜。接著以 p-type Si 為基板製作 n-AgI/p-Si 異質結構二極體，並於背面蒸鍍鋁電極完成元件製作。薄膜製備完成後，利用 SEM 觀察表面與截面形貌，並以 EDS 分析元素比例；再透過 XRD、Raman、XPS 與 UPS 分析 AgI 薄膜之晶體結構、鍵結狀態與能帶特性，並配合 UV-Vis 與 霍爾量測確認其光學能隙、載子型態與電性特性。在元件量測方面，使用 I–V 量測分析 n-AgI/p-Si 異質結構之整流與光伏特性。此外，由於 n-AgI/p-Si 元件在照光下於 0 V 即可產生光電流，因此進一步進行持續性光電導（PPC）、變頻光響應與變光功率量測，以分析其光響應速度與光電特性。

三、結果與討論

3.1 材料結構與晶體特性分析

(1) SEM 表面形貌分析

圖一為 AgI 薄膜正面的 SEM 薄膜影像，看到 P-Type 的 Si 基板上，生長出的 AgI 薄膜存在些許孔隙，但可看到薄膜的結晶品質也相當良好。

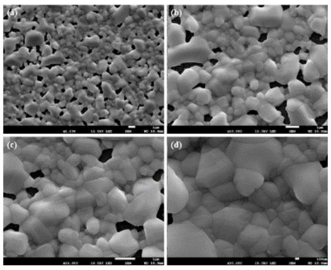

圖一：n-AgI/p-Si 薄膜 SEM 影像，(a)5K，(b)10K，(c)15K，(d)30K

(2) EDS 樣品組成分析

可看到其原子比分別為 Ag 53.45 %、I 為 46.55 %，其比例也非常接近理論值 1：1 的化學計量比，也進一步的呈現我們所生長的 AgI 的優勢之一，製程相對容易、低成本，卻能擁有品質不錯的薄膜的優勢。

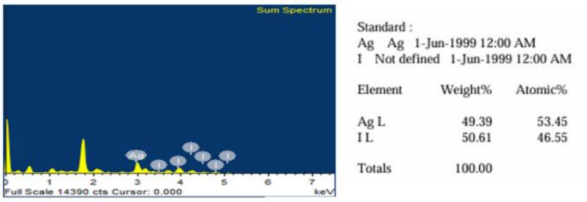

Standard :
Ag Ag 1-Jun-1999 12:00 AM
I Not defined 1-Jun-1999 12:00 AM

Element	Weight%	Atomic%
Ag L	49.39	53.45
I L	50.61	46.55
Totals	100.00	

圖二：AgI 薄膜 EDS 元素比例分析

(3) Raman 散射光譜分析

AgI 在拉曼 112cm^{-1} 處有明顯拉曼訊號峰，與 Delaney, M. J 等人對 AgI 的研究相符，此峰 Ag-I 的振動所產生，振動模式為 TO(橫向光學)的振動模式。[6]

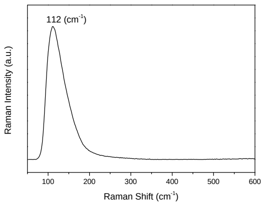

圖三：AgI 拉曼光譜圖

(4) XRD 晶體結構分析

生長於玻璃基板與矽基板上的 AgI 薄膜 XRD 數據，可看出 AgI 即使在室溫下生長，也能成為結晶性良好的薄膜，而後我們分別將數據與 AgI 的三種不同相的 JCPDS 標準數據進行比對，比對後可確認本論文生長出的 AgI 為 β 相，且並無雜相或是混合相的峰存在。

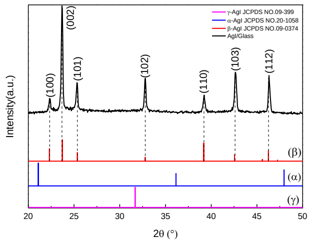

圖四：AgI XRD 和各面相 JCPDS 標準數據[7]

(5) X 射線光電子能譜儀分析

下圖為 AgI 的 XPS 全譜圖，透過全譜圖可發現在 619 eV 和 630 eV 有非常強的特徵峰，這兩個特徵峰為 I 3d 自旋軌道分裂出的兩個峰，透過這一發現可判定再 AgI 當中是有 I 的存在，而 Ag 3d 的特徵峰會出現在 368 eV 和 374 eV，透過量測出的 XPS 全譜圖，觀測到有明顯兩特徵峰，與 S. Sarojini 等人對 AgI 的 XPS 研究結果相符，因此判定本論文生長的 Ag 跟 I 是有成功鍵結。[8]

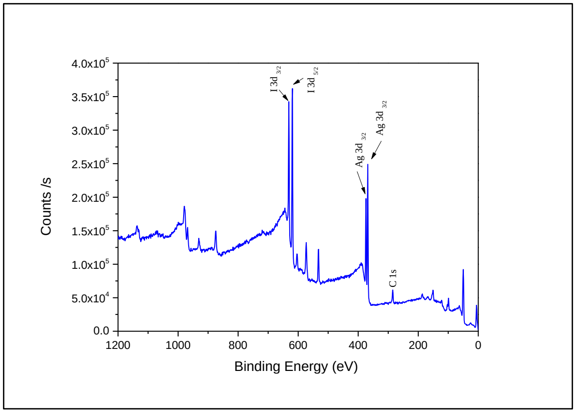

圖五：AgI XPS 全譜圖

3.2 材料光學電性分析

(1) 電流-電壓特性曲線分析

為生長於玻璃基板的 AgI 的電流-電壓特性量測，透過數據可看到對其做照光、不照光的電流-電壓量測，黑色的數據為不照光時的電流數據，紅色的數據為照光下的電流，發現 AgI 對光有明顯反應。

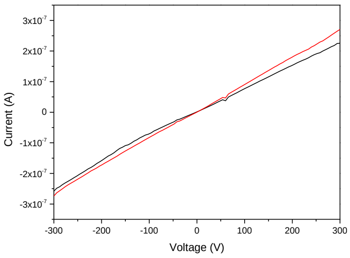

圖六 ：AgI/Glass 照光、不照光 I-V 量測

(2) 吸收光譜分析

下圖，呈現的分別是 n-AgI 的穿透和吸收光譜，透過穿透、吸收譜確認本論文生長的 AgI 能隙為 2.8eV

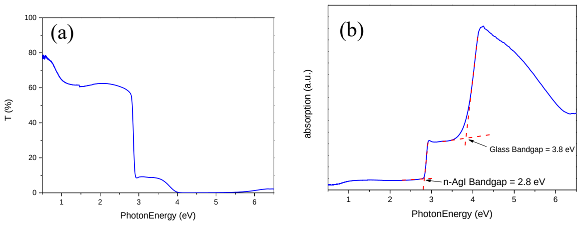

圖七: (a) n-AgI/Glass 穿透光譜(b) n-AgI/Glass 吸收光譜

(3) 光致發光(Photoluminescence, PL)分析

透過 PL 數據可看到位於 427nm 有非常明顯的特徵峰，此峰為 AgI 發出的光，並利用 1240/427nm 公式計算出 AgI 的能隙位於 2.9eV，此結果與上方的穿透、吸收數據得到的數據非常相近，因此可確定本論文生長出的 AgI 能隙為 2.9eV，屬於寬能隙的半導體。

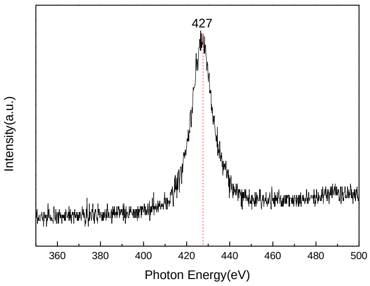

圖八: AgI PL 光致發光量測數據

3.3 異質結構二極體特性分析

(1)電流-電壓特性曲線分析

n-AgI/p-Silicon 為異質結構二極體，照光/不照光的 I-V 曲線，也同樣具有良好的二極體整流特性。

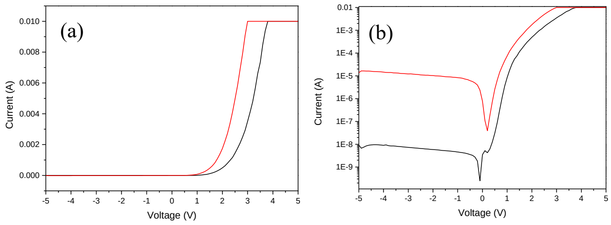

圖九: n-AgI/p-Silicon 異質結構二極體，(a)照光/不照光 I-V 曲線，(b)照光/不照光電流以對數尺度表示

(2) 太陽能電池參數分析

表一：太陽能電池參數量測結果。

	n-AgI / p-Silicon
V_{mp}（V）	0.08
I_{mp}（A）	3.04028E-6
P_{max}（W）	2.4322E-7
V_{oc}（V）	0.27
I_{sc}（A）	-6.857982E-6
Sample Area（cm²）	0.0076
Light Power（mW/cm²）	100
Fill Factor（%）	13.1315
Efficiency η（%）	0.03

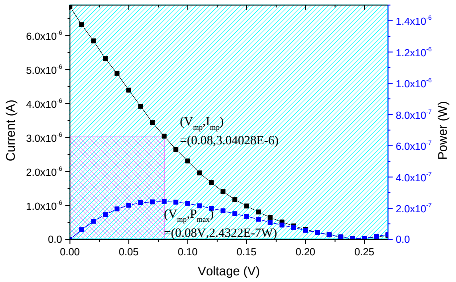

圖十：n-AgI/p-Silicon 電流對功率做雙 Y 圖

(3) 持續性光電導分析

透過持續性光電導的量測，可量測 n-AgI/p-Silicon 異質結構對雷射光的響應速度，此實驗是量測當樣品照射到雷射光時摻生的光電流，當光電流到飽和時，即為上升時間(Rise Time)，當下降至起始暗電流值則為下降時間(Fall Time)。使用 808nm 的雷射光進行持續性光電導分析的量測，由於 AgI/p-Si 異質結構在偏壓為零時，有出電的現象，因此樣品皆在不施加外部偏壓的情況下進行量測。

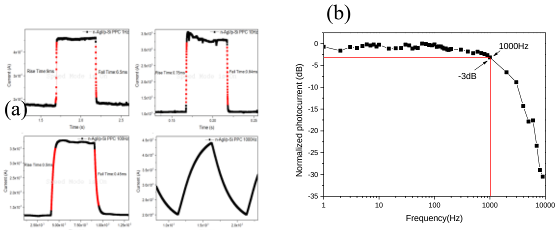

圖十一：(a) n-AgI / p-Silicon 分別在 1 Hz、10 Hz、100 Hz 及 1 kHz 的量測圖(b) n-AgI/p-Si 變頻 PC。

表二：n-AgI / p-Silicon 上升時間與下降時間數據。

Frequency（Hz）	**Rise Time（s）**	**Fall Time（s）**
1Hz	9 ms	6.5s
10Hz	0.75ms	0.84s
100Hz	0.5ms	0.45s
1KHz		

(4) 變光功率光響應分析

圖為 n-AgI/p-Si 異質結構的變光功率響應實驗數據，實驗時分別會使用三個 ND Filter，分別是：無衰減、衰減 10 倍以及衰減 100 倍。

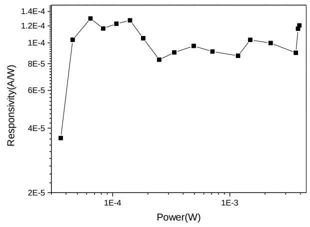

圖十二：n-AgI/p-Si 變光功率響應數據

四、結論

本研究以室溫氣相碘化法成功製備 AgI 薄膜，展現低成本與簡化製程之優勢。材料分析結果顯示，所製備 AgI 薄膜具有良好結晶性，雖表面仍存在部分孔隙且膜厚分布略不均勻，但仍可形成約 700 nm 之薄膜。EDS 與 XPS 分析顯示 Ag 與 I 元素比例接近 1：1，與理論化學計量比相符；XRD 結果則證實所生長之 AgI 為六方晶系 β-AgI，且其晶體結構與文獻結果一致。光學量測結果顯示 AgI 為寬能隙半導體，其能隙約介於 2.8 – 2.9 eV。元件方面，AgI 與 p-Si 基板可成功形成 n-AgI/p-Silicon 異質結構二極體，並展現良好的整流與光響應特性。於照光條件下，元件在 0 V 下即可產生光電流，顯示其具備自供電光響應能力；此外，持續性光電導與變頻量測結果亦顯示元件具備一定之光響應速度與應用潛力。綜合而言，本研究證實室溫製備之 AgI 薄膜在材料特性與異質結構光電元件應用上皆具有良好發展潛力。

References

[1] X.-J. Wen et al., “Recent developments on AgI-based heterojunction photocatalytic systems in photocatalytic application,” Chemical Engineering Journal, vol. 383, pp. 123083, 2020.

[2] W. Zeng et al., “AgI–Ag2S heterostructures for photothermal conversion and solar energy harvesting,” Journal of the Taiwan Institute of Chemical Engineers, vol. 95, pp. 273-280, 2019.

[3] D. M. Smyth and M. Cutler, “Tarnishing reactions of silver in iodine atmospheres,”Journal of The Electrochemical Society, vol. 106, pp. 107-112, 1959.

[4] S. K. Bose and S. C. Sircar, “Estimation of hole conductivity of AgI through tarnishing studies of silver in iodine vapour at about room temperature,” Journal of Materials Science, vol. 11, pp. 129-133, 1976.

[5] L. Hu et al., “In-situ fabrication of AgI–BiOI nanoflake arrays film photoelectrode for efficient wastewater treatment, electricity production and enhanced recovery of copper in photocatalytic fuel cell,” Catalysis Today, vol. 355, pp. 379-390, 2020.

[6] M. J. Delaney and S. Ushioda, “Raman spectra of the superionic conductors AgI and RbAg4I5,” Superionic Conductors, Boston, MA, USA: Springer US, pp. 218–219, 1976.

[7] L. Luo, R. Liang, J. Zhong, and J. Li, “Polyethylene glycol assisted preparation of AgI with enhanced photocatalytic activity,” Solid State Sciences, vol. 116, pp. 106610, 2021.

[8] S. Sarojini and R. V. Vijayalakshmi, “XPS studies on silver ion conducting solid electrolyte SbI3–Ag2MoO4,” Materials Today: Proceedings, vol. 68, pp. 314-318, 2022.

報告型式：

□英文口頭報告競賽 (□無機材料， □有機材料)
□海報展示並參加壁報論文競賽(□無機材料， □有機材料)
☑只參加海報展示 (☑無機材料， □有機材料)